

4D-MRI for thoracic radiotherapy treatment planning and guidance on an MR-linac

A thesis submitted for the degree of
Doctor of Philosophy

Joshua Nathan Freedman

Joint Department of Physics

The Institute of Cancer Research and
The Royal Marsden NHS Foundation Trust

University of London, United Kingdom

I, Joshua Nathan Freedman, confirm that the work presented in this thesis is my own. Where information has been derived from other sources, I confirm that this has been indicated in the work.

Abstract

Lung cancer currently has a poor prognosis in England and Wales with only 10 % of adults surviving five years or more after diagnosis. The poor survival rate demonstrates the need to improve contemporary treatment approaches such as external beam radiotherapy, which is part of the treatment course for approximately 30 % of lung cancer patients. In thoracic radiotherapy workflows, the tumour site is treated with targeted radiation over several treatment sessions (fractions). Conventionally, each fraction is planned based on a single 4D-CT scan acquired prior to the first fraction. This planning approach does not account for changes in patient anatomy or respiratory pattern occurring throughout the treatment course, which can cause unnecessary irradiation of healthy tissue and under-dosage of the tumour site. Inter-fractional changes in anatomy and respiratory pattern could be corrected for by adapting the treatment plan using 4D-MRI acquired at the beginning of each fraction. It is feasible to perform MR imaging, plan adaptation and treatment delivery in the same fraction using an MR-linac system. In this studentship, methods to obtain 4D-MRI for thoracic radiotherapy treatment planning and guidance on an MR-linac were explored. In particular, methods to calculate T2-weighted 4D-MRI (4D-T2w MRI) and synthetic 4D-CT (4D-sCT) were investigated.

Compared to 4D-CT and T1-weighted 4D-MRI, the high soft-tissue contrast exhibited by 4D-T2w MRI could facilitate delineation of tumour sites affected by respiratory motion, especially when adjacent to areas of healthy tissue. Two methods to obtain 4D-T2w MRI were developed and verified. In the motion vector field projection (MVFP) method, 4D-T2w MRI were calculated by applying

the motion information from 4D-T1w to 3D-T2w MRI. In the super-resolution approach, continuously acquired axial and sagittal 2D-T2w images were combined into one high-resolution 4D-T2w image using binning, image registration and super-resolution reconstruction. Unlike existing techniques based on slice-selection, the MVFP and super-resolution methods resulted in geometrically accurate 4D-T2w MRI with high spatio-temporal resolution.

4D-sCT can provide motion-compensated electron density information required for treatment planning. Three consecutive techniques (Dixon-based, Dixon-Spine and Dixon-Spine-Lung) to generate 4D-sCT were developed and validated. In the Dixon-Spine-Lung method, 4D-sCT were obtained using bulk-density assignment (Dixon), best-atlas segmentation (spine), polynomial fitting (lung) and motion-modelling (4D component). Overall, good dosimetric agreement was found between Dixon-Spine-Lung 4D-sCT and 4D-CT. Prior to this studentship, no MRI-derived 4D-sCT implementation was published.

Deep learning was utilised to accelerate motion-compensated 4D-T1w MRI reconstruction from 9-12 hours to 28 seconds. The MVFP method was accelerated using deep learning-based 4D-T1w MRI and then applied to obtain 4D-T2w MRI from MR-linac data. Compared to super-resolution reconstructed and phase binned 4D-T2w MRI, MVFP-generated 4D-T2w MRI was found best suited for on-line application in an MR-linac workflow. In particular, it exhibited good spatio-temporal resolution and required less than 6 minutes to reconstruct.

Acknowledgements

Firstly, I would like to express enormous gratitude to Andreas Wetscherek for all of his help, support and guidance over the last four years. The work presented in this thesis would not have been possible without his day-to-day supervision and encouragement. I would also like to thank David Collins, Simeon Nill, Uwe Oelfke and Martin Leach for their continual supervision and support throughout the project.

I am extremely grateful to the many clinicians I have collaborated with during my PhD. In particular, special thanks go to Hannah Bainbridge for her valuable clinical input and time spent performing radiotherapy treatment planning. I would also like to thank Anna-Maria Shiarli, Fiona McDonald, Dow-Mu Koh and Nina Tunariu for their help acquiring and analysing MRI data. Thanks also to the the MRI and MR-linac radiographers Erica Scurr, Cynthia Eccles, Trina Herbert and Helen McNair for scanning patients and volunteers for me.

I am indebted to my collaborators Christopher Rank and Marc Kachelrieß from DKFZ for developing and sharing the 4D joint MoCo-HDTV reconstruction tool. I am also grateful to Jamie McClelland from UCL for his assistance with installing and applying the NiftyReg software.

I would like to thank everyone in the Joint Department of Physics. First, I wish to acknowledge the Physics secretaries for all of their administrative support. In addition, thank you to Annette and Cheryl for always making me laugh in the morning! I am also grateful to the Physicists Alex Dunlop, Dualta McQuaid, Matt Orton and Simon Doran for many interesting discussions and support with data analysis. Special thanks go to Oliver for becoming one of my closest friends

Acknowledgements

and also for helping me to develop the super-resolution and Dracula 4D-MRI methods. You will be especially missed! Thanks also to my fellow PhD students, in particular to Jennifer and Filipa for all the fun had travelling around New South Wales and California.

I would like to acknowledge NHS funding to the NIHR Biomedical Research Centre and the Clinical Research Facility at the Institute of Cancer Research and The Royal Marsden NHS Foundation Trust. I wish also to acknowledge Cancer Research UK grants C309/A20926, C1060/A16464 and C33589/A19727, which contributed to funding the studies described in this thesis. I gratefully acknowledge the support of NVIDIA Corporation with the donation of the Quadro P6000 GPU.

I am extremely grateful for the love and support from my sister Lauren and parents Roger, Lynette, Angie, Robert, Rachel and David. I would also like to thank Granny Anne Fairweather for keeping me company whilst developing the Dracula method. Finally, I would like to dedicate this thesis to my wife Anna. Thank you Anna for your brightness and unlimited patience with all things PhD-related, I couldn't have done it without you!



Last but not least thanks to Barney.

Contents

Contents	7
List of Figures	13
List of Tables	16
List of Abbreviations	17
1 Introduction	20
1.1 Introduction	21
1.2 Lung cancer	21
1.3 External beam radiotherapy	22
1.3.1 External beam radiotherapy workflow	22
1.3.2 Limitations of the external beam radiotherapy workflow . .	24
1.4 MR guided radiotherapy treatment planning	26
1.4.1 Advantages of MR guided radiotherapy treatment planning	26
1.4.2 Challenges of MR guided radiotherapy treatment planning	28
1.4.3 Hybrid MR guided radiotherapy systems	30
1.4.4 4D-MRI on an MR-linac	32
1.5 Thesis aims and outline	33
2 Principles of 4D-MRI - an outline	35
2.1 MRI physics	36
2.1.1 Nuclear magnetic resonance	36
2.1.1.1 Magnetic moments and the Bloch equations . . .	36

2.1.1.2	Free induction decay	39
2.1.1.3	Rotating frame of reference	42
2.1.1.4	Radio-frequency pulses	43
2.1.2	Magnetic resonance imaging	44
2.1.2.1	Magnetic field gradients and the Fourier transform	44
2.1.2.2	K-space	46
2.1.2.3	Slice-selection	48
2.1.3	Pulse sequences	50
2.1.3.1	Spoiled gradient echo	50
2.1.3.2	2-point Dixon	51
2.1.3.3	Spin echo	53
2.1.3.4	Turbo spin echo	54
2.2	Principles of 4D-MRI	55
2.2.1	Binning	55
2.2.1.1	Amplitude binning	55
2.2.1.2	Phase binning	56
2.2.2	Slice-selective methods	57
2.2.2.1	Prospective acquisitions	57
2.2.2.2	Retrospective acquisitions	57
2.2.2.3	Artefacts associated with retrospective slice-selective methods	58
2.2.3	Volumetric methods	59
2.2.3.1	Radial stack-of-stars pulse sequence	60
2.2.3.2	4D joint MoCo-HDTV algorithm	61
2.2.4	Deformable image registration	63
2.2.4.1	Demons registration	64
2.2.4.2	B-splines registration	66
2.2.5	Machine learning and deep convolutional neural networks .	68

3	Development of the motion vector field projection method to calculate T2-weighted 4D-MRI	71
3.1	Introduction	72
3.2	Materials and methods	73
3.2.1	Data acquisition	73
3.2.2	Reconstruction of T1w data	74
3.2.3	Overview of the MVFP method	76
3.2.4	Calculation and application of motion vector fields	77
3.2.5	Verification of 4D-T2w MRI	79
3.2.5.1	Edge-detection method	79
3.2.5.2	Delineated control points	81
3.2.5.3	Volumetric image similarity	83
3.3	Results	83
3.3.1	Verification of 4D-T2w MRI	85
3.3.2	Image artefacts	89
3.3.3	Clinical evaluation	90
3.4	Discussion	92
3.5	Conclusion	96
4	Development of a super-resolution reconstruction method to calculate T2-weighted 4D/midposition MRI	97
4.1	Introduction	98
4.2	Materials and methods	99
4.2.1	Data acquisition	99
4.2.2	Workflow	100
4.2.2.1	Binning	100
4.2.2.2	Motion-modelling	104
4.2.2.3	Principles of super-resolution reconstruction	105
4.2.2.4	Super-resolution reconstruction	106
4.2.3	Verification of T2-weighted 4D/midposition MRI	108

4.2.3.1	Deformable image registration	108
4.2.3.2	Image resolution	108
4.2.3.3	Phantom measurements	109
4.2.3.4	Colour intensity projections	111
4.2.4	Midposition dependence on number of dynamics	112
4.3	Results	113
4.4	Discussion	119
4.5	Conclusion	122
5	Development of three Dixon-based methods to calculate synthetic 4D/midposition CT	123
5.1	Introduction	124
5.2	Materials and methods	125
5.2.1	Data acquisition	125
5.2.2	Motion-modelling	127
5.2.3	Atlas	129
5.2.4	Dixon-based synthetic CT (sCT_D)	129
5.2.5	Dixon-Spine synthetic CT (sCT_{DS})	131
5.2.6	Dixon-Spine-Lung synthetic CT (sCT_{DSL})	131
5.2.7	Validation of synthetic CT	132
5.3	Results	133
5.3.1	Validation: Hounsfield units	136
5.3.2	Validation: dose-volume metrics	136
5.3.3	Comparison of synthetic CT methods	137
5.4	Discussion	140
5.5	Conclusion	145
6	Application of deep convolutional neural networks to reconstruct motion vector fields and T1-weighted 4D/midposition MRI	146
6.1	Introduction	147
6.2	Materials and methods	149

6.2.1	Data acquisition	149
6.2.2	Reconstruction of T1w data	150
6.2.3	Calculation of midposition images and motion vector fields	151
6.2.4	Pre-processing of T1w data	151
6.2.5	Implementation of Dracula	153
6.2.6	Training and application of Dracula	156
6.2.7	Verification of Dracula-reconstructed images	157
6.3	Results	159
6.3.1	Dracula-reconstructed MoCo 4D-MRI	159
6.3.2	Dracula-reconstructed MidP-MoCo images	160
6.3.3	Dracula-reconstructed MidP-Warped 4D-MRI	164
6.4	Discussion	166
6.5	Conclusion	170
7	Comparison of T2-weighted 4D-MRI methods for application on an MR-linac	171
7.1	Introduction	172
7.2	Materials and methods	173
7.2.1	Data acquisition	173
7.2.2	Calculation of 4D-T2w MRI	177
7.2.2.1	Phase binning	177
7.2.2.2	Optimising the super-resolution method	178
7.2.2.3	Optimising the motion vector field projection method	180
7.2.3	Comparison of 4D-T2w MRI	180
7.3	Results	181
7.4	Discussion	184
7.5	Conclusion	187
8	Discussion	188
8.1	Summary of thesis studies	189
8.2	Clinical applications of 4D-T2w MRI and 4D-sCT	192

8.3	Future work	194
8.3.1	Methodological improvements	194
8.3.2	Deep learning-based image reconstruction	196
8.4	Final conclusion	197
	References	198
	Dissemination of research	221
	Appendix A: T2-Weighted 4D Magnetic Resonance Imaging for Application in Magnetic Resonance–Guided Radiotherapy Treatment Planning, Freedman <i>et al</i> 2017	224
	Appendix B: Super-resolution T2-weighted 4D MRI for image guided radiotherapy, Freedman <i>et al</i> 2018	236
	Appendix C: Synthetic 4D-CT of the thorax for treatment plan adaptation on MR-guided radiotherapy systems, Freedman <i>et al</i> 2019	245

List of Figures

1.1	An overview of the conventional external beam radiotherapy workflow	23
1.2	An example comparison between CT, T1w MRI and T2w MRI . .	27
1.3	An overview of the Elekta Unity MR-linac	31
2.1	An illustration of a spinning proton	37
2.2	An example simulation of free induction decay	41
2.3	An example diagram of 2D k-space	47
2.4	An illustration of a sinc-pulse and top-hat Fourier transform pair	49
2.5	Pulse sequence diagram for a 2D spoiled gradient echo sequence .	51
2.6	Pulse sequence diagram for a 2-point Dixon gradient echo sequence	52
2.7	Pulse sequence diagram for a 2D spin echo sequence	53
2.8	Pulse sequence diagram for a 2D turbo spin echo sequence	54
2.9	An illustration of amplitude binning	56
2.10	An illustration of artefacts associated with slice-selective techniques	59
2.11	Pulse sequence diagram for a 3D radial stack-of-stars sequence . .	61
2.12	An example comparison of Gridded and 4D joint MoCo-HDTV-reconstructed images	64
2.13	An illustration of deformable image registration	65
2.14	An overview of B-spline deformable image registration	67
2.15	An example of B-spline deformable image registration	68
2.16	An illustration of a 2D convolution	69
2.17	An illustration of max pooling	70

3.1	Patient set-up used to obtain MRI for the MVFP method	74
3.2	An overview of the MVFP method	76
3.3	An overview of the chain method	78
3.4	An illustration of the edge-detection tool	80
3.5	Example screenshots of the control point delineation toolkit . . .	81
3.6	An example of control point delineation	82
3.7	An example 4D-T2w image obtained using the MVFP method . .	84
3.8	Verification of the MVFP method: edge-detection results	86
3.9	Verification of the MVFP method: control-point results	87
3.10	Verification of the MVFP method: NMI results	88
3.11	An illustration of MVFP-related registration artefacts	89
3.12	An example of intensity inhomogeneity artefacts in T2w MRI . .	90
3.13	An additional example MVFP-generated 4D-T2w image	91
4.1	Volunteer set-up used for the super-resolution method	100
4.2	An overview of the motion-modelling and super-resolution method	102
4.3	An overview of the principle respiratory signal calculation	103
4.4	A detailed flow-chart describing the super-resolution method . . .	107
4.5	An example of edge-detection in the presence of stitching artefacts	108
4.6	An overview of the QUASAR TM respiratory motion phantom . . .	110
4.7	A comparison between low- and super-resolution T2w MRI at inhalation	113
4.8	A comparison of low- and super-resolution T2w MRI at midposition	114
4.9	A comparison of the motion information contained in low- and super-resolution T2w MRI	115
4.10	Verification of the super-resolution method: phantom results . . .	117
4.11	Verification of the super-resolution method: CIPs	118
4.12	An overview of the data subsampling results	118
5.1	Patient set-up used to obtain MRI for the sCT methods	126
5.2	An overview of the Dixon-Spine-Lung sCT method	128

5.3	An example of intensity-based segmentation and assignment of HUs	130
5.4	An example comparison between MidP-CT and sCT _{D,DS,DSL}	134
5.5	An illustration of the overlapping structure artefact in MidP-CT	134
5.6	An example 4D-sCT image obtained using the Dixon-Spine-Lung method	135
5.7	A comparison between HUs exhibited by CT and sCT images	137
5.8	Differences in selected dose-volume metrics between CT and sCT	138
5.9	An example dosimetric comparison between planning on sCT _{D,DS,DSL} and evaluation on CT	140
5.10	An example of emphysematous tissue displayed in CT and T1w MRI	144
6.1	An overview of the 3D Dracula neural network architecture	155
6.2	Example optimizer loss convergence curves for networks 1-3	157
6.3	An example comparison between Gridded, Dracula-reconstructed and joint MoCo-HDTV-reconstructed 4D-T1w images	161
6.4	An example comparison between Gridded (exhalation phase), Dracula-reconstructed MidP and joint MoCo-HDTV-reconstructed MidP images	163
6.5	An example comparison of the 4D Gridded, Dracula-reconstructed MidP-Warped and 4D joint MoCo-HDTV-reconstructed images	165
7.1	Experimental set-up used to acquire MRI on the MR-linac	174
7.2	A screen-shot of the modified MR-linac user interface and a snapshot of the patched 3D radial stack-of-stars pulse sequence diagram	175
7.3	An example of a 1D navigator signal acquired on the MR-linac	177
7.4	An example comparison of super-resolution reconstructed T2w MRI calculated using different regularisation weightings	180
7.5	An example comparison between two navigator signals	182
7.6	An example comparison of 4D-MRI obtained using an MR-linac	183

List of Tables

3.1	Acquisition parameters of the T1w and T2w sequences used in the MVFP method	75
4.1	Acquisition parameters of the T2w sequences used in the super-resolution method	101
5.1	Acquisition parameters of the T1w and Dixon sequences used in the sCT methods	127
5.2	A summary of the absolute dose-volume metric differences between sCT _{DSL} and CT	139
6.1	Acquisition parameters of the T1w sequence used to train and validate Dracula	149
6.2	A summary of the observer study results	162
7.1	Acquisition parameters of the sequences applied on the MR-linac .	176
7.2	A comparison of the liver-dome positional ranges in 4D-T2w MRI to the amplitude ranges extracted from the navigator signal . . .	182

List of Abbreviations

1D	one-dimensional.
2D	two-dimensional.
3D	three-dimensional.
4D	four-dimensional.
ADC	analog-to-digital.
CBCT	cone beam computed tomography.
CIP	colour intensity projection.
CT	computed tomography.
CTV	clinical target volume.
dCNN	deep convolutional neural network.
DIR	deformable image registration.
DNA	deoxyribonucleic acid.
Dracula	deep radial convolutional.
emf	electromotive force.
FDG	fluorodeoxyglucose.
FOV	field-of-view.
<i>G_{PO}</i>	phase-encoding gradient.

List of Abbreviations

G_{RO}	read-out gradient.
G_{SB}	slab-select gradient.
G_{SS}	slice-select gradient.
GPU	graphics processing unit.
GTV	gross tumour volume.
Gy	Gray.
HASTE	half Fourier turbo spin echo.
HU	Hounsfield unit.
IRS	image-driven respiratory surrogate signals.
ITV	internal target volume.
joint MoCo-HDTV	joint motion-compensated high-dimensional total variation.
MidP	midposition.
MR	magnetic resonance.
MRgRT	magnetic resonance guided radiotherapy.
MRI	magnetic resonance imaging.
MR-linac	magnetic resonance linear accelerator.
MVF	motion vector field.
MVFP	motion vector field projection.
NMI	normalised mutual information.
OAR	organ at risk.
PET	positron emission tomography.
PRS	principle respiratory signal.

List of Abbreviations

PTV	planning target volume.
ReLU	rectified linear unit.
ROI	region of interest.
RTP	radiotherapy treatment planning.
SABR	stereotactic ablative radiotherapy.
SAR	specific absorption rate.
sCT	synthetic-CT.
SI	superior-inferior.
SNR	signal-to-noise ratio.
SSIM	structural similarity index metric.
SS-TSE	single shot turbo spin echo.
T_E	echo time.
T_R	repetition time.
T1w	T1-weighted.
T2w	T2-weighted.
TSE	turbo spin echo.
UTE	ultrashort echo time.
VMAT	volumetric modulated arc therapy.

Chapter 1

Introduction

This thesis considers 4D-MRI for thoracic radiotherapy treatment planning and guidance on an MR-linac. In this chapter, MR guided radiotherapy is introduced in response to limitations of the conventional external beam radiotherapy workflow. MR-linac systems are then discussed and potential 4D-MRI applications are reviewed. This chapter concludes with an outline of the studies presented in the remainder of the thesis.

1.1 Introduction

In this chapter, a short overview of lung cancer and its available treatments is provided. Afterwards, the conventional thoracic radiotherapy workflow is introduced and its limitations are outlined. Subsequently, magnetic resonance (MR) guided radiotherapy, including magnetic resonance linear accelerator (MR-linac) systems and four-dimensional (4D) magnetic resonance imaging (MRI), is introduced. Advantages and challenges associated with MR guided radiotherapy treatment planning are also discussed. The final section describes the thesis aims and outline.

1.2 Lung cancer

Lung cancer is the main cause of cancer mortality worldwide and, in 2018, was responsible for approximately 1.76 million deaths globally (World Health Organization, 2019). In England and Wales, lung cancer has a poor prognosis, as only 10 % of adults survive for five years or more after diagnosis (Cancer Research UK, 2019a). In the UK, lung cancer survival statistics have changed little over the past 40 years (Cancer Research UK, 2019a), demonstrating the need to improve contemporary treatment approaches and detection strategies. Early disease detection and diagnosis could be improved by introducing a nationwide lung cancer screening program (Field et al., 2016).

Current lung cancer treatments include: surgery (e.g. lobectomy), radiotherapy, immunotherapy and chemotherapy. The chosen treatment pathway largely depends on the disease's histological subtype, molecular biology and stage. This thesis will focus on external beam radiotherapy, which is part of the treatment course in England for approximately 42 % and 27 % of small and non-small cell lung cancer patients, respectively (Cancer Research UK, 2019b).

1.3 External beam radiotherapy

In external beam radiotherapy, the tumour is exposed to high doses of ionizing radiation delivered from a source outside the patient anatomy. Note that delivered dose (dE/dM) refers to the mean energy dE deposited in a material with mass dM and is measured in grays (Gy)s, where $1 \text{ Gy} = 1 \text{ J/kg}$ (Khan and Gibbons, 2014) p.106. The delivered radiation damages deoxyribonucleic acid (DNA) in both healthy and cancerous cells along its path, either by direct or indirect interactions (Joiner and Kogel, 2016). In direct interactions, ionizing radiation induces single and double-strand breaks in DNA. In indirect interactions, DNA is damaged by free radicals, which are created in cell cytoplasm by ionizing radiation. Radiation delivery is carefully designed to minimise the damage to healthy tissue and organs, whilst maintaining the prescribed dose to the tumour site and spread of microscopic malignant disease.

1.3.1 External beam radiotherapy workflow

In UK hospitals, external beam radiotherapy is currently performed for lung cancer patients according to the National Institute for Health and Care Excellence guidelines (NICE, 2019), as summarised in Figure 1.1. The conventional external beam radiotherapy workflow employs computed tomography (CT), cone-beam CT (CBCT) and ^{18}F -fluorodeoxyglucose (FDG) position emission tomography (PET) images (Bainbridge et al., 2017).

First, diagnostic CT and ^{18}F -FDG PET scans are obtained for disease staging, which informs future treatment decisions and the radiotherapy dose prescription. Next, planning CT and potentially ^{18}F -FDG PET scans are acquired with the aid of immobilisation devices for radiotherapy treatment planning (RTP). Based on the planning scans, a radiation oncologist delineates the gross tumour volume (GTV) and organs at risk (OARs), e.g. lungs and heart. Margins are added to the GTV to account for spread of microscopic malignant disease [clinical target volume (CTV)] (ICRU, 1999). The CTV margin is then increased to include

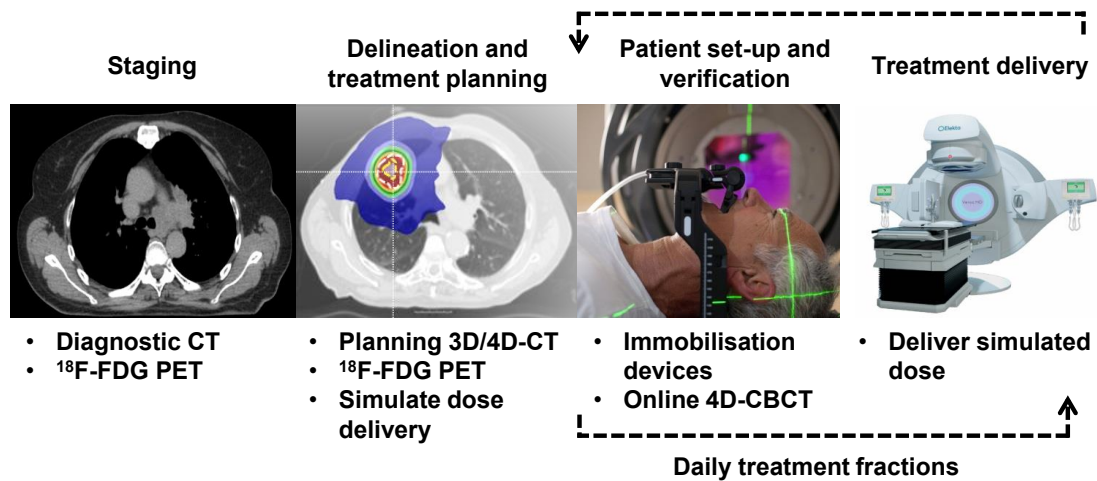


Figure 1.1: An overview of the conventional external beam radiotherapy workflow for lung cancer patients. The third and fourth images (left to right) were adapted from (Elekta, 2017a) and (Elekta, 2017b), respectively.

uncertainties associated with respiratory motion [internal target volume (ITV)]. Afterwards, the ITV margin is expanded to account for errors in patient set-up and delivery [planning target volume (PTV)]. The ITV margin can be calculated from an additionally acquired 4D-CT image, based on the range of exhibited tumour motion (Wolthaus et al., 2008b). Four-dimensional CT refers to a time series of 3-dimensional (3D) CT images, where each image corresponds to a different phase (i.e. time-point) in the respiratory cycle. Often, 3D-CT obtained by averaging over the respiratory phases of 4D-CT is employed instead of the above-described planning CT scan.

Alternatively, a midposition (MidP) (time-weighted mean position of the respiratory cycle) image can be calculated from 4D-CT and applied for target and OAR delineation (Wolthaus et al., 2008a). The MidP image exhibits reduced respiratory motion artefacts and noise compared to planning CT (acquired in free-breathing) or individual phases of 4D-CT, respectively. In the MidP planning concept, periodic respiratory-related tumour displacement is considered as a random localisation error, relative to MidP, during treatment delivery. Whereas in the ITV approach, periodic respiratory tumour motion is treated as a systematic localisation error in the planning images. Unlike in the MidP planning concept,

the error associated with periodic respiratory motion is overestimated in the ITV approach, leading to a comparatively large planning margin. The relatively smaller margin applied in the MidP planning concept permits reduced irradiation of healthy tissues. In this thesis, MidP images were calculated from amplitude-binned 4D-MRI following the same methodology outlined for phase-binned 4D-CT images (Wolthaus et al., 2008a). More details regarding the MidP planning concept and a discussion of other possible 4D planning methodologies can be found in (Wolthaus et al., 2008b).

In the treatment planning stage, dosimetrists or physicists design and simulate the treatment delivery, such that dose to healthy tissues and radio-sensitive OARs is minimised, whilst concomitantly maintaining the prescribed dose to the tumour site. Note that dose calculations in the treatment planning workflow require electron density information contained in CT images.

Prior to treatment delivery, the patient is placed on the treatment couch in the same position as for the planning scans, which is facilitated using immobilisation devices. Afterwards, the patient's position is verified by comparing 4D images acquired on an on-board CBCT system to the planning CT images. Differences in positioning between the CBCT and planning CT images are then corrected for by translating the treatment couch. For locally-advanced lung cancer patients, the displacement between carina positions in CBCT and planning CT images is used to define couch translation (Bainbridge et al., 2017). Once positioned, treatment delivery is performed as per the simulated plan. Patient positioning, verification and treatment delivery are repeated daily until a set number of fractions have been completed.

1.3.2 Limitations of the external beam radiotherapy workflow

There are several limitations associated with the conventional external beam radiotherapy workflow. For instance, it can be challenging to delineate tumour

adjacent to healthy tissue in the planning CT image, due to its poor soft-tissue contrast. In the literature, the uncertainty associated with target delineation on CT images has been quantified by comparing GTV delineations performed by multiple observers (Louie et al., 2010; Steenbakkers et al., 2006; Versteijne et al., 2017). In (Steenbakkers et al., 2006), 11 observers delineated the GTV on planning CT images of 22 lung cancer patients. For each patient, the median GTV surface was calculated using the GTV delineations performed by all observers. Observer variations were then determined, for each patient, as the distances between individually delineated GTV surfaces and the median GTV surface. Overall, a high inter-observer variation (standard deviation of all calculated observer variations) of approximately 1.0 cm was found. More reproducible lung target delineations can be obtained by instead contouring on fused ^{18}F -FDG PET and CT planning images (Steenbakkers et al., 2006). However, the efficacy of ^{18}F -FDG PET is currently limited for delineation purposes by its low spatial resolution (5-7 mm) (Hanna et al., 2012; Kumar et al., 2016).

An additional limitation is that each fractionated delivery is based on the same pre-treatment planning images, which does not account for changes in respiratory pattern or patient anatomy throughout the treatment course (Bainbridge et al., 2017). For eight lung cancer patients, Britton et al. (2007) investigated inter-fractional changes in tumour motion by comparing the GTV-centroid positions extracted from weekly acquired 4D-CT images with those calculated from a base-line 4D-CT (week 0). They reported average (mean and standard deviation over all patients) superior-inferior changes in GTV-centroid positions of magnitude 0.54 ± 0.32 cm, highlighting the need to account for inter-fractional changes in respiratory motion. Kwint et al. (2014) investigated the type and severity of inter-fractional anatomical changes occurring in 177 lung cancer patients using 1793 CBCT images. Inter-fractional anatomical changes were observed in 128 patients, which predominately included tumour regression (35 %), tumour base-line shift (27 %) and changes in atelectasis (19 %). Inter-fractional changes in respiratory pattern and patient anatomy could be accounted for by replanning on weekly

acquired 4D-CT (Ramella et al., 2017). However, repetitive 4D-CT acquisition is sub-optimal for paediatric populations where exposure to ionizing radiation needs to be carefully controlled (Kumar et al., 2016; Schmidt and Payne, 2015). Further limitations of the conventional external beam radiotherapy workflow have been described elsewhere (Bainbridge et al., 2017).

1.4 MR guided radiotherapy treatment planning

1.4.1 Advantages of MR guided radiotherapy treatment planning

The advantages of integrating MRI into the external beam radiotherapy workflow have long been recognised (Khoo et al., 1997). Unlike CT, MRI offers a range of complementary high soft-tissue contrasts, which can be optimised to facilitate tumour and OAR visualisation (e.g. Figure 1.2). For instance, in the thorax T1-weighted (T1w) MRI is recommended for detection of pulmonary nodules and masses, and T2-weighted (T2w) MRI for visualisation of lesions with high fluid content (Biederer et al., 2012; Kumar et al., 2016). Improved tumour visualisation in MRI enables more reproducible target delineations when compared to CT, which has been demonstrated for several sites including head and neck (Rasch et al., 1997), prostate (Rasch et al., 1999) and pancreas (Gurney-Champion et al., 2017). For the thorax, Karki et al. (2017) did not find significant differences in inter-observer variability when comparing CT, fused PET-CT and MRI for lung target delineation. Nevertheless, it is expected that contouring variability associated with MRI might be reduced for tumours adjacent to the mediastinum or oesophagus (Riddell et al., 2006). Decreased contouring uncertainties might reduce unwanted irradiation of OARs by enabling smaller planning margins. Sparing healthy OARs from unnecessary irradiation could reduce the risk of side-effects such as acute oesophagitis (Rose et al., 2009).

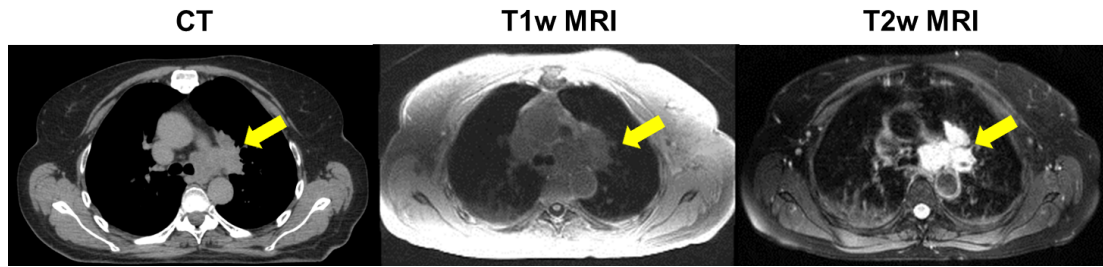


Figure 1.2: A comparison between CT, T1-weighted (T1w) and T2-weighted (T2w) MRI for a lung cancer patient. The tumour (yellow arrows) extent and structure is better defined on MRI than CT.

Inter-fractional changes in patient anatomy could be accounted for using MRI acquired shortly before each treatment fraction (Bostel et al., 2014; Jaffray et al., 2014; Karlsson et al., 2009; Paulson et al., 2015). Similarly to reducing contouring uncertainties, accounting for inter-fractional changes would also enable sparing of healthy OARs. In one approach to incorporate MRI into the radiotherapy workflow (Karlsson et al., 2009), a special trolley was developed to shuttle patients between an MRI unit and a close-by room equipped with a linear accelerator. In another approach, the MRI scanner itself was transferred to and from the accelerator room via a rail-system (Jaffray et al., 2014). Alternatively, an existing diagnostic scanner might be modified for RTP purposes using commercially available equipment, such as a flat table-top and elevated coil-holder (Paulson et al., 2015). Repetitive MRI scanning prior to each treatment fraction is feasible for the majority of populations, as MRI uses non-ionizing radio-frequency (RF) radiation for signal acquisition (Schmidt and Payne, 2015). For the thorax, both anatomical and respiratory motion information could be regularly updated using 4D-MRI (Stemkens et al., 2018). In this thesis, 4D-MRI is defined in analogy to 4D-CT, as a time-series of 3D MR images in the respiratory phase domain.

Magnetic resonance imaging has many other applications in the radiotherapy workflow, but these are beyond the scope of this thesis. Further information regarding MR guided RTP can be found elsewhere (Owrangi et al., 2018; Schmidt and Payne, 2015).

1.4.2 Challenges of MR guided radiotherapy treatment planning

Integrating MRI into the radiotherapy workflow has been hampered by several challenges. For instance, scanner and patient-dependent perturbations in magnetic field homogeneity result in geometrical image distortions (Khoo et al., 1997; Schmidt and Payne, 2015), which could diminish the geographical accuracy of delivered dose (Weygand et al., 2016). Scanner-dependent geometrical distortions predominantly arise from gradient non-linearities (Baldwin et al., 2007) and increase in magnitude away from iso-centre (Doran et al., 2005). Gradient non-linearity distortion errors can be reduced using a spherical harmonics deconvolution method (Doran et al., 2005; Janke et al., 2004). Patient-dependent distortions are caused by off-resonance due to chemical shift and magnetic susceptibility differences between tissues (Weygand et al., 2016). In the thorax, large susceptibility-induced distortions are expected due to multiple microscopic lung-air interfaces in the alveoli and airways (Wild et al., 2012). Patient-dependent distortions can be accounted for using separately acquired B_0 maps (Jezzard and Balaban, 1995) or reduced through pulse-sequence optimisation (e.g. bandwidth can be increased) (Schmidt and Payne, 2015). In a recent consensus by the Elekta MR Linac Research Consortium (Paulson et al., 2016), geometrical distortion errors within 2 mm were deemed acceptable by medical Physicists for RTP in several sites including head and neck, cervix and brain. At the time of writing, no similar consensus had been reached for the thorax.

As mentioned in section 1.3.1, electron density information is required for dose calculations in RTP. Unlike CT, MR image intensities are dependent on proton density and tissue relaxation times (T_1 , T_2 and T_2^*), and therefore do not directly correspond to electron density (Khoo et al., 1997). One approach to obtain representative electron density information is to register CT to MRI (Schmidt and Payne, 2015). However, CT-MRI registration has been demonstrated to result in errors of magnitude 2-5 mm for treatment sites including head and neck (Daisne

et al., 2003), prostate (Nyholm et al., 2009) and rectum (Dean et al., 2012). In the thorax, registration errors might be larger due to poor signal-to-noise ratio (SNR) exhibited by MRI and discrepancies in respiratory phase between MRI and CT scans. Furthermore, errors are expected to increase when registering pre-treatment CT with MRI acquired at subsequent fractions in the treatment course, since the patient anatomy might be substantially different (Kwint et al., 2014). Registration errors can be eliminated by instead extracting electron density information from a synthetic-CT (sCT) image directly calculated from MRI (Edmund and Nyholm, 2017). Application of sCT in treatment planning would obviate the need to acquire a planning CT image (Johnstone et al., 2018), which is advantageous as it would simplify the radiotherapy workflow by reducing the total number of scheduled examinations.

In the literature, sCT is validated against CT by comparison of Hounsfield units (HUs) and metrics associated with RTP, which include gamma analysis and dose-volume metrics (Owrangi et al., 2018). However, such comparisons are limited as MRI-derived sCT cannot be directly evaluated against CT without performing multi-modal deformable image registration (DIR). As discussed above, high CT-MRI registration errors are expected in the thorax. Confounding registration errors can be mitigated using physical phantoms to validate sCT (Kraus et al., 2017; Rank et al., 2013; Soliman et al., 2017). For the thorax, several anthropomorphic phantoms have been developed, which include varying degrees of deformable motion (Haas et al., 2014; Perrin et al., 2017). However, widely available commercial phantoms instead concentrate on solid thoracic geometries with simplistic translational and rotational target motions, e.g. the QUASARTM MRI-compatible respiratory motion phantom (Quasar, Modus, Medical Devices Inc., London, Canada).

There are several challenges associated with the application of 4D-MRI in the radiotherapy workflow. Similarly to thoracic sCT, validating 4D-MRI remains problematic due to lack of ground-truth data and no widely available anthropomorphic 4D phantom (Perrin et al., 2017). In a separate problem, it is currently not

clear which 4D-MRI technique most accurately represents the motion of targets and OARs for RTP. For instance, in state-of-the-art non-Cartesian iterative reconstructions (Feng et al., 2014, 2018; Rank et al., 2017) image quality is improved using spatio-temporal regularisation. Whilst this approach facilitates contouring, spatio-temporal regularisation might result in an underestimation of respiratory motion extent and consequently PTV margin size.

As discussed in section 1.4.1, T2w MRI could find application in thoracic MR guided radiotherapy (MRgRT) workflows to facilitate tumour visualisation. Yet, 4D-T2w MRI techniques have received little attention in the radiotherapy literature. This is because it is difficult to obtain 4D-T2w MRI using existing non-Cartesian techniques, due to the long echo and repetition time required to achieve T2w contrast. Further challenges remaining in 4D-MRI have been discussed by (Stemkens et al., 2018).

1.4.3 Hybrid MR guided radiotherapy systems

Although repeated MRI acquisitions can account for inter-fractional changes, they cannot account for changes during treatment delivery, such as breathing or peristalsis. This issue has motivated efforts to develop hybrid MRgRT systems, which combine an MRI scanner and a linac unit (Fallone, 2014; Lagendijk et al., 2014; Mutic and Dempsey, 2014; Raaymakers et al., 2009; Thwaites et al., 2014). Magnetic resonance guided radiotherapy systems enable the target and OARs to be visualised whilst irradiating and, in principle, enable low-latency intra-fractional adaptive radiotherapy.

The scope of this thesis was limited to the Elekta Unity MR-linac system (Elekta AB, Stockholm, Sweden), which combines a closed 1.5 T MRI scanner (modified Philips Ingenia system) with a 7 MV standing wave linac (Raaymakers et al., 2009) (Figure 1.3). Elekta and Philips have overcome the main technical hurdles of combining an MRI scanner with a linac, which are: RF interference between the MRI transmit-receive coils and the linac magnetron, magnetic interference between the B_0 field and linac components, and beam attenuation through the

MRI cryostat. These problems have been solved by complete re-design of the Faraday cage, MR-shimming, RF coil and gradient systems; see (Lagendijk et al., 2014) for more information. The Elekta Unity MR-linac system offers improved SNR and potential for functional imaging when compared to low field (0.35 T) systems (Mutic and Dempsey, 2014). However, images obtained at 1.5 T are more susceptible to patient-dependent geometrical distortions than those obtained with similar acquisition parameters at 0.35 T.

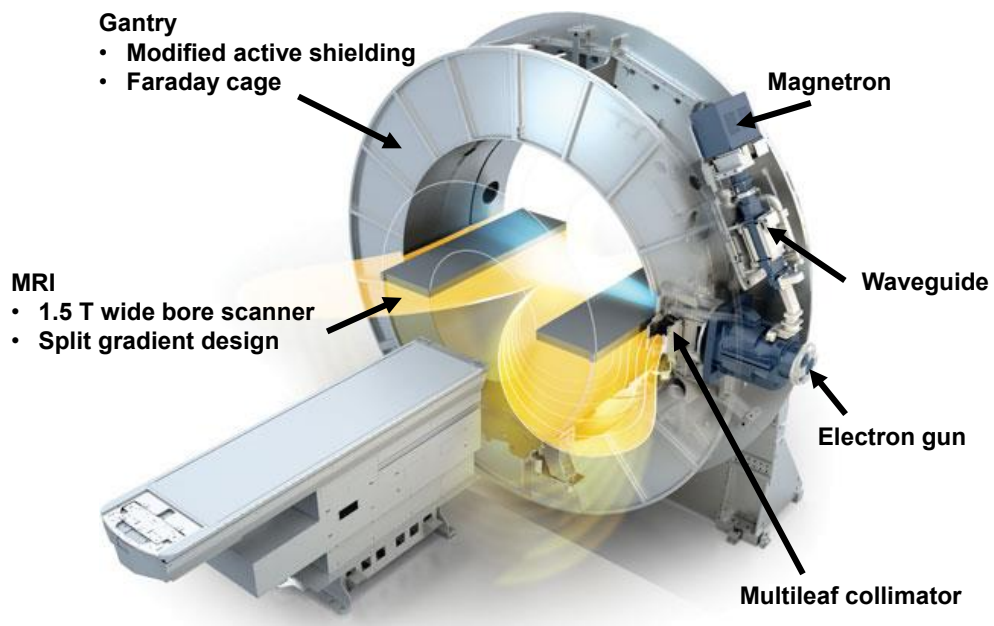


Figure 1.3: Overview of the key components of the Elekta Unity MR-linac. Image courtesy of Elekta AB.

For lung cancer patients, 4D-MRI could be acquired on the MR-linac several minutes prior to treatment delivery and used to rapidly adapt the plan for changes in shape, volume and position of the target and OARs (Bainbridge et al., 2017). Additionally, Bainbridge et al. (2017) highlighted the potential for dynamic multileaf collimator tracking during treatment delivery using volumetric MRI acquired with low-latency. They also discussed the prospect of acquiring functional MRI directly after irradiation for treatment response assessment. This thesis focussed on advancing 4D-MRI methodologies for thoracic radiotherapy treatment planning and guidance on an MR-linac.

1.4.4 4D-MRI on an MR-linac

There are many methods to incorporate 4D-MRI in an MR-linac workflow (Stemkens et al., 2018). In one approach, the treatment plan could be completely re-designed using high-quality 4D-sCT, contour and margin information obtained from 4D-MRI, which was acquired during a pre-beam imaging phase of the workflow. In a separate approach, MidP-MRI and MidP-CT (Wolthaus et al., 2008a) could be calculated from pre-beam 4D-MRI and previously acquired 4D-CT, and then registered (CT to MRI). Afterwards, an updated treatment plan could be generated using the transformed MidP-CT image, transformed MidP-CT contour set and up-to-date respiratory motion information from pre-beam 4D-MRI.

Pre-beam 4D-MRI might also be combined with motion information from rapidly acquired two-dimensional (2D) MRI to obtain a patient-specific motion-model (Harris et al., 2016; Stemkens et al., 2016), which can be applied to generate volumetric MRI with low-latency. Three-dimensional sCT might be continuously acquired with low-latency (≈ 2 Hz) using a similar motion-model to e.g. (Stemkens et al., 2016) by replacing 4D-MRI with 4D-sCT. Three-dimensional sCT rapidly obtained throughout treatment delivery would enable the overall dose delivered during that fraction to be retrospectively calculated (Stemkens et al., 2018; Stemkens et al., 2017).

In intra-fractional strategies, MidP-MRI could be calculated from pre-beam 4D-MRI and then continuously updated throughout the treatment session based on 2D cine MRI (Fast et al., 2019; Kontaxis et al., 2017). Continuously adjusted MidP-MRI could enable adaptation to baseline drifts during treatment delivery.

State-of-the-art non-Cartesian 4D-MRI reconstructions are currently limited for use on MR-linacs by long calculation times of several minutes to hours. Long calculation times might potentially be reduced using deep learning-based image reconstruction techniques (Hammernik et al., 2018; Han et al., 2018).

1.5 Thesis aims and outline

As mentioned in section 1.4.1, T2w contrast is expected to offer improved visualisation of tumours with high fluid content, particularly when adjacent to healthy soft-tissue regions. Prior to this studentship, no method existed to obtain geometrically accurate 4D-T2w MRI with high spatio-temporal resolution. For this reason, the first thesis aim was to develop methods to calculate high-quality 4D-T2w MRI to facilitate delineation of targets and OARs undergoing respiratory motion. In an envisioned thoracic MR-linac workflow, 4D-T2w MRI could be combined with 4D-sCT to enable inter-fractional adaptive RTP. Daily plan adaptation might improve patient outcome by reducing irradiation of normal tissues and by ensuring that the tumour is exposed to the prescribed dose. However, until the work presented in this thesis, no method was published in the literature to obtain 4D-sCT for RTP. The second thesis aim was therefore to develop and validate methods to calculate 4D-sCT for daily plan adaptation.

In Chapter 2, a brief introduction to nuclear magnetic resonance physics and MRI is presented. Furthermore, the principles of 4D-MRI are introduced and state-of-the-art image reconstruction techniques are outlined. Chapter 3 describes the development and validation of a method to obtain high-quality 4D-T2w MRI by transferring the motion information from 4D-T1w to 3D-T2w MRI. Although calculated 4D-T2w MRI exhibited high spatio-temporal resolution, it required a long reconstruction time (9-12 hours) and use of a work-in-progress technique to acquire. In Chapter 4, the development of an alternative method to obtain 4D-T2w MRI is described, in which a super-resolution reconstruction was applied to combine continuously acquired 2D-T2w MRI. The method presented in Chapter 4 employed clinical sequences and required a reduced reconstruction time (23 minutes) compared to the method introduced in Chapter 3. In Chapter 5, three methods were introduced to obtain 3D-sCT based on binning, image registration and polynomial fitting. Using a similar motion-modelling method to that described in Chapter 3, 3D-sCT was then combined with 4D-T1w MRI to

calculate 4D-sCT. High-quality geometrically accurate 4D-sCT was calculated, yet required a long reconstruction time (9-12 hours). To reduce calculation times, a deep learning-based image reconstruction technique was introduced in Chapter 6 and applied to perform 4D-T1w reconstruction in approximately 28 seconds. In Chapter 7, the 4D-T2w MRI techniques introduced in Chapters 3 and 4 were implemented and compared against each other for use on an MR-linac. Note that the technique of Chapter 3 was accelerated using the deep learning approach described in Chapter 6. In Chapter 8 the thesis is concluded with a discussion of the key findings and suggestions to further develop the presented work. Three journal articles have arisen as a consequence of this studentship, a summary and copies of which can be found in the appendices.

Chapter 2

Principles of 4D-MRI - an outline

This chapter provides a brief outline of nuclear magnetic resonance physics and MR imaging theory relevant to this thesis. Afterwards, the principles of 4D-MRI are introduced and background literature on 4D-MRI is critically appraised.

2.1 MRI physics

In this section, the physics of nuclear magnetic resonance and MRI will be briefly introduced to support the material presented in this thesis. A detailed introduction to MRI physics can be found in (Bernstein et al., 2004; Brown et al., 2014b) and references therein. For simplicity and brevity, extensive use is made of the classical description of a spinning proton, which is sufficient for illustrative purposes. In reality, quantum mechanics is required to fully describe nuclear magnetic resonance.

2.1.1 Nuclear magnetic resonance

2.1.1.1 Magnetic moments and the Bloch equations

The majority of molecules in the human body contain hydrogen atoms, which are the main source of signal in clinical MRI examinations. In the classical picture, the proton can be treated as a miniature spinning charge with an associated circulating electrical current (Webb et al., 2012) pp. 493-494. As detailed by (Brown et al., 2014b) p.26, the circulating electrical current gives rise to a magnetic moment $\boldsymbol{\mu}$ described by:

$$\boldsymbol{\mu} = \gamma \mathbf{J} \tag{2.1}$$

Where γ is the gyromagnetic ratio and \mathbf{J} represents the spin angular momentum. For hydrogen, the gyromagnetic ratio can be experimentally measured as: $\frac{\gamma}{2\pi} \approx 42.58 \text{ MHzT}^{-1}$. From quantum mechanics, the spin angular momentum values of a proton can be determined as: $|\mathbf{J}| = \pm \frac{1}{2}\hbar$; where $\hbar = \frac{h}{2\pi}$ and h is Planck's constant; see (Brown et al., 2014b) pp. 68-72 for more information. In the classical picture, spin angular momentum can be described by clock-wise (spin-up \uparrow) or anti-clockwise (spin-down \downarrow) rotation around a central-axis (Figure 2.1).

In normal conditions (i.e. no magnetic field) magnetic moments are randomly

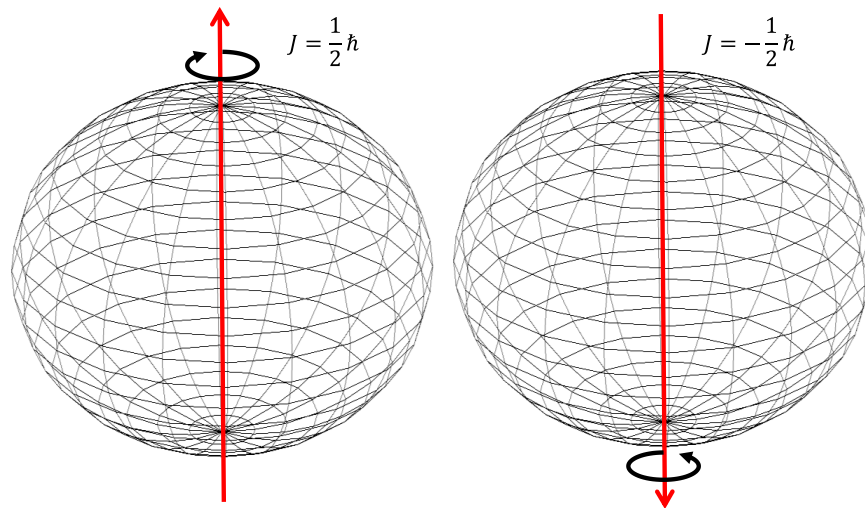


Figure 2.1: In the classical picture, protons can be described as tiny circuits with circulating charge and a magnetic moment. From quantum mechanics, the proton has two spin angular momentum states: spin-up ($|\mathbf{J}| = \frac{1}{2}\hbar$) and spin-down ($|\mathbf{J}| = -\frac{1}{2}\hbar$).

orientated due to non-uniform thermodynamic fluctuations. When applying an external magnetic field \mathbf{B}_0 , magnetic moments experience a torque and either align (spin-up) or anti-align (spin-down) with \mathbf{B}_0 . Magnetic moments with spin-up or spin-down angular momentum have energy levels described by $E = -\boldsymbol{\mu} \cdot \mathbf{B}_0$:

$$E \uparrow = -\frac{1}{2}\hbar\gamma|\mathbf{B}_0| \qquad E \downarrow = \frac{1}{2}\hbar\gamma|\mathbf{B}_0| \qquad (2.2)$$

Where the energy difference ΔE is given by:

$$\begin{aligned} \Delta E &= E \uparrow - E \downarrow \\ &= -\hbar\gamma|\mathbf{B}_0| \end{aligned} \qquad (2.3)$$

The ratio between spin-up and spin-down states $\left(\frac{n_\uparrow}{n_\downarrow}\right)$ can be determined from the Boltzmann distribution:

$$\frac{n_\uparrow}{n_\downarrow} = e^{\frac{-\Delta E}{kT}} \approx 1 - \frac{\Delta E}{kT} + \mathcal{O}\left(\frac{\Delta E}{kT}\right)^2 \qquad (2.4)$$

Where the temperature and Boltzmann constant are denoted by T and k ,

respectively. Note, a Maclaurin series expansion was applied and \mathcal{O} represents the function's order. When applying an external field $|\mathbf{B}_0| = 1.5$ T to a hydrogen sample at room temperature (293 K), $\frac{n_\uparrow}{n_\downarrow} \approx 1.00001$. Because of the large abundance of hydrogen in the body, the excess of protons in the spin-up state is detectable as a net magnetisation \mathbf{M} :

$$\mathbf{M} = \frac{1}{V} \sum_{k=1}^N \boldsymbol{\mu}_k \quad (2.5)$$

Where N describes the total number of protons contained in the volume V . From expression 2.4, \mathbf{M} can be increased by either decreasing the temperature or by applying higher field strengths. Higher \mathbf{M} results in improved SNR in MRI examinations and is one argument for high-field MRI scanners. In thoracic examinations, \mathbf{M} could also be increased using hyperpolarized noble gases, such as ^3He (Möller et al., 2002).

The torque $\boldsymbol{\tau}$ experienced by a magnetic moment when placed in an external magnetic field can be derived as:

$$\boldsymbol{\tau} = \boldsymbol{\mu} \times \mathbf{B}_0 \quad (2.6)$$

The equation of motion of a magnetic moment in an external magnetic field can be derived by substituting expression 2.1 into 2.6, and using $\boldsymbol{\tau} = \frac{d\mathbf{J}}{dt}$:

$$\frac{d\boldsymbol{\mu}}{dt} = \gamma \boldsymbol{\mu} \times \mathbf{B}_0 \quad (2.7)$$

Applying the derived equation of motion with the net magnetization vector of equation 2.5, results in a simplified version of the Bloch equations:

$$\frac{d\mathbf{M}}{dt} = \gamma \mathbf{M} \times \mathbf{B}_0 \quad (2.8)$$

The Bloch equations describe the time-dependent behaviour of the net magnetization vector. Empirically, Bloch proposed a similar set of equations (Bloch,

1946), which included the equilibrium magnetization M_0 , spin-lattice $T1$ and spin-spin $T2$ relaxation times. The Bloch equations assume that the \mathbf{B}_0 field is orientated along the z-dimension. Using the notation: $\mathbf{M} = M_x\hat{x} + M_y\hat{y} + M_z\hat{z}$, the Bloch equations can be written as:

$$\begin{aligned}\frac{dM_x}{dt} &= \gamma(B_zM_y - B_yM_z) - \frac{M_x}{T2} \\ \frac{dM_y}{dt} &= \gamma(B_xM_z - B_zM_x) - \frac{M_y}{T2} \\ \frac{dM_z}{dt} &= \gamma(B_yM_x - B_xM_y) - \frac{M_z - M_0}{T1}\end{aligned}\tag{2.9}$$

2.1.1.2 Free induction decay

This section will introduce free induction decay, which is the time-evolution of an ensemble of protons (i.e. spin packet) when placed in a static magnetic field $\mathbf{B} = B_0\hat{z}$. In free induction decay, the Bloch equations 2.9 simplify to:

$$\begin{aligned}\frac{dM_x}{dt} &= \gamma B_0 M_y - \frac{M_x}{T2} \\ \frac{dM_y}{dt} &= -\gamma B_0 M_x - \frac{M_y}{T2} \\ \frac{dM_z}{dt} &= \frac{M_0 - M_z}{T1}\end{aligned}\tag{2.10}$$

The transverse components can be combined into a separable differential equation using the transformation $M_\perp = M_x + iM_y$:

$$\frac{dM_\perp}{M_\perp} = -\left(i\gamma B_0 + \frac{1}{T2}\right)dt\tag{2.11}$$

After integrating both sides, the solutions $M_x(t)$ and $M_y(t)$ can be extracted as the real and imaginary components, respectively. It is straightforward to find the longitudinal $M_z(t)$ solution, e.g. using an integrating factor: $e^{\frac{t}{T1}}$. The complete

set of solutions can be derived as:

$$\begin{aligned}
 M_x(t) &= [M_x(0)\cos(\gamma B_0 t) + M_y(0)\sin(\gamma B_0 t)]e^{-\frac{t}{T_2}} \\
 M_y(t) &= [M_y(0)\cos(\gamma B_0 t) - M_x(0)\sin(\gamma B_0 t)]e^{-\frac{t}{T_2}} \\
 M_z(t) &= M_z(0)e^{-\frac{t}{T_1}} + M_0 \left[1 - e^{-\frac{t}{T_1}}\right]
 \end{aligned} \tag{2.12}$$

The derived solutions show that the transverse magnetization components exhibit damped sinusoidal motion, at the Larmor frequency $\omega_0 = \gamma B_0$, around the z axis. Transverse sinusoidal motion is damped at a rate defined by the T_2 relaxation time. The longitudinal magnetization component exhibits recovery at a rate determined by the T_1 relaxation time. For a magnetization vector initialised in the transverse plane ($\mathbf{M}(0) = M_0 \hat{x}$), $\mathbf{M}(t)$ will exhibit a corkscrew trajectory, as demonstrated in Figure 2.2. A method to initialise magnetization in the transverse plane will be introduced in section 2.1.1.4.

The phenomenon of T_2 relaxation decay arises from a time-dependent loss of transverse phase coherence between individual spins in the ensemble. Loss of phase coherence is caused by local field inhomogeneities (Brown et al., 2014b) pp. 57-58, which originate from dipole-dipole interactions. In addition, local field inhomogeneities can arise from externally dependent factors, such as susceptibility variations in the patient (Bernstein et al., 2004) p.581 or imperfections in magnet production (Webb et al., 2012) p.514. Overall, T_2 relaxation can be grouped into decays associated with thermodynamic (T_2) effects (i.e. dipole-dipole interactions) and externally dependent (T_2') effects by introducing:

$$\frac{1}{T_2^*} = \frac{1}{T_2} + \frac{1}{T_2'} \tag{2.13}$$

Note that phase incoherence associated with T_2' relaxation can be reversed using refocusing pulses; see section 2.1.3.3. T_1 relaxation decay arises from interactions between protons and neighbouring nuclei, see (Webb et al., 2012) pp. 512-513 for more information. Image contrast is obtained in clinical MRI examinations by exploiting differences in relaxation times between different types

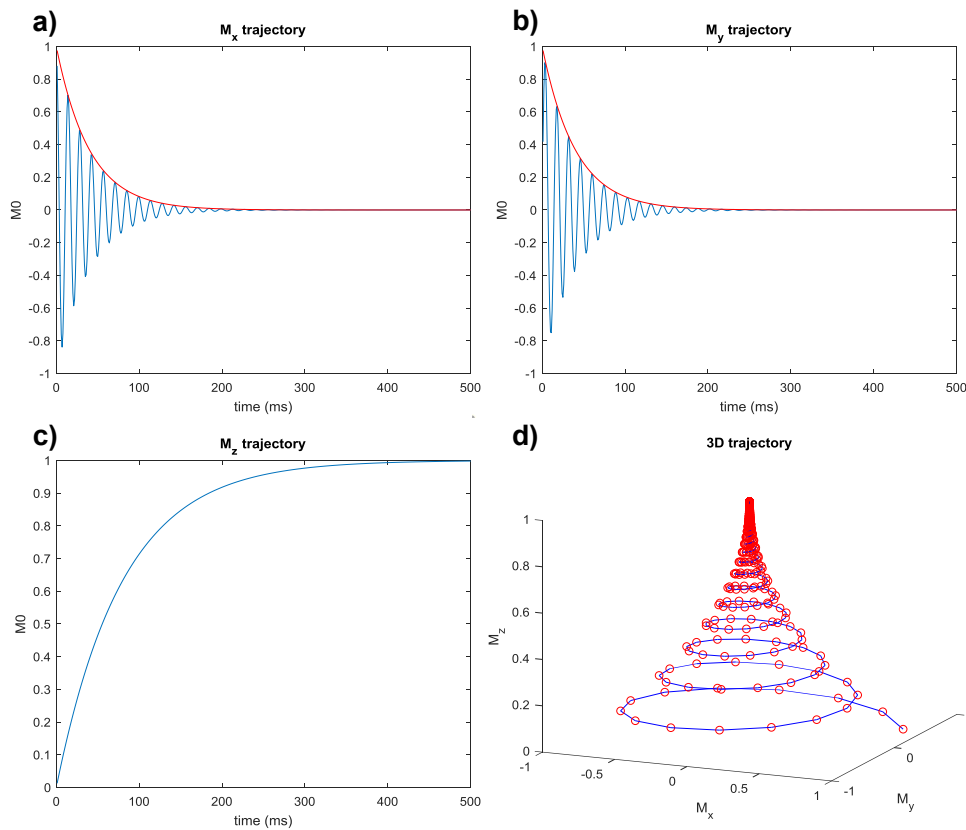


Figure 2.2: Example simulation of free induction decay using $T1 = 400$ ms and $T2 = 200$ ms. a), b) and c) display the M_x , M_y and M_z trajectories resulting from initialised magnetization $\mathbf{M}(0) = \hat{x}$. d) shows the overall 3D corkscrew trajectory.

of tissues.

From Faraday's law of induction, the changing magnetic flux produced by precessing magnetization can induce an electromotive force (emf) in a nearby conductive loop. The induced emf is the source of signal acquisition in MRI examinations and is detected using receiver coils placed around the patient. According to (Brown et al., 2014b), the induced emf can be described as:

$$emf = -\frac{d}{dt} \int_V d^3\mathbf{r} \mathbf{M}(\mathbf{r}, t) \cdot \mathbf{B}^{rec}(\mathbf{r}) \quad (2.14)$$

Where \mathbf{B}^{rec} is the receiver coil sensitivity profile. Amongst other sources, the emf is affected by noise originating from random thermal fluctuations in both the receive coil electronics and the object being scanned (Brown et al., 2014b) pp.

328-329.

2.1.1.3 Rotating frame of reference

The Bloch equations have a simpler form when applied in a frame of reference rotating at the Larmor frequency around the z-axis. Following the approach by Bernstein et al. (2004) pp. 22-25, the rotating frame of reference concept can be understood by analysing the transformation between a static $\mathbf{p}'(t)$ and rotating $\mathbf{p}(t)$ co-ordinate system:

$$\begin{aligned}\mathbf{p}'(t) &= p'_x(t)\hat{x}' + p'_y(t)\hat{y}' + p'_z(t)\hat{z}' \\ \mathbf{p}(t) &= p_x(t)\hat{x} + p_y(t)\hat{y} + p_z(t)\hat{z}\end{aligned}\tag{2.15}$$

The magnitude components and unit vectors of the rotating co-ordinate system are related to those in the static co-ordinate system by a rotation matrix \mathcal{R} :

$$\begin{aligned}[p_x, p_y, p_z]^T &= \mathcal{R}[p'_x, p'_y, p'_z]^T \\ [\hat{x}, \hat{y}, \hat{z}]^T &= \mathcal{R}[\hat{x}', \hat{y}', \hat{z}']^T\end{aligned}\tag{2.16}$$

The rotation matrix \mathcal{R} is given by:

$$\mathcal{R} = \begin{bmatrix} \cos\omega t & -\sin\omega t & 0 \\ \sin\omega t & \cos\omega t & 0 \\ 0 & 0 & 1 \end{bmatrix}\tag{2.17}$$

By differentiating the rotating co-ordinate system with respect to time and applying the transformation specified in equations 2.16 and 2.17, it can be shown that:

$$\frac{d\mathbf{p}(t)}{dt} = \frac{d\mathbf{p}'(t)}{dt} + \omega\hat{z} \times \mathbf{p}(t)\tag{2.18}$$

Applying expression 2.18 to the simplified Bloch equation 2.8 with $\mathbf{B}_0 = B_0\hat{z}$

returns:

$$\begin{aligned}
 \frac{d\mathbf{M}}{dt} &= \frac{d\mathbf{M}'}{dt} + \omega\hat{z} \times \mathbf{M} \\
 &= \omega_0\mathbf{M} \times \hat{z} + \omega\hat{z} \times \mathbf{M} \\
 &= (\omega_0 - \omega)\mathbf{M} \times \hat{z}
 \end{aligned} \tag{2.19}$$

If the rotating frame of reference is chosen to spin at the Larmor frequency ($\omega = \omega_0$), then $\frac{d\mathbf{M}}{dt} = 0$. On MRI systems, acquired signal (i.e. *emf*) is electronically transformed to the rotating frame of reference by quadrature demodulation, see (Brown et al., 2014b) pp. 104-105 for more information.

2.1.1.4 Radio-frequency pulses

Magnetization can be flipped from the longitudinal plane to the transverse plane using a circularly polarized external magnetic field:

$$\mathbf{B} = B_1 \cos(\omega_0 t) \hat{x} - B_1 \sin(\omega_0 t) \hat{y} \tag{2.20}$$

In the rotating frame of reference, the expression for the applied field becomes: $\mathbf{B} = B_1 \hat{x}$. Applying the Bloch equations 2.9 in the rotating frame of reference with $\mathbf{B} = B_1 \hat{x}$, yields:

$$\begin{aligned}
 \frac{dM_x}{dt} &= 0 \\
 \frac{dM_y}{dt} &= \gamma B_1 M_z \\
 \frac{dM_z}{dt} &= -\gamma B_1 M_y
 \end{aligned} \tag{2.21}$$

Note that exponential $T1$ and $T2$ relaxation components were neglected by applying the external field as a rapid pulse ($t = 5-10$ ms). For the initial condition

of $\mathbf{M}(0) = M_0\hat{z}$, equations 2.21 can be solved as:

$$\begin{aligned} M_x(t) &= 0 \\ M_y(t) &= M_0 \sin\left(\gamma \int_0^t B_1(t') dt'\right) \equiv M_0 \sin(\alpha) \\ M_z(t) &= M_0 \cos\left(\gamma \int_0^t B_1(t') dt'\right) \equiv M_0 \cos(\alpha) \end{aligned} \quad (2.22)$$

Where the flip-angle was defined as $\alpha = \gamma \int_0^t B_1(t') dt'$. By applying $\alpha = \frac{\pi}{2}$, the initial longitudinal magnetization ($M_z = M_0, M_y = 0$) can be tipped into the transverse plane ($M_z = 0, M_y = M_0$). Rapidly applied ($t = 5-10$ ms) transverse magnetic fields, as described in equation 2.20, are known as RF-pulses and are produced using transmit coils. The longitudinal magnetization can be rotated with any desired α by varying the time-duration and amplitude of the applied RF-pulse.

2.1.2 Magnetic resonance imaging

2.1.2.1 Magnetic field gradients and the Fourier transform

Linearly varying magnetic fields ($\mathbf{G} = \nabla B_z = \frac{\partial B_z}{\partial x} \hat{x} + \frac{\partial B_z}{\partial y} \hat{y} + \frac{\partial B_z}{\partial z} \hat{z}$) can be applied to distinguish signals arising from different spatial locations. Consider the magnetization evolution associated with the application of an external magnetic field $\mathbf{B} = [B_0 + \mathbf{r} \cdot \mathbf{G}] \hat{z}$. In the rotating frame of reference the B_0 component can be ignored and the Bloch equations 2.9 become:

$$\begin{aligned} \frac{dM_x}{dt} &= \gamma \mathbf{r} \cdot \mathbf{G}(t) M_y - \frac{M_x}{T_2} \\ \frac{dM_y}{dt} &= -\gamma \mathbf{r} \cdot \mathbf{G}(t) M_x - \frac{M_y}{T_2} \\ \frac{dM_z}{dt} &= \frac{M_0 - M_z}{T_1} \end{aligned} \quad (2.23)$$

Employing the solution of equations 2.12 for the longitudinal magnetization and applying the transformation $M_{\perp} = M_x + iM_y$ for the transversal components

yields:

$$\begin{aligned} M_{\perp}(\mathbf{r}, t) &= M_{\perp}(\mathbf{r}, 0)e^{\frac{-t}{T_2}} e^{-i\gamma\mathbf{r}\cdot\int_0^t \mathbf{G}(t')dt'} \\ M_z(\mathbf{r}, t) &= M_z(\mathbf{r}, 0)e^{\frac{-t}{T_1}} + M_0\left[1 - e^{\frac{-t}{T_1}}\right] \end{aligned} \quad (2.24)$$

Following a similar approach to (Brown et al., 2014b) pp. 101-102, an expression for the signal (S) generated by the precessing magnetization vector can be obtained by substituting the solutions 2.24 into expression 2.14. Note, in the following algebra the time-derivatives of the $e^{\frac{-t}{T_1}}$ and $e^{\frac{-t}{T_2}}$ factors were ignored as per (Brown et al., 2014b) p.102.

$$\begin{aligned} S &\propto -\frac{d}{dt} \int_V d^3\mathbf{r} [M_x \mathbf{B}_x^{rec}(\mathbf{r}) + M_y \mathbf{B}_y^{rec}(\mathbf{r}) + M_z \mathbf{B}_z^{rec}(\mathbf{r})] \\ &\propto -\frac{d}{dt} \int_V d^3\mathbf{r} [Re(M_{\perp}) \mathbf{B}_{\perp}^{rec}(\mathbf{r}) \cos(\theta_B) + Im(M_{\perp}) \mathbf{B}_{\perp}^{rec}(\mathbf{r}) \sin(\theta_B) \\ &\quad + \mathbf{B}_z^{rec}(\mathbf{r}) (M_z(\mathbf{r}, 0)e^{\frac{-t}{T_1}} + M_0[1 - e^{\frac{-t}{T_1}}])] \\ &\propto -\int_V d^3\mathbf{r} M_{\perp}(\mathbf{r}, 0)e^{\frac{-t}{T_2}} \mathbf{B}_{\perp}^{rec}(\mathbf{r}) \frac{d}{dt} \left(\cos(\theta_B) \left[\cos\left(\gamma\mathbf{r}\cdot\int_0^t \mathbf{G}(t')dt'\right) \right] \right. \\ &\quad \left. - \sin(\theta_B) \left[\sin\left(\gamma\mathbf{r}\cdot\int_0^t \mathbf{G}(t')dt'\right) \right] \right) \\ &\propto \int_V d^3\mathbf{r} M_{\perp}(\mathbf{r}, 0)e^{\frac{-t}{T_2}} \mathbf{B}_{\perp}^{rec} \Omega_G(\mathbf{r}) \sin\left(\gamma\mathbf{r}\cdot\int_0^t \mathbf{G}(t')dt' + \theta_B\right) \end{aligned} \quad (2.25)$$

Where the definitions $\mathbf{B}_x^{rec} = \mathbf{B}_{\perp}^{rec} \cos(\theta_B)$ and $\mathbf{B}_y^{rec} = \mathbf{B}_{\perp}^{rec} \sin(\theta_B)$ were employed. Furthermore, the definition $\Omega_G(\mathbf{r}) = \gamma \frac{d}{dt} \mathbf{r} \cdot \int_0^t \mathbf{G}(t')dt'$ was used to describe the rate of phase accumulation due to the applied linear gradients. As described in (Brown et al., 2014b) pp. 104-106, quadrature demodulation is performed to measure the signal using two channels, which, as mentioned in section 2.1.1.3, enables the signal to be measured in the rotating frame of reference. Moreover, quadrature demodulation permits a complex signal to be generated from the real signal described in equations 2.25. The complex magnetization

signal is given by:

$$S \propto \int_V d^3\mathbf{r} M_{\perp}(\mathbf{r}, 0) e^{\frac{-t}{T_2}} \mathbf{B}_+^{rec}(\mathbf{r}) \Omega_G(\mathbf{r}) e^{-i\gamma\mathbf{r} \cdot \int_0^t \mathbf{G}(t') dt'} \quad (2.26)$$

Where $\mathbf{B}_+^{rec} = \mathbf{B}_{\perp}^{rec} e^{-i\theta_B}$. Using the definition:

$$\mathbf{k} = \frac{\gamma}{2\pi} \int_0^t \mathbf{G}(t') dt' \quad (2.27)$$

The derived signal is proportional to the multi-dimensional Fourier transform of the weighted magnetization:

$$\begin{aligned} S(\mathbf{k}) &\propto \int_V d^3\mathbf{r} M_{\perp}(\mathbf{r}, 0) e^{\frac{-t}{T_2}} \mathbf{B}_+^{rec}(\mathbf{r}) \Omega_G(\mathbf{r}) e^{-i2\pi\mathbf{r} \cdot \mathbf{k}} \\ &\propto \mathcal{F} \left[M_{\perp}(\mathbf{r}, 0) e^{\frac{-t}{T_2}} \mathbf{B}_+^{rec}(\mathbf{r}) \Omega_G(\mathbf{r}) \right] \end{aligned} \quad (2.28)$$

In MRI examinations, a range of signals at different spatial frequencies, or k-space values, are collected by varying the gradient strength or duration of the applied gradient - see equation 2.27. The measured signals can then be transformed into a spatially resolved map of the magnetization vector (MR image) through application of an inverse Fourier transform:

$$\begin{aligned} M_{\perp}(\mathbf{r}, 0) &\propto \frac{1}{e^{\frac{-t}{T_2}} \mathbf{B}_+^{rec}(\mathbf{r}) \Omega_G(\mathbf{r})} \int_{V_{\mathbf{k}}} d^3\mathbf{k} S(\mathbf{k}) e^{i2\pi\mathbf{r} \cdot \mathbf{k}} \\ &\propto \frac{1}{e^{\frac{-t}{T_2}} \mathbf{B}_+^{rec}(\mathbf{r}) \Omega_G(\mathbf{r})} \mathcal{F}^{-1} S(\mathbf{k}) \end{aligned} \quad (2.29)$$

2.1.2.2 K-space

It is not possible to acquire signal at infinite k-space values due to the limited scan time available for data acquisition. Conventionally, $S(\mathbf{k})$ is sampled at uniformly distributed k-space values and converted into an MR image using the discrete inverse Fourier transform. According to (Webb et al., 2012) pp. 530-531, the structure of k-space required to fully sample a 2D image can be calculated from

the Nyquist sampling theorem (Shannon, 1949) as:

$$\Delta k_x = \frac{1}{FOV_x} \qquad \Delta k_y = \frac{1}{FOV_y} \qquad (2.30)$$

$$kmax_x = \frac{1}{2\Delta x} \qquad kmax_y = \frac{1}{2\Delta y} \qquad (2.31)$$

Where $\Delta k_{x/y}$, $\Delta x/y$ are the step-lengths along the x and y dimensions in k-space and image-space, respectively. Furthermore, $2kmax_{x/y}$ and $FOV_{x/y}$ are the fields-of-view (FOV)s in k-space and image space, respectively. From equations 2.30 and 2.31, the required k-space structure depends on the desired imaging FOV and resolution. An example discrete 2D k-space is displayed in Figure 2.3. Insufficient sampling of k-space can result in aliasing artefacts, which, for Cartesian sequences, manifest as overlapping structures in the reconstructed image.

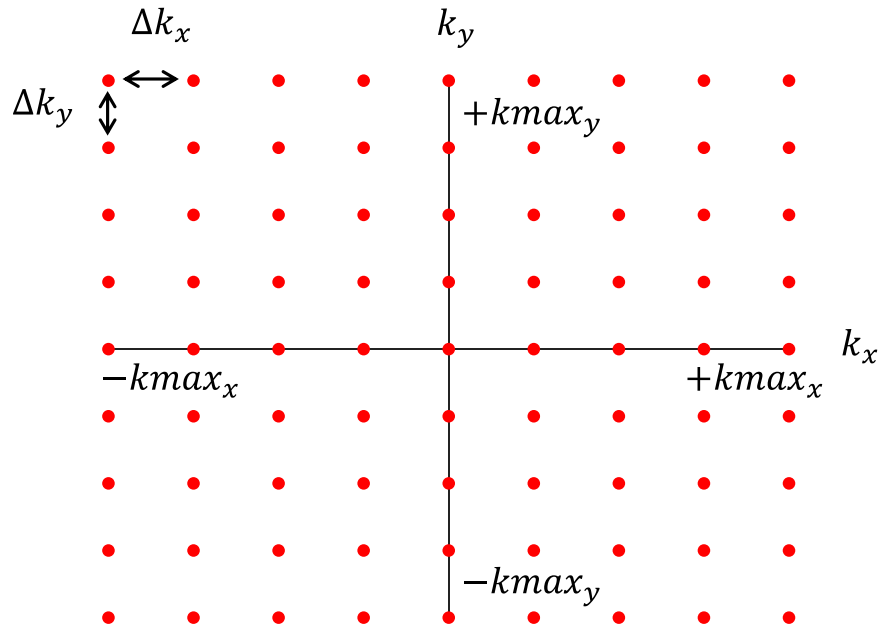


Figure 2.3: Fully sampled 2D k-space. The k-space step-lengths and field-of-view are represented by $\Delta k_{x/y}$ and $2kmax_{x/y}$, respectively. The k-space centre ($k_x = 0$, $k_y = 0$) is at the intersection of the k_x and k_y axes.

2.1.2.3 Slice-selection

In section 2.1.1.4, RF-pulses were introduced as a method to tip longitudinal magnetization into the transverse plane. Radio-frequency pulses can be combined with imaging gradients to excite magnetization in a specific slice. Following the explanation by (Brown et al., 2014b) pp. 175-179, a slice-select gradient $\mathbf{G}_{SS} = G_z \hat{z}$ can be applied to vary the precession frequency along the z -dimension:

$$f(z) = \frac{\gamma}{2\pi} G_z z \quad (2.32)$$

Whilst applying the slice-select gradient, an RF-pulse with central carrier frequency $f(z_0)$ and bandwidth BW_{RF} can be turned on to tip a component of the longitudinal magnetization, in a slice with centre position z_0 and thickness Δz , into the transverse plane. The required BW_{RF} can be calculated from equation 2.32 as:

$$BW_{RF} = \frac{\gamma}{2\pi} G_z \Delta z \quad (2.33)$$

In order to achieve uniform flip-angle (α) over the slice profile, the RF-pulse must exhibit a top-hat frequency profile in the rotating frame of reference:

$$B_1(z, f) = \Theta \left[f - \frac{\gamma}{2\pi} G_z \left(z_0 - \frac{1}{2} \Delta z \right) \right] - \Theta \left[f - \frac{\gamma}{2\pi} G_z \left(z_0 + \frac{1}{2} \Delta z \right) \right] \quad (2.34)$$

Where Θ represents the Heaviside function. As described by (Bernstein et al., 2004) p.72, for small α , the RF-pulse frequency profile is related to the Fourier transform of the RF envelope $[B_1(z, t)]$ by:

$$\alpha(\Delta f) \approx \pm \gamma \left| \int_0^t B_1(t') e^{-i2\pi \Delta f t'} \right| \quad (2.35)$$

If $B_1(z, t)$ is chosen to be a sinc function, then, according to equation 2.35, an RF-pulse with a top-hat frequency profile given by expression 2.34 could be generated, which would result in a slice with thickness Δz being excited with

uniform flip-angle. In practice, an RF-pulse with a perfect sinc profile cannot be generated, since it would be infinite along the temporal domain. Instead, an RF-pulse with a truncated sinc profile can be applied to tip components of the longitudinal magnetization into the transverse plane. As demonstrated in Figure 2.4, the Fourier transform of a truncated sinc function corresponds to a stretched top-hat function with multiple side-lobes. The imperfect top-hat frequency profile results in spin excitation outside the slice of interest. In particular, cross talk can occur if imperfect excitation of a given slice affects the signal from an adjacent slice.

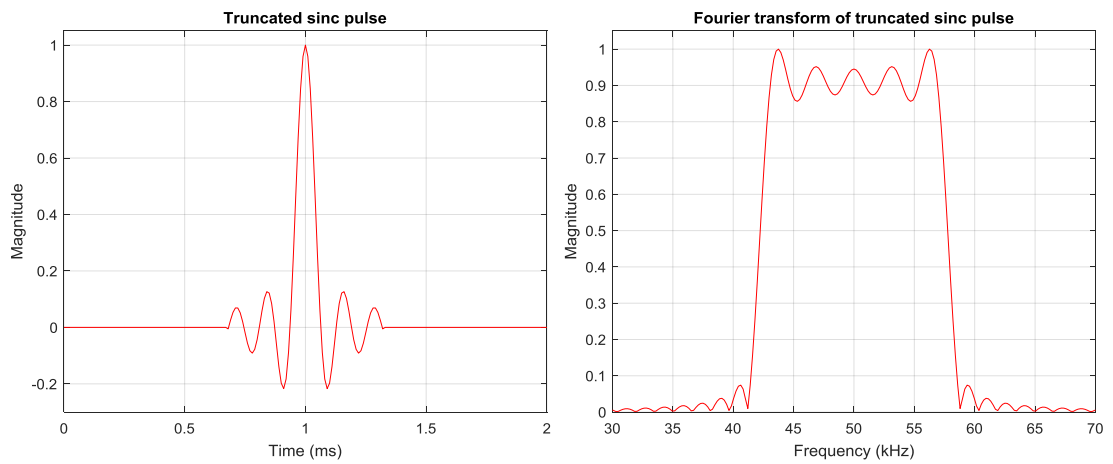


Figure 2.4: An example truncated sinc pulse and its Fourier transform. The Fourier transform exhibits a stretched top-hat profile with multiple side-lobes.

Whilst applying a \mathbf{G}_{SS} gradient enables slice-selective excitation, it also causes magnetization to dephase across the excited slice according to equation 2.32:

$$\begin{aligned}\phi(z, t) &= \int_0^t \omega(t') dt' \\ &= \gamma G_z z t\end{aligned}\tag{2.36}$$

Undesirable dephasing induced by a slice-select gradient can be corrected for by applying a rephasing gradient after the RF-pulse is switched off.

2.1.3 Pulse sequences

A pulse sequence is a series of instructions followed by an MRI system when performing image acquisition. Pulse sequences involve RF-pulses, gradient waveforms and signal acquisition. Pulse sequences can be represented using diagrams, where time progresses from left to right. In this thesis, RF-pulses and signal acquisition are displayed in pulse sequence diagrams along the first and fifth lines (i.e. top and bottom), respectively. Signal acquisition is shown as a series of discrete blocks representing operation of an analog-to-digital (ADC) converter. In the second to fourth lines the time varying waveform of each gradient vector is shown. Gradient waveforms are conventionally described as either slice-select (G_{SS}), phase encoding (G_{PE}) or readout (G_{RO}). Several pulse sequences integral to this thesis will be described below.

2.1.3.1 Spoiled gradient echo

Figure 2.5a displays a 2D spoiled gradient echo sequence diagram. Initially, an RF-pulse is applied together with a G_{SS} gradient to generate transverse magnetization in a chosen slice. Next, G_{PE} and dephasing gradients are played out to encode the transverse magnetization with a spatially-dependent phase. In Figure 2.5b, this is equivalent to moving diagonally through k-space (e.g. from zero to top left corner). A G_{RO} gradient is then switched on, which results in a gradient echo at time $t = T_E$ (echo time). Whilst applying the G_{RO} gradient, signal is measured along k_{RO} using the ADC converter. Afterwards, a spoiler gradient is played out to dephase residual transverse magnetization. If left unspoiled, residual transverse magnetization can interfere with the signal acquired in subsequent excitations, leading to image artefacts (Bernstein et al., 2004) pp. 349-351. Different k_{PE} frequencies are sampled by repeating the pulse sequence after a time $t = T_R$ (repetition time) with modulated G_{PE} gradient amplitude values. Spoiled gradient echo sequences permit rapid signal acquisition due to application of a single RF-pulse and small flip angles.

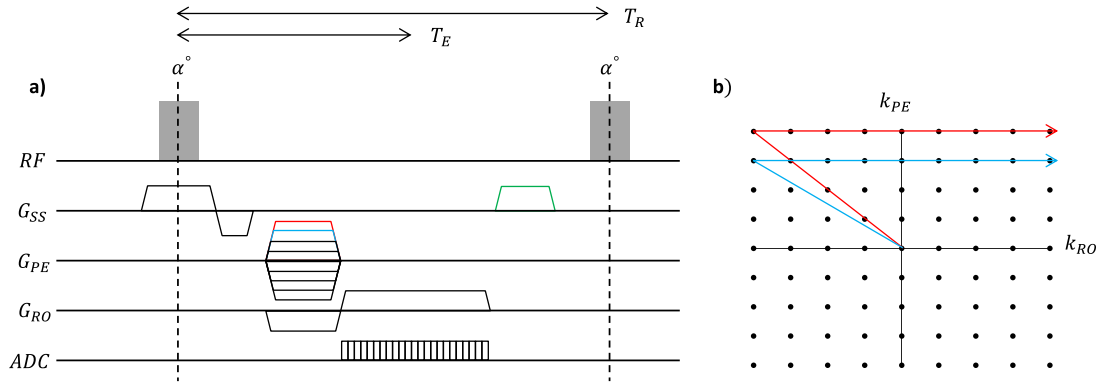


Figure 2.5: a) Pulse sequence diagram for a spoiled gradient echo sequence. The spoiler gradient is displayed in green. b) Example k-space trajectories corresponding to two separate colour-coded phase encoding gradients.

2.1.3.2 2-point Dixon

Protons in lipids and water exhibit variations in resonant frequency due to their different molecular environments. The difference in resonant frequency ($\Delta\omega_{fw}$) between fat (ω_f) and water (ω_w) is given by:

$$\begin{aligned}\Delta\omega_{fw} &= \omega_f - \omega_w \\ &= -\sigma_{fw}\gamma B_0\end{aligned}\tag{2.37}$$

Where σ_{fw} is the chemical shift between fat and water (≈ 3.35 ppm). Assuming static field homogeneity, equation 2.37 can be applied to model the total signal in a given voxel $[p(t)]$ as a mixture of water (p_w) and fat (p_f) signals:

$$p(t) = |p_w| + |p_f|e^{i\Delta\omega_{fw}t}\tag{2.38}$$

Fat and water signals can be separated using two gradient echo images with fat and water signals in opposed-phase (p_{Op}), and fat and water signals in-phase (p_{In}). Applying equation 2.38, p_{Op} and p_{In} signals can be obtained by setting

$T_{E1} = \frac{\pi}{\Delta\omega_{fw}}$ and $T_{E2} = 2T_{E1}$, respectively:

$$\begin{aligned} p_{Op}(T_{E1}) &= |p_w| - |p_f| \\ p_{In}(T_{E2}) &= |p_w| + |p_f| \end{aligned} \quad (2.39)$$

Fat and water magnitude signals can then be calculated by:

$$\begin{aligned} |p_w| &= \frac{1}{2}(p_{In} + p_{Op}) \\ |p_f| &= \frac{1}{2}(p_{In} - p_{Op}) \end{aligned} \quad (2.40)$$

Note that $T2^*$ decay was ignored in this calculation. In practice, p_{Op} and p_{In} signals can be acquired using a 2-point Dixon gradient echo sequence with monopolar readout (Figure 2.6). This sequence is similar to the spoiled gradient echo sequence of section 2.1.3.1, except a second G_{RO} gradient is employed to acquire an additional line of k-space in each T_R . The dual readout enables two images to be acquired with echo times T_{E1} and T_{E2} .

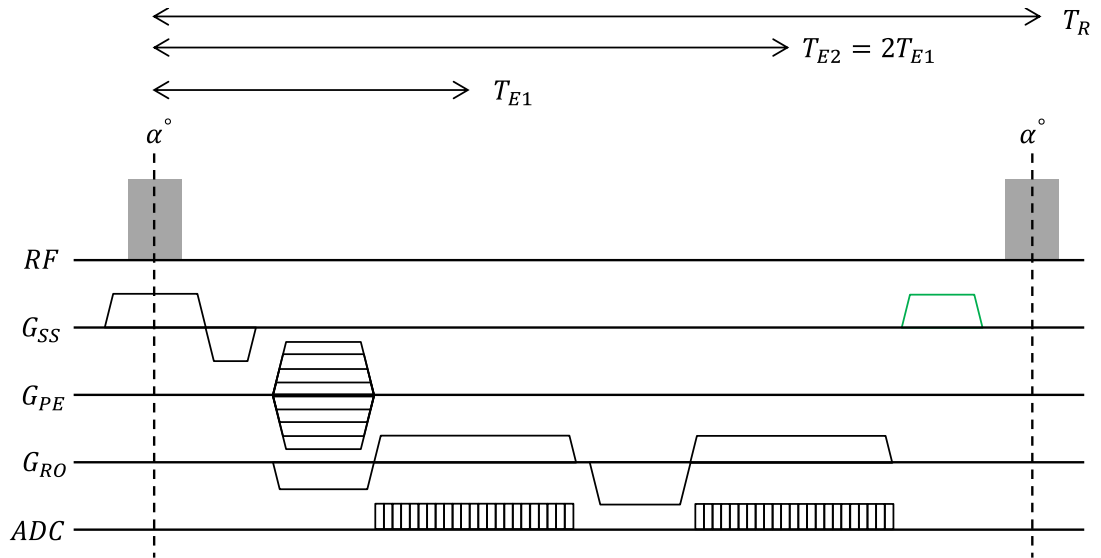


Figure 2.6: Pulse sequence diagram for a 2-point Dixon gradient echo sequence. In each repetition time (T_R), a single line of k-space is measured in both opposed-phase and in-phase at echo times T_{E1} and T_{E2} , respectively. The spoiler gradient is shown in green.

2.1.3.3 Spin echo

Figure 2.7a shows a sequence diagram for a spin echo imaging experiment (Hahn, 1950). First, a $\pi/2$ RF-pulse is applied alongside a G_{SS} gradient to tip the longitudinal magnetization into the transverse plane. The transverse magnetization is then encoded with k_{RO} and k_{PE} -dependent phase by simultaneously applying G_{RO} and G_{PE} gradients, respectively. Afterwards, a refocusing (π) RF-pulse is applied together with a symmetric G_{SS} gradient to invert the transverse phase, which results in an echo at time $t = T_E$. During the echo, a G_{RO} gradient is played out to enable acquisition of a line along k_{RO} . The imaging sequence is then repeated for different G_{PE} gradient amplitudes. Figure 2.7b demonstrates an example k-space trajectory for one G_{PE} gradient amplitude.

Spin echo sequences require longer acquisition times due to use of two RF-pulses and large flip-angles. One advantage of spin echo sequences, is that local variations in the magnetic field due to externally dependent factors, e.g. variations in patient susceptibility, are refocused by the π RF-pulse. Consequently spin echo images exhibit pure T2w contrast and reduced signal dropout.

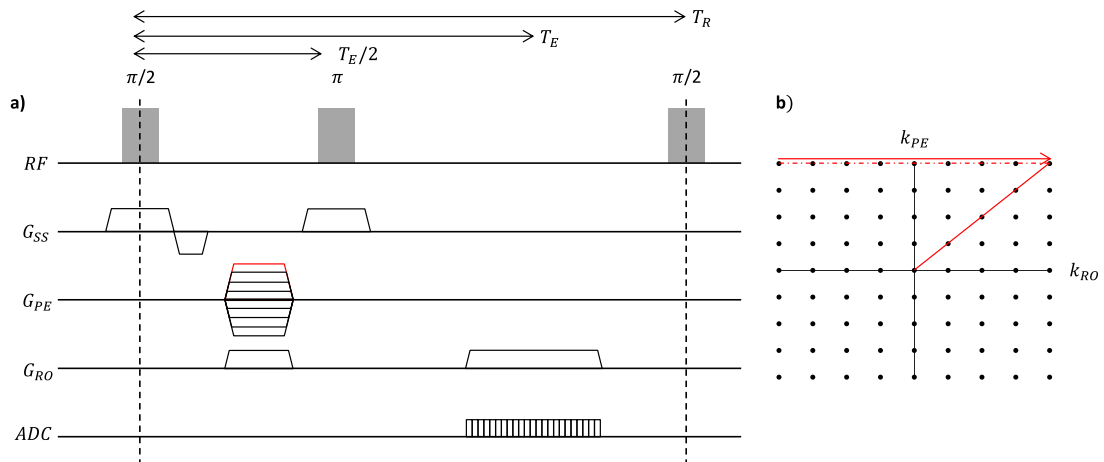


Figure 2.7: a) Pulse sequence diagram for a spin echo sequence. b) Example k-space trajectory for the red phase encoding gradient. A dashed line (right to left) is employed to illustrate the reversal of transversal phase by the π RF-pulse.

2.1.3.4 Turbo spin echo

The spin echo sequence presented in section 2.1.3.3 can be modified by applying variable phase encoding between repeated refocusing pulses (Figure 2.8). This approach, known as a turbo spin echo (TSE) sequence, enables multiple k-space lines to be acquired in a given T_R and subsequently reduces acquisition time (Hennig et al., 1986). The number of refocusing pulses is referred to as the echo train length or turbo factor. One limitation of TSE sequences is a high specific absorption rate (SAR) due to application of multiple RF-pulses with large flip-angle; SAR refers to the rate at which energy is deposited in the patient by RF-pulses. The SAR can be decreased by reducing the refocusing flip-angle or by increasing the T_R .

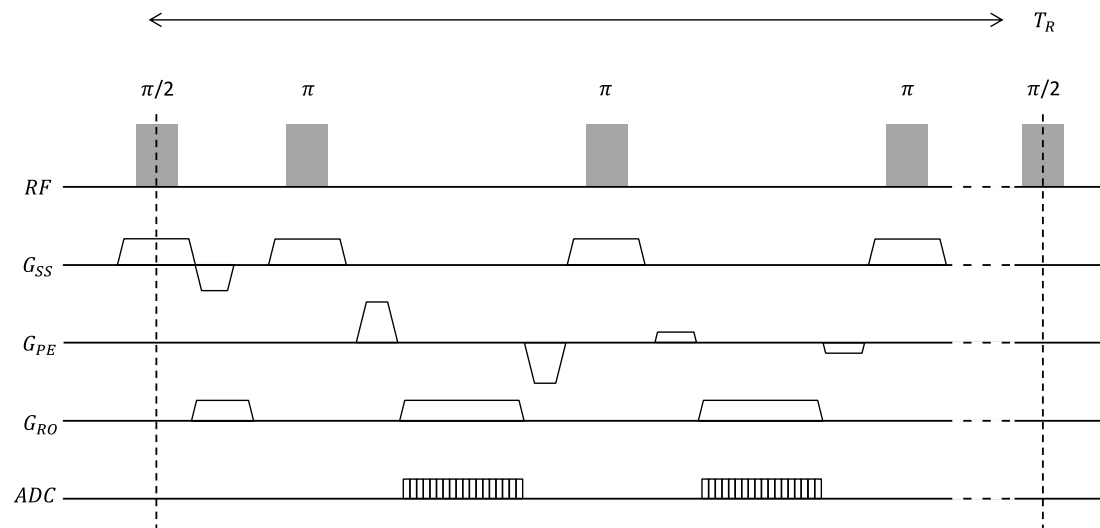


Figure 2.8: Pulse sequence diagram for a turbo spin echo sequence. In this example, only three refocusing pulses from the echo train are displayed. The remainder of the echo train is represented by ellipses immediately to the right of the third refocusing pulse.

2.2 Principles of 4D-MRI

The concept of 4D-MRI and its applications in MRgRT were introduced in sections 1.4.1 and 1.4.4. In this section, methods to reconstruct 4D-MRI will be outlined. Furthermore, a brief introduction to DIR techniques and deep convolutional neural networks (dCNN)s will be provided.

2.2.1 Binning

One key step in all 4D-MRI techniques is amplitude or phase binning of image or k-space data into different respiratory phases using information (i.e. amplitude or phase values) extracted from a synced respiratory surrogate signal.

2.2.1.1 Amplitude binning

In amplitude binning, data are sorted into respiratory phases based on the amplitude values of a respiratory surrogate signal, which was time-synced with the data. Figure 2.9 shows an example of amplitude binning for data acquired together with a respiratory surrogate signal, where inspiration and expiration were distinguished based on its gradient. The edges of five equal width respiratory bins were calculated by dividing the amplitude range of all data acquired during inspiration by the value five. Data were sorted based on the respiratory bins, e.g. the first and second data points were assigned to respiratory bins 3 and 4, respectively.

Expiration data can be sorted following the same process as per the inspiration data. Grouping the sorting process into expiration and inspiration components accounts for hysteresis, i.e. differences in respiratory pattern between exhaling and inhaling. More information regarding amplitude binning and examples of different implementations can be found in (Li et al., 2017b; Rank et al., 2017; Tryggestad et al., 2013; van Kesteren et al., 2019). In one particular variation, Rank et al. (2017) sorted k-space data into respiratory bins with non-equidistant width based on the amplitude values of a self-gating signal. Using respiratory bins

with non-equidistant width enabled an equal amount of data to be assigned to each respiratory phase.

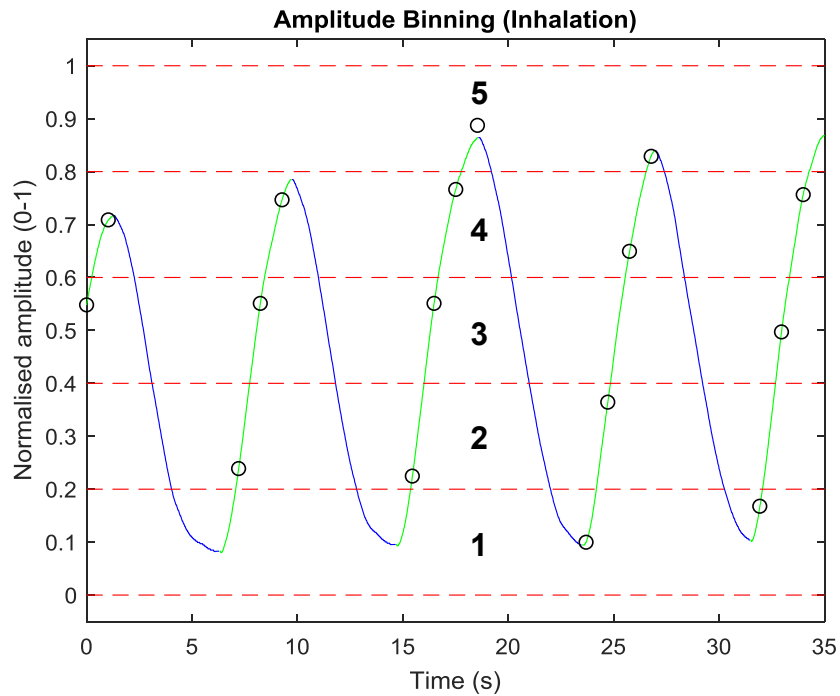


Figure 2.9: Example amplitude binning of data points (black circles) using amplitude values extracted from a respiratory surrogate signal; green and blue signals display the inspiration and expiration components, respectively. Dashed red lines show the edges of five respiratory bins, which are numbered 1 to 5.

2.2.1.2 Phase binning

In phase binning, the respiratory surrogate signal is converted to a phase-signal for instance using a Hilbert transform (van de Lindt et al., 2018a) or by temporal interpolation between peaks and troughs (Liu et al., 2015b; Lu et al., 2006). Based on the phase-signal, respiratory bins of equal time duration can be calculated for each respiratory cycle. Data points can then be sorted into different respiratory bins depending on their phase.

Respiratory phases of 4D-MRI resulting from phase binning represent an equal time duration, which is advantageous for RTP. For instance, a 3D image of the time-weighted average anatomy can be calculated by averaging over respiratory

phases of 4D-MRI. A detailed comparison between amplitude and phase binning can be found in (Abdelnour et al., 2007; Lu et al., 2006; van Kesteren et al., 2019).

2.2.2 Slice-selective methods

In slice-selective methods, 4D-MRI is generated by sorting continuously acquired 2D images into volumetric respiratory phases. Slice-selective techniques can be grouped into those using prospective or retrospective acquisitions.

2.2.2.1 Prospective acquisitions

In prospective methods, 2D images are acquired at specific respiratory phases by triggering acquisition with the aid of a synchronised respiratory surrogate signal. A complete 4D-MRI is then constructed by continuously measuring slices at all required planes and respiratory phases (Du et al., 2018; Hu et al., 2013). Prospective methods have high acquisition efficiency, as each slice in any given respiratory phase is obtained only once. However, acquisition efficiency can be reduced by triggering delays, where triggering of the current respiratory phase is ignored due to continuing measurement of the preceding respiratory phase (Du et al., 2015).

2.2.2.2 Retrospective acquisitions

In retrospective methods, 2D images are continuously acquired and then sorted into respiratory phases using amplitude or phase binning. For binning, both external and image-driven respiratory surrogate signals (IRS) have been utilised. Amongst others, body area (Cai et al., 2011; Hu et al., 2013; Yang et al., 2014), liver-dome displacement (van de Lindt et al., 2018a) and mutual information (Paganelli et al., 2015) were applied as IRS.

External respiratory surrogate signals are typically acquired using a breathing belt (Li et al., 2017b; Liu et al., 2015a; Vedam et al., 2002), which can exhibit poor respiratory correlation (Koch et al., 2004) or clock drifts (Tryggestad et al., 2013). Unlike the breathing belt, IRS are available from the acquired data and do

not require a manual set-up. However, IRS exhibit a phase-shift (Liu et al., 2014) between different slices, since they are calculated on a slice-by-slice basis.

2.2.2.3 Artefacts associated with retrospective slice-selective methods

Four-dimensional MRI obtained using a retrospective slice-selective method suffers from several artefacts including data incompleteness, where a 2D image was not acquired in all respiratory phases (Liu et al., 2015b). Data incompleteness artefacts can be accounted for using post-processing methods. For instance, van de Lindt et al. (2018b) applied an iterative interpolation algorithm (Garcia, 2010; Wang et al., 2012) to estimate missing-data in liver 4D-T2w MRI. Alternatively, data incompleteness can be reduced by increasing acquisition time, since more respiratory bins can be filled (Liu et al., 2015b). Example data incompleteness artefacts are displayed as black stripes in Figure 2.10.

Discontinuities in position between adjacent slices (i.e. stitching artefacts) present an additional challenge in retrospective slice-selective techniques (Figure 2.10). Stitching artefacts arise from irregular breathing during acquisition and errors in the respiratory surrogate signal applied for sorting (Cai et al., 2011; Li et al., 2017b). The development of highly accurate respiratory surrogate signals remains an intensive area of research (Hui et al., 2016; Meschini et al., 2019).

Slice-selective implementations are also limited by large slice thickness (e.g. 5 mm) (Liu et al., 2015b; Tryggestad et al., 2013; van de Lindt et al., 2018a), which, as shown in Figure 2.10, leads to staircasing when reformatting data into orthogonal views. Compared to thin slices, thick slices require a shorter acquisition time for a given FOV. Furthermore, thick slices result in increased SNR, since SNR is proportional to slice thickness (Brown et al., 2014b) pp. 340-341.

Moreover, 4D-MRI obtained using slice-selective techniques can exhibit potato-chip-shaped through-plane geometrical distortion (Bernstein et al., 2004) pp. 268-269, since scanner software typically only corrects in-plane distortion (Stemkens et al., 2018). This point has been addressed by (Tryggestad et al., 2013) who per-

formed an off-line 3D distortion correction to 4D-MRI constructed from repetitively acquired 2D-MRI.

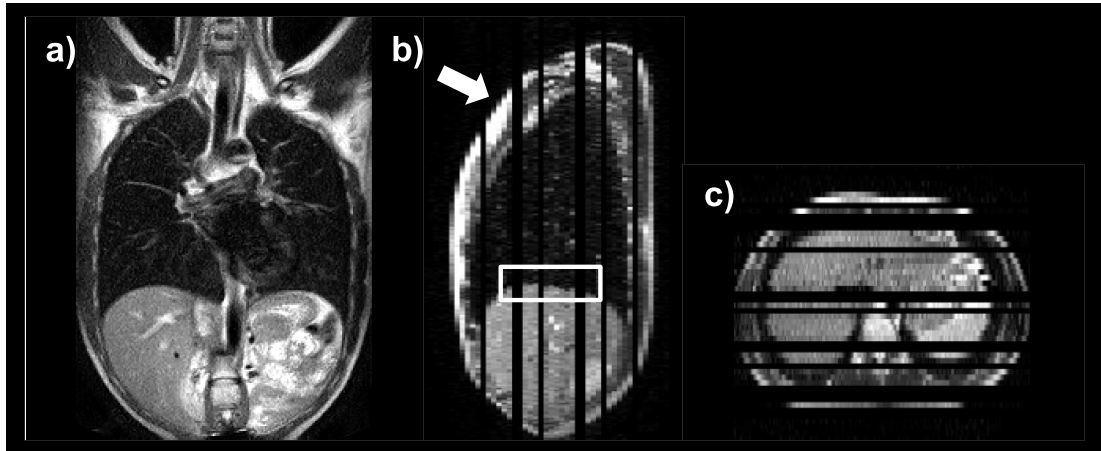


Figure 2.10: Exhalation respiratory phase of 4D-MRI reconstructed through phase binning of thick coronal slices (5 mm). a), b) and c) display coronal, sagittal and axial views, respectively. In b), stitching artefacts are visible inside the white rectangle as discontinuities along the diaphragm. Furthermore, the white arrow points to staircasing artefacts. In b) and c), black stripes represent data incompleteness artefacts. Detailed acquisition parameters are given in Table 7.1.

2.2.3 Volumetric methods

In volumetric techniques, 4D-MRI is calculated by first sorting continuously measured 3D k-space data into respiratory phases, and then applying a reconstruction algorithm. Volumetric methods can be categorised into those employing pulse sequences with Cartesian (Han, 2017), non-Cartesian (Deng et al., 2015) and hybrid readouts (Buerger et al., 2013; Cruz et al., 2016; Feng et al., 2014, 2016; Kolbitsch et al., 2018a; Rank et al., 2017). The scope of this section will be limited to methods involving the hybrid radial stack-of-stars pulse sequence, which was applied throughout this thesis. More information regarding Cartesian and non-Cartesian techniques is given in (Stemkens et al., 2018).

2.2.3.1 Radial stack-of-stars pulse sequence

Figure 2.11a displays the radial stack-of-stars 3D spoiled gradient echo pulse sequence diagram (Block et al., 2014), which shares similar concepts with the 2D spoiled gradient echo sequence of section 2.1.3.1. First, an RF-pulse is applied along with a slab-select gradient (G_{SB}) to excite transverse magnetization in a 3D volume. The G_{SB} rewinder gradient includes Cartesian phase encoding along the slice dimension. Afterwards, G_{PE} and G_{RO} gradients are simultaneously played out to radially traverse through k-space, at angular increment φ , according to:

$$G_{PE} = A \sin(\varphi) \qquad G_{RO} = A \cos(\varphi) \qquad (2.41)$$

Where A represents the gradient amplitude. Signal is recorded using an ADC during readout. For a given φ , the same spoke is acquired for all phase encoding steps along the slice dimension; see Figure 2.11b. This is possible by repeating the pulse sequence of Figure 2.11a with variable k_z -encoding, whilst keeping the G_{PE} and G_{RO} gradient waveforms the same. Afterwards, acquisition is repeated for subsequent φ by modulating the G_{RO} and G_{PE} waveforms. For $\Delta\varphi$, the golden-angle (111.25 °) was chosen, because it was shown to give an approximately uniform k-space coverage for any arbitrary number of spokes (Winkelmann et al., 2007).

Because of varying readout directions, artefacts caused by subject motion or undersampling of k-space manifest as blurring and incoherent radial streaking (Block et al., 2007). Streaking artefacts do not obfuscate targets and OARs as severely as coherent aliasing artefacts arising from Cartesian sequences (Block et al., 2014).

The radial stack-of-stars pulse sequence has advantageous properties for 4D-MRI reconstruction. In 4D-MRI techniques, raw data are sorted into multiple highly undersampled respiratory phases, which consequently exhibit incoherent streaking artefacts when reconstructed using a Gridded fast Fourier transform algorithm (Rank et al., 2017); see section 2.2.3.2. Unlike coherent aliasing artefacts,

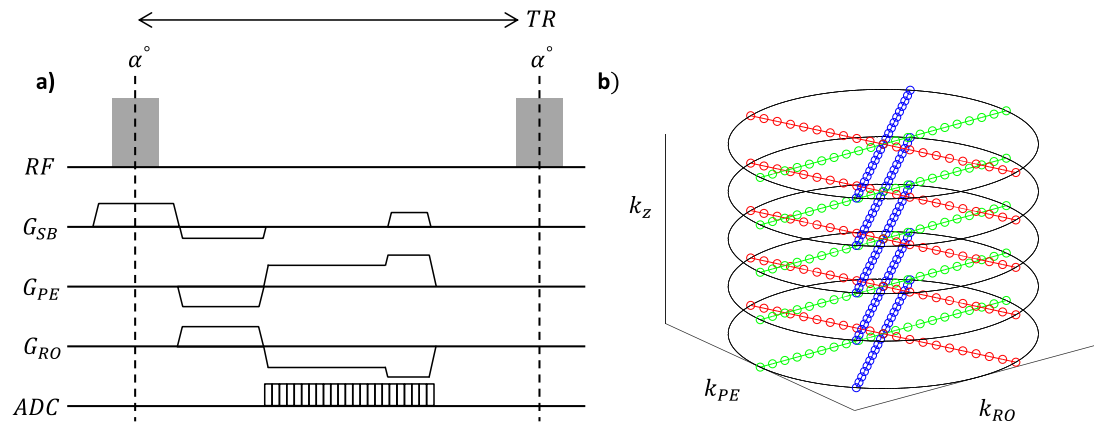


Figure 2.11: a) Radial stack-of-stars 3D gradient echo pulse sequence diagram, which corresponds to one spoke in b). Spoiling gradients are employed at the end of the sequence to remove residual magnetization. b) Example k-space trajectory for five partitions and three angular increments. All partitions for each angular increment, as shown by distinct colours, were acquired before rotating by the golden-angle.

incoherent streaking artefacts can be reduced using compressed sensing iterative reconstruction algorithms (Block et al., 2007; Cruz et al., 2016; Feng et al., 2014, 2016, 2018; Lustig et al., 2007; Mickevicius and Paulson, 2017; Rank et al., 2017). Furthermore, due to continuous measurement of the k-space centre, a high-quality respiratory surrogate (self-gating) signal can be directly calculated from the data (Paul et al., 2015), which obviates the requirement for external motion-monitoring devices such as a respiratory bellows (Tryggstad et al., 2013).

2.2.3.2 4D joint MoCo-HDTV algorithm

Iterative compressed sensing reconstructions can be applied to reduce streaking artefacts exhibited by highly undersampled 4D-MRI that was obtained using a radial stack-of-stars sequence. This section will focus on introducing the 4D joint motion-compensated high-dimensional total variation (4D joint MoCo-HDTV) algorithm (Rank et al., 2017), which was employed throughout this thesis. Note that *joint* refers to a framework performing dual motion vector field (MVF) estimation and image reconstruction.

Based on principle component analysis, a self-gating respiratory surrogate signal was calculated from the magnitude of the 9 central k-space points on each

radial spoke that passed through the k-space centre. The self-gating signal was then applied to sort k-space data into N overlapping respiratory phases with an equal amount of data in each respiratory phase. For sorting, amplitude binning (see section 2.2.1.1) was employed with separate bins for inspiration and expiration phases.

Sorted k-space data were then reconstructed using a Gridding-based algorithm. First, k-space data were corrected using a Ram-Lak density compensation filter and then interpolated onto a rectilinear grid by convolution with a Kaiser-Bessel kernel. Afterwards, a fast Fourier transform was applied to reconstruct the data. Gridded images were used to verify the output of the 4D joint MoCo-HDTV reconstruction.

The 4D joint MoCo-HDTV reconstruction is solving an inverse problem, by minimising a cost function C dependent upon data fidelity and spatio-temporal regularisation:

$$C = \|X_{pc}Sf - p\|^2 + \mu R_{HDTV}f \quad (2.42)$$

In the first term of equation 2.42: f represents the 4D image data matrix, S is a matrix operator describing the coil sensitivity profiles, X_{pc} is a matrix which operates by translating the image data into k-space (phase correlated forward transform), and p is the raw data matrix. In the second term of equation 2.42, μ is the spatio-temporal regularisation weighting factor and R_{HDTV} represents the spatio-temporal difference HDTV operator.

The first term of equation 2.42 compares the calculated 4D image data with the raw data, which yields N fidelity update terms $u_{t,q+1}$ at iteration $q + 1$ and phase $t \in [1, \dots, N]$. At each iteration, DIR (diffeomorphic Demons; see section 2.2.4.1) is performed between adjacent phases in f to obtain a set of MVFs, which describe the transformations between all adjacent phases. Afterwards, the MVFs are applied to warp each update term to all other phases. For the t^{th} phase, the overall update term is composed of a weighted sum of the update term originating

from the same phase ($u_{t,q+1}$) and the N warped fidelity update terms. The overall update is applied to iteratively minimise the first term of equation 2.42, for each phase t , as:

$$f_{t,q+1} = f_{t,q} + \alpha \left[(1 - \beta)u_{t,q+1} + \frac{\beta}{N} \sum_t T_t^{t',q+1} u_{t',q+1} \right] \quad (2.43)$$

Note, α adjusts the update step-size. The β weighting parameter enables a compromise between undersampling artefacts affecting the raw update term ($u_{t,q+1}$) and blurring introduced by inaccurate MVFs in the warped update term ($\sum_t T_t^{t',q+1} u_{t',q+1}$). The operator $T_t^{t',q+1}$ transforms the fidelity update term at phase t' to phase t by application of the calculated MVFs.

The second term of expression (2.42) constrains the reconstruction by spatio-temporal smoothing of the 4D image data; resulting in a reduction of noise, streak artefacts and local MVF errors. The HDTV operator is given by:

$$R_{HDTV} f = \sum_{x,y,z,t} \left(\frac{1}{\Delta x^2} [f_{x,y,z,t} - f_{x-\Delta x,y,z,t}]^2 + \frac{1}{\Delta y^2} [f_{x,y,z,t} - f_{x,y-\Delta y,z,t}]^2 \right. \\ \left. + \frac{1}{\Delta z^2} [f_{x,y,z,t} - f_{x,y,z-\Delta z,t}]^2 + \frac{\Upsilon^2}{\bar{v}^2 \Delta t^2} [f_{x,y,z,t} - f_{x,y,z,t-\Delta t}]^2 \right) \quad (2.44)$$

Where $\Delta x, \Delta y, \Delta z$ and Δt describe the spatio-temporal step-sizes between neighbouring voxels. Furthermore, Υ describes the temporal regularisation weighting and \bar{v} represents the average motion velocity, see (Rank et al., 2017) for more information. Figure 2.12 displays an example of Gridded and 4D joint MoCo-HDTV reconstructed images.

2.2.4 Deformable image registration

Deformable image registration can find application in image reconstruction algorithms (Cruz et al., 2016; Rank et al., 2017). The aim of DIR is to find the non-rigid deformation vector field or MVF M_j^i which maps the moving image I_i

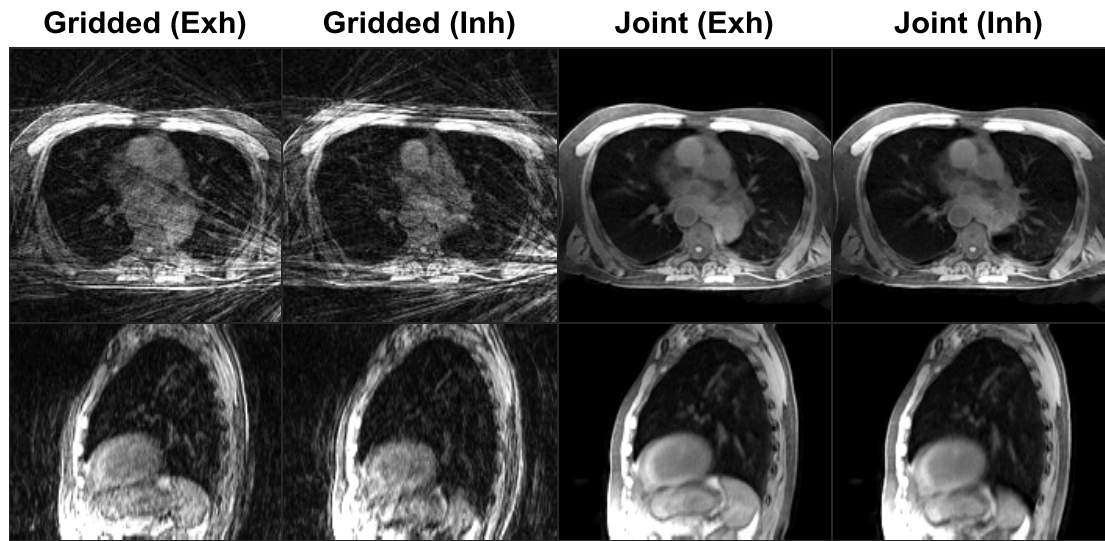


Figure 2.12: Example comparison of Gridded and 4D joint MoCo-HDTV (Joint) reconstructed images for a lung cancer patient. Exh and Inh indicate exhalation and inhalation respiratory phases, respectively. Compared to the Gridded images, the Joint images exhibit greatly reduced streaking artefacts.

to the fixed image I_j (Figure 2.13). The warping (i.e. interpolation) operator W_j^i will be employed to describe application of M_j^i to I_i , such that: $I_j' = W_j^i I_i$. Note, $I_j' = I_j$, if M_j^i is optimal. The scope of this section will be limited to specific Demons (Thirion, 1998; Vercauteren et al., 2009) and B-spline algorithms (Rueckert et al., 1999) that were employed in this thesis. A general review of DIR in medical imaging can be found in (Sotiras et al., 2013).

2.2.4.1 Demons registration

In Demons registration methods, spatio-temporal gradients in image intensity determine the transformation between two images. Consider Figure 2.13, which shows the centre pixel intensities of the dashed rectangles in the moving and fixed images as $I_i(\mathbf{x}, \mathbf{y}, t)$ and $I_j(\mathbf{x}', \mathbf{y}', t')$, respectively. By requiring that the centre pixels exhibit the same intensity and that the transformations between the moving

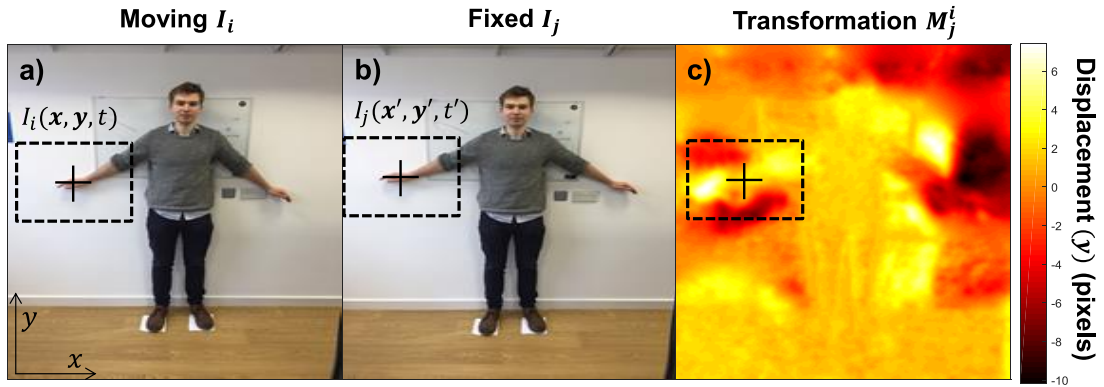


Figure 2.13: a) The moving image I_i is registered to b) The fixed image I_j to determine c) The transformation M_j^i . Crosses demarcate the centre pixels of the dashed rectangles, which exhibit the same intensity in the moving and fixed images. Note, centre pixels are not at the same relative spatial location in the moving and fixed images.

and fixed images are small, then it can be shown that:

$$\begin{aligned} I_i(\mathbf{x}, \mathbf{y}, t) &= I_j(\mathbf{x}', \mathbf{y}', t') \\ &= I_i(\mathbf{x} + \delta\mathbf{x}, \mathbf{y} + \delta\mathbf{y}, t + \delta t) \end{aligned} \quad (2.45)$$

A Taylor series expansion about $I_i(\mathbf{x}, \mathbf{y}, t)$ shows that this assumption is true at the zeroth order:

$$I_i(\mathbf{x}, \mathbf{y}, t) = I_i(\mathbf{x}, \mathbf{y}, t) + \frac{\partial I_i}{\partial x} \delta\mathbf{x} + \frac{\partial I_i}{\partial y} \delta\mathbf{y} + \frac{\partial I_i}{\partial t} \delta t + \mathcal{O}(\delta\mathbf{x}^2, \delta\mathbf{y}^2, \delta t^2) \quad (2.46)$$

By discarding the higher order terms and using $\mathbf{v} = \left(\frac{\delta\mathbf{x}}{\delta t}, \frac{\delta\mathbf{y}}{\delta t}\right)$, expression 2.46 can be rearranged into the optical flow equation:

$$\nabla I_i \cdot \mathbf{v} + \frac{\partial I_i}{\partial t} = 0 \quad (2.47)$$

Where ∇I_i is the spatial intensity gradient $\left(\frac{\partial I_i}{\partial x}, \frac{\partial I_i}{\partial y}\right)$, and \mathbf{v} describes the optical flow at pixel (\mathbf{x}, \mathbf{y}) and time t . Thirion (1998) determined one specific solution of 2.47 as:

$$\mathbf{v} = \frac{(I_i - I_j) \nabla I_i}{|\nabla I_i|^2 + (I_i - I_j)^2} \quad (2.48)$$

Equation 2.48 is the basis of the Demons algorithm, which can be implemented as follows:

1. Define a subset of Demons (or control points) in I_i , e.g. one Demon per voxel.
2. Apply equation 2.48 to I_i and I_j to obtain the displacement ($-\mathbf{v}$) for each Demon. The transformation matrix M_j^i is then estimated by combining the individual displacements of all Demons.
3. Apply a global Gaussian filter, with constant standard deviation, to M_j^i .
4. Apply M_j^i to I_i using the warping operator: $I_j' = W_j^i I_i$.
5. Repeat steps 2 to 4 using $I_i = I_j'$ until $I_j' \approx I_j$.

2.2.4.2 B-splines registration

One drawback of optical flow registration methods is that corresponding features in the moving I_i and fixed I_j images are assumed to exhibit small displacements. This assumption is not strictly true for 4D-MRI as displacements can be large, for instance between the inhalation and exhalation respiratory phases. Free-form deformation basis-spline (B-spline) registration methods (Rueckert et al., 1999) do not make this assumption and might yield improved results.

In B-spline algorithms, I_i is divided into a grid containing N equally spaced control points along each dimension (Figure 2.14b). For a 2D image, control points have pixelwise co-ordinates in the ranges: $0 \leq \mathbf{a} \leq N - 1$ and $0 \leq \mathbf{b} \leq N - 1$. The region bound by 4 control points is denoted as a tile. Within the tile, pixel locations can be represented using the normalised co-ordinate systems: $0 \leq \mathbf{u} \leq 1$ and $0 \leq \mathbf{v} \leq 1$ (Figure 2.14a).

Rueckert et al. (1999) demonstrated that M_j^i can be represented by the piecewise smooth cubic spline basis set. For instance, the x-component of the transformation matrix M_j^i (\mathcal{X}_j^i) for a pixel at co-ordinates (\mathbf{x}, \mathbf{y}) in a 2D image,

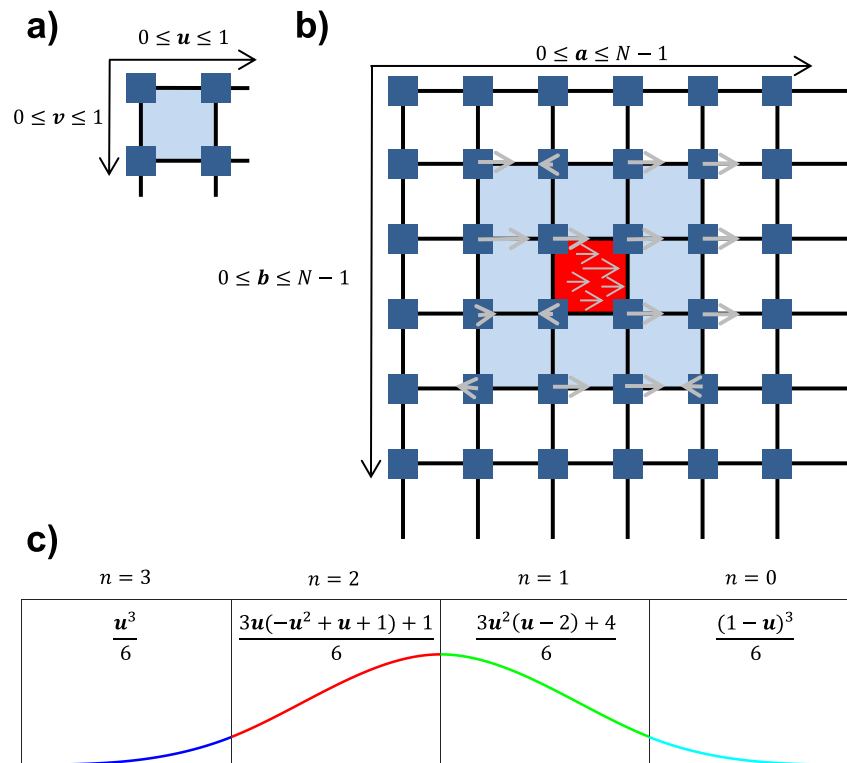


Figure 2.14: a) In 2D, 4 control points are used to define a tile, which has normalised local co-ordinates \mathbf{u} and \mathbf{v} . b) A 2D image is split into a regular grid of $N \times N$ control points, which have co-ordinates \mathbf{a} and \mathbf{b} . Equation 2.49 is used to calculate the x-component displacements of M_j^i for pixels within the central red tile using information from the surrounding 16 control points in the shaded blue region. The x-component magnitude \mathcal{P}_x at the control points are demonstrated by the gray arrows. c) A depiction of the four ($n = 0 : 3$) cubic B-spline polynomial functions for $0 \leq \mathbf{u} \leq 1$.

can be constructed as:

$$\mathcal{X}_j^i(\mathbf{x}, \mathbf{y}) = \sum_{m=0}^3 \sum_{n=0}^3 B_m(\mathbf{u})B_n(\mathbf{v})\mathcal{P}_x(\mathbf{a} + m, \mathbf{b} + n) \quad (2.49)$$

Where B_n refers to the n^{th} cubic B-spline polynomial and \mathcal{P}_x is the x-component magnitude of a control point. The cubic B-spline polynomials are described in Figure 2.14c. Expansion of expression 2.49 demonstrates that there are 16 components contributing to $\mathcal{X}_j^i(\mathbf{x}, \mathbf{y})$, which arise from the four polynomials in the cubic B-splines basis and the two image dimensions (Figure 2.14b).

The optimal transformation is estimated by iteratively warping the underlying control point grid of I_i by searching for the \mathcal{P}_x coefficients that minimise the differ-

ences between $I'_j = W_j^i I_i$ and I_j . Detailed information regarding implementation of the full 3D version of equation 2.49 can be found in (Rueckert et al., 1999). In (Rueckert et al., 1999), normalised mutual information (NMI) was employed to test for similarity between I'_j and I_j , and bending energy was used to regularise M_j^i . Figure 2.15 shows an example deformation of I_i and its control point grid, obtained using B-splines registration.

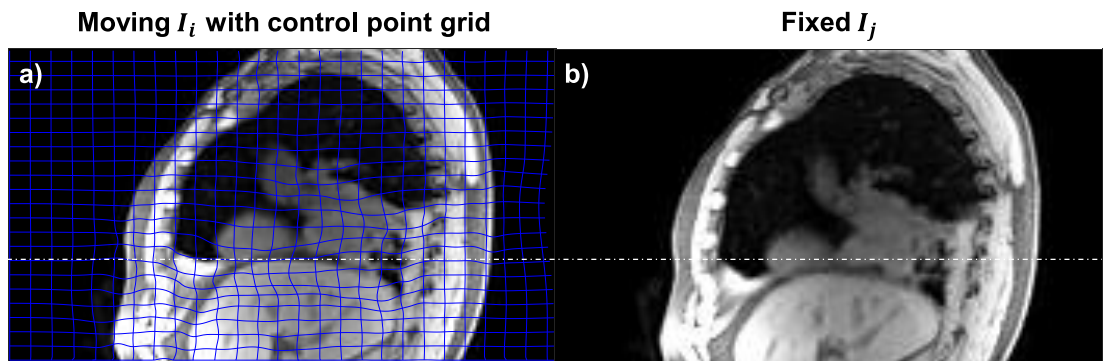


Figure 2.15: a) The moving image I_i overlaid with its warped control point grid. b) The fixed image I_j .

2.2.5 Machine learning and deep convolutional neural networks

Machine learning algorithms employ statistical methods to learn functions relating input (\mathbf{x}) and output data [$\mathbf{y} = g(\mathbf{x})$] (Goodfellow et al., 2016). One type of machine learning algorithm is the neural network, which can be represented as a chain (i.e. network) of n composed functions: $g(\mathbf{x}) = f^n(f^{n-1}(\dots(f^1(\mathbf{x}))))$. The n composed functions are known as layers of the neural network, e.g. f^1 and f^2 represent the first and second layers. If there are three or more layers, the term deep neural network is used. Neural networks can be trained to approximate a desired function $g^*(\mathbf{x})$ using a training data set $[\mathbf{x}, \mathbf{y}]$. During training, parameters in the n layers of $g(\mathbf{x})$ are iteratively optimised until $g(\mathbf{x}) \approx g^*(\mathbf{x})$. The learnt transformation $g(\mathbf{x})$ can be applied to infer \mathbf{y} from data \mathbf{x} previously unseen by the network.

A dCNN is a type of deep neural network (LeCun et al., 1998), which is applied to process data with a grid-like topology, for instance a 2D image. Deep convolutional neural network architectures typically contain multiple convolutional, pooling and fully connected layers (Goodfellow et al., 2016).

Convolutional layers include convolution and non-linear activation operations. Convolution operations are equivalent to image filtering, e.g. edge-detection or Gaussian blurring. The type of filtering is determined by the kernel weights employed in the convolution operation. For example, as shown in Figure 2.16, the following 3×3 kernel can be applied in a 2D convolution operation to extract the horizontal edges contained in a red-green-blue image I :

$$I' = \sum_{n=0}^2 \begin{bmatrix} -1 & 0 & +1 \\ -2 & 0 & +2 \\ -1 & 0 & +1 \end{bmatrix} * I(:, :, n) \quad (2.50)$$

Where I' is the filtered image (i.e. feature map) and the numbers contained in the matrix are the kernel weights. One advantage of dCNNs is that the kernel weights can be learnt from training data without supervision, which obviates the need to hand-craft the representation of individual functions employed in the network.

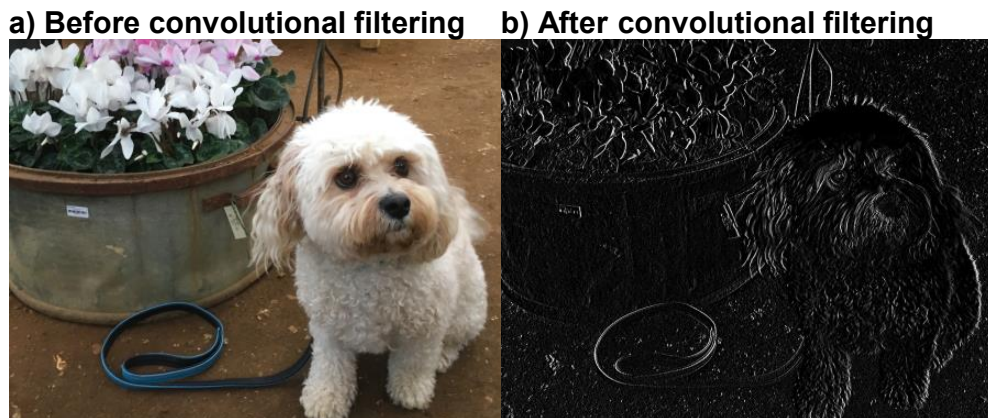


Figure 2.16: a) Before and b) After convolutional filtering. In this example, the convolution operation emphasises horizontal gradients contained in a).

Application of non-linear activations, such as the rectified linear unit (ReLU) function, enable the dCNN to approximate non-linear operations. The ReLU function is defined as:

$$\text{ReLU}(x) = \begin{cases} x & x \geq 0 \\ 0 & x < 0 \end{cases} \quad (2.51)$$

Pooling layers are employed in dCNNs to reduce the matrix-size of feature maps output following a convolutional layer. In this thesis, pooling (i.e. downsampling) is performed using a max pooling operator, which is demonstrated in Figure 2.17. Fully connected layers can be implemented after several successive convolutional and pooling layers to calculate classes or labels from downsampled feature maps, e.g. see the Alexnet classification network (Krizhevsky et al., 2012).

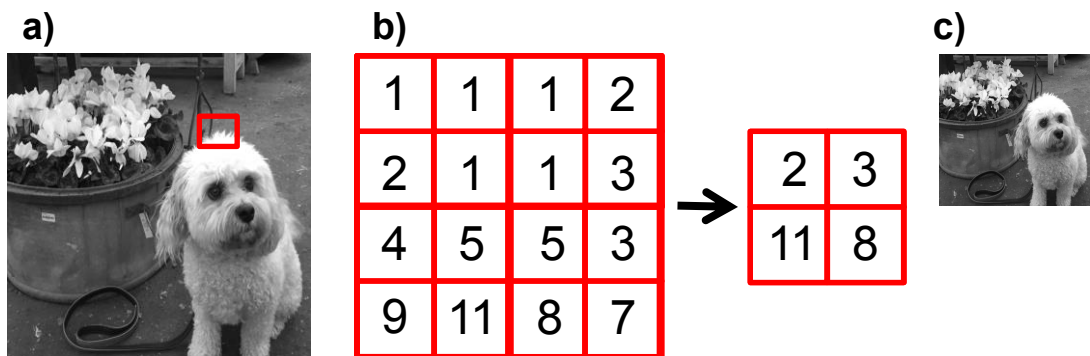


Figure 2.17: a) The 2D image to be downsampled. The exaggerated red rectangle shows an example 4×4 image patch. b) The example patch in a) is downsampled to a matrix-size of 2×2 by taking the maximum intensity values. c) The image exhibited in a) is downsampled by repeating the max pooling process of b) for all patches contained in a).

Examples of dCNNs used for image analysis and reconstruction include ResNet (He et al., 2016), Xception (Chollet, 2017), Automap (Zhu et al., 2018) and U-net (Çiçek et al., 2016; Ronneberger et al., 2015). A detailed introduction to the U-net architecture is given in section 6.2.5. Specific examples of dCNNs utilised for medical image analysis can be found in the following review articles (Lee et al., 2017; Sahiner et al., 2019).

Chapter 3

Development of the motion vector field projection method to calculate T2-weighted 4D-MRI

This chapter introduces a method to obtain high-quality 4D-T2w MRI by retrospectively transforming 3D-T2w MRI with motion vector fields calculated from 4D-T1w MRI. For ten lung cancer patients, resulting 4D-T2w MRI were verified against 4D-T1w MRI by comparison of diaphragm positions, anatomical landmarks and normalised mutual information. The potential of 4D-T2w MRI to aid target and OAR delineation in thoracic radiotherapy treatment planning was evaluated. The work described in this chapter was published in part by Freedman et al. (2017).

3.1 Introduction

As discussed in section 1.4.1, T2w MRI exhibits improved soft-tissue contrast for lesions with high fluid content when compared to T1w MRI and CT (Kumar et al., 2016). High soft-tissue contrast T2w MRI could facilitate delineation of radiotherapy target structures. To date, there have been few studies investigating the efficacy of 4D-T2w MRI for RTP of moving anatomies, such as the liver (van de Lindt et al., 2018a,b) or abdomen (van Kesteren et al., 2019). Lack of studies might be due to the challenges involved in generating 4D-T2w MRI using TSE sequences, which are high SAR and long repetition time. Long repetition times are required in TSE sequences to enable the longitudinal magnetization to return to equilibrium following each echo train.

Four-dimensional T2w MRI can be constructed from aggregated and sorted 2D-T2w single-shot TSE data, where the problem of long repetition times is overcome using an interleaved multi-slice acquisition (Tryggestad et al., 2013). Yet, calculated 4D-T2w MRI suffers from artefacts associated with slice-selective techniques; see section 2.2.2.3. Three-dimensional acquisition schemes do not have the limitations of 2D acquisition schemes and resulting 4D-T2w MRI could be of higher quality. However, it is not possible to apply an interleaved strategy to conventional 3D acquisitions because Cartesian 3D-T2w MRI cannot be dynamically acquired with sufficient spatio-temporal resolution.

Four-dimensional T2w MRI might instead be obtained using the 3D non-Cartesian pulse sequences introduced in section 2.2.3, such as the radial stack-of-stars sequence. To achieve T2-weighting, this sequence would need to be modified to include a TSE readout to acquire the same radial spoke in all partitions (Benkert et al., 2018). Alternatively, a TSE radial phase encoding sequence (Boubertakh et al., 2009; Prieto et al., 2010) could be utilised to acquire 4D-T2w MRI (Kolbitsch et al., 2018a). However, the two above-mentioned radial sequences would also suffer from high SAR and a long repetition time.

Four-dimensional MRI could also be generated by applying a motion-model to

a reference volume (McClelland et al., 2013). For instance, Blackall et al. (2005) obtained 4D-MRI by applying a single-parameter motion-model, with MVFs extracted from intraoperative ultrasound images, to static MRI. Using similar methods, McClelland et al. (2006) developed a temporal-fitting motion-model for CT, which was based on performing DIR between reference and free breathing volumes. Furthermore, Marx et al. (2014) generated 4D-CT by applying the motion information from 4D-MRI to 3D-CT.

Until the work presented in this chapter, no method or motion-model had been developed to generate 4D-T2w MRI from data acquired using 3D pulse sequences. The aims of this chapter were therefore to:

1. Develop a method to generate 4D-T2w MRI using data obtained from 3D acquisitions.
2. Verify calculated 4D-T2w MRI.
3. Evaluate the potential of 4D-T2w MRI for target and OAR delineation in thoracic RTP.

3.2 Materials and methods

3.2.1 Data acquisition

Ten patients with non-small cell lung cancer (6 female, 4 male; aged 63-86 years; 5 squamous cell carcinoma and 5 adenocarcinoma) were scanned with an axial 3D-T1w stack-of-stars spoiled gradient echo sequence in free breathing with golden angle spacing (Block et al., 2014; Winkelmann et al., 2007), and an axial 3D-T2w TSE sequence (Lichy et al., 2005) with respiratory gating to exhalation at 1.5 T (MAGNETOM Aera; Siemens Healthcare, Erlangen, Germany). All patients included in this study gave written informed consent. Axial orientation was chosen to facilitate delineation for the purpose of RTP. The T2w sequence was gated to exhalation using a liver-dome navigator. Furthermore, the T2w sequence employed

variable refocusing flip angles along its echo train (Lichy et al., 2005), which were optimised for lung T1 and T2 relaxation times. Figure 3.1 shows the patient set-up used to acquire MR images, as demonstrated by a healthy volunteer. More information regarding TSE and radial stack-of-stars sequences can be found in sections 2.1.3.4 and 2.2.3.1, respectively.

Patient set-up on diagnostic MRI

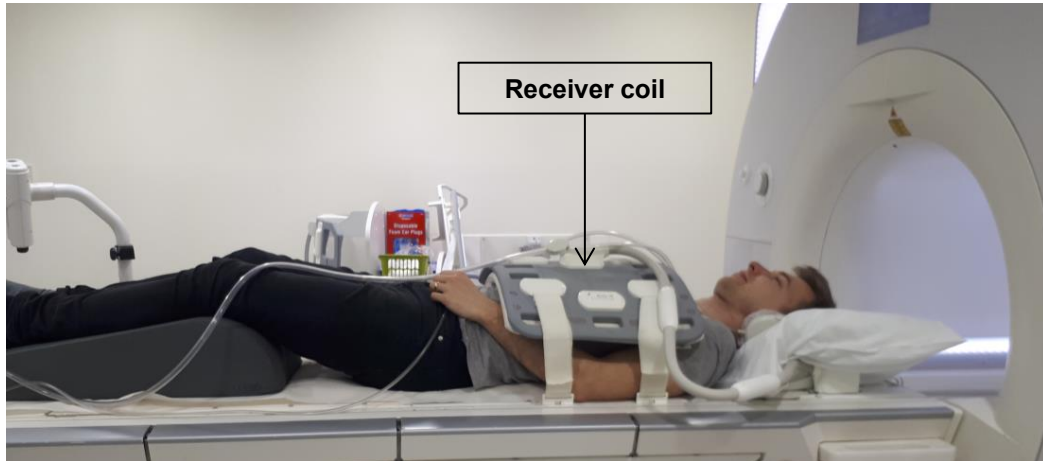


Figure 3.1: Patient set-up used to acquire T1-weighted and T2-weighted MRI, as demonstrated by a healthy volunteer.

A range of sequence parameters were used due to variation in patient habitus. Initially, a relatively high bandwidth (1085 Hz) was selected (patients 1 to 6) but was later found to be suboptimal regarding image quality of reconstructed 4D-T1w MRI. After protocol optimisation, a lower bandwidth (630 Hz) was used (patients 7 to 10), which resulted in an incremental improvement in image quality of 4D-T1w MRI and also enabled a smaller voxel size. Detailed acquisition parameters are listed in Table 3.1.

3.2.2 Reconstruction of T1w data

The acquired data were retrospectively reconstructed using the 4D joint MoCo-HDTV algorithm (Rank et al., 2017), which was introduced in section 2.2.3.2. Before reconstruction, an adaptive gradient-delay compensation was applied to the

Table 3.1: Acquisition parameters of the T1w and T2w sequences. Fat suppression was used in 8 out of 10 cases for the T2w sequence. Variable refocusing flip angles were employed in the T2w sequence. T1w indicates T1-weighted; T2w, T2-weighted; NA, not applicable.

Parameter	T1w	T2w
No. patients	10	10
Orientation	Axial	Axial
Echo train length	NA	62
No. slices	88 - 96	80 - 96
Slice oversampling, %	16.7 - 27.7	25.0 - 40.0
No. spokes per slice	935 - 1440	NA
Total acquisition time, min	04:58 - 07:42	05:34 - 09:16
Field-of-view, mm ³	336 × 336 × 288 - 384 × 384 × 290	420 × 242 × 264 - 480 × 288 × 290
Voxel size, mm ³	1.31 × 1.31 × 3.0 - 1.5 × 1.5 × 3.3	1.31 × 1.31 × 3.0 - 1.5 × 1.5 × 3.3
Echo time, ms	1.24 - 1.55	108 - 115
Repetition time, ms	2.51 - 3.18	1000 - 1500
Flip angle, °	8 - 12	variable
Readout bandwidth, $\frac{Hz}{Pixel}$	630 - 1085	560 - 600
Fat suppression	Yes	8:Yes, 2:No

raw data, to reduce artefacts associated with inaccuracies in the timing of gradients (Block and Uecker, 2011). Afterwards, the raw data were sorted into 20 overlapping respiratory phases based on the amplitude of the self-gating respiratory surrogate signal (Paul et al., 2015). Weightings of the HDTV operator (see equation 2.44) were optimised by reducing temporal regularisation such that the images remained clear of undersampling artefacts whilst avoiding over-regularisation of true motion. Optimisation of the HDTV weightings was possible by comparing the joint MoCo-HDTV reconstructed images to those obtained using a Gridding reconstruction (Rank et al., 2017), which, although severely affected by streaking artefacts, did not exhibit motion regularisation. Subsequently, an offline gradient non-linearity

distortion correction was applied to each respiratory phase of the reconstructed 4D-T1w image, using a spherical harmonics deconvolution method (Doran et al., 2005; Janke et al., 2004).

3.2.3 Overview of the MVFP method

The motion vector field projection (MVFP) method generates 4D-T2w MRI by extracting motion information from 4D-T1w MRI, using DIR, and applying it to 3D-T2w MRI. An overview of the MVFP method can be found in Figure 3.2.

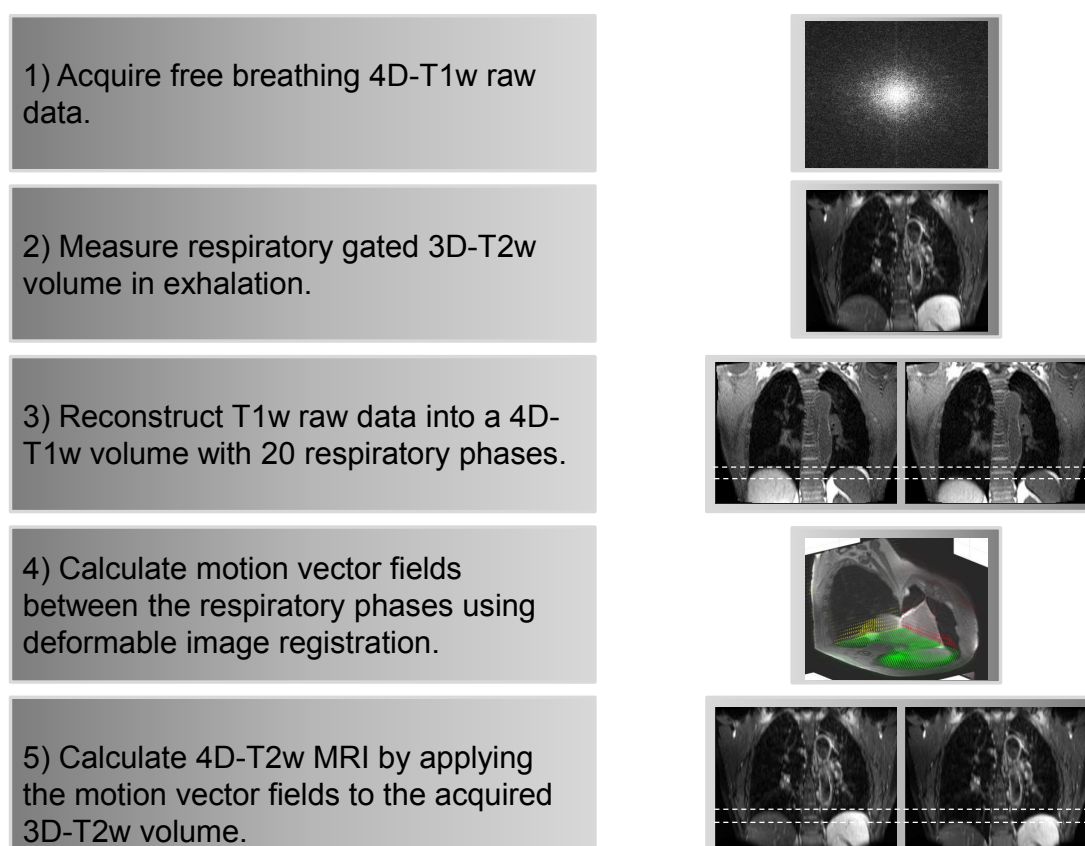


Figure 3.2: A visual overview of the motion vector field projection method. Note that the green, red, and yellow arrows in step 4 display the motion vector fields corresponding to the shown axial, coronal, and sagittal planes. Dashed white lines aid visualisation of the diaphragm position on T1w and T2w MRI.

3.2.4 Calculation and application of motion vector fields

A one-dimensional (1D) signal describing image similarity was obtained by calculating the NMI (Pluim et al., 2003) (calculated in-plane and averaged over all slices) between the 3D-T2w image and each respiratory phase j contained in the 4D-T1w image; where $j \in [1, \dots, N]$ (total number) respiratory phases. The respiratory phase i of the 3D-T2w image was set equal to the respiratory phase j that corresponded to the signal maximum. In this way, a tie-phase was established between the 4D-T1w and 3D-T2w images.

Motion vector fields between the respiratory phases i and j of the reconstructed images ($T1_i, T1_j$) were calculated by DIR. A B-spline graphics processing unit (GPU) accelerated implementation of NiftyReg (Modat et al., 2010; Rueckert et al., 1999) was used to calculate all registrations.

A chain method, similar to that proposed by (Boldea et al., 2008), was developed to enable a balance between errors resulting from large deformations and concatenation of sequential deformations. In the chain method, the 3D-T1w image at the n^{th} phase $T1'_n$ is obtained by sequentially applying a number of smaller deformations that are linked together at calculated chain-point phases κ , to the tie-phase ($T1_i$). The chain method can be applied using the following notation. Let the warping operator W_m^l describe application of the MVF M_m^l to the l^{th} phase $T1_l$, such that:

$$T1'_m = W_m^l T1_l \quad (3.1)$$

Consider an example where $T1'_n$ is calculated from $T1_i$ using two chain-point phases (κ_1 and κ_2). This concatenation can be expressed by applying equation 3.1 as:

$$\begin{aligned} T1'_n &= W_n^i T1_i \\ &= W_n^{\kappa_2} W_{\kappa_2}^i T1_i \\ &= W_n^{\kappa_2} W_{\kappa_2}^{\kappa_1} W_{\kappa_1}^i T1_i \end{aligned} \quad (3.2)$$

In this chapter, warping operators were applied sequentially in image-space as in expression 3.2. However, in all later chapters, MVFs were composed in MVF-space and applied once to $T1_i$ using W_n^i . The chain-point phases were determined based on fractions of the calculated image similarity signal range. This was possible because the image similarity signal indirectly corresponded to the deformation size between phases. The chain-point phases corresponding to inspiration were set equal to those of expiration, which was feasible because of the symmetry present in the observed respiratory patterns. A maximum of 3 deformations were chosen, and phases closest to 33 % and 67 % of the signal range were set as chain-points. An overview of the chain method can be found in Figure 3.3.

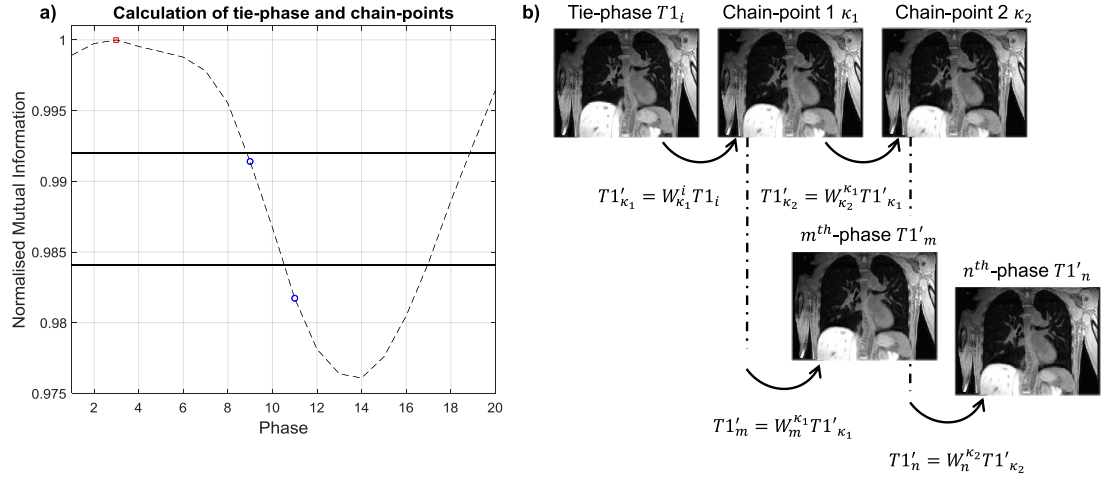


Figure 3.3: a) Displays the image similarity signal with the tie-point phase (red square) and chain-point phases (blue circles). Percentages of the signal range (33 % and 67 %) used to calculate the chain-point phases are shown by horizontal solid lines. b) The images corresponding to the chain-point phases (κ_1 and κ_2) are determined by sequentially warping the tie-phase with the required motion vector fields. The chain-point phases are used as a starting point to generate any arbitrary phase. For instance, the m^{th} phase is calculated with 2 deformations (tie-phase \rightarrow chain-point 1; chain-point 1 $\rightarrow m^{th}$ phase) and the n^{th} phase requires 3 deformations (tie-phase \rightarrow chain-point 1; chain-point 1 \rightarrow chain-point 2; chain-point 2 $\rightarrow n^{th}$ phase). Note, W_m^l is an operator which transforms $T1_l$ to $T1'_m$ through application of a motion vector field.

The parameters of NiftyReg were optimised by comparing the estimated ($T1'$) and reconstructed ($T1$) 4D-T1w images. The root mean square error, dice

coefficient (averaged over all respiratory phases), and visual image quality were analysed as metrics. An NMI cost function with number of levels performed = 3, control point spacing = 3 mm, bending energy weighting = 0, Jacobian penalty weighting = 0, and maximum iterations = 500 was best able to reproduce the reconstructed 4D-T1w image (dice > 0.965, root mean square error < 5%, good qualitative agreement). A detailed description of the NiftyReg parameters can be found online (CMIC, 2015).

The 3D-T2w image was registered (global affine (Ourselin et al., 2001)) and then resampled (cubic interpolation) to the matrix size of the 4D-T1w tie-phase. Using the chain method, 4D-T2w MRI was then obtained by applying the calculated MVFs to the processed 3D-T2w image.

3.2.5 Verification of 4D-T2w MRI

The calculated 4D-T2w images were verified against their corresponding 4D-T1w images. A semi-automated edge-detection method was developed and used to verify the diaphragm positions, a radiation oncologist manually delineated control points for comparison of anatomical landmarks and the NMI was calculated to assess volumetric image similarity. For each metric, the differences between 4D-T1w and 4D-T2w MRI were compared to those between 4D-T1w and 3D-T2w MRI.

3.2.5.1 Edge-detection method

In the edge-detection method, the user manually places a rectangular 2D region of interest (ROI) over the right hemi-diaphragm surface, orientated along the superior-inferior (SI) direction, on a coronal or sagittal slice. Along the SI dimension, the ROI should be sufficiently large to encompass expected respiratory motion (approximately 2-3 cm) and narrow in the medial-lateral dimension such that the bounded diaphragm surface is approximately flat. An example of ROI positioning is shown in Figure 3.4a. For consistency, an ROI was placed on the coronal slice that exhibited both the aortic arch and the descending aorta.

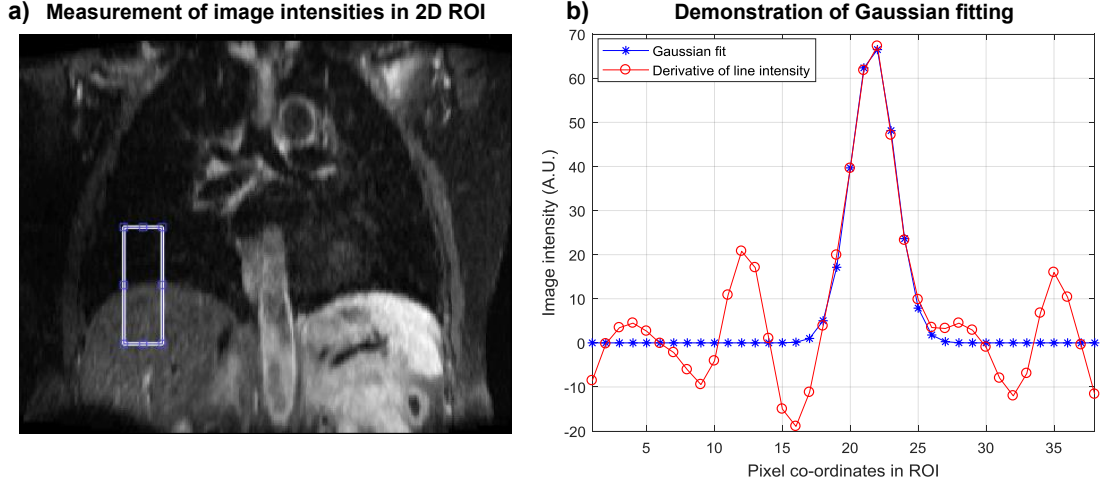


Figure 3.4: a) Measurement of superior-inferior lines of image intensity within the manually placed 2D region of interest (ROI). b) A Gaussian function (blue stars) is fitted to the derivative of a measured line of image intensity (red circles).

Image intensity was measured along all SI lines within the 2D ROI. For each SI line, the diaphragm position was calculated by fitting a Gaussian to the derivative of the measured line intensity $y'(x)$ (matrix of size $[1, N]$) according to:

$$y_0 = \operatorname{argmin}_{a, b, \mu} \sum_{x=1}^N \left(y'(x) - a \exp \left[-\frac{1}{2} \left(\frac{x - \mu}{b} \right)^2 \right] \right)^2 \quad (3.3)$$

Where a , b and μ represent the amplitude, width and position of the Gaussian function, respectively. Least squares minimisation was applied for fitting. An example showing the results of fitting for one SI line is displayed in Figure 3.4b. Outliers in diaphragm position across all SI lines were removed based on the interquartile range of the detected diaphragm positions. The diaphragm position was chosen as the mean of the remaining diaphragm positions within the 2D ROI and the standard deviation corresponded to the diaphragm width.

3.2.5.2 Delineated control points

Using a developed delineation toolkit, a radiation oncologist (6 years experience) identified 5 anatomical control points (1 static and 4 mobile) in even numbered respiratory phases in both 4D-T1w and 4D-T2w MRI:

1. Posterior spinal canal at the superior aspect of T4.
2. Inferior point of the carina.
3. Bifurcation of the right middle and lower lobe bronchus.
4. Bifurcation of the left main bronchus and left upper lobe bronchus.
5. Right costophrenic angle.

The right costophrenic angle was delineated on coronal images, with the coronal slice chosen to correspond with the level of the bifurcation of the right upper and middle lobe bronchus. The delineation toolkit offered coronal, sagittal, and axial views and delineation could be performed on either of them. Example screenshots of the delineation toolkit are shown in Figure 3.5.

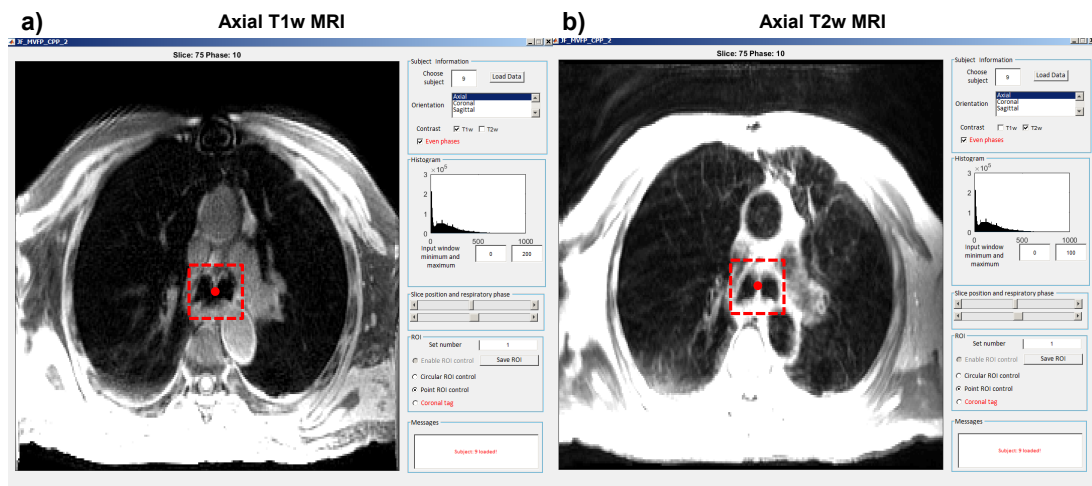


Figure 3.5: Example screenshots of the developed control point delineation toolkit. Delineation of the inferior point of the carina is shown by a red circle contained within a dashed red box in axial a) T1w and b) T2w images. The windowing scheme was optimised by the radiation oncologist for viewing the carina.

Figure 3.6 shows an example of control point delineation for patient 8. These particular control points were chosen because they are visible in both 4D-T1w and 4D-T2w MRI, as well as being reproducible across patient sets. To assess spatial coherence between landmarks, Euclidean distances (E_d) were calculated between pairs of delineated points in both 4D-T1w ($T1_x, T1_y, T1_z$) and 4D-T2w MRI ($T2_x, T2_y, T2_z$) according to:

$$E_d = \sqrt{(T1_x - T2_x)^2 + (T1_y - T2_y)^2 + (T1_z - T2_z)^2} \quad (3.4)$$

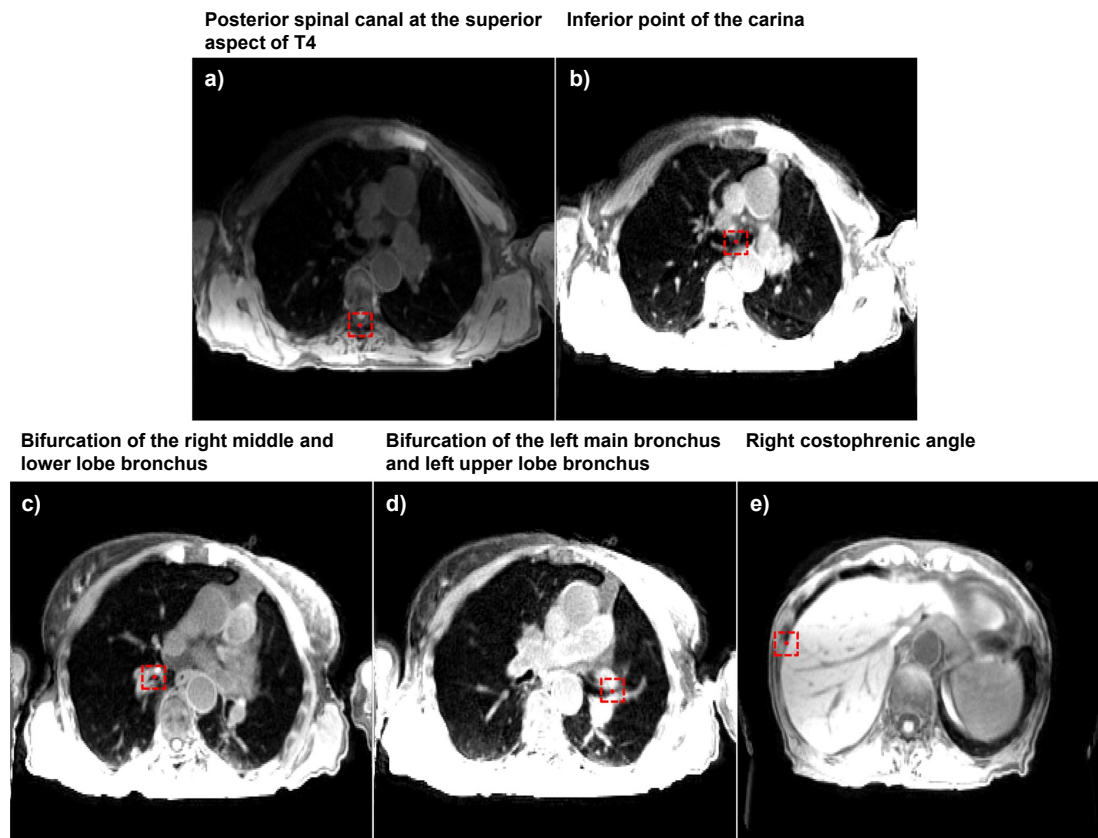


Figure 3.6: An example of control point delineation for patient 8 on snapshot images of 4D-T1w MRI. a)-e) Displays the five delineated control points (red circles), which are contained within dashed red boxes to assist visualisation. The presented windowing schemes were optimised by the radiation oncologist for viewing of the anatomical landmarks and not for surrounding anatomy.

3.2.5.3 Volumetric image similarity

Normalised mutual information (Pluim et al., 2003) was calculated between each corresponding respiratory phase of the 4D-T1w and 4D-T2w images. The result was compared with the NMI measured between each respiratory phase of the 4D-T1w image and the 3D-T2w image. If 4D-T1w and 4D-T2w MRI exhibit comparable respiratory phase and geometrical position, then the NMI for all respiratory phases should be similar to the NMI assessed between the tie-phase of the 4D-T1w image and the 3D-T2w image.

3.3 Results

Four-dimensional T2w MRI were calculated for 10 patients with primary lung malignancies. Four-dimensional T1w MRI reconstruction, using a nonoptimised prototype implementation, took between 9 and 12 hours for 20 respiratory phases and the chain method took between 25 and 30 minutes. The mean period of the respiratory cycle averaged over patients was 4.1 ± 0.95 seconds. Figure 3.7 shows an example reconstructed 4D-T1w image and a calculated 4D-T2w image at respiratory phases corresponding to exhalation, mid-cycle and inhalation. For all patients, 4D-T2w MRI exhibited qualitatively similar respiratory motion to corresponding 4D-T1w MRI.

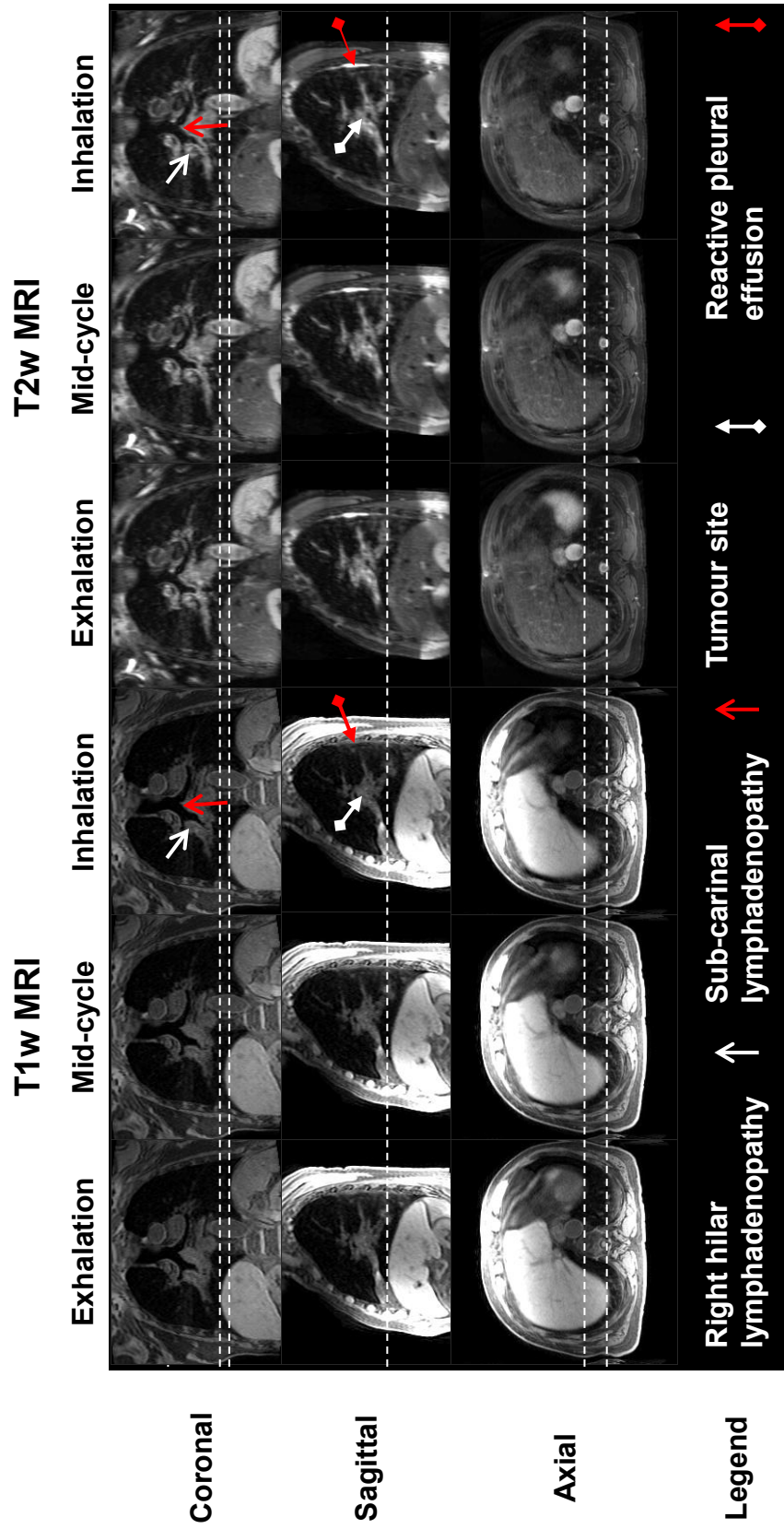


Figure 3.7: Example T1w and T2w coronal, sagittal, and axial views at exhalation, mid-cycle, and inhalation respiratory phases for patient 7. This patient was diagnosed with T1aN2 primary lung squamous cell carcinoma and had a small reactive pleural effusion. The dashed white lines aid visualisation of the diaphragm surface position. The respiratory pattern of T1w MRI is preserved in T2w MRI. The tumour site, lymphadenopathy, and reactive pleural effusion are shown more clearly in T2w MRI than T1w MRI.

3.3.1 Verification of 4D-T2w MRI

Mean diaphragm surface positions were calculated using the edge-detection method for all patients on both T1w and T2w images. Figure 3.8a displays an example of the diaphragm surface displacement for patient 5. Figure 3.8b shows the range of diaphragmatic displacement of 4D-T1w MRI, as calculated by the edge-detection method. Figure 3.8c shows the spread of the displacement between diaphragm positions on both T1w and T2w images across all respiratory phases. Median diaphragm positions were consistent with less than 1 slice thickness (3.3 mm) for all patients, except patient 7, which exhibited median displacements within 6.6 mm. For all patients, T1w and T2w MRI were less consistent at inhalation than at exhalation. The Pearson correlation coefficient was calculated between the median diaphragm differences of 4D-T1w and 4D-T2w MRI, and the range of diaphragmatic displacements in 4D-T1w MRI. No significant correlation ($r = -0.19$, $p = 0.60$) was observed.

There was a reduction in the mean and standard deviation, averaged over all patients, of the interquartile range of the differences in diaphragm positions over all respiratory phases, between 4D-T1w and 4D-T2w MRI (1.11 ± 0.81 mm) compared to 4D-T1w and 3D-T2w MRI (9.83 ± 3.95 mm).

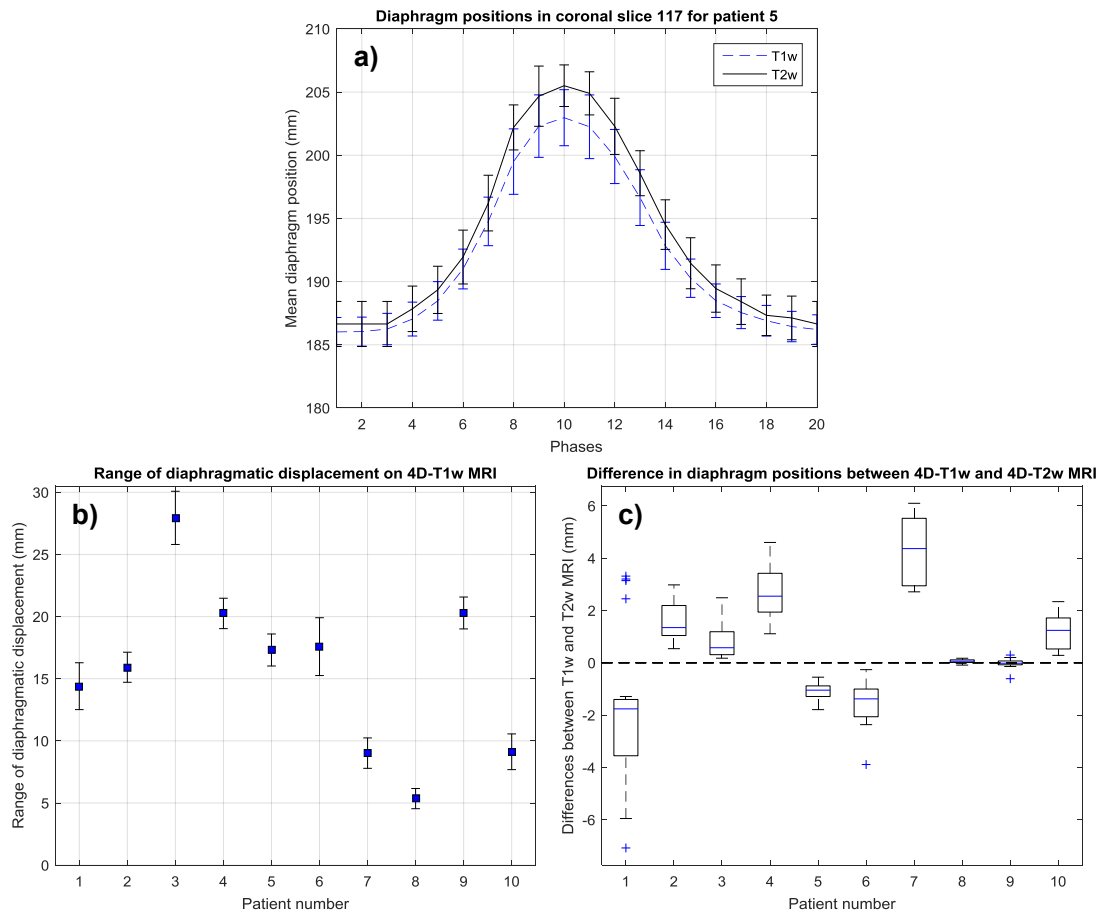


Figure 3.8: a) Example diaphragm surface positions, calculated using the edge-detection method, of the 4D-T1w and 4D-T2w images for patient 5. Error bars correspond to the standard deviation across superior-inferior lines and represent the width of the diaphragm surface. b) The ranges of diaphragmatic displacements in 4D-T1w MRI calculated using the edge-detection method. Errors bars show the uncertainty in the range. c) Box plot of the spread of the difference in diaphragm surface positions, between the 4D-T1w and 4D-T2w images, as calculated by the edge-detection method, for the 10 patients.

Euclidean distances between anatomical landmarks in 4D-T1w and 4D-T2w MRI are shown in Figure 3.9. Euclidean distances between all corresponding anatomical landmarks were within or better than 7.6 mm (Euclidean distance of 2 voxels) and less than 3.8 mm (Euclidean distance of 1 voxel) for 355 of 470 delineated pairs of anatomical control points. Three anatomical landmarks were excluded from delineation: for patient 2, the posterior spinal canal at the superior aspect of T4 was removed because of poor visibility on T2w MRI; for patient 6,

the bifurcation of the left main bronchus and left upper lobe bronchus was omitted due to partial collapse of the left upper lobe; for patient 4, the right costophrenic angle was outside the acquired FOV. There was a reduction in the mean and standard deviation, averaged over patients, of the interquartile range, calculated over respiratory phases, of the Euclidean distances (in mm) for the mobile ROIs (ROIs, 2–5) between 4D-T1w and 4D-T2w MRI (0.80 ± 0.35 , 0.85 ± 0.39 , 0.78 ± 0.28 , 1.62 ± 0.70) and between 4D-T1w and 3D-T2w MRI (1.23 ± 0.48 , 2.02 ± 0.98 , 1.19 ± 0.94 , 5.16 ± 2.08).

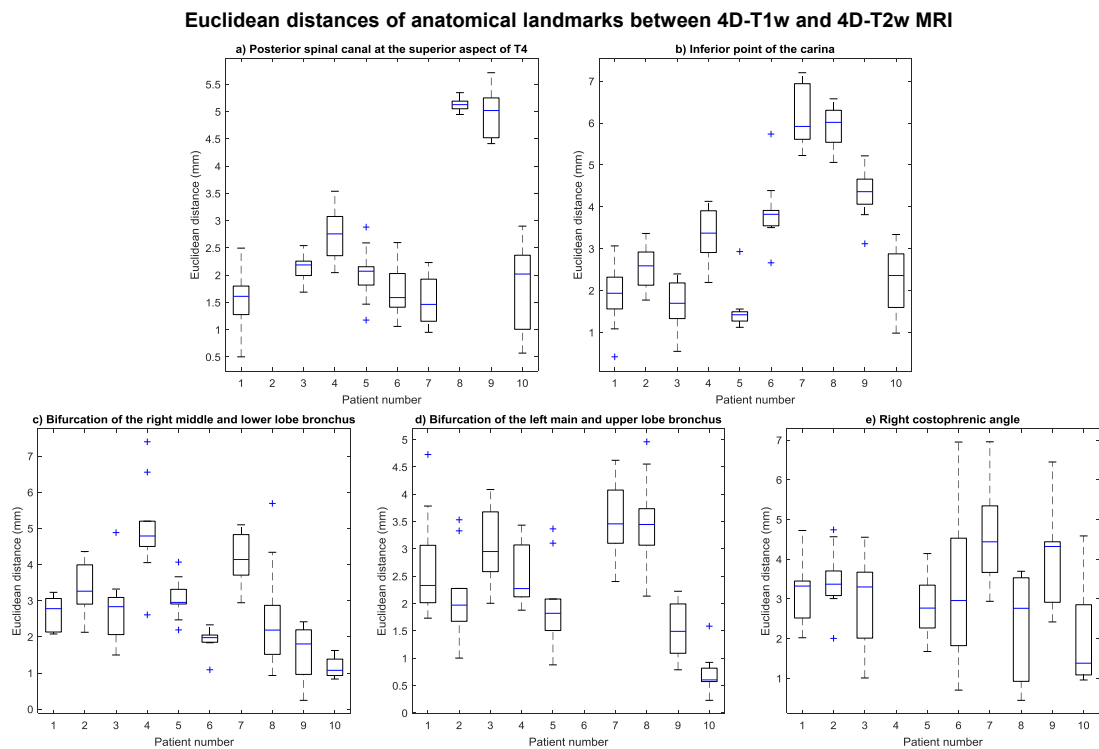


Figure 3.9: Box plot of spread of Euclidean distances, for all even respiratory phases, between pairs of anatomical landmarks that were delineated in both 4D-T1w and 4D-T2w MRI. All Euclidean distances agreed to less than 7.6 mm (Euclidean distance of 2 voxels) and 355 of 470 pairs of anatomical landmarks were consistent with less than 3.8 mm (Euclidean distance of 1 voxel).

The NMI was calculated between corresponding respiratory phases of 4D-T1w and 4D-T2w MRI, and was compared with the NMI of 4D-T1w and 3D-T2w MRI. Comparisons were made in relation to the NMI calculated between the tie-phase of 4D-T1w and 3D-T2w MRI. Figure 3.10 shows an example comparison for patient 10. Compared to the tie-phase, percentage differences in NMI (mean and standard deviation, calculated over all respiratory phases and patients) of 4D-T1w and 4D-T2w MRI were $0.41 \% \pm 0.37 \%$ and between 4D-T1w and 3D-T2w MRI were $-1.82 \% \pm 1.7 \%$.

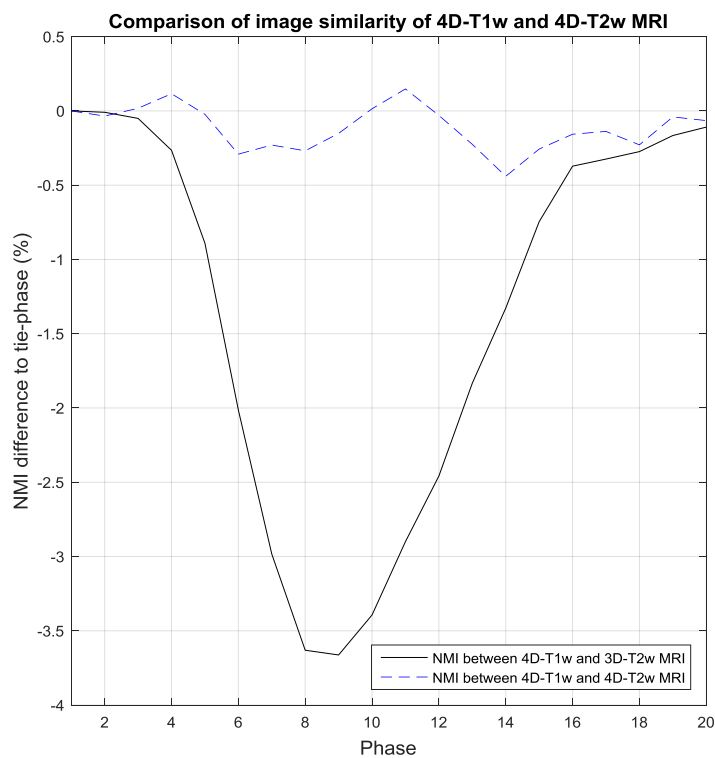


Figure 3.10: Shows an example comparison for patient 10, where results are relative to the normalised mutual information (NMI) calculated between the tie-phase of 4D-T1w and 3D-T2w MRI. In this case, the tie-phase is respiratory phase 1. NMI between 4D-T1w and 3D-T2w MRI (black solid line) indirectly corresponds to a respiratory signal. This pattern is not observed when examining NMI between 4D-T1w and 4D-T2w MRI (blue dashed curve).

3.3.2 Image artefacts

The dominant image artefact observed after application of the MVFP method was associated with inaccuracies in DIR, which led to a reduction in the quality of 4D-T2w MRI for all patients and was found to increase in magnitude with deformation size. An example is shown in Figure 3.11.

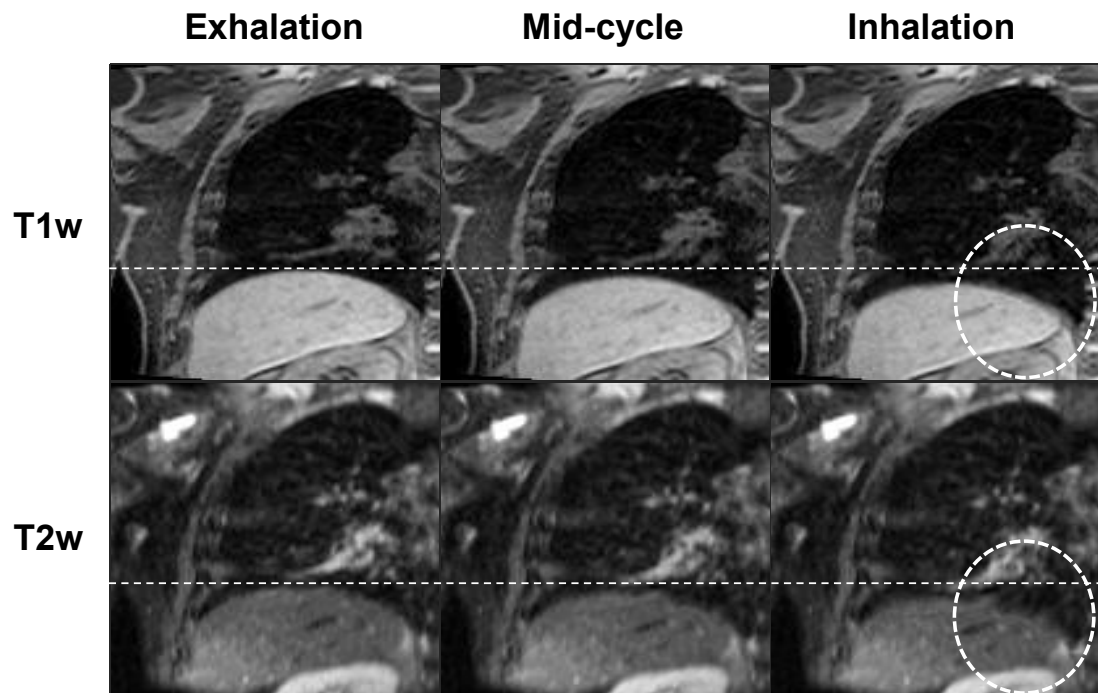


Figure 3.11: An example of the deformation artefact for patient 7. In the T2w snapshots, a deformation of the right hemi-diaphragm boundary is seen at mid-cycle and a comparatively large deformation at inhalation (dashed circle). The deformation is worse at inhalation than at mid-cycle and is not displayed in the corresponding T1w snapshots.

Artefacts that were already present in 3D-T2w MRI were propagated into 4D-T2w MRI. For all patients, minor ghosting was displayed and for two patients intensity inhomogeneity artefacts were found. An example of intensity inhomogeneity artefacts is presented in Figure 3.12.

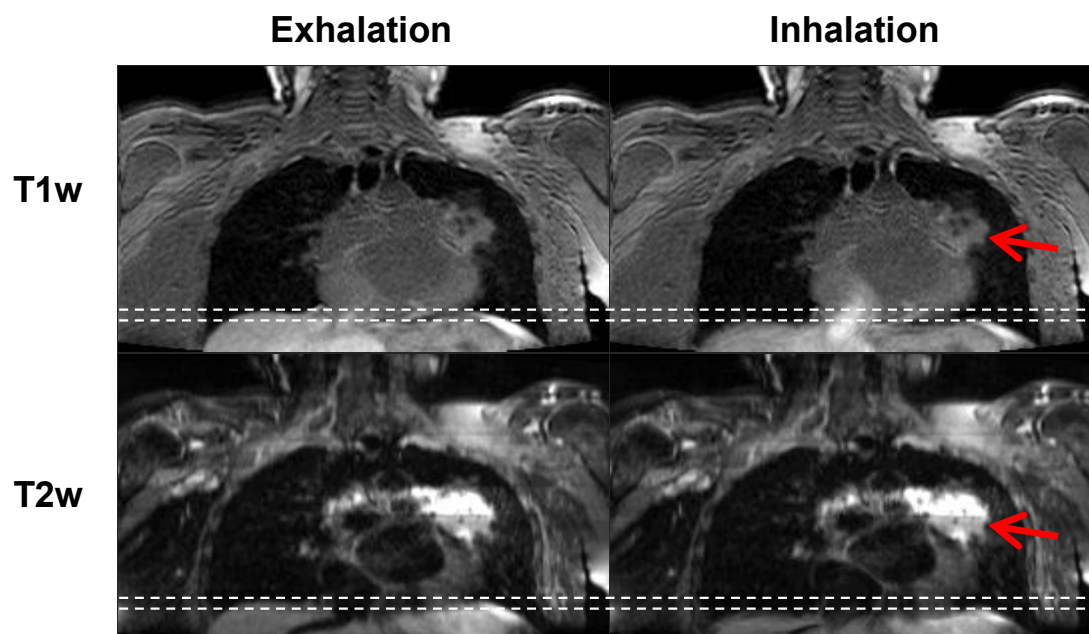


Figure 3.12: T2w MRI of patient 6 exhibits intensity inhomogeneity artefacts around the tumour site, as labelled by the red arrows. Nevertheless, the tumour extent and structure is better defined in T2w than T1w MRI.

3.3.3 Clinical evaluation

The radiation oncologist reported improved tumour definition in 4D-T2w MRI when qualitatively compared against 4D-T1w MRI. Furthermore, important clinical information was displayed in 4D-T2w MRI. In the case presented in Figure 3.7, T2w MRI better highlighted the extent and position of reactive pleural effusion and the lymphadenopathy than T1w MRI. In some situations, 4D-T2w MRI was particularly advantageous when compared with 4D-T1w MRI, for instance when mobile tumour beds were attached to or adjacent to OARs, as demonstrated in Figure 3.13. In the case displayed in Figure 3.13, the tumour was challenging to visualise in the T1w images due to poor tumour-tissue contrast. However, the tumour extent and structure were clearly visible in the T2w images. Furthermore, the anterior part of the tumour site was sliding non-rigidly against the chest wall. The extent of chest wall attachment and sliding motion were more easily visualised in T2w MRI compared to T1w MRI.

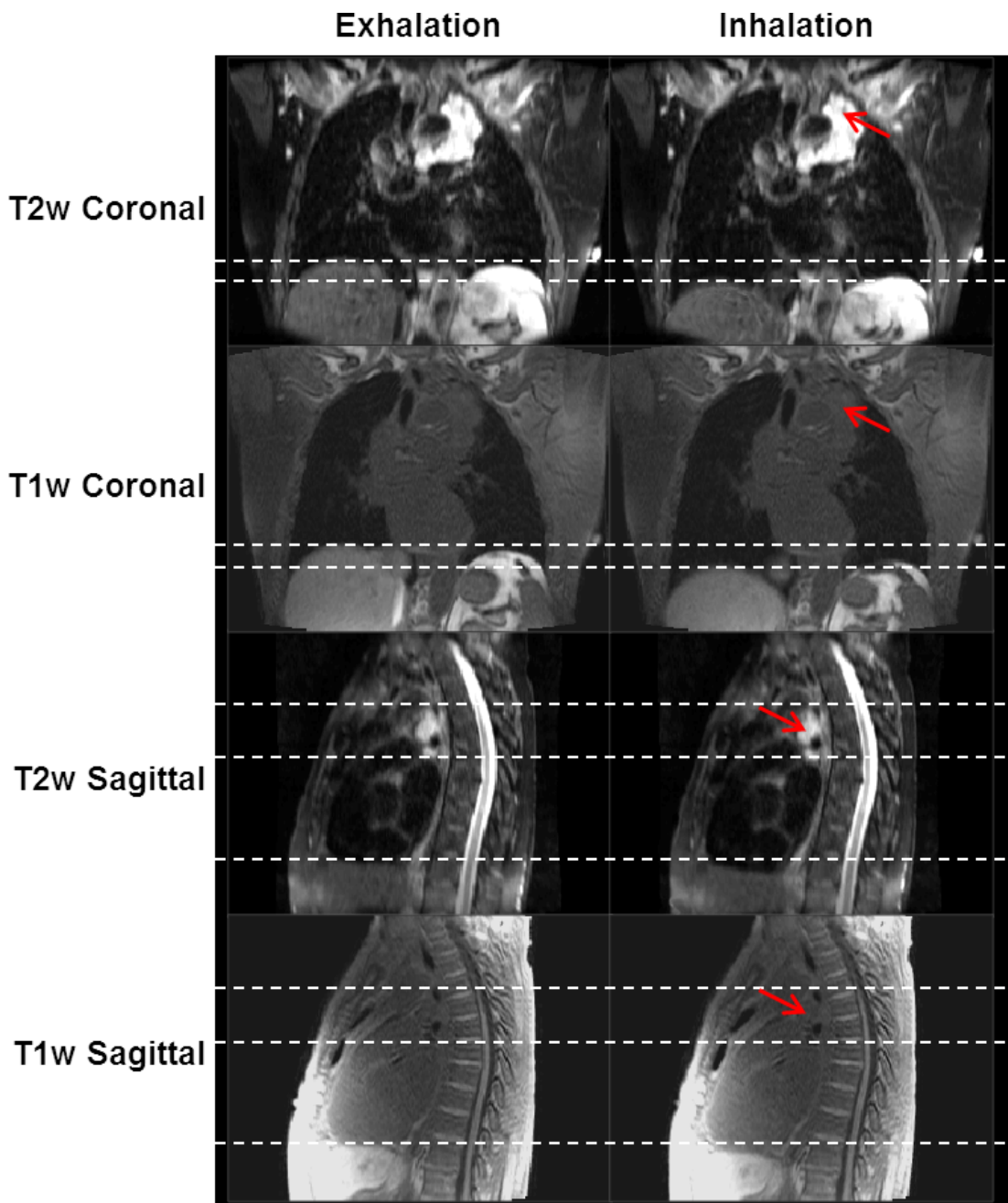


Figure 3.13: Snapshots of 4D-T1w and 4D-T2w MRI at the exhalation and inhalation respiratory phases for patient 3, who was diagnosed with T4N2 adenocarcinoma. The tumour is radically treatable, but is embedded around the heart and oesophagus. Unlike T1w MRI, T2w MRI displays a high tumour-tissue contrast enabling tumour position and structure to be clearly delineated. Sliding motion of the tumour site against the chest wall is displayed in the sagittal plane and is more clearly presented in T2w than T1w MRI. Red arrows point to the tumour site and dashed white lines aid assessment of both superior-inferior diaphragm and sliding motion.

3.4 Discussion

The first aim of this chapter was met, which was to develop a workflow to obtain 4D-T2w MRI from data acquired using 3D pulse sequences. In the presented workflow, high-quality 4D-T2w MRI were generated by applying the respiratory motion information from 4D-T1w to 3D-T2w MRI.

The workflow is not limited to 4D-T2w MRI and could be applied to simulate 4D-MRI displaying any required contrast. For instance, in Chapter 5, a modified implementation of the MVFP method was applied to (MRI-derived) 3D-sCT to obtain 4D-sCT. For specific contrasts, such as diffusion-weighted MRI or ultrashort echo time (UTE) imaging, it is not possible to use a stack-of-stars k-space sampling scheme (Triphan et al., 2015), making it more difficult to apply state-of-the-art 4D reconstruction methods. In these cases, the MVFP method could act as a solution to generate high-quality 4D-MRI.

In the PET-MRI literature, motion-corrected reconstruction techniques have been employed to obtain high-quality MVFs, 3D-T1w (Buerger et al., 2013; Cruz et al., 2016) and 3D-T2w images (Kolbitsch et al., 2018a) of the abdomen. The approach developed by Kolbitsch et al. (2018a) could be extended to calculate 4D-T2w MRI by looping the proposed motion-compensated reconstruction component over all required respiratory phases. Alternatively, the MVFP method could be applied to transform the generated 3D-T2w image to all other respiratory phases using the MVFs output by the motion-compensated 3D-T1w reconstruction.

A sequence with a radial trajectory and golden angle spacing was selected to acquire the T1w data because of advantages in image quality, such as incoherent aliasing and insensitivity to motion (Block et al., 2014). Moreover, the selected radial sequence enabled a self-gating signal to be obtained through frequent measurements of the k-space centre (Paul et al., 2015). Alternative non-Cartesian sequences could be used (Deng et al., 2015), but a stack-of-stars approach is more efficient during reconstruction, as a Fourier transform can be applied along the slice direction (Block et al., 2014). One limitation of the applied radial stack-of-

stars sequence is that it is not readily available for all centres, as it is currently a work-in-progress method.

An incremental improvement was used during the study in reducing the readout bandwidth of the 4D-T1w MRI acquisition. However, there was no significant difference in median diaphragm displacements on T1w and T2w MRI between patients 1 to 6 and patients 7 to 10 (unpaired 2-tailed t-test, significance level $\alpha = 0.05$, $p = 0.34$). Therefore, a group analysis was justified.

The 4D joint MoCo-HDTV algorithm was chosen to reconstruct 4D-T1w MRI, because it not only enables high undersampling factors by using 100 % of the raw data for reconstruction of each respiratory phase, but also results in good image quality with comparatively low streaking artefacts and high sharpness (Rank et al., 2017). One drawback of the 4D joint MoCo-HDTV algorithm is that it is currently not freely available for use by other centres, as it is a work-in-progress prototype. An additional drawback of the prototype implementation is its long run time (9-12 hours), which restricts its on-line application on MR-linac systems. However, as presented in Chapter 6, reconstruction time can be drastically accelerated to a clinical time-frame using a dCNN.

In this study, all 3D-T2w MRI were obtained in a clinically acceptable period (5-9 minutes) using a gated acquisition. However, gated acquisitions can be time-consuming (10-20 minutes) for subjects with slow or irregular breathing. This is because the respiratory navigator triggers signal acquisition based on the peak respiratory waveform amplitude extracted from past respiratory cycles.

The second aim of this chapter was achieved by verifying 4D-T2w MRI with respect to 4D-T1w MRI. Another option might have been to compare the inhalation respiratory phase of 4D-T2w MRI to 3D-T2w MRI acquired in breath-hold. However, this approach was not pursued because inhalation in breath-hold can be deeper than in free-breathing (Blackall et al., 2006; McClelland et al., 2013).

Diaphragm positions in 4D-T2w MRI were compared to those in 4D-T1w MRI using an edge-detection method. Median diaphragm positions were consistent to

less than 6.6 mm (2 voxels) for all 10 patients and less than 3.3 mm (1 voxel) for 9 out of 10 patients. Furthermore, the mean of the interquartile range of observed differences between 4D-T1w and 4D-T2w MRI was approximately 8.7 mm smaller than between 4D-T1w and 3D-T2w MRI, demonstrating that calculated 4D-T2w MRI not only contained similar motion information to 4D-T1w MRI but were also spatially coherent. One hypothesis was that the differences in diaphragm positions depended on the range of diaphragm displacements during the respiratory cycle. However, no significant correlation was found. The larger differences in diaphragm positions observed for patient 7 might result from a collapse of the middle lobe of the right lung. The observed differences were partly due to a mismatch in respiratory phase between 4D-T1w and 3D-T2w MRI; as for all patients, comparison of the diaphragm positions in 4D-T1w and 3D-T2w MRI indicated that no exact match could be found. In later chapters, the problem of diaphragm mismatch was addressed by modifying the MVFP workflow to include a B-spline non-rigid registration (Rueckert et al., 1999), immediately after the affine registration, between 3D-T2w MRI and the tie-phase of 4D-T1w MRI. The additional non-rigid registration step was not initially implemented in the MVFP workflow in an attempt to reduce expected blurring, originating from multiple registration steps, in calculated 4D-T2w MRI.

Euclidean distances between corresponding control points in 4D-T2w and 4D-T1w MRI were evaluated. Four-dimensional T2w MRI were anatomically similar to 4D-T1w MRI because all Euclidean distances were consistent to less than 7.6 mm (Euclidean distance of 2 voxels) and Euclidean distances of 355 out of 470 pairs of control points agreed to less than 3.8 mm (Euclidean distance of one voxel). Applying the MVFP method led to improved similarity of T1w and T2w MRI as the mean interquartile range of Euclidean distances between mobile ROIs of 4D-T1w and 4D-T2w MRI were smaller than those between 4D-T1w and 3D-T2w MRI by approximately 1.39 mm. Verification by manual delineation is limited, because it is a subjective process such that part of the presented differences, between pairs of anatomical control points, could be attributed to

user dependence. Multiple observers might increase the accuracy of determined anatomical landmark positions.

A high volumetric image similarity was found between 4D-T1w and 4D-T2w MRI, as NMI, relative to the tie-phase of 4D-T1w and 3D-T2w MRI, was coherent within 0.41 ± 0.37 %. No dependence on respiration of the NMI calculated between corresponding respiratory phases of 4D-T1w and 4D-T2w MRI was apparent, as demonstrated in Figure 3.10. Four-dimensional T2w MRI were therefore commensurate to 4D-T1w MRI in spatio-temporal location. One drawback of this approach is that the NMI metric is not only sensitive to relevant spatio-temporal information but also to both image artefacts and noise. This metric was chosen because it can handle analysis between different image contrasts (Pluim et al., 2003).

Four-dimensional T2w MRI were visually compared against 4D-T1w MRI and were found to exhibit registration artefacts around the diaphragm surface at inhalation (Figure 3.11). A similar artefact was reported by (Modat et al., 2010) when applying NiftyReg to thoracic 4D-CT data. In the presented case, the artefact was observed in the estimated 4D-T1w image ($T1'$) but not in the reconstructed 4D-T1w image ($T1$) and, therefore, was due to errors accumulated during application of the chain method. The extent of the artefact can be loosely quantified as the interquartile range of the difference in diaphragm positions between 4D-T1w and 4D-T2w MRI; the mean (calculated over all patients) of which is 1.11 mm (less than 0.5 voxel). This small value demonstrates that the artefact had only a minor impact on diaphragm continuity of 4D-T2w MRI.

The final aim of this chapter was also met, which was to assess the potential of 4D-T2w MRI for application in thoracic RTP. Using high soft-tissue contrast 4D-T2w MRI, clinicians can manually delineate radiotherapy target structures in any given respiratory phase. In order to reduce contouring time, the tumour site and OARs might instead be delineated solely on the gated 3D-T2w image. Then, using the calculated MVFs, the delineated contours could be propagated to any available respiratory phase. The preferred application of the MVFP method is

expected to vary between clinicians.

As demonstrated in Figures 3.12 and 3.13, the improved tumour-tissue contrast exhibited by 4D-T2w MRI might be particularly beneficial when moving tumour sites are adjacent to OARs, as it can be challenging to delineate such sites on 4D-T1w MRI or 4D-CT (Brown et al., 2014a; Riddell et al., 2006). In addition, as shown in Figure 3.13, 4D-T2w MRI could improve the reliability and specificity of chest wall invasion when compared with 4D-T1w MRI and 4D-CT (Khalil et al., 2016). Four-dimensional T1w MRI, reconstructed in the MVFP workflow, can provide additional clinical information to calculated 4D-T2w MRI. For instance, 4D-T1w MRI can support 4D-sCT reconstruction (Chapter 5). Moreover, 4D-T1w MRI could assist detection of contrast-filled vascular lesions (Biederer et al., 2012).

Four-dimensional T2w MRI were reconstructed with a spatial resolution of $1.5 \times 1.5 \times 3.0 \text{ mm}^3$. Whilst no consensus has yet been reached for thoracic RTP, the achieved spatial resolution approximately met the standard desired for RTP in other anatomical sites, such as the prostate (Paulson et al., 2016). Twenty overlapping (i.e. 10 non-overlapping) respiratory phases were chosen based on the number of phases conventionally used in 4D-CT reconstruction (10 phases) (Wolthaus et al., 2008b). Four-dimensional T2w MRI could be obtained at a lower spatio-temporal resolution in a reduced acquisition time. However, contours delineated on low-resolution 4D-T2w MRI might be inaccurate and consequently diminish the efficacy of the treatment plan.

3.5 Conclusion

Four-dimensional T2w MRI were calculated retrospectively by applying the motion information from 4D-T1w to 3D-T2w MRI. Good quality geometrically accurate 4D-T2w images were obtained, providing high temporal resolution. Four-dimensional T2w MRI may assist clinicians in delineating lesions within volumes affected by respiratory motion that are challenging to outline on 4D-T1w MRI, making it a promising candidate for applications in RTP.

Chapter 4

Development of a super-resolution reconstruction method to calculate T2-weighted 4D/midposition MRI

This chapter introduces a super-resolution reconstruction technique to generate high-quality 4D/midposition T2w MRI from continuously acquired 2D-T2w MRI. The super-resolution reconstruction method was validated using a respiratory motion phantom. The work described in this chapter was published in part by Freedman et al. (2018).

4.1 Introduction

In Chapter 3, the MVFP method was introduced to obtain 4D-T2w MRI using data acquired with 3D pulse sequences. Applying the MVFP method resulted in high-quality 4D-T2w MRI but had several drawbacks including: use of work-in-progress sequences, long overall calculation time (9-12 hours) and long acquisition time (15-25 minutes) for patients with slow or irregular breathing.

Standard clinical slice-selective methods, which rapidly calculate 4D-T2w MRI from continuously acquired 2D-T2w MRI, could overcome these drawbacks. However, as outlined in section 2.2.2.3, slice-selective techniques are currently limited by: thick slices, stitching artefacts, lack of 3D geometrical distortion correction and data incompleteness artefacts. Prior to the work presented here, no slice-selective implementation existed in the literature to overcome all of these limitations.

Large slice-thickness could be reduced using a super-resolution reconstruction (Van Reeth et al., 2012), which combines several low-resolution images containing independent information into one high-resolution (i.e. super-resolution) image. The concept of super-resolution reconstruction has been applied in 4D-MRI (Chilla et al., 2017; Li et al., 2017b; Mickevicius and Paulson, 2019; Van Reeth et al., 2015) but was not translated to 4D-T2w MRI until the work described in this chapter.

As discussed in section 2.2.2.3, data incompleteness artefacts might be mitigated using image processing techniques or a prolonged acquisition. However, prolonged acquisitions are not viable for MR-linac workflows, as rapid acquisition and reconstruction of 4D-MRI is required (< 5 minutes (van de Lindt et al., 2018a)) for plan adaptation prior to treatment. In one possible plan adaptation approach, a MidP image (Wolthaus et al., 2008a), and its associated PTV margin, could be extracted from 4D-MRI and used to obtain a treatment plan representative of the patient anatomy and respiratory pattern of the day; see section 1.4.4 for more information. To facilitate application in MR-linac workflows, it might be possible

to calculate representative MidP-T2w MRI from rapidly acquired 4D-T2w MRI, which has been corrected for data incompleteness and stitching artefacts using post-processing methods. The aims of this chapter were to:

1. Develop a method to obtain MidP/4D-T2w MRI from 2D-T2w images without the conventional limitations of slice-selective implementations.
2. Verify calculated MidP/4D-T2w MRI.
3. Establish the feasibility of calculating representative MidP-T2w MRI from rapidly acquired 4D-T2w MRI.

4.2 Materials and methods

4.2.1 Data acquisition

Eight healthy volunteers (aged 24–35, 4 female) were included in this study after giving written informed consent. Volunteers were scanned in both sagittal and axial orientations, using repeated acquisitions (referred to below as dynamics), with a 2D-T2w single-shot half Fourier TSE (HASTE) sequence in free breathing at 1.5 T (MAGNETOM Aera; Siemens Healthcare, Erlangen, Germany). A brief introduction to TSE sequences can be found in section 2.1.3.4. For each orientation, an interleaved slice ordering scheme was repetitively employed (slice ordering: 1,3,5, . . . , 2,4,6 . . .) to enable longitudinal magnetization recovery between acquisitions and obviate inter-slice cross talk effects; see section 2.1.2.3. An in-house developed coil holder was used to prevent compression of the body contour by the 18-channel receive array. Scans were acquired with the volunteer’s arms down. The default gradient non-linearity 2D distortion correction was disabled. Figure 4.1 displays the volunteer set-up used to acquire the HASTE images. Detailed acquisition parameters are given in Table 4.1.

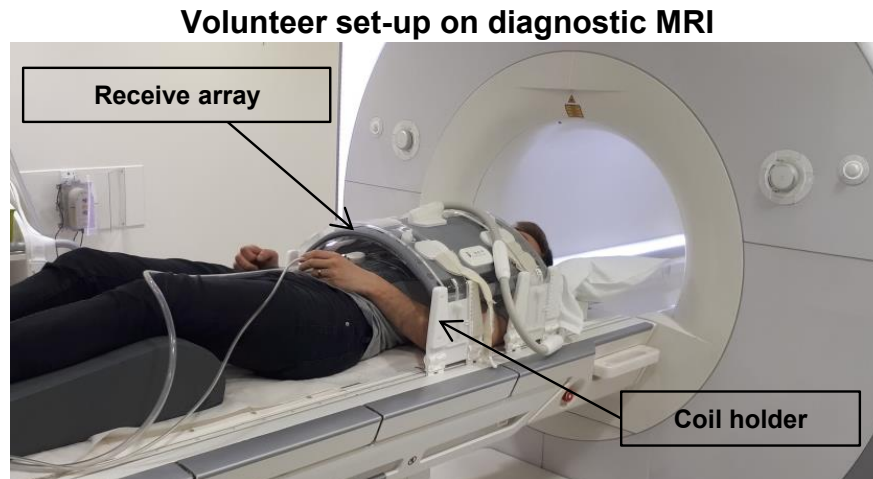


Figure 4.1: Volunteer set-up used to acquire the HASTE images. The receive array is elevated above the volunteer using a custom designed coil holder.

4.2.2 Workflow

Low-resolution sagittal and axial 4D-T2w MRI were first calculated with a binning method and then aggregated into a high-resolution MidP-T2w image using a super-resolution reconstruction as described below. High-resolution 4D-T2w MRI was then calculated by transforming the MidP-T2w image with MVFs calculated from the low-resolution sagittal 4D-T2w MRI. A summary is given in Figure 4.2. In this chapter, all calculations were carried out in MATLAB (version 2017a; The MathWorks, Natick, MA). The following binning and motion-modelling workflow was separately undertaken for both the axial and sagittal acquisitions.

4.2.2.1 Binning

For each slice, five IRS were calculated using the concepts of: body area (Cai et al., 2011), mutual information (Paganelli et al., 2015) and artificial k-space (Hui et al., 2016). To determine the body area IRS, each image was first pre-processed by morphologically closing gaps (1 pixel; disk-shaped structuring element). A binary mask (background and lungs = 0, remaining = 1) was calculated by thresholding the processed image; thresholds were automatically calculated as $2/5^{th}$ of the mean image intensity. A second binary mask was calculated (background = 0,

Table 4.1: Acquisition parameters of the axial and sagittal HASTE sequences, which were performed separately.

Parameter	Axial HASTE	Sagittal HASTE
No. volunteers	8	8
Orientation	Axial	Sagittal
Echo train length	87	87
In-plane field-of-view, mm ²	264 × 384	264 × 384
No. slices	44 - 55	50 - 60
Voxel size, mm ³	1.5 × 1.5 × 5.0	1.5 × 1.5 × 5.0
Echo time, ms	64	64
Effective repetition time per slice, s	13.6 - 14.2	13.6 - 14.2
Flip angle, °	90 - 92	90 - 92
Readout bandwidth, $\frac{Hz}{Pixel}$	590	590
Fat suppression	No	No
No. dynamics	30	30
Slice acquisition order	interleaved	interleaved
Acquisition time, min	6.4 - 8.8	8.0 - 9.6

body area = 1), by taking the largest connected component of the first binary mask. The resulting body area mask was then post-processed by morphologically closing remaining gaps (20 pixels; disk-shaped structuring element). The body area IRS was calculated as the sum over all elements in the post-processed body area mask. The mutual information IRS was calculated as the change in mutual information between exhalation and all other phases. The exhalation phase was determined as the minimum of the pre-calculated body area IRS. Three k-space IRS were generated from the magnitude of the centre (0,0), centre-upper (0,1) and centre-right (1,0) pixels of the 2D Fourier transform of each magnitude image (Hui et al., 2016). All five IRS were combined into one principle respiratory signal (PRS) using principle component analysis (first principle component). The first principle component is a good approximation of the underlying respiratory signal

because it explains the highest percentage of the total variance exhibited by the five IRS. A visual overview of the PRS calculation is displayed in Figure 4.3.

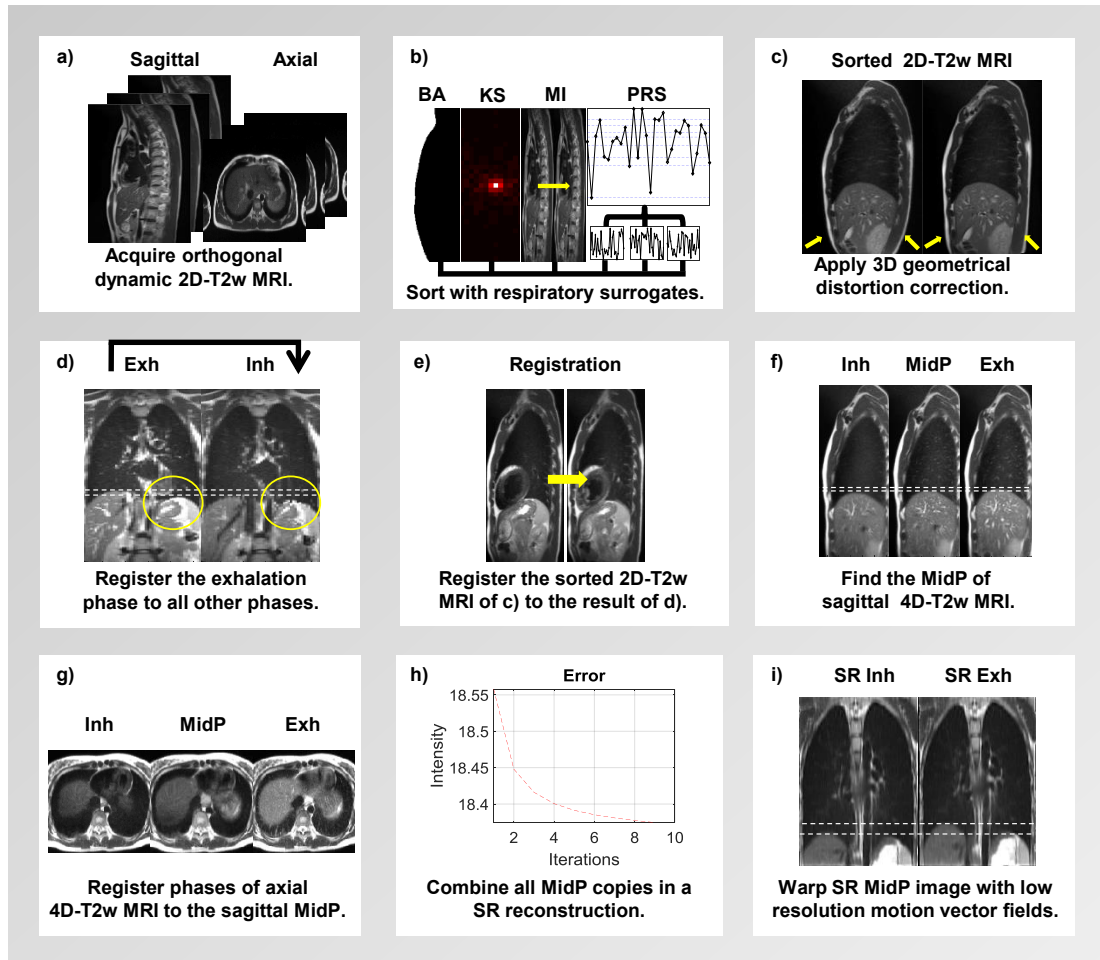


Figure 4.2: (a) Axial and sagittal 2D-T2w MRI are continuously acquired, (b) retrospectively sorted by the principle respiratory surrogate (PRS), which combines body area (BA), artificial k-space (KS) and mutual information (MI), and (c) distortion corrected. (d) For both axial and sagittal 4D-T2w MRI, stitching and binning artefacts, visible within the yellow circle, are reduced by registering the exhalation phase to all other respiratory phases. (e) Sorted images in (c) are corrected by registering to the results of (d). (f) Each phase of the sagittal 4D-T2w image of (e) is warped to midposition (MidP). (g) Each phase of the axial 4D-T2w image in (e) is registered to the sagittal MidP. (h) Super-resolution (SR) reconstruction is performed using the sagittal and axial MidP copies. (i) SR 4D-T2w MRI is obtained by warping the SR MidP image with the low-resolution motion vector fields calculated from the corrected sagittal 4D-T2w MRI in (f).

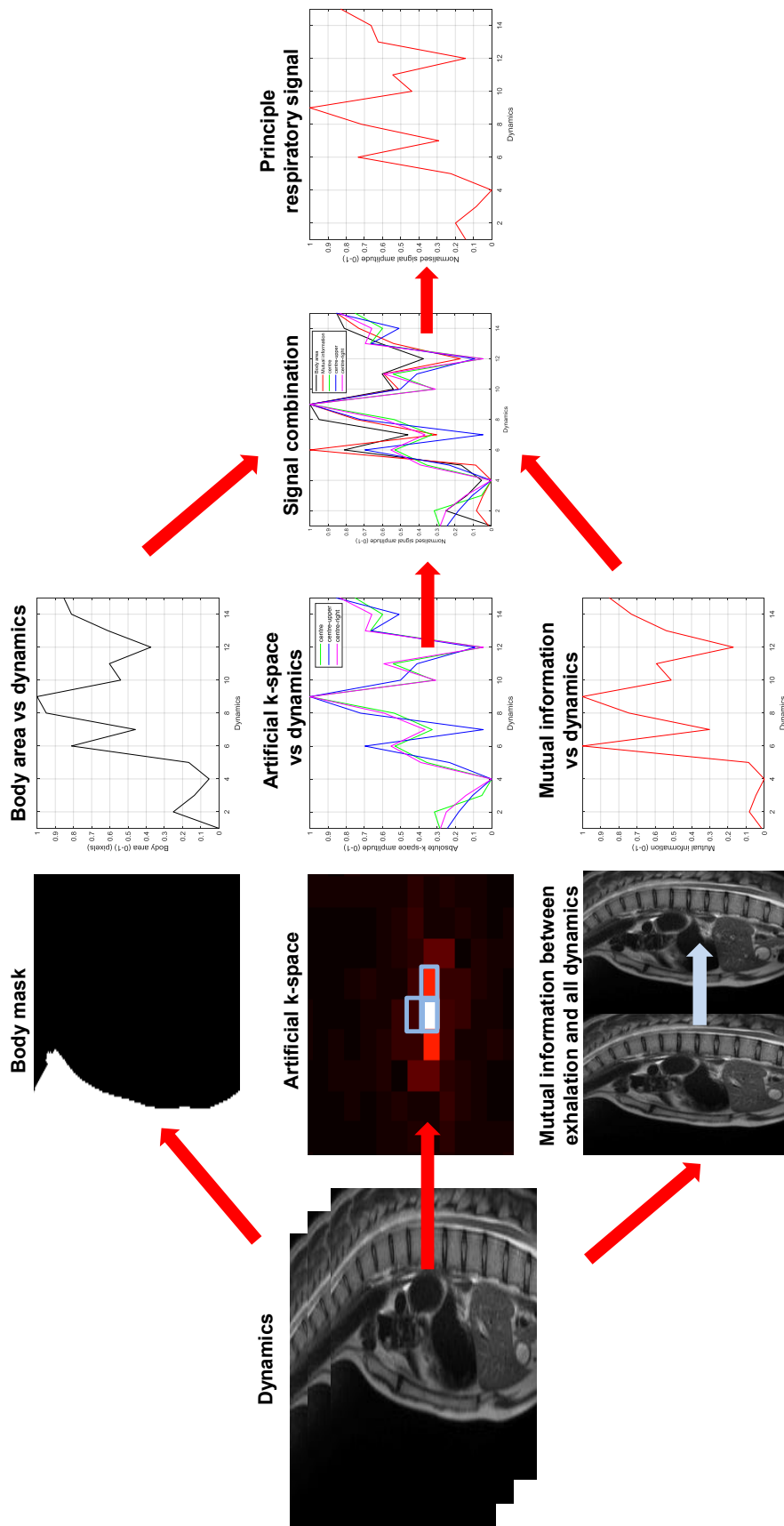


Figure 4.3: A visual overview of the principle respiratory signal calculation. Using all dynamics of each slice, five image-driven respiratory surrogate signals were calculated based on body area, artificial k-space (3 signals) and mutual information. Light blue rectangles surround the centre, centre-upper and centre-right pixels employed in the artificial k-space calculation. The principle respiratory signal was obtained by combining all normalised signals using principle component analysis.

The PRS was employed to retrospectively sort each slice into eight respiratory-bins. The edges of the respiratory-bins were defined using percentiles of the PRS amplitude values, such that there was an equal amount of data in each respiratory-bin. Magnitude images assigned to the same respiratory-bin were averaged. Defining respiratory-bins separately for each slice mitigates data incompleteness artefacts, as all bins can be filled (Liu et al., 2015a). However, defining respiratory bins for each slice introduces stitching artefacts or phase-shifts between slices (Liu et al., 2014), due to the particular sampling scheme or changes in the respiratory pattern during measurement. Finally a 3D gradient non-linearity distortion correction was applied to each phase of the sorted images, using the spherical harmonic coefficients provided by the vendor (Doran et al., 2005).

4.2.2.2 Motion-modelling

Compared to other respiratory phases, exhalation exhibited reduced stitching and binning artefacts. The exhalation image was used to correct the stitching artefacts exhibited by the remaining respiratory phases.

In this approach, the exhalation image was registered to all eight respiratory phases using a diffeomorphic implementation of a Demons 3D DIR algorithm (Thirion, 1998; Vercauteren et al., 2009) with diffusion-like smoothing ($\sigma = 1.0$ pixel). Applying diffusion-like smoothing greatly increased robustness of the registration to stitching artefacts. An introduction to the Demons DIR algorithm was provided in section 2.2.4.1. The diffusion-like smoothing parameter (σ) was optimised heuristically in a subset of volunteers by visually assessing the quality of transformed images generated from registrations with varying σ values ($0.1 \leq \sigma \leq 2.0$ pixels). Values in the range ($0.7 \leq \sigma \leq 1.2$ pixels) were found to provide the best compromise between reduction of stitching artefacts and over-regularisation of respiratory motion. The calculated MVFs were then applied to warp the exhalation image to all other respiratory phases; resulting in a simulated 4D-T2w MRI with reduced stitching artefacts. Afterwards, each slice from the original sorted 4D-T2w MRI was corrected by registering to the corresponding slice

and phase in the simulated 4D-T2w MRI, using a similar Demons 2D non-rigid registration ($\sigma = 1.0$ pixel). This approach retained the independent information needed for the super-resolution reconstruction.

4.2.2.3 Principles of super-resolution reconstruction

Large slice thickness was overcome in low-resolution 4D-T2w MRI using a super-resolution reconstruction algorithm based on iterative back-projection (Irani and Peleg, 1991). In MRI-based super-resolution reconstructions (Van Reeth et al., 2012), a high-resolution MR image (S) of an object is calculated by combining independent information contained in several separate low-resolution MR images (L_k) of the same object; where $k \in [1, \dots, N]$ total number of low-resolution MR images. Super-resolution reconstruction is enabled using an image degradation model which simulates the MR imaging process by sequential application of warping G_k , blurring P_k and downsampling H_k matrix operators to S such that it is comparable to L_k (Van Reeth et al., 2012):

$$L'_k = H_k P_k G_k S \quad (4.1)$$

Where L'_k is the degraded version of S . The high-resolution image (S_Ω) can be calculated by minimising a cost function, which is the sum of the squared differences of L'_k and L_k :

$$C_{min} = \underset{S}{\operatorname{argmin}} \sum_{k=1}^N \|H_k P_k G_k S - L_k\|^2 \quad (4.2)$$

The cost function can be minimised by iteratively back-projecting the differences between L_k and the estimated high-resolution image S_n (Irani and Peleg, 1991):

$$S_{n+1} = S_n - \frac{1}{N} \sum_{k=1}^N (G_k^+ P_k^+ H_k^+ [H_k P_k G_k S_n - L_k]) \quad (4.3)$$

Where, G_k^+ , P_k^+ and H_k^+ represent unwarping, deblurring and upsampling

operators, respectively.

4.2.2.4 Super-resolution reconstruction

Prior to super-resolution reconstruction, low-resolution 4D-T2w images were transformed to MidP using NiftyReg (Modat et al., 2010; Rueckert et al., 1999). First, the eight respiratory phases of sagittal 4D-T2w MRI were employed to generate eight copies of the MidP image (L_{Sk}) ($k \in [1, \dots, 8]$) (Wolthaus et al., 2008a). Eight additional copies (L_{Ak}) were then obtained by non-rigidly registering each respiratory phase of the axial 4D-T2w image to the sagittal MidP copy that was generated from the corresponding respiratory phase. Transforming respiratory phases of low-resolution 4D-T2w MRI to MidP enabled a reduction in calculation time by obviating the need for warping operations during super-resolution reconstruction, i.e. $G_k^+ = G_k = I$, where I is the identity operator.

The blurring operator P_k convolved S_n with a non-isotropic Gaussian point spread function (in-plane: 1.8 mm, through-plane: 5 mm) (Kuklisova-Murgasova et al., 2012) and was the same for all k in each orientation ($P_k = P_A$ or $P_k = P_S$). The deblurring operators were set to the identity ($P_A^+ = P_S^+ = I$) (Manivannan et al., 2013). Downsampling operators H_k were applied to interpolate the blurred S_n from the super-resolution space ($1.0 \times 1.0 \times 1.0 \text{ mm}^3$) to the low-resolution axial or sagittal spaces. Downsampling operators were equivalent for all k in each orientation, i.e. $H_k = H_A$ or $H_k = H_S$. Upsampling operators were similarly equivalent ($H_k^+ = H_A^+$ or $H_k^+ = H_S^+$). Iterative backprojection (Irani and Peleg, 1991) was implemented by applying the above mentioned modifications to expression 4.3:

$$S_{n+1} = S_n - \frac{1}{16} \left(\sum_{k=1}^8 [H_A^+(H_A P_A S_n - L_{Ak}) + H_S^+(H_S P_S S_n - L_{Sk})] \right) \quad (4.4)$$

The initial estimate S_0 was obtained by averaging all independent MidP copies, which were upsampled by interpolating to the super-resolution space. High-resolution MidP-T2w MRI (S_Ω) was calculated following eight iterations of 4.4.

Motion vector fields, which were calculated by non-rigidly registering the respiratory phases of low-resolution sagittal 4D-T2w MRI, were applied to high-resolution MidP-T2w MRI to obtain super-resolution 4D-T2w MRI. Because super-resolution reconstruction was limited to the overlapping FOV of the sagittal and axial images, the original low-resolution axial images were used outside the thorax (arms). A detailed overview of the super-resolution workflow is given in Figure 4.4.

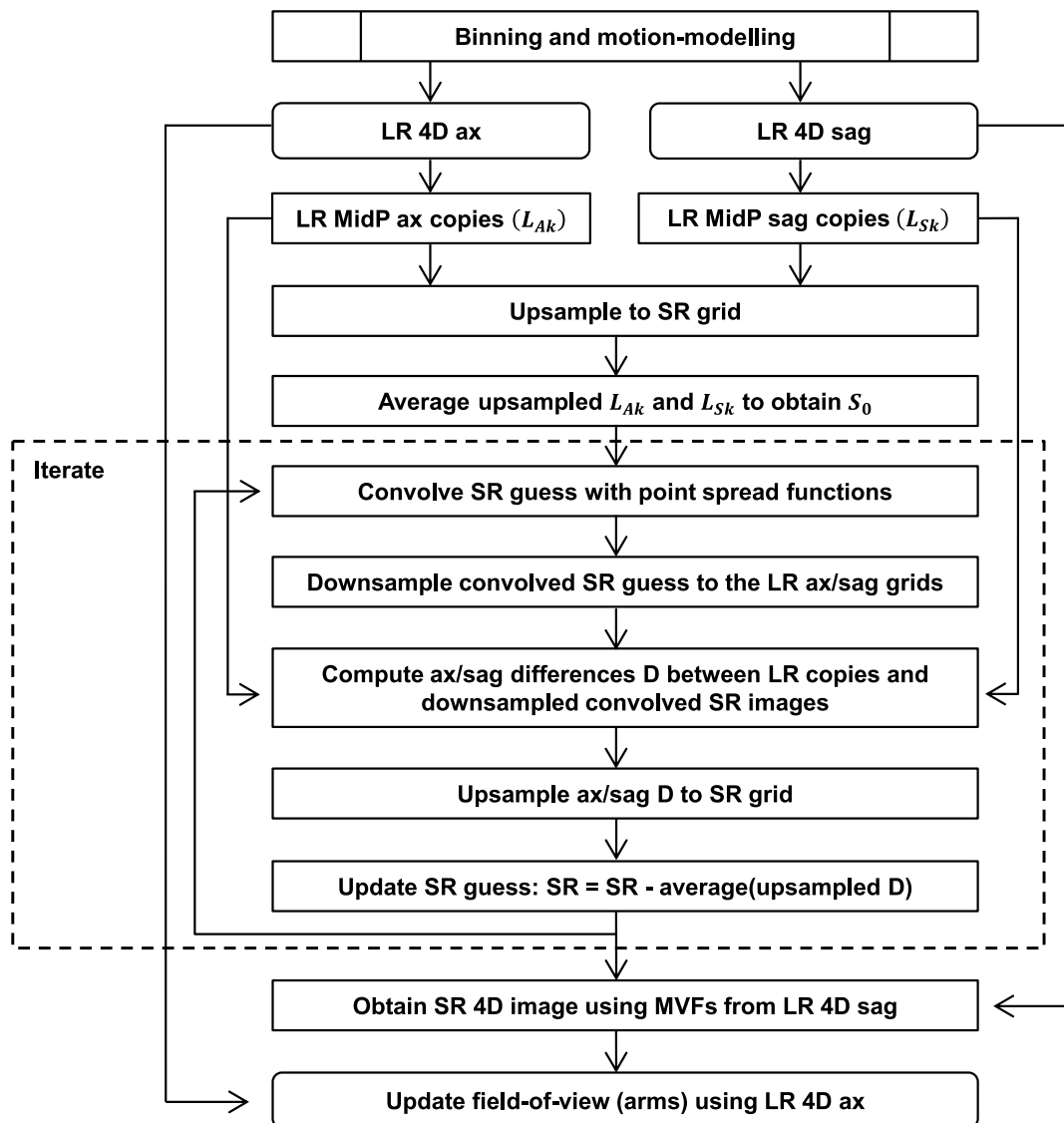


Figure 4.4: Details of the super-resolution reconstruction workflow. LR indicates low-resolution; SR, super-resolution; MidP, midposition; Ax, axial; Sag, sagittal; MVFs, motion vector fields; S_0 , initial guess.

4.2.3 Verification of T2-weighted 4D/midposition MRI

4.2.3.1 Deformable image registration

Liver-dome positions in the inhalation phase of sagittal 4D-T2w MRI, before and after stitching artefact correction, were compared to assess the accuracy of DIR in the presence of stitching artefacts. Liver-dome positions were measured along eight lines in four coronal slices (separated by 15 mm) using the edge-detection method, which was introduced in section 3.2.5.1. Edge-detection employed the same ROI for corrected and uncorrected images. An example liver-dome comparison is shown in Figure 4.5. Registration error was calculated as the mean difference between liver-dome positions in the inhalation phase of corrected and uncorrected 4D-T2w MRI, which assumed that the average liver-dome position in uncorrected 4D-T2w MRI was unaffected by stitching artefacts (Figure 4.5c).

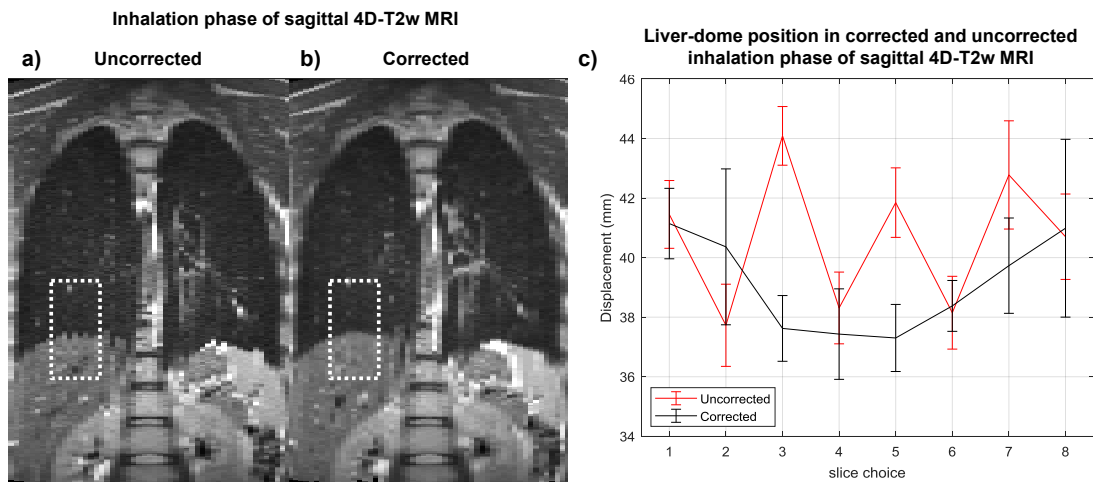


Figure 4.5: Example of edge-detection. a-b): Regions of interest (white dashed boxes) are placed at the same position in the uncorrected and corrected inhalation phase of 4D-T2w MRI. The liver-dome positions for eight lines in the chosen coronal slice are compared. c) Stitching artefacts (red) are greatly reduced after correction (black).

4.2.3.2 Image resolution

Deformable image registration and interpolation steps in the workflow result in smoothing of the image data and potentially a loss of resolution. The edge-

detection method of section 3.2.5.1 was used to compare the resolutions of:

1. The inhalation phase of axial 4D-T2w MRI obtained following the binning workflow.
2. The axial contribution to the initial guess S_0 , i.e. the mean of all eight L_{Ak} which were upsampled to the super-resolution space.
3. The MidP super-resolution reconstructed image S_Ω .

In this approach, a 2D ROI was manually defined on the anterior skin-air boundary in the central axial slice of each volunteer. The image resolution was obtained by averaging the calculated width b over all lines in the ROI; see equation 3.3. For each volunteer, the same 2D ROI was used to measure the resolution in all images.

4.2.3.3 Phantom measurements

The QUASARTM MRI-compatible respiratory motion phantom (QUASAR, Modus Medical Devices Inc., London, Canada), into which a kiwi and corn test-object was inserted, was employed to validate the binning and motion-modelling workflow. Figure 4.6 gives an overview of the QUASARTM phantom. Two sinusoidal waveforms (S1-S2) with period and peak amplitude: (4 s, 15 mm) and (3 s, 20 mm), and two randomly chosen volunteer waveforms (S3-S4) (self-gating signals of two radial stack-of-stars spoiled gradient echo sequences; see Table 3.1) with peak amplitude 15 mm were chosen to drive the phantom. Translational motion of the phantom insert along the bore was coupled to rotation around the axis of translational motion. The rotation angle θ was given by the position A (between -20 and 20 mm):

$$\theta(A) = \sin^{-1} \left(\frac{1}{2} \sqrt{1 - \frac{1}{4} \left[\frac{A}{20} \right]^2} \right) \quad (4.5)$$

The volunteer waveform amplitude values of 15 mm were chosen to be representative of patient respiratory tumour motion (Suh et al., 2008). Images were

obtained with identical sequence parameters to the volunteer acquisitions, except that they were acquired in the coronal and sagittal orientations. Due to the different acquisition scheme, operators in super-resolution reconstruction were adapted from expression 4.4 to handle coronal instead of axial MidP images. Because the main compartment of the phantom was a static water tank and only the insert exhibited motion, the body area IRS was not applicable. In addition, the artificial k-space IRS were not used as the insert was fully contained in the chosen FOV at all programmed positions. For these reasons, the PRS, described in section 4.2.2.1, was replaced with a signal based on the position of the lower kiwi boundary, which was measured using the edge-detection method of section 3.2.5.1.

The Demons non-rigid registration was optimised ($\sigma = 0.5$ pixel) to capture the rotation of the test-object. Using the same edge-detection method, the MidP displacement was compared to the mean displacement over N dynamics ($N = 10, 15, 20, 25$ and 30) measured in the ground-truth low-resolution images. Both the MidP and mean displacements were measured at the lower kiwi boundary as per the PRS.

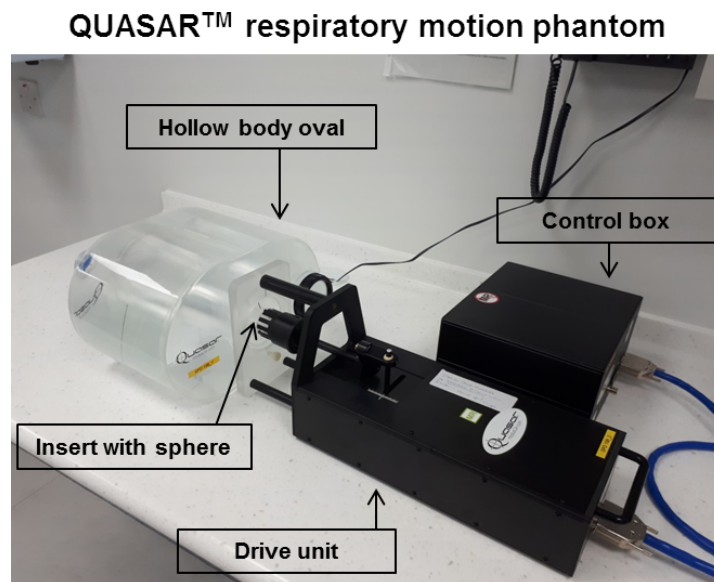


Figure 4.6: Overview of the key components of the QUASARTM MRI-compatible respiratory motion phantom.

4.2.3.4 Colour intensity projections

Colour intensity projection images (CIPs) can be used to encode the intensity variation within a 4D image by colour. For objects similar to an isolated lung tumour, colour approximately represents the time spent by the object in any one position. Following the approach by Cover et al. (2006), CIPs were calculated by converting a hue-saturation-brightness (*HSV*) representation of a normalised greyscale 4D image to a red-green-blue representation. The hue-saturation-brightness channels were obtained using the maximum (*MaxIP*), minimum (*MinIP*) and mean (*MeanIP*) intensity projections along the 4th dimension of the greyscale 4D image according to:

$$\begin{aligned}
 H &= \frac{2}{3} \left(\frac{MeanIP - MinIP}{MaxIP - MinIP} \right) \\
 S &= \frac{MaxIP - MinIP}{MaxIP} \\
 V &= MaxIP
 \end{aligned}
 \tag{4.6}$$

Colour intensity projection images display greyscale values when intensity does not change at a particular spatial location in the 4D image. Calculated CIPs enable a comparison of the motion information contained in low-resolution 4D-T2w MRI and in the unprocessed ground-truth phantom data. For the volunteer images, CIPs were calculated from both the unprocessed ground-truth data and the generated super-resolution 4D-T2w MRI.

4.2.4 Midposition dependence on number of dynamics

To minimise acquisition time, the number of dynamics required to obtain a representative MidP image was investigated by retrospectively discarding data prior to generating the 4D-MRI. Following Figure 4.2(b–f), MidP images were calculated from only the first 10–30 sagittal dynamics. For each MidP image, the position of the right hemi-diaphragm was calculated for five consecutive sagittal slices, using the edge-detection method of section 3.2.5.1, and then averaged. It was compared to the diaphragm position of the MidP image obtained with 30 dynamics, which was considered to contain sufficient dynamics for data completeness based on (Liu et al., 2015b). In order to separate the impact of the number of dynamics N from possible changes in respiratory pattern during acquisition, the change in MidP was estimated from the unprocessed groundtruth data, by calculating the average diaphragm position over N dynamics for $N = 10$ –30; carried out using the edge-detection method on the same slices and settings as for the above MidP images.

4.3 Results

For eight volunteers, distortion corrected super-resolution 4D/MidP-T2w MRI ($1.0 \times 1.0 \times 1.0 \text{ mm}^3$) were calculated using a fully automatic workflow. Low-resolution 4D-T2w MRI was reconstructed in 3.2 min for each orientation and total reconstruction time for super-resolution 4D/MidP-T2w MRI was less than 23 min. Super-resolution 4D-T2w MRI exhibited no missing-data artefacts and, when compared to the initially binned low-resolution 4D-T2w MRI, displayed greatly reduced stitching artefacts; as demonstrated in Figure 4.7 for the inhalation respiratory phase.

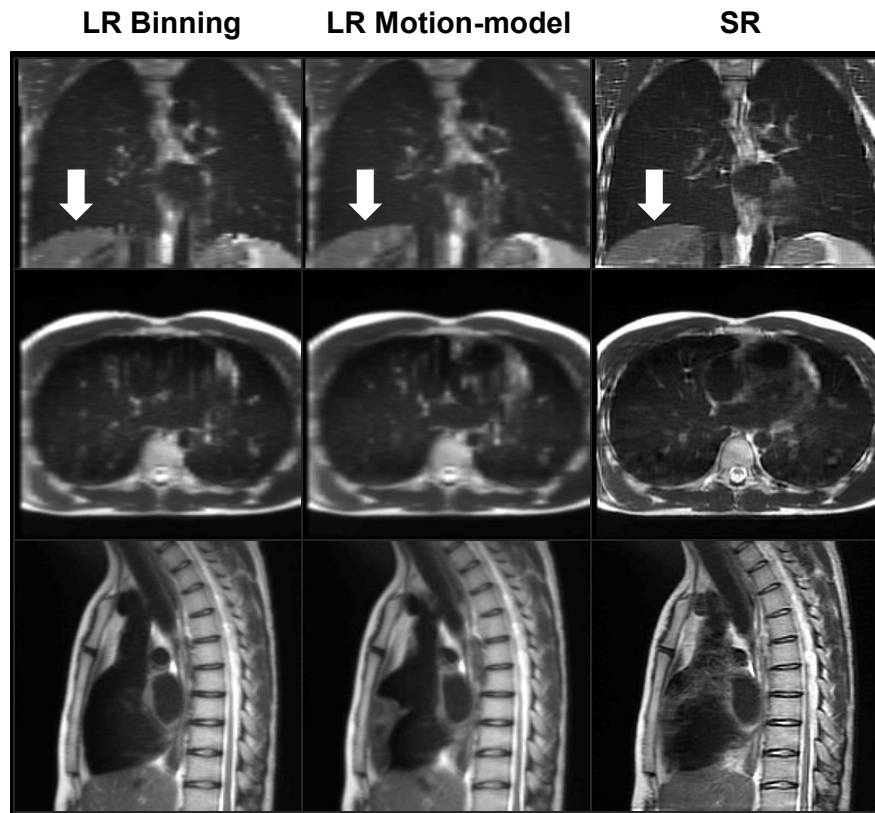


Figure 4.7: An example comparison of the inhalation respiratory phases of sagittal 4D-T2w MRI which were obtained following the binning (Figure 4.2a-c), motion-modelling (Figure 4.2a-e) and super-resolution workflows (Figure 4.2a-i). Compared to the binned low-resolution (LR) images, the super-resolution (SR) images exhibit enhanced sharpness and reduced stitching artefacts (white arrows).

Figure 4.8 shows an example comparison between super-resolution MidP-T2w MRI, the initial guess for super-resolution reconstruction (mean of all 16 interpolated low-resolution copies) and the low-resolution MidP sagittal and axial images (averaged over 8 interpolated copies). Super-resolution reconstruction maintained the in-plane quality and image features of both the axial and sagittal acquisitions, whilst increasing the image sharpness in the coronal plane.

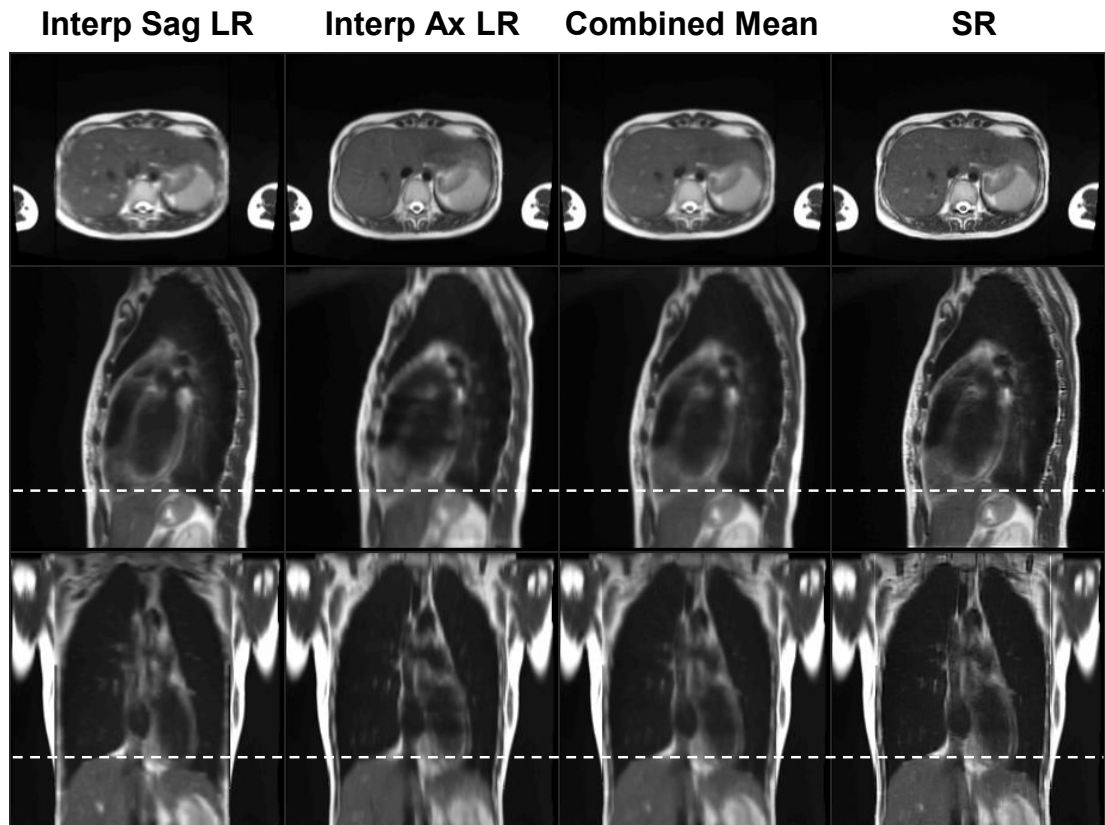


Figure 4.8: A comparison between the low-resolution (LR) individual and combined mean interpolated (Interp) sagittal (Sag) and axial (Ax) images, and the super-resolution (SR) reconstruction. Dashed white lines aid evaluation of the relative liver-dome positions in the different midposition images. The suppressed average cardiovascular pulsations in the Interp LR Sag and Ax columns (e.g. bright liver vessels in the axial view) were retained in the SR image.

The motion information exhibited by the low-resolution sagittal 4D-T2w MRI was well preserved in the super-resolution 4D-T2w MRI, as shown in Figure 4.9.

As described in section 4.2.3.1, registration accuracy in the presence of stitching artefacts was evaluated by comparing the inhalation phase of sagittal 4D-T2w

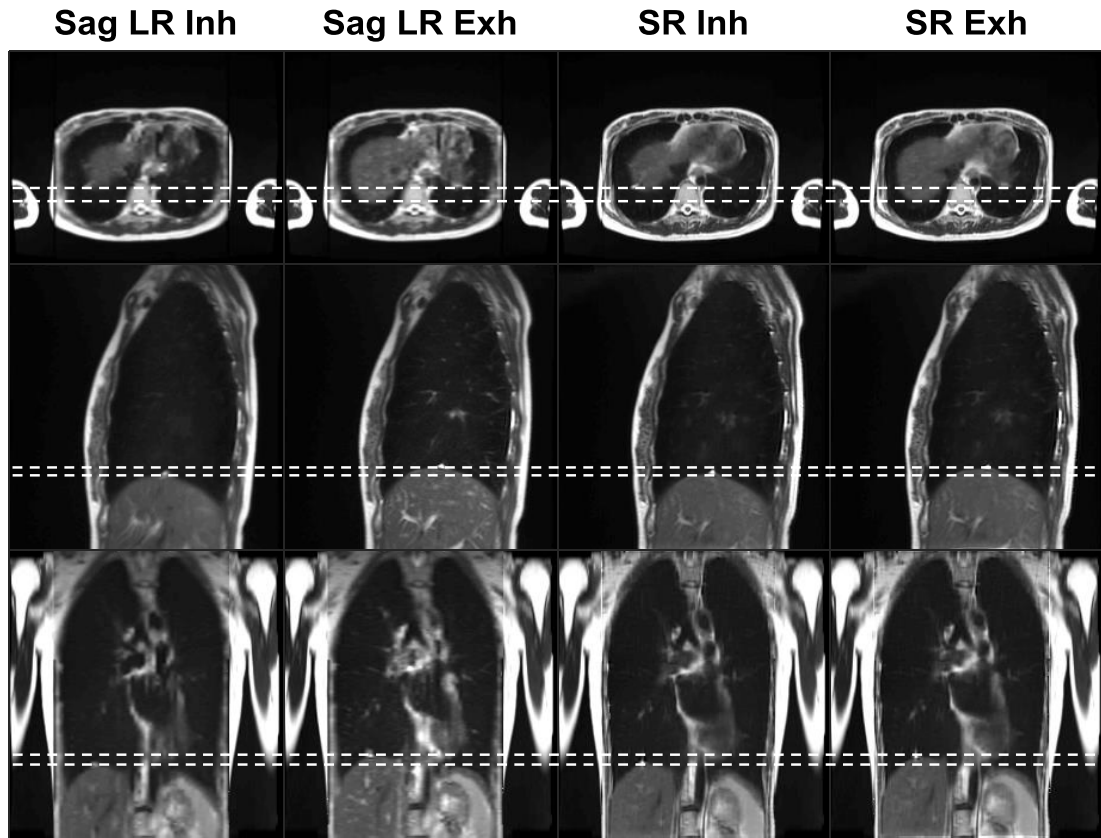


Figure 4.9: Comparison of the four-dimensional (4D) super-resolution (SR) reconstruction to the sagittal (Sag) 4D low-resolution (LR) reconstruction. Dashed white lines demarcate diaphragm surface positions in the inhalation (Inh) and exhalation (Exh) phases. Respiratory motion information contained in LR Sag 4D-T2w MRI was retained in SR 4D-T2w MRI.

MRI that was generated before and after stitching artefact correction. Overall registration error (mean \pm standard deviation) was 0.7 ± 1.0 mm, which was calculated by averaging the mean liver-dome positional differences of all volunteers.

The measured skin-air resolutions in the central axial slices of the inhalation phase of binned axial 4D-T2w MRI, initial guess (axial contribution) and super-resolution reconstructed images were: (mean and standard deviation in mm) 1.4 ± 0.2 , 2.2 ± 0.2 and 1.5 ± 0.2 , respectively. The small resolution difference between the binned and super-resolution images suggests that the super-resolution reconstruction can overcome the smoothing associated with the registration and interpolation steps.

As illustrated in Figure 4.10a, super-resolution reconstruction results in an increase in image sharpness, better enabling visualisation of high-detail features such as the sweetcorn kernels within the test-object. As shown in Figure 4.10b, the differences (mean and standard deviation over all dynamics) in the MidP displacement calculated from the low-resolution motion-model and the unprocessed ground-truth images for the sinusoidal waveforms (S1-S2) were: 1.2 ± 0.6 mm and 1.6 ± 0.9 mm, and for the volunteer waveforms (S3-S4) were: 0.3 ± 0.1 mm and 0.0 ± 0.5 mm. The motion range in the 4D-T2w MRI slightly underestimated the full motion range of the unprocessed ground-truth images. This is reflected in Figure 4.10c, where the CIPs of S4 reveal that this slight underestimation of motion occurred in inhalation.

Colour intensity projections were generated from the unprocessed ground-truth images and from the results of super-resolution reconstruction; an example is shown in Figure 4.11. In terms of diaphragm motion, the CIPs obtained using the super-resolution reconstructed images were in good agreement when compared to those calculated from the ground-truth images. The observable range of motion exhibited by the CIPs only varied slightly with number of dynamics. Due to averaging, cardiovascular motion and pulsations observed in the ground-truth images were reduced in the super-resolution reconstruction. The averaging effect was observed in the super-resolution-CIPs as increased greyscale values in the blood vessels.

A negative correlation (Pearson's $r = -0.89$) was found between the absolute differences in diaphragm position of MidP calculated from N and 30 dynamics. As shown in Figure 4.12a, the average absolute differences, displayed as grey circles, ranged from 1.1 ± 0.6 to 0.3 ± 0.3 mm (mean and standard deviation over volunteers) for 10 and 29 dynamics, respectively, and all were within 1.1 mm. As displayed in Figure 4.12b, a drift in MidP was observed for all volunteers and the mean absolute difference between 10 and 30 dynamics was 1.0 ± 0.8 mm over an average acquisition of 5.2 min. The differences in diaphragm position were corrected for the change in MidP and the absolute differences (mean and standard

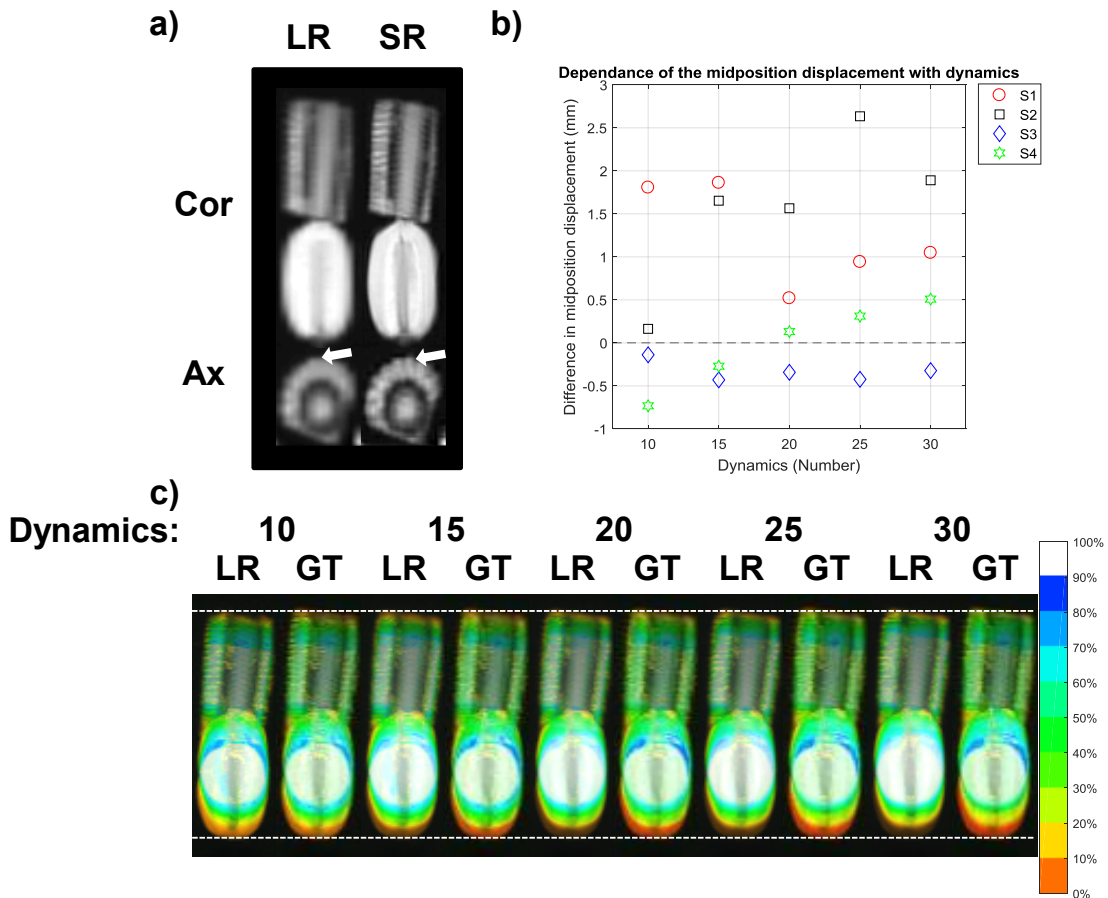


Figure 4.10: (a) Low-resolution (LR) and super-resolution (SR) images of a motion phantom (waveform S3), for one coronal (Cor) and axial (Ax) slice in midposition. Sweetcorn kernels (white arrows) are more easily distinguished in the SR images than in the LR images. (b) Depicts the difference in midposition displacement of the phantom (lower kiwi boundary) versus the number of dynamics for the sinusoidal (S1-S2) and volunteer (S3-S4) waveforms in the low-resolution T2w MRI (Motion-model) and in the ground-truth (GT) images. (c) LR and GT colour intensity projection images of one coronal slice for different numbers of dynamics (waveform S4). The LR images show a slight underestimation of motion. Colour encodes time spent in each position. 100 % of the time represents constant image intensity at that position in all respiratory phases. Dashed white lines show exhalation and inhalation (top and bottom) for the GT data set of 30 dynamics.

deviation) were 0.6 ± 0.6 and 0.3 ± 0.4 mm for 10 and 29 dynamics (blue squares in Figure 4.12a). Figure 4.12c shows super-resolution MidP images for varying number of dynamics. Similarity to the image obtained from 30 dynamics slightly increased with number of dynamics, but was nevertheless high for all images.

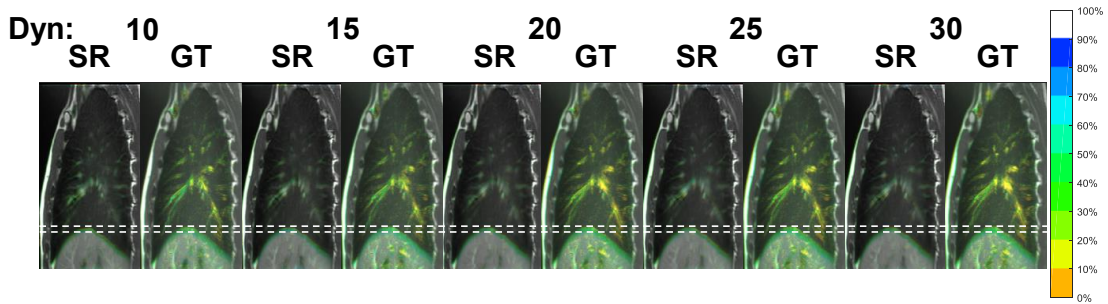


Figure 4.11: Colour intensity projection images displaying time-weighted motion information contained in the dynamics (Dyn) of the unprocessed sagittal ground-truth (GT) images and respiratory phases of the super-resolution (SR) images of volunteer 1. Dashed white lines aid visual comparison of inhalation and exhalation. In the lung, colour approximately represents time spent in each position. 100 % (greyscale) means that image intensity is not changing in that position for all respiratory phases. The respiratory motion in the GT images is preserved in the SR images, which can be recognised by comparing the extent of the liver-dome motion. Pulsations due to cardiac motion in the GT images are reduced in the SR images.

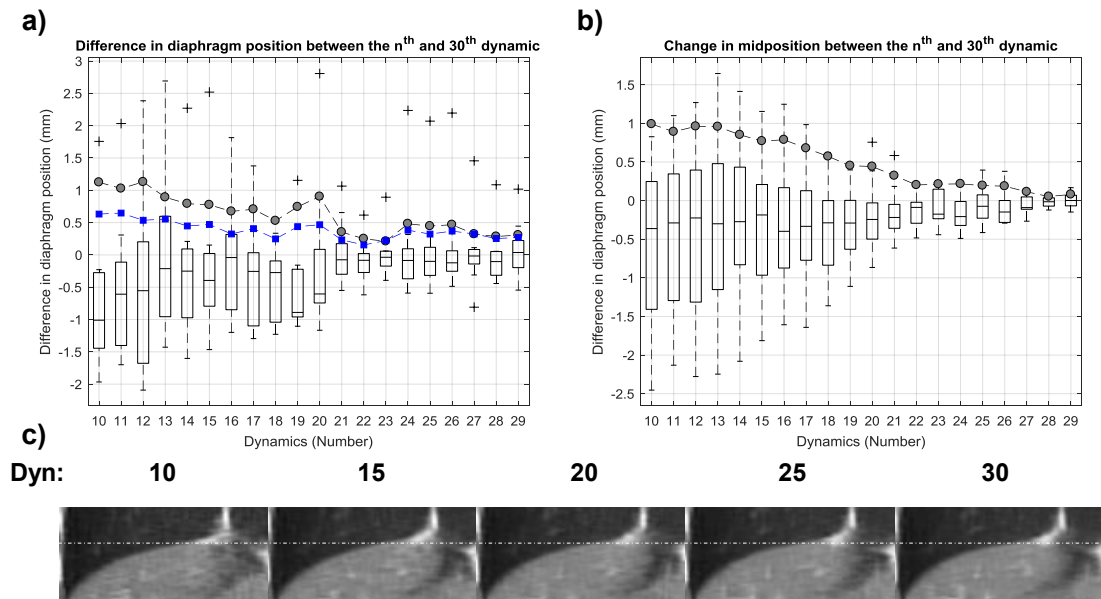


Figure 4.12: (a) Differences in diaphragm position between the low-resolution sagittal midposition images obtained from N (10 to 29) and 30 dynamics. Boxplots summarise the results from the eight volunteers. Mean absolute differences are depicted by grey circles (uncorrected) and blue squares (corrected for drift in midposition). (b) Changes in midposition with number of dynamics; boxplots summarise results for different volunteers. The mean absolute difference in midposition compared to the full 30 dynamics is depicted by grey circles. (c) Coronal views of super-resolution midposition images of volunteer 1 for different number of dynamics (Dyn). Images exhibit high similarity. White dashed lines aid comparison of the diaphragm position.

4.4 Discussion

The first aim of this chapter was to develop a workflow to calculate MidP/4D-T2w MRI without the current drawbacks of slice-selective implementations. Midposition/4D-T2w MRI ($1.0 \times 1.0 \times 1.0 \text{ mm}^3$) was calculated from continuously acquired low-resolution ($1.5 \times 1.5 \times 5.0 \text{ mm}^3$) axial and sagittal 2D-T2w MRI using an automated workflow based on binning and super-resolution reconstruction.

The challenge of large slice-thickness (5 mm) was overcome by combining 16 low-resolution images into one super-resolution image, which maintained high SNR and a full thoracic FOV. The resulting high-resolution 4D-T2w MRI exhibited similar in-plane resolution, improved through-plane resolution and fewer respiratory phases compared to 4D-T2w MRI obtained using the MVFP method of Chapter 3 ($1.5 \times 1.5 \times 3.0 \text{ mm}^3$; 20 respiratory phases). Chilla et al. (2017) demonstrated that errors due to pre-registering inputs might be overcome by including warping operators ($G_k; G_k^+$) in the super-resolution reconstruction. This approach was not pursued because it would have greatly prolonged reconstruction time. Iterative back-projection was employed for super-resolution reconstruction due to its ease of implementation and widespread use in the literature. One disadvantage of iterative back-projection was that resulting images exhibited high amounts of noise, which originated from unconstrained optimisation of the applied cost function (equation 4.2). In Chapter 7, constraints will be implemented in the super-resolution framework to regularise the optimisation process.

The problem of data incompleteness artefacts was addressed by sorting images on a slice-by-slice basis. This approach could enable a reduced scan time compared to alternative binning strategies which overcome data incompleteness artefacts using prolonged acquisitions (Hui et al., 2016; Liu et al., 2015b; van Kesteren et al., 2019). The average acquisition time (16.8 minutes) was longer than that required by the MVFP method (13.8 minutes). Unlike the MVFP method, acquisition time of the super-resolution approach was pre-determined and therefore might be shorter for patients with slow or irregular breathing patterns. Acquisition time

of the super-resolution approach might be reduced by obtaining dynamics in the coronal orientation, which would enable the use of higher acceleration factors for parallel imaging due to favourable orientation of coil elements.

A stitching artefact correction was implemented to overcome artefacts caused by a variable respiratory pattern during data acquisition and phase-shifts resulting from slice-by-slice sorting. The stitching artefact correction might permit a reduction in acquisition time by enabling robust 4D-T2w MRI to be calculated from fewer dynamics.

In contrast to other slice-selective methods (Hui et al., 2016; Li et al., 2017b), a 3D gradient non-linearity distortion correction was applied to ensure geometrical fidelity for RTP. A 3D geometrical distortion correction was also employed in the MVFP method. The presented super-resolution approach can therefore compete with the MVFP method in terms of geometrical accuracy.

Four-dimensional T2w MRI was reconstructed in a considerably shorter time (23 minutes) to that generated in Chapter 3 (9-12 hours). Yet, reconstruction time of the super-resolution prototype implementation currently limits its on-line use on MR-linac systems. The prototype implementation has scope for improvement, for instance by exploiting a reconstruction server to accelerate calculation of its parallelisable components (Mickevicius and Paulson, 2017).

Unlike the MVFP workflow, the outlined super-resolution approach used standard clinical sequences for data acquisition and therefore can be readily implemented at other centres. The work-in-progress radial stack-of-stars trajectory employed in the MVFP workflow provides a large degree of flexibility regarding the imaging contrast, for instance a balanced implementation with a mixed T2/T1 contrast is possible. Likewise, the proposed super-resolution method could be applied to generate 4D-MRI of any contrast accessible using a fast 2D imaging sequence.

The second aim of this chapter was to verify calculated MidP/4D-T2w MRI, which was achieved using CIPs and phantom measurements. For all waveforms in the phantom experiment, the MidP displacement in the low-resolution 4D-MRI exhibited a maximum error of 1.6 ± 0.9 mm compared to the ground-truth image data, suggesting that the MidP displacement was well preserved within the proposed workflow. The remaining differences might be associated with the reduction of stitching artefacts. Validation provided by the phantom experiment was limited due to necessary optimisation of the Demons smoothing parameter (σ) and application of an alternative PRS.

Compared to the ground-truth CIPs of the phantom and volunteer measurements, the low-resolution and super-resolution reconstructed CIPs both showed a slight underestimation towards inhalation. Overall, the range of diaphragmatic motion was well preserved in the super-resolution-CIPs, which suggests that the motion-model accurately covered the motion range.

The third aim of this chapter was to determine the feasibility of calculating representative MidP-T2w MRI from rapidly acquired 4D-T2w MRI, which was investigated in data subsampling experiments. For all volunteer MidP images (obtained from N dynamics), the average diaphragm displacement was concurrent with that at 30 dynamics to within 1.1 mm, which was in rough agreement with the phantom results. These results suggest that 10 dynamics in each orientation are sufficient to obtain representative MidP-T2w MRI. Generating MidP-T2w MRI with only 10 dynamics in each orientation facilitates application on MR-linac systems, since only an acquisition time of approximately 5.6 minutes would be necessary.

4.5 Conclusion

The feasibility of obtaining high-resolution MidP/4D-T2w MRI ($1.0 \times 1.0 \times 1.0$ mm³) from axial and sagittal 2D-T2w MRI with a binning and super-resolution reconstruction method was demonstrated. Additionally, 10 repeated dynamic measurements of data were found sufficient to obtain representative MidP-T2w MRI. The resulting MidP/4D-T2w MRI were distortion corrected, exhibited reduced stitching artefacts, and were free of data incompleteness artefacts. Super-resolution MidP/4D-T2w MRI is a promising technique to facilitate target delineation for radiotherapy treatment planning.

Chapter 5

Development of three Dixon-based methods to calculate synthetic 4D/midposition CT

In this chapter, three consecutive methods (Dixon-based, Dixon-Spine, Dixon-Spine-Lung) are introduced to obtain synthetic 4D-CT from 4D-T1w and 3D-Dixon MRI. For six lung cancer patients, calculated synthetic 4D-CTs were validated against 4D-CT in midposition by comparison of Hounsfield units and dose-volume metrics. The work described in this chapter was published in part by Freedman et al. (2019)

5.1 Introduction

In Chapters 3 and 4, two methods to obtain 4D-T2w MRI were described. Four-dimensional/MidP T2w MRI might be employed in MR-linac workflows to adapt delineations and PTV margins in the pre-determined treatment plan to better represent the anatomy and respiratory pattern of the day. Dose delivery according to the adapted treatment plan could then be simulated using up-to-date electron density information obtained from co-registered 4D/MidP-sCT images. More information regarding MidP planning and alternative 4D planning approaches can be found in sections 1.3.1 and 1.4.4, respectively.

Calculation of sCT by registering the pre-treatment CT image to daily MRI acquired prior to each treatment fraction was demonstrated (Kraus et al., 2017). However, as discussed in section 1.4.2, generating sCT directly from MRI is more desirable because it would reduce registration errors and simplify the radiotherapy workflow by decreasing the total number of scheduled examinations (Edmund and Nyholm, 2017).

Synthetic-CT can be directly calculated from MRI using bulk-density assignment, atlas-based, voxel-based (including machine learning) and hybrid methods. To date, the above-described approaches were mostly applied to relatively immobile sites, such as the brain or the prostate (Edmund and Nyholm, 2017; Johnstone et al., 2018). In the abdominothoracic region, most current methods are based on tissue-segmentation and bulk-density assignment. Of the methods which do not include bone-density information, dosimetric differences of the D95 % metric (dose delivered to at least 95 % of the PTV) between sCT and CT were reported to be less than 1 % using 3D conformal RTP (thorax) (Jonsson et al., 2010), and greater than 5 % using volumetric modulated arc therapy (VMAT) RTP (thorax) (Prior et al., 2017). In methods which include bone-density information, for instance by using an anterior vertebral body model (VMAT RTP) (abdomen) (Bredfeldt et al., 2017) or an atlas (intensity modulated RTP) (thorax) (Wang et al., 2017), mean dosimetric differences for all regions and metrics were reported to be within

1 %.

There is scope to improve abdominothoracic sCT. Prior et al. (2017) demonstrated that incorrect bulk-density assignment in the lung leads to errors up to 19.6 % in the PTV dose-volume metrics. Patient specific lung electron density values should therefore be implemented to account for underlying lung pathology (Durham and Adcock, 2015; Rosenblum et al., 1980; Soejima et al., 2000). Furthermore, prior to the work described here, no method had been applied to obtain 4D/MidP-sCT for RTP purposes. Four-dimensional/MidP-sCT could be calculated by transferring the motion information from 4D-T1w MRI to 3D-sCT using the MVFP method introduced in Chapter 3. This approach would be advantageous to use with MVFP-generated 4D-T2w MRI, since 4D-sCT would be intrinsically registered. The aims of this chapter were therefore to:

1. Develop methods to generate 4D/MidP-sCT, using motion information from 4D-T1w MRI, for treatment planning purposes.
2. Verify and evaluate calculated 4D/MidP-sCT against 4D-CT.

5.2 Materials and methods

5.2.1 Data acquisition

Six patients with early stage non-small cell lung cancer (5 adenocarcinoma, 1 adenosquamous carcinoma), all of whom were treated with stereotactic radiotherapy, were included in this study after giving written informed consent. A 4D-CT scan was obtained for all patients using a Brilliance Big Bore CT scanner at 120kV (Philips Medical Systems, Best, The Netherlands), with voxel-size $(0.98 \times 0.98 - 1.17 \times 1.17) \times 2 \text{ mm}^3$ and ten respiratory phases. Within a median of 2 (range: 0-14) days, MRI was acquired at 1.5 Tesla (MAGNETOM Aera; Siemens Healthcare, Erlangen, Germany) using a T1w golden-angle radial stack-of-stars spoiled gradient echo sequence (Block et al., 2014) in free breathing and a Cartesian 2-point Dixon gradient echo sequence in breath-hold (exhalation). More

information regarding the 2-point Dixon and radial stack-of-stars pulse sequences can be found in sections 2.1.3.2 and 2.2.3.1, respectively. Patients unable to hold their breath were scanned in free-breathing with four averages, resulting in an image close to exhalation. All 2-point Dixon images were reconstructed using the vendor provided fat-water separation algorithm available in the scanner software. Patients were scanned in the same treatment position in both MRI and CT acquisition, which was enabled using an MR compatible immobilisation board (Extended Wing Board; Civco Radiotherapy, Coralville, IA, USA). During MR acquisition, an in-house built body coil holder was used to prevent compression of the body contour by the 18-channel receive array. Figure 5.1 displays the patient set-up used to acquire the Dixon and T1w images, as demonstrated by a healthy volunteer. Detailed MRI acquisition parameters can be found in Table 5.1.

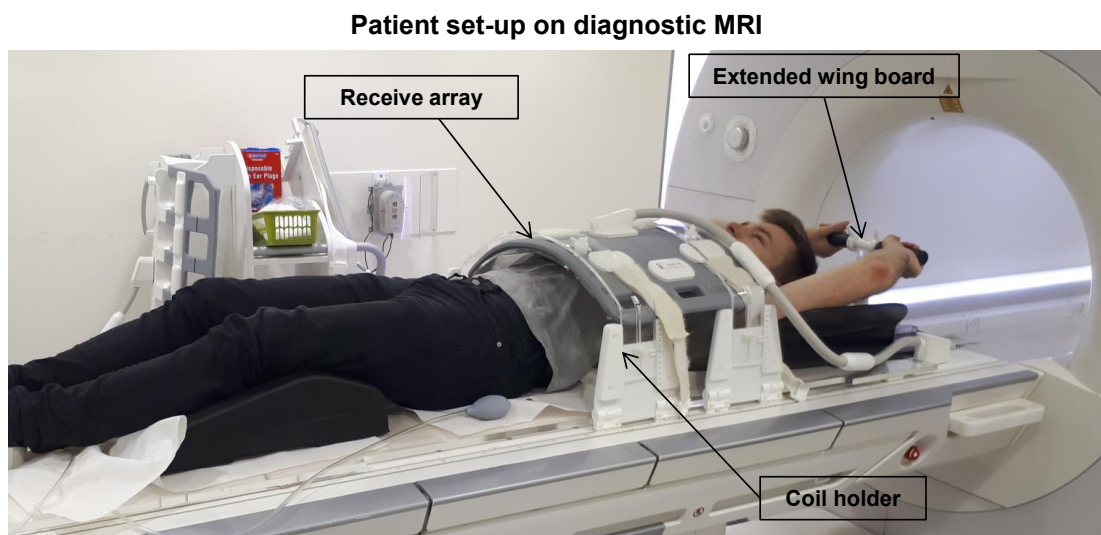


Figure 5.1: Patient set-up used to acquire T1-weighted and Dixon MRI, as demonstrated by a healthy volunteer. The receive array is elevated above the volunteer using a custom designed coil holder. An MR compatible extended wing board was employed to enable the patient to be scanned in the same position as for the CT acquisition.

Table 5.1: Detailed acquisition parameters of the radial stack-of-stars and Dixon sequences. No indicates number; Acq, acquisition; NA, not applicable.

Parameter	Radial	Dixon (exhalation)	Dixon (free-breathing)
Orientation	Axial	Axial	Axial
No. slices	80 - 88	64 - 88	72 - 88
No. spokes	1005	NA	NA
Acq. time, min	05:19 - 05:45	00:20 - 00:21	02:02 - 02:49
Field-of-view, mm ²	320 × 320 -	322 × 430 -	312 × 400 -
	336 × 336	360 × 480	368 × 469
Voxel size, mm ³	(1.25 × 1.25 -	(1.68 × 1.68 -	(1.25 × 1.25 -
	1.31 × 1.31) × 3.5	1.88 × 1.88) × 4.2	1.34 × 1.34) × 3.5
Echo time, ms	1.55	2.39, 4.77	2.39, 4.77
Repetition time, ms	3.18	7.6	7.6
Flip angle, °	8	8	8
Bandwidth, $\frac{Hz}{Pixel}$	630	400	400
No. signal averages	1	1	4
Fat suppression	Yes	No	No

5.2.2 Motion-modelling

All calculations in this chapter were carried out in MATLAB (version 2017a; The Mathworks, Natick, MA). Key components of the motion-modelling method, that is introduced in this chapter, are provided in Figure 5.2 A.

Four-dimensional T1w MRI was reconstructed using the joint MoCo-HDTV algorithm and then corrected for geometrical distortion, as per section 3.2.2. Using 4D-T1w MRI, MVFs ($M_{T_n}^{T_j}$) describing the transformation from the tie-phase (T_j) to all remaining respiratory phases (T_n) were calculated following the method described in section 3.2.4; except for 3D-T2w MRI being replaced by in-phase 3D-Dixon MRI (D_j). The transformation $M_{T_{MidP}}^{T_j}$ was determined from the $M_{T_n}^{T_j}$ set (Wolthaus et al., 2008a) and applied to obtain MidP-T1w MRI:

$T1_{MidP} = W_{T_{MidP}}^{T_j} T1_j$. The transformation $M_{T_j}^{D_j}$ was obtained by registering D_j to T_j . Water, fat and in-phase Dixon images were then warped to MidP using the composition: $W_{T_{MidP}}^{T_j} W_{T_j}^{D_j}$. Four-dimensional sCT was calculated by warping MidP-sCT to all other respiratory phases using the composition of the $M_{T_n}^{T_j}$ and inverse $M_{T_{MidP}}^{T_j}$ transformations: $sCT_n = W_{T_n}^{T_j} W_{T_j}^{T_{MidP}} sCT_{MidP}$.

MidP-CT was independently calculated from 4D-CT in the same way that MidP-T1w MRI was obtained from 4D-T1w MRI.

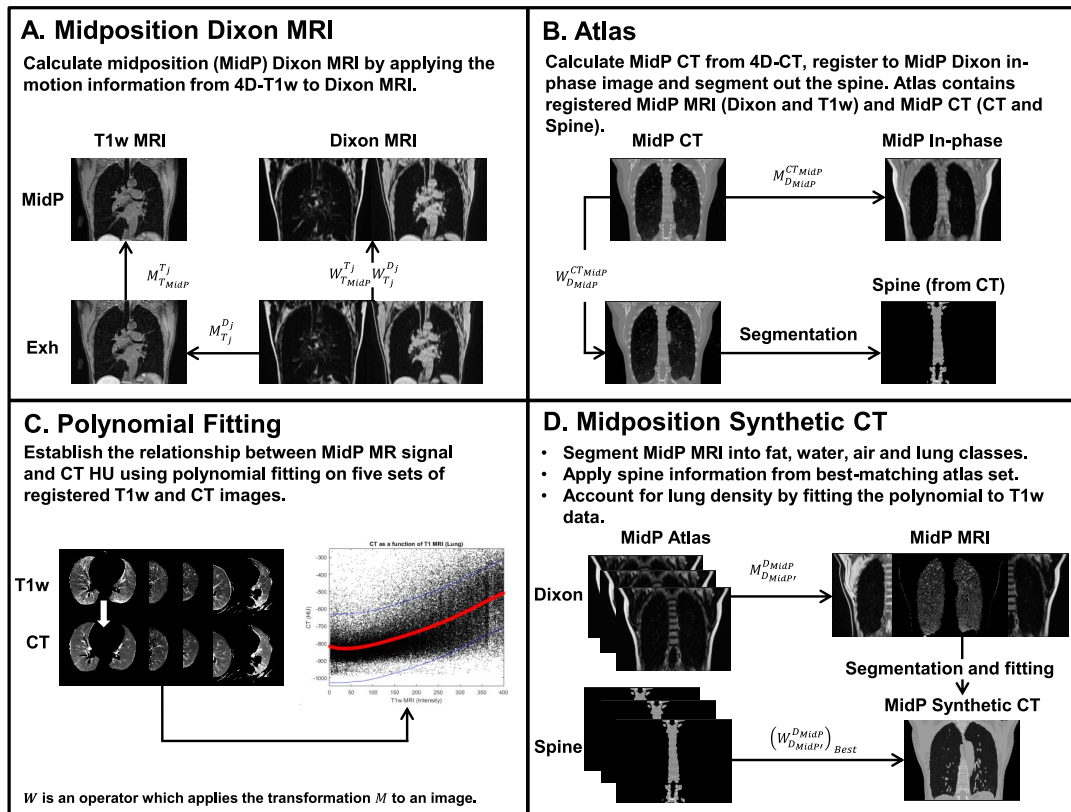


Figure 5.2: A, the transformation from the j^{th} respiratory phase to midposition (MidP) of 4D-T1w MRI is calculated ($M_{T_{MidP}}^{T_j}$). MidP-Dixon MRI is obtained by composing the transformation found by registering Dixon MRI to the j^{th} respiratory phase of 4D-T1w MRI ($M_{T_j}^{D_j}$) with $M_{T_{MidP}}^{T_j}$: $D_{MidP} = W_{T_{MidP}}^{T_j} W_{T_j}^{D_j} D_j$. B, describes the key steps involved in generating the atlas. C, describes polynomial fitting. The data used to calculate the polynomial coefficients (5 patients) were obtained from the atlas. D, synthetic MidP-CT is calculated by tissue-segmentation and bulk-density assignment (sCT_D), updated with spine-density information from the best-matching atlas image set (sCT_{DSL}), and variable lung density information (sCT_{DSL}). $M_{D_{MidP'}}^{D_{MidP}}$ describes the transformation of each atlas MidP-Dixon (fat) MRI to the incoming MidP-Dixon (fat) MRI; $(W_{D_{MidP'}}^{D_{MidP}})_{Best}$ describes application of the best matching $M_{D_{MidP'}}^{D_{MidP}}$.

5.2.3 Atlas

The atlas contained MidP-T1w, MidP-Dixon (MidP-Fat, MidP-Water and MidP in-phase), MidP-CT and MidP-spine (segmented from MidP-CT) images. The MidP-CT atlas images were obtained by registering the MidP-CT images to the MidP in-phase images. The MidP-spine atlas images were extracted from the MidP-CT atlas images using thresholding and ROI analysis (Figure 5.2: B):

Bone was segmented from MidP-CT by thresholding (125 to 1500 HUs) and connected component analysis; the largest connected component corresponded to the rib cage, which included the thoracic vertebrae. Stray pixels were removed by morphologically dilating and closing the rib cage image using an ellipsoid structuring element (1, 1, 2 pixels). A rectangular ROI was manually placed around the spine on the central axial slice of the processed rib cage image. Pixels outside the ROI were set to zero on all slices. Holes were filled using a morphological flood-fill operation (Soille, 1999).

A leave-one-out cross-validation was enabled by truncating the atlas to include all acquired data except the patient for which MidP-sCT was being generated (referred to as the incoming patient or image).

5.2.4 Dixon-based synthetic CT (sCT_D)

Dixon-based sCT was generated from the MidP-Dixon images using intensity-based segmentation and assignment of HUs for fat (-110), soft-tissue (70), air (-1000) and lung (-767) (Figure 5.3); Dixon-based sCT in MidP is referred to below as sCT_D. Hounsfield unit values were the same as those applied for sCT generation by (Wang et al., 2017). Segmentation was carried out using thresholding and connected component analysis:

A binary mask \mathcal{M} (background and lungs = 1, remaining = 0) was calculated by thresholding the composite image $I_{FW} = \text{MidP-Fat} + \text{MidP-Water}$. The threshold was set as the volumetric mean image intensity of I_{FW} . Intensity values above and below the threshold were set to 0 and 1, respectively. \mathcal{M} was zero

padded and subjected to connected component analysis; the largest component was the background mask \mathcal{B} . The difference $\mathcal{M} - \mathcal{B}$ corresponded to the lung mask \mathcal{L} .

Fat and water masks were initialised by applying the $(1 - \mathcal{M})$ mask to the MidP-Fat and MidP-Water images. The initialised fat mask was thresholded using the volumetric mean non-zero intensity value of the MidP-Fat image and then post-processed, to reduce stray pixels and holes, by keeping only the largest connected component. The post-processed fat mask was applied to remove fat components from the initialised water mask.

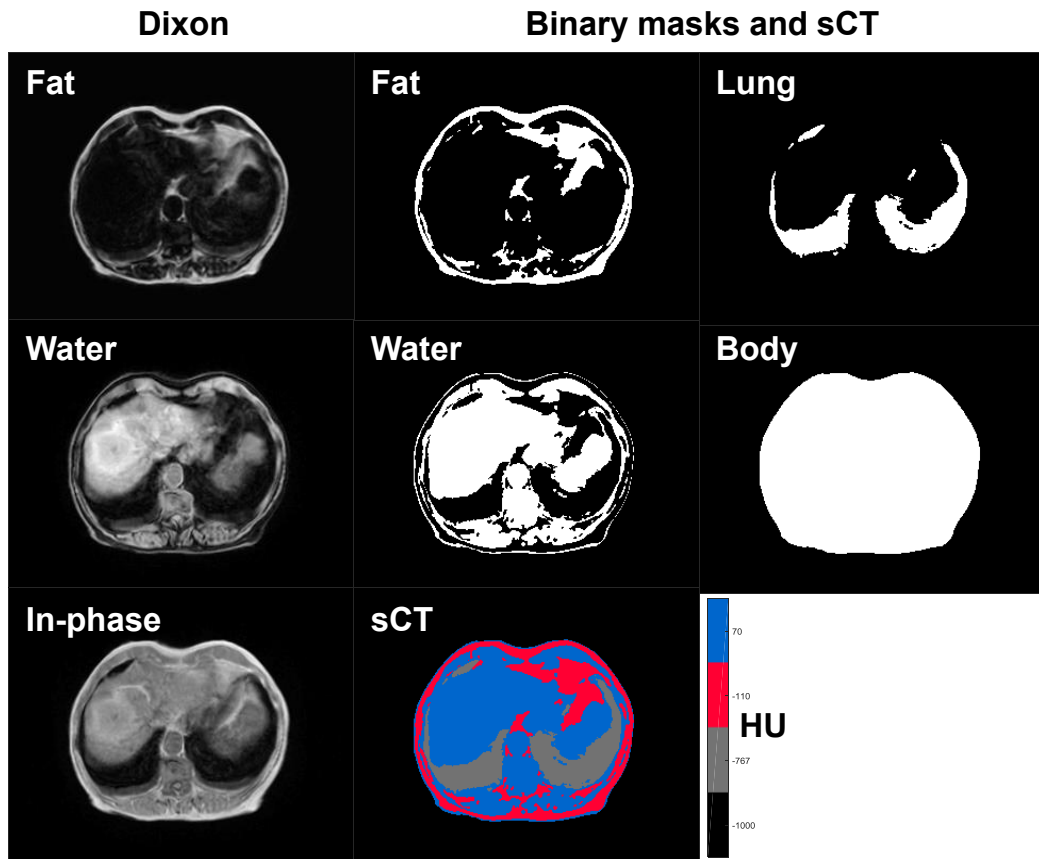


Figure 5.3: An example of intensity-based segmentation and assignment of Hounsfield units (HU)s for patient 1. Binary masks were calculated by thresholding midposition Dixon images and then applied to obtain synthetic CT (sCT) through bulk-density assignment. In sCT: blue, red, grey and black colours correspond to soft-tissue, fat, lung and air HUs, respectively.

5.2.5 Dixon-Spine synthetic CT (sCT_{DS})

Dixon-based sCT were improved to include spine density information (sCT_{DS}) from the best-matching MidP-spine atlas image. All MidP-Fat atlas images were registered to the incoming MidP-Fat image. The corresponding MidP-spine atlas images were warped with the resulting transformations and applied as a binary mask to the registered MidP-Fat images. Normalised mutual information was calculated between the incoming and registered masked MidP-Fat images. The MidP-spine atlas image corresponding to the best-matching registered masked MidP-Fat image (highest NMI) was fused with sCT_D by intensity override.

5.2.6 Dixon-Spine-Lung synthetic CT (sCT_{DSL})

Dixon-Spine sCT were modified to include variable lung density information (sCT_{DSL}). The relationship between signal intensity in MidP-T1w images and HUs of co-registered MidP-CT images was modelled in the lung with a fifth order polynomial (Figure 5.2: C).

Midposition T1w images were corrected for intensity inhomogeneity (Hofmann et al., 2011): First the scanner-reconstructed T1w images were passed through 3D median and image guided filters (He et al., 2013). MidP-T1w images were then divided by the filtered scanner-reconstructed images. Afterwards, inhomogeneity corrected MidP-T1w images were normalised such that the mean intensity values of the water components in each image were equal. Ten million non-zero points were randomly selected in the lung components of MidP-T1w MRI and MidP-CT. Data support over the entire intensity range was assured by further sorting the data into 20 bins of equal width, and then extracting 5000 random data points from each bin. The polynomial weights were then obtained by linear least squares fitting to the selected data.

In order to enable a leave-one-out cross-validation, the truncated MidP atlas (see section 5.2.3) data were used to calculate separate polynomial weights for each incoming patient. Variable lung density information was included by applying the

atlas-fitted polynomial to incoming MidP-T1w intensity values. A summary of sCT_{DSL} generation can be found in Figure 5.2: D.

For incoming patient 2 additional sCT images were generated by linearly scaling the lung HU values of $sCT_{D,DS,DSL}$ to match the median lung CT HU value (-865 HU). Scaled sCT images were calculated because patient 2 exhibited co-existent lung disease (severe emphysema) and did not fit into the group of other patients, which exhibited a mean (over patients 1 and 3-6) median HU value of -808.

5.2.7 Validation of synthetic CT

Midposition sCT images were validated by comparison to MidP-CT, both dosimetrically and in terms of HUs. Radiation oncologists performed delineation and treatment planning. Using the information from non-rigidly registered MidP-T1w and MidP-Dixon images, one set of contours was generated for the primary tumour and OARs for each patient. The contours represented the “best fit” between CT and MR images. Single full arc coplanar stereotactic VMAT plans at 6 MV were designed for all patients using a collapsed cone algorithm and an Agility multileaf collimator on RayStation (v5.99, RaySearch Laboratories, Sweden) with a dose grid of 2.5 mm and collimator angle of 2 °. Five patients had peripheral lesions with a PTV close to the chest wall, and were planned according to the UK stereotactic ablative radiotherapy (SABR) consortium guidelines with a five fraction regimen (55 Gy in 5 fractions) using the constraints stipulated in a recent UK SABR consensus publication (Hanna et al., 2018). One patient had a central lesion and was planned using an eight fraction regimen (60 Gy in 8 fractions) as per the LungTech EORTC phase II trial protocol (Adebahr et al., 2015; Lambrecht et al., 2016). As MidP images were used, PTV margins were personalised for each patient, and this was dependent on tumour motion. Planning target volume margins were calculated using motion information from the 4D-T1w images, but applying the same principles as reported elsewhere for 4D-CT planning (Wolthaus et al., 2008b). Once contours had been finalised, they

were copied onto the registered sCT images. Two planning techniques were used: initial planning on MidP-CT and independent re-calculation on $sCT_{D,DS,DSL}$ (Plan 1); and initial planning on $sCT_{D,DS,DSL}$ (using all sCT methods independently) and re-calculation on MidP-CT (Plan 2). Differences in the following dose-volume metrics were compared: Dose delivered to at least 95 or 99 % of the PTV (PTV D95 or 99 % respectively), total PTV volume divided by the total isodose volume (Conformity Index at Isodose), volume of lung receiving ≥ 20 Gy (v20 Gy), Proximal Airways near-point maximum dose (Dmax), which was defined as minimum dose to the 0.5 cm^3 volume of the organ receiving the highest dose (Hanna et al., 2018), Oesophagus Dmax 0.5 cm^3 , Brachial Plexus Dmax 0.5 cm^3 , Heart Dmax 0.5 cm^3 , Spinal Canal Dmax 0.1 cm^3 , and Chest Wall D 30 cm^3 , which is defined as the minimum dose to 30 cm^3 of the organ that receives the highest dose. Differences in dose-volume metrics were calculated with respect to CT for both Plans 1 and 2. In an exploratory analysis, a Wilcoxon signed-rank test with a significance level of $p = 0.05$ was applied to evaluate the dosimetric differences found by comparing $sCT_{D,DS,DSL}$ and CT. Using the same analysis, the absolute values of the above-mentioned dosimetric differences were compared for significance between methods ($sCT_{D \rightarrow DS}$, $sCT_{DS \rightarrow DSL}$, $sCT_{D \rightarrow DSL}$).

5.3 Results

For six patients with early stage node-negative primary lung malignancies, three variations of MidP-sCT ($sCT_{D,DS,DSL}$) were calculated. These patients exhibited a mean PTV volume of 34 (range: 22 – 40) cm^3 . Motion-compensated 4D-T1w MRI reconstruction took between 9 and 12 hours, and calculation of sCT_D , sCT_{DS} and sCT_{DSL} was finished in 30, 51 and 54 minutes, respectively. Figure 5.4 shows an example of reconstructed MidP-CT compared to $sCT_{D,DS,DSL}$. All generated sCT exhibited qualitatively similar respiratory phase to MidP-CT. In addition, sCT_{DSL} provided good visual agreement with MidP-CT due to comparable spine and variable lung density. For one patient, MidP-CT exhibited overlapping

structure artefacts associated with multi-slice 4D-CT reconstruction (Yamamoto et al., 2008) (Figure 5.5). Overlapping structure artefacts were not displayed by the corresponding MidP-sCT image. Figure 5.6 shows snapshots of the inhalation and exhalation phases of 4D-sCT (sCT_{DSL} , 20 respiratory phases) for patient 4.

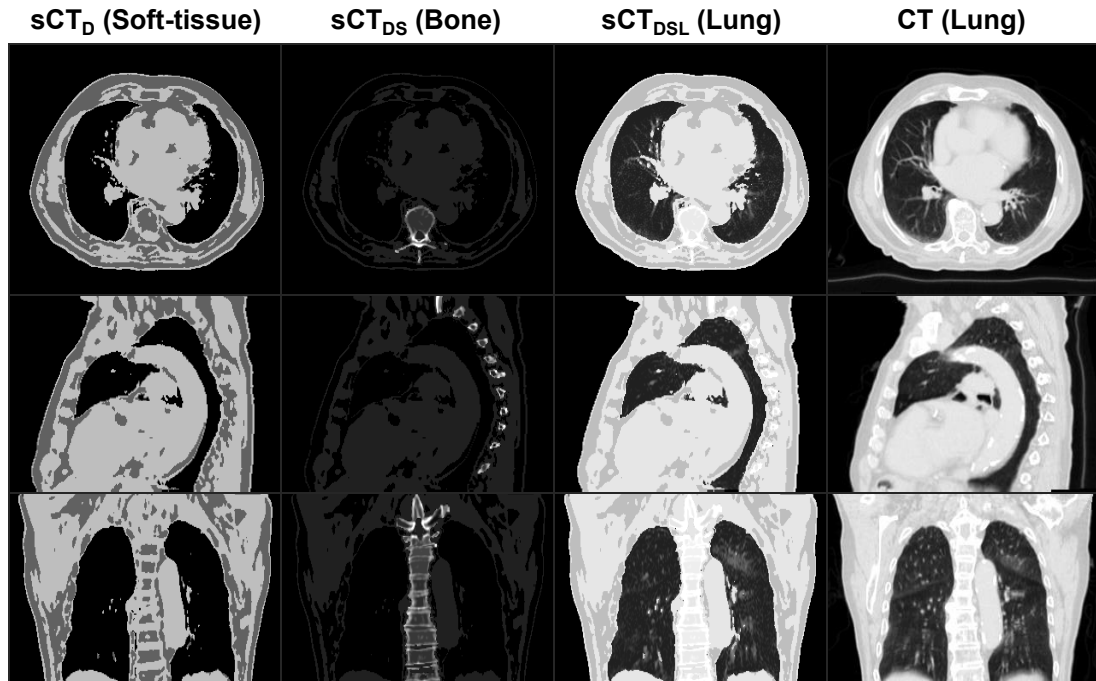


Figure 5.4: A comparison of Dixon-based (sCT_D), Dixon-Spine (sCT_{DS}) and Dixon-Spine-Lung (sCT_{DSL}) synthetic CT to midposition CT for patient 4. sCTs are windowed differently (Soft-tissue/Bone/Lung) to optimally display the new information that was introduced in each consecutive step.

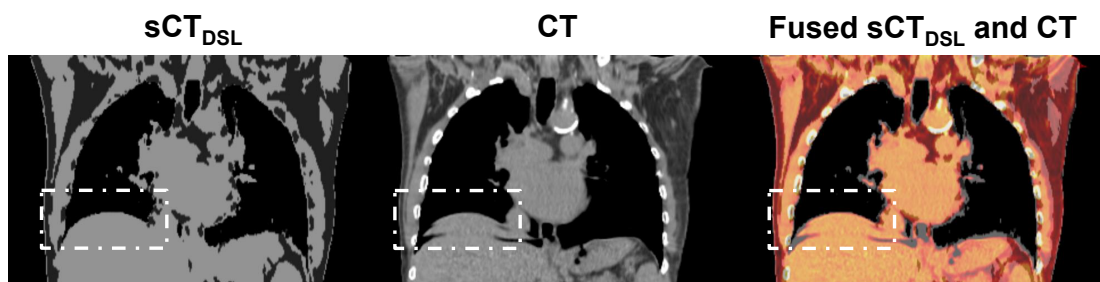


Figure 5.5: An example comparison of Dixon-Spine-Lung synthetic-CT (sCT_{DSL}) to midposition CT. Unlike CT, sCT_{DSL} does not exhibit the overlapping structure artefact (white dashed boxes).

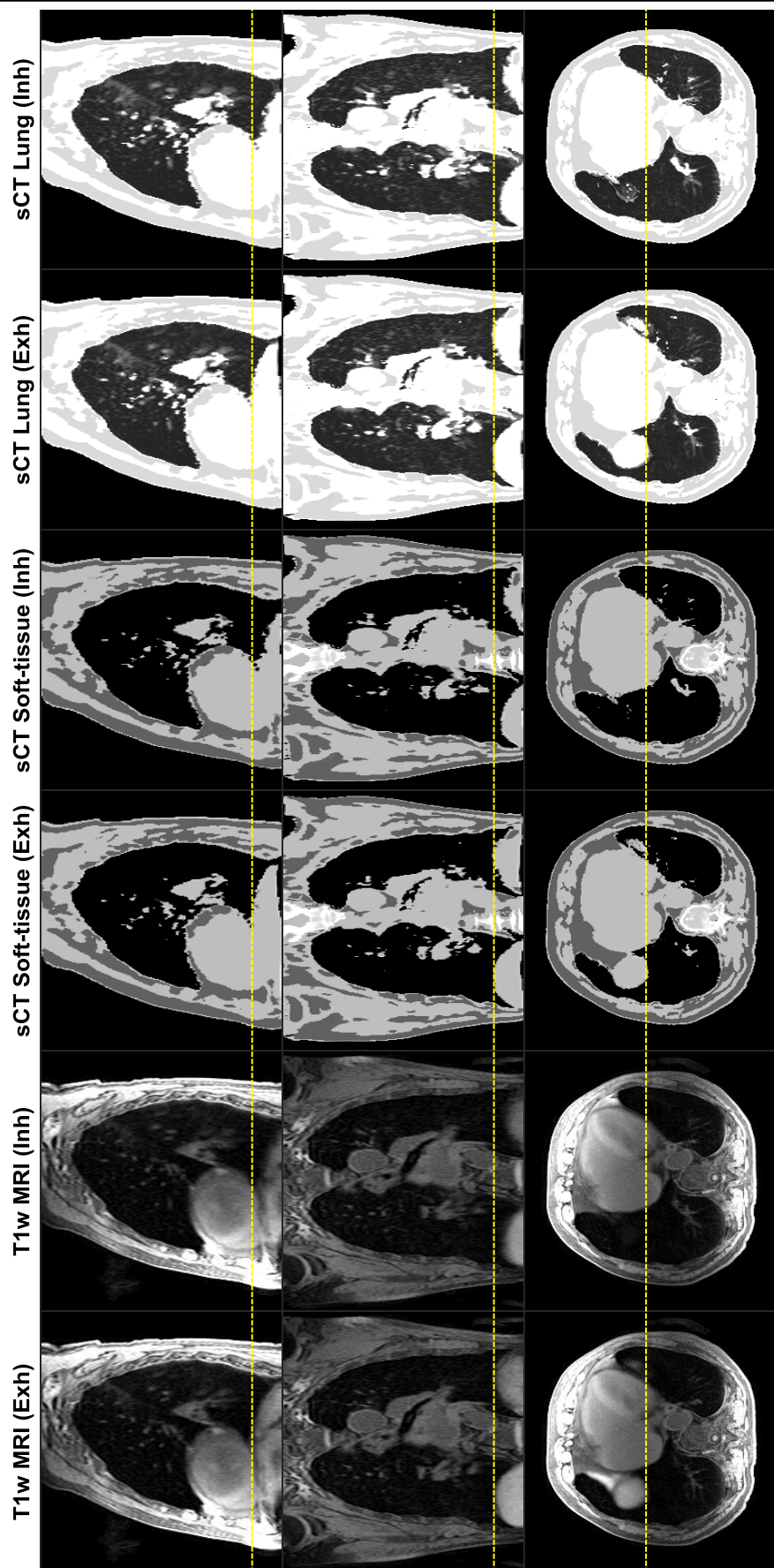


Figure 5.6: An example comparison of 4D Dixon-Spine-Lung synthetic CT (sCT) (soft-tissue and lung windows) to 4D-T1w MRI in the exhalation (Exh) and inhalation (Inh) respiratory phases. Yellow dashed lines aid comparison of the diaphragm position.

5.3.1 Validation: Hounsfield units

The median and standard deviation of the absolute differences in HUs, over all patients, between CT and sCT of the Dixon-based and Dixon-Spine-Lung methods were: 43 ± 187 and 42 ± 188 for the soft-tissue region, 43 ± 146 and 40 ± 144 for the fat region, 71 ± 114 and 43 ± 106 for the lung region, and 174 ± 186 and 96 ± 161 for the spine region; demonstrating that overall sCT_{DSL} exhibited the highest similarity with the CT images (Figure 5.7). Minor differences in average fat and soft-tissue HUs between sCT and sCT_{DSL} were due to inclusion of variable spine HUs.

5.3.2 Validation: dose-volume metrics

As presented in Figure 5.8, differences in selected dose-volume metrics between sCT_{D,DS,DSL} and CT were significant for PTV metrics, but not for OAR metrics. The significant differences for Plan 1 (planned on CT and re-calculated on sCT) and Plan 2 (planned on sCT and re-calculated on CT) represent a systematic over-dose and under-dose to the PTV, respectively. Unlike sCT_D and sCT_{DS}, sCT_{DSL} only exhibited a significant difference for the PTV D99 % metric ($p = 0.03$) of Plan 2. For the PTV D95 % and D99 % metrics, sCT_{DSL} exhibited the lowest absolute difference with CT, which was (mean \pm standard deviation in %) 1.7 ± 2.5 and 1.4 ± 2.3 for Plan 1, and 1.6 ± 2.4 and 1.7 ± 2.2 for Plan 2. The mean and standard deviations were skewed by the results of patient 2, where absolute differences up to 6.7 % were found. If the lung HU values of patient 2 were linearly scaled to match the median lung HU value of CT (Figure 5.8; black diamonds), the average absolute differences of the PTV D95 % and D99 % metrics were reduced to: 0.91 ± 0.89 and 0.77 ± 1.1 for Plan 1, and 0.77 ± 0.93 and 1.0 ± 1.1 for Plan 2. The average absolute differences (over all patients) of the investigated dose-volume metrics between sCT_{DSL} and CT are summarised in Table 5.2. For the OAR dose-volume metrics, minor differences were observed, but did not violate the pre-defined clinical goals.

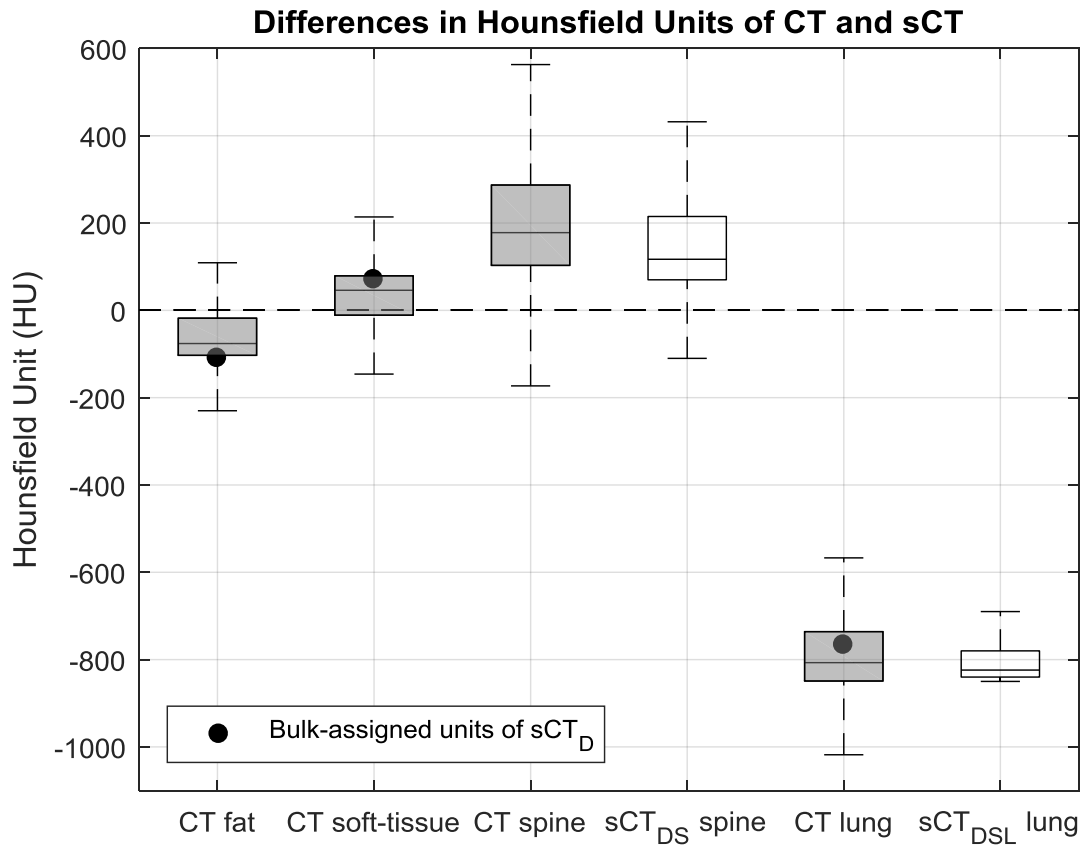


Figure 5.7: Regional comparison of Hounsfield unit (HU) in CT and synthetic CT (sCT) images. Boxplots summarise the HU distributions of each segmented region (fat, soft-tissue, spine and lung) for all patients; shading distinguishes between data obtained from CT (shaded) and sCT (unshaded) images. Black circles depict the bulk-assigned HU values of sCT_D. Outliers in the data, determined as 1.5 times the interquartile range above the upper quartile or below the lower quartile, were removed for display. Overall, HUs of CT best matched sCT_{DSL} due to the inclusion of variable spine and lung density values.

5.3.3 Comparison of synthetic CT methods

Significant reductions in absolute differences were found for the PTV D95 % (sCT_{D→DS}, sCT_{DS→DSL} and sCT_{D→DSL}) and Conformity Index at Isodose metrics (sCT_{DS→DSL} and sCT_{D→DSL}) of Plan 1, and for the PTV D95 % (sCT_{D→DSL} and sCT_{DS→DSL}) metric of Plan 2. For all OAR metrics, except the Proximal Airways Dmax 0.5 cm³ metric, the mean absolute dosimetric difference over all patients decreased between sCT_D and sCT_{DSL}.

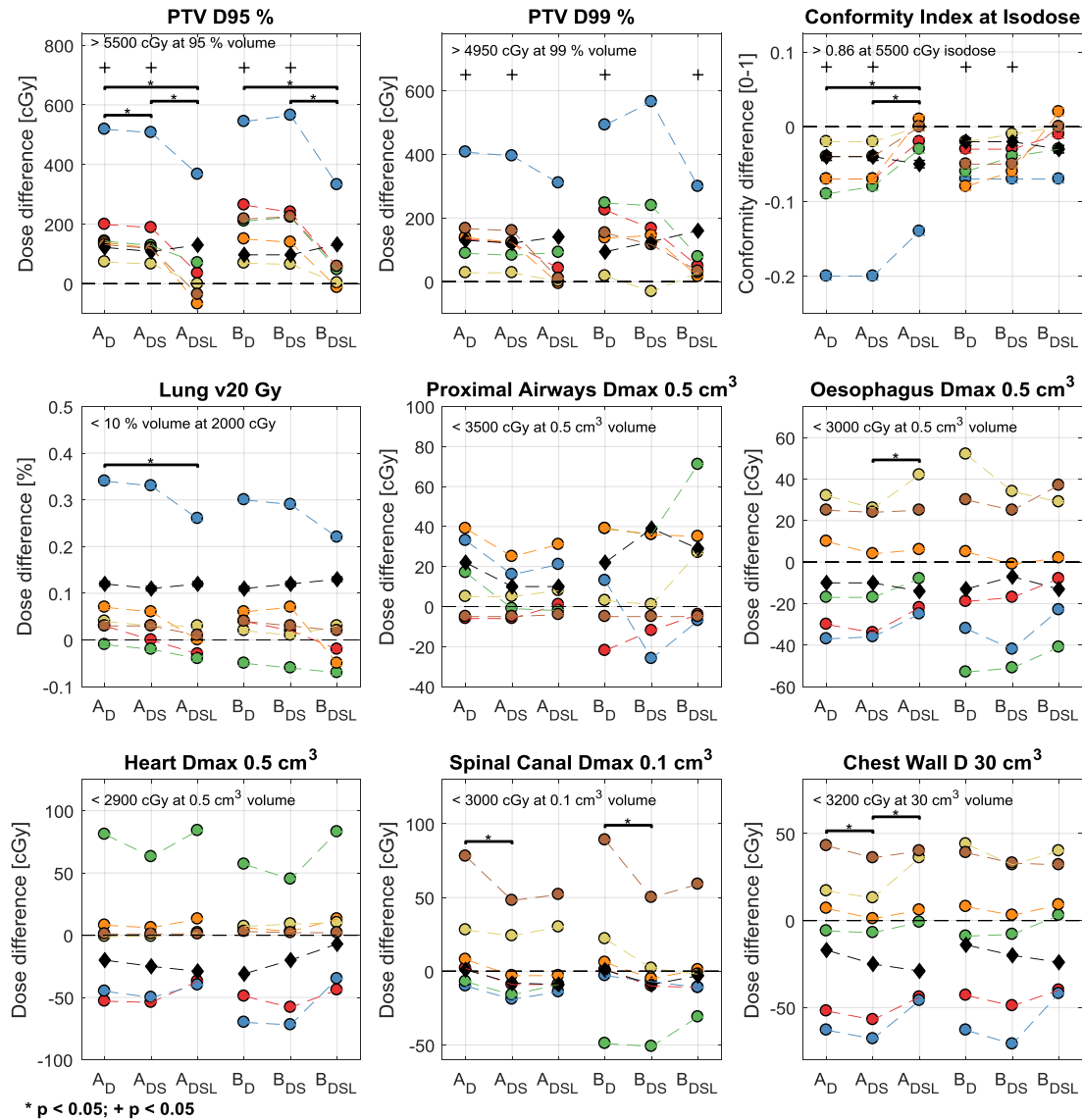


Figure 5.8: Differences in selected dose-volume metrics between the three methods of synthetic CT (sCT) and CT. $A_{D,DS,DSL}$ denotes planning on CT and re-calculating on the $sCT_{D,DS,DSL}$ images (Plan 1). $B_{D,DS,DSL}$ codifies planning on the $sCT_{D,DS,DSL}$ images and re-calculating on CT (Plan 2). Differences were taken with respect to CT for both Plan 1 and Plan 2. Coloured circles encode patient number (red, blue, green, orange, yellow and brown codify patients 1 to 6, respectively). Black diamonds show the results of re-planning patient 2 (blue) with rescaled lung HUs. Black crosses (+) indicate significant differences between sCT and CT; brackets and stars label significant absolute differences between sCT methods. Mandatory clinical goals for the five patients planned with 55 Gy in 5 fractions are listed on the top left-hand side of each subplot.

Table 5.2: The mean and standard deviation of the absolute differences (abs diff) between the Dixon-Spine-Lung sCT method (sCT_{DSL}) and CT for the: Spinal Canal Dmax 0.1 cm³, Lung v20 Gy, Proximal Airways Dmax 0.5 cm³, Oesophagus Dmax 0.5 cm³, Brachial Plexus Dmax 0.5 cm³, Heart Dmax 0.5 cm³, Chest Wall D 30 cm³, Conformity Index at Isodose, PTV D95 % and PTV D99 % dose-volume metrics. Differences were taken with respect to CT for both Plan 1 (planned on CT and re-calculated on sCT_{DSL}) and Plan 2 (planned on sCT_{DSL} and re-calculated on CT), and did not include the rescaled sCT of patient 2.

Metric	Plan 1	Plan 2	Plan 1	Plan 2
	(abs diff)	(abs diff)	(% diff)	(% diff)
Spinal Canal	20 ± 18 (cGy)	19 ± 22 (cGy)	1.2 ± 0.8	1.2 ± 1.1
Lung v20 Gy	0.06 ± 0.10 (%)	0.07 ± 0.08 (%)	1.1 ± 1.7	1.3 ± 1.6
Proximal Airways	11 ± 12 (cGy)	25 ± 26 (cGy)	2.2 ± 3.3	3.1 ± 3.9
Oesophagus	21 ± 13 (cGy)	23 ± 16 (cGy)	1.3 ± 0.6	1.3 ± 0.8
Brachial Plexus	10 ± 17 (cGy)	8 ± 16 (cGy)	1.9 ± 2.9	1.4 ± 3.4
Heart	30 ± 32 (cGy)	31 ± 30 (cGy)	1.7 ± 1.0	3.0 ± 2.7
Chest Wall	29 ± 20 (cGy)	28 ± 17 (cGy)	1.0 ± 0.7	1.0 ± 0.6
Conformity Index	0.03 ± 0.05 (0-1)	0.02 ± 0.03 (0-1)	3.9 ± 6.3	2.5 ± 2.8
PTV D95 %	96 ± 135 (cGy)	85 ± 123 (cGy)	1.7 ± 2.5	1.6 ± 2.4
PTV D99 %	77 ± 119 (cGy)	84 ± 108 (cGy)	1.4 ± 2.3	1.7 ± 2.2

Figure 5.9 displays an example illustrating the differences between the three sCT methods. Compared to sCT_D , inclusion of spine density information in sCT_{DS} resulted in a reduction of local hot spots in the differences between the simulated dose distributions of sCT and CT. Inclusion of variable lung density in sCT_{DSL} led to a further reduction in dose differences. In particular, a reduction in the area of hot spots around the PTV was observed.

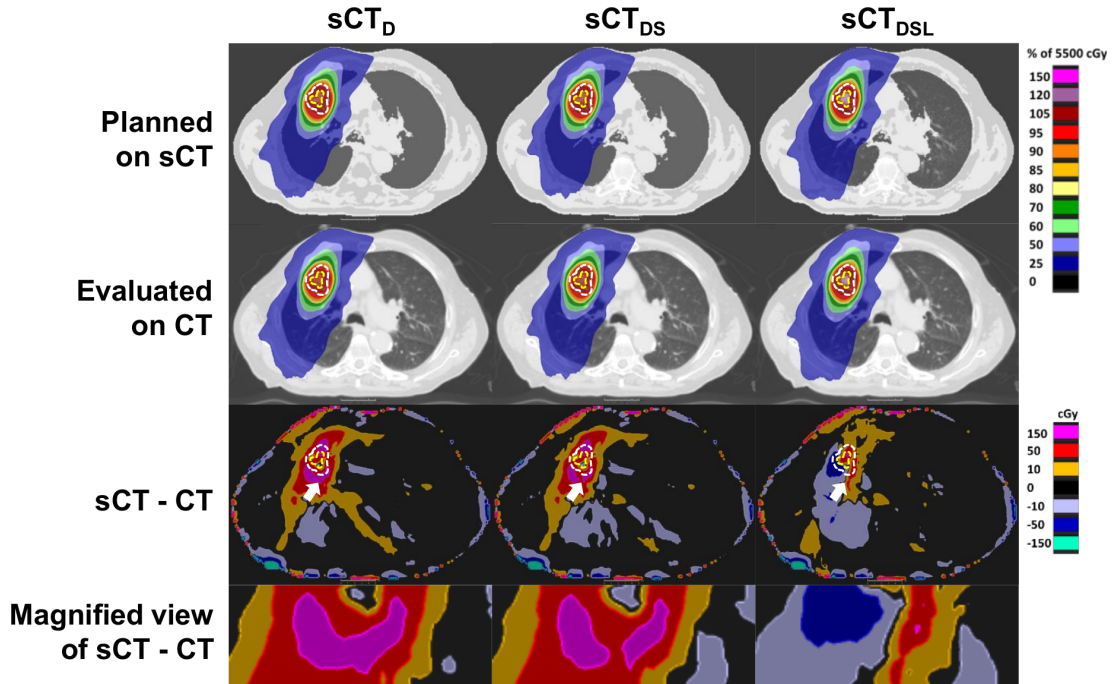


Figure 5.9: An example dosimetric comparison between planning on either of the three midposition synthetic CT images ($sCT_{D,DS,DSL}$) and evaluation on the midposition CT (patient 4). First and second rows: simulated dose planned on sCT and re-evaluated on CT. Third row: differences between the first and second rows. The planning target and gross tumour volumes are contoured in dashed white and yellow lines. White arrows assist viewing of an example hot spot reduction when comparing successive sCT methods. Fourth row: magnified view of the region indicated by the white arrows. Overall, differences in the calculated dose-distributions are reduced with consecutive sCT method.

5.4 Discussion

The first aim of this chapter was achieved by developing three methods to calculate 4D/MidP-sCT, which employ motion information from 4D-T1w MRI. In thoracic MR-linac workflows, 4D/MidP-sCT might be registered with 4D/MidP-T2w MRI and applied to adapt plans for anatomical differences and changes in respiratory pattern occurring throughout the treatment course. Daily plan adaptation could enable improved target coverage and permit reduced dose to OARs; see section 1.4.4 for more information. Calculated 4D/MidP-sCT could be directly applied for plan adaptation with MVFP-generated 4D/MidP-T2w MRI (Chapter 3), since both are intrinsically registered to 4D/MidP-T1w MRI.

Using the first method, sCT_D was obtained by tissue-segmentation and bulk-density assignment, and was extended in the second method using an atlas to include bone-density information (sCT_{DS}). Because of its ease of implementation, a best-atlas method was employed for multi-atlas label-fusion when performing spine segmentation. Alternative label-fusion techniques, such as majority voting (Iglesias and Sabuncu, 2015; Kieselmann et al., 2018) or a two-step local weighting method (Arabi et al., 2016), might provide dosimetric improvements related to spine density. The third method employed a polynomial fitting approach to overcome errors associated with bulk-assignment of HUs in the lung (sCT_{DSL}) (Prior et al., 2017). The polynomial fitting method is sensitive to intensity inhomogeneity resulting from non-uniform receiver coil profiles. This problem was addressed by implementing an intensity correction based on the vendor-provided image normalisation. A fifth order polynomial was chosen because it well represented the function returned using Gaussian Process Regression (Rasmussen and Williams, 2006), but was faster to train and apply to incoming data. In this chapter, the polynomial weights and spine density information were calculated from truncated atlas data, which enabled a leave-one-out cross-validation. In clinical practice, the same atlas would be employed for all incoming patients.

In all methods, MVFs obtained from 4D-T1w MRI were applied to transform $sCT_{D,DS,DSL}$ to all respiratory phases. The reconstruction time of 4D-T1w MRI currently limits intra-fractional application of 4D/MidP-sCT on MR-linac systems. However, as shown in Chapter 6, the problem of long reconstruction time can be overcome using deep learning techniques.

Instead of 4D-T1w and 3D-Dixon MRI, 4D-Dixon MRI (Benkert et al., 2017) could be directly acquired and used to obtain 4D-sCT (Kolbitsch et al., 2018a,b,c). Direct application of 4D-Dixon MRI for sCT generation would be advantageous, as no registration between 3D-Dixon and 4D-T1w (tie-phase) MRI would be required. Four-dimensional Dixon MRI was not directly acquired in the proposed Dixon-Spine-Lung method because the specialist pulse sequences employed by Benkert et al. (2017) and Kolbitsch et al. (2018a) were not readily available.

The second aim of this chapter was to verify and evaluate generated sCT, which was met by comparison with corresponding MidP-CT in terms of HU and dose-volume metric differences. For Plan 2, the most clinically relevant scenario (planned on sCT and evaluated on CT), significant differences were observed between the PTV dose-volume metrics of sCT_{D,DS} and CT. The significant differences represent a systematic under-dose to the PTV. No significant differences were found between dose-volume metrics of sCT_{DSL} and CT, except for the PTV D99 % metric. Absolute differences between sCT_{DSL} and CT for the PTV D95 % and D99 % metrics were on average less than 1.7 %. For sCT_{DSL}, dose to OAR metrics varied over patients, but did not violate pre-defined clinical goals. In (Wang et al., 2017), absolute mean errors in the PTV dose-volume metrics were reported to be less than 1 %. However in (Wang et al., 2017), lung cancer was simulated using homogeneous spherical lung lesions in mostly patients that did not have lung cancer. Due to the strong relationship between lung cancer and underlying lung pathology (Durham and Adcock, 2015), it is possible that the low errors reported in (Wang et al., 2017) are not fully representative of actual lung cancer patients, which were the target population in this chapter.

Compared to sCT_D, employing sCT_{DS} resulted in a reduction of the median and standard deviation HU errors in the spine by 78 and 25 HUs. Furthermore a significant dosimetric error reduction in the PTV D95 % metric was obtained between sCT_D and sCT_{DS} for Plan 1. Inclusion of variable spine density was shown to decrease local hot spots in the differences between the simulated dose distributions of CT and sCT (Figure 5.9), which might explain the reductions in HUs and dose-volume metric values. A further reduction in the median and standard deviation lung HU error of 28 and 8 HUs was achieved by sCT_{DSL}, which resulted in a significant reduction of absolute dose differences in the PTV D95 % metric for Plans 1 and 2. The reported sensitivity of the PTV metrics to the assigned lung HUs is in agreement with work by (Prior et al., 2017), who showed that the difference in the PTV D95 % metric can vary up to 9.06 % (target population average) when assigning bulk lung electron densities between 0.1 – 0.5

gcm^{-3} .

For patient 2, lung HU values of $\text{sCT}_{D,DS,DSL}$ were scaled to match the median lung HU value of CT. For the PTV D95 % metric, scaled sCT_D and sCT_{DSL} had absolute differences of: 122 and 130 cGy for Plan 1; 97 and 132 cGy for Plan 2. These differences were lower than corresponding unscaled values for sCT_D and sCT_{DSL} , which were: 518 and 367 cGy for Plan 1; 544 and 332 cGy for Plan 2 (Figure 5.8). On closer imaging review, patient 2 had severe emphysema - a disease which causes destruction of the alveolar septa, leaving enlarged air spaces and a loss of elastic recoil (Longmore et al., 2014). Large differences in PTV dose-volume metrics might be explained by low SNR in the lung, which might have led to incorrect assignment of enlarged air spaces as lung tissue (Figure 5.10). As demonstrated for patient 2, scaling of lung HU values to the average value on an available CT scan might be employed to correct for enlarged air spaces, without introducing DIR errors between CT and MRI. If no CT scan existed, as in a strict MR-only workflow, UTE time (Ohno et al., 2016) or balanced steady-state free-precession sequences (Bauman et al., 2009) could be employed to distinguish emphysema from healthy lung tissue.

One limitation of the validation study is that the static B_0 magnetic field associated with an MR-linac was not accounted for during treatment planning, which will result in dosimetric uncertainties associated with the electron return effect (Raaijmakers et al., 2005). Menten et al. (2016) compared conventional lung stereotactic treatment plans with and without the magnetic field and reported significant dosimetric differences only for the skin OAR, which suggests that the presented results remain applicable to MRgRT. An additional drawback of the validation study is the necessary comparison of sCT against CT. This comparison is problematic because electron density information exhibited by 4D-CT might have been corrupted by artefacts (Yamamoto et al., 2008), e.g. the overlapping structure artefact displayed in Figure 5.5. Furthermore, potential 4D-CT artefacts manifesting in the GTV (Persson et al., 2010) might have contributed to the significant differences obtained between sCT and CT for the PTV D99 % metric.

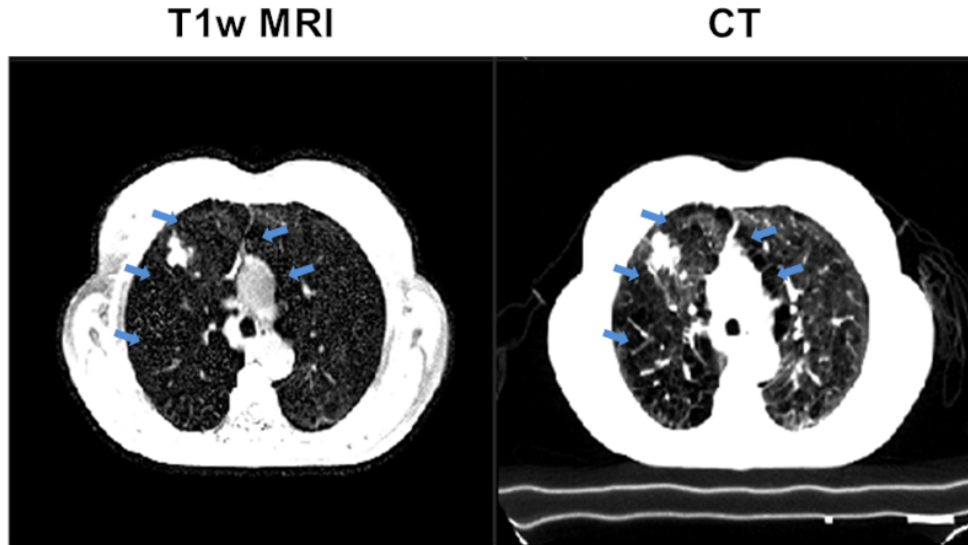


Figure 5.10: A comparison between T1w MRI and CT of patient 2 who presented with severe emphysema (lung window). Blue arrows assist viewing of emphysematous tissue, which appears as air spaces in CT, but cannot clearly be distinguished from healthy lung tissue in T1w MRI.

Dosimetric accuracy of sCT might be affected by scanner and patient-dependent geometrical distortions (Weygand et al., 2016); see section 1.4.2 for more information. Stanescu et al. (2012) and Wild et al. (2012) estimated the susceptibility-induced field inhomogeneity in the lung as 5.6 - 8.0 ppm, which corresponds for the presented acquisition to a maximum distortion of 0.90 - 1.3 pixels in the Dixon images (pixel bandwidth = 400 Hz). In the T1w images, patient-dependent distortions manifest as blurring, due to the radial readout. The impact of minor patient-dependent distortions in the Dixon images was mitigated by non-rigidly registering to the radial T1w images. As mentioned in section 1.4.2, patient-dependent distortions could also be corrected for using B_0 maps. Although scanner-dependent gradient non-linearity distortions were corrected for, residual distortions are expected, which increase in magnitude with distance from isocenter (Doran et al., 2005). Huang et al. (2016) reported average residual distortion errors within 1.5 mm over radial distances up to 200 mm from isocenter. Accuracy of sCT, in particular the body contour, is therefore subject to the specified tolerances by the vendor. The impact of residual geometrical distortions was minimised in

the validation study by registering MRI to CT.

5.5 Conclusion

Three methods to calculate 4D-sCT were developed and validated on six lung cancer patients by comparison with 4D-CT using HUs and dose-volume metrics in the midposition of the respiratory cycle. Inclusion of variable spine and lung density led to significantly reduced dosimetric differences in PTV metrics when compared to bulk-density assignment. For sCT generated using the Dixon-Spine-Lung method, dosimetric differences were clinically acceptable for OAR metrics, and they were on average ≤ 98 cGy (1.7 %) for PTV metrics. The feasibility of calculating dosimetrically accurate thoracic 4D/MidP-sCT from 4D-T1w and Dixon MRI was demonstrated. Four-dimensional sCT could be combined with 4D-T2w MRI for treatment plan adaptation in thoracic MR-linac workflows.

Chapter 6

Application of deep convolutional neural networks to reconstruct motion vector fields and T1-weighted 4D/midposition MRI

In this chapter, six deep radial convolutional (Dracula) neural networks were separately applied to reconstruct 4D-T1w MRI, MidP-T1w MRI and motion vector fields from gridded data. Dracula-reconstructed MRI and motion vector fields were verified against 4D joint MoCo-HDTV-reconstructed MRI by comparison of image similarity (structural similarity index metric). In addition, Dracula-reconstructed 4D-T1w MRI were visually assessed against joint MoCo-HDTV-reconstructed 4D-T1w MRI by two experienced observers.

6.1 Introduction

As outlined in section 1.4.4, 4D-T1w MRI has many potential applications in an MR-linac workflow. For instance, 4D-T1w MRI could be acquired before irradiation, with the patient in treatment position, to support plan adaptation and position verification (Bainbridge et al., 2017). Alternatively, 4D-T1w MRI can provide MVFs to enable calculation of 4D-T2w MRI or 4D-sCT using the MVFP (Chapter 3) or Dixon-Spine-Lung (Chapter 5) methods, respectively.

High-quality 4D-T1w MRI can be calculated from heavily undersampled data using iterative compressed sensing-based reconstructions (Feng et al., 2014, 2016; Rank et al., 2017). However, state-of-the-art reconstructions are currently of limited use for on-line application in MR-linac workflows because of long calculation times. In particular, the unoptimised 4D joint MoCo-HDTV prototype implementation (Rank et al., 2017), which was employed in Chapters 3 and 5, took on average 9-12 hours.

Deep learning techniques could bypass the long calculation times required by iterative compressed sensing algorithms to reconstruct highly undersampled data (Hammernik et al., 2018; Qin et al., 2019; Schlemper et al., 2017; Zhu et al., 2018). Deep learning-based MR image reconstruction techniques can be loosely categorised into data-driven, model-based and hybrid methods (Liang et al., 2019).

In data-driven approaches, a mapping is obtained between input and target data using a dCNN architecture, with either minor or no use of a priori information; see section 2.2.5 for a brief introduction to dCNNs. For instance, Han et al. (2018) applied a dCNN to reconstruct undersampled 2D-T1w images, which were acquired using a radial stack-of-stars spoiled gradient echo sequence. In their approach, a dCNN was pre-trained using 3602 pairs of undersampled and fully-sampled CT images. Afterwards, the pre-trained dCNN was fine-tuned using 15 pairs of undersampled and fully-sampled 2D-T1w images. Reconstruction of one 2D-T1w image using the fine-tuned dCNN took only 50 ms, which was less time-consuming when compared to the 29-60 seconds required by the PR-FOCUSS compressed

sensing reconstruction (Han et al., 2018; Ye et al., 2007). In a similar method, Hyun et al. (2018) trained and applied a dCNN to reduce aliasing artefacts in 2D-T2w images, which were acquired using a Cartesian TSE sequence. In their approach, the applied dCNN was trained on 1400 pairs of undersampled (29 % of k-space data) and fully-sampled (100 % of k-space data) 2D-T2w images.

In model-based techniques, image reconstruction is formulated as an iterative optimisation problem with free parameters and functions. By unrolling the optimisation algorithm, on an iteration by iteration basis, a deep network can be constructed and then trained to perform image reconstruction (Hammernik et al., 2018). Hybrid approaches combine data-driven and model-based techniques. For example, Aggarwal et al. (2018) and Schlemper et al. (2017) proposed frameworks utilising dCNN-based regularizers (data-driven component) and data consistency steps (model-based component) to reconstruct undersampled MR images.

As discussed above, dCNNs can be used to rapidly reduce aliasing artefacts present in undersampled MR images. However, prior to the work presented in this chapter, dCNNs had not yet been applied to accelerate compressed sensing-based 4D-MRI reconstructions. In addition to a long 4D-MRI reconstruction time, the Dixon-Spine-Lung and MVFP methods were limited by the processing time required to obtain the MidP image and/or MVFs from 4D-T1w MRI. For instance, as described in section 3.3, calculation of MVFs from 4D-T1w MRI using the chain method required 25-30 minutes. Combined reconstruction and processing time might be drastically reduced by directly generating the MidP image and/or MVFs from heavily undersampled data. This might be possible using similar deep learning techniques to those applied by (Han et al., 2018; Hyun et al., 2018). The aims of this chapter were therefore to:

1. Train and apply dCNNs to rapidly reconstruct 4D-T1w MRI, MidP-T1w MRI and MVFs from heavily undersampled data.
2. Verify resulting 4D-T1w MRI, MidP-T1w MRI and MVFs.

6.2 Materials and methods

6.2.1 Data acquisition

Twenty adult healthy volunteers and 47 patients (27 lung cancer [adult]; 3 liver cancer [adult]; 17 abdominal cancer [paediatric]) were scanned in free breathing with a T1w radial stack-of-stars spoiled gradient echo sequence with golden-angle spacing at 1.5 T (MAGNETOM Aera; Siemens Healthcare; Erlangen, Germany). More information regarding the radial stack-of-stars sequence is given in section 2.2.3.1. All subjects included in this study gave written informed consent. Lung cancer patients were scanned in the same treatment position as per CT acquisitions using the set-up described in section 5.2.1. All other subjects were scanned using the set-up introduced in section 3.2.1. Detailed acquisition parameters are displayed in Table 6.1.

Table 6.1: Acquisition parameters of the radial stack-of-stars sequence. No indicates number.

Parameter	Radial stack-of-stars
Orientation	Axial
No. slices	64 - 96
Slice oversampling, %	20.0 - 27.7
No. spokes per slice	1005 - 1008
Acquisition time, min	04:21 - 05:45
In-plane field-of-view, mm ²	400 × 400 - 480 × 480
Pixel size, mm ²	1.25 × 1.25 - 1.5 × 1.5
Slice thickness, mm	3.0 - 3.5
Echo time, ms	1.48 - 1.57
Repetition time, ms	3.18
Flip angle, °	8
Readout bandwidth, $\frac{Hz}{Pixel}$	630
Fat suppression	Yes

6.2.2 Reconstruction of T1w data

Similarly to section 3.2.2, raw data were corrected for gradient-delays and then sorted into 16 overlapping respiratory phases using a self-gating signal. Afterwards, 4D magnitude images were calculated from the sorted raw data using a Gridding reconstruction and the 4D joint MoCo-HDTV algorithm (Rank et al., 2017). See section 2.2.3.2 for detailed introductions to the Gridding and 4D joint MoCo-HDTV reconstructions.

The reconstructed 4D magnitude images were cropped along the slice-select dimension to remove oversampled data. Additionally, the in-plane FOV of each 4D magnitude image was symmetrically cropped from 320×320 to 256×256 pixels. Using cubic interpolation, the in-plane matrix-size of each cropped 4D magnitude image was then downsampled to 176×176 . Both the high-resolution (in-plane matrix-size: 256×256) and low-resolution (in-plane matrix-size: 176×176) cropped 4D magnitude images were retained for future calculations. In this chapter, the (high- and low-resolution) 4D magnitude images derived from the Gridding and 4D joint MoCo-HDTV reconstructions are referred to as (high- and low-resolution) Gridded and MoCo 4D-MRI, respectively.

6.2.3 Calculation of midposition images and motion vector fields

Midposition images were calculated from high-resolution MoCo 4D-MRI using a similar approach to that described in section 5.2.2. Motion vector fields ($M_{T_n}^{T_1}$) between the end-exhalation phase (T_1) and all other respiratory phases (T_n) of high-resolution MoCo 4D-MRI were calculated using the chain method introduced in section 3.2.4, with T_1 taking the place of the tie-phase. The average transformation ($M_{T_{MidP}}^{T_1}$) was then calculated from the $M_{T_n}^{T_1}$ set (Wolthaus et al., 2008b). Next, MVFs describing the transformation between MidP and all respiratory phases (T_n) were obtained by composing the $M_{T_n}^{T_1}$ and inverse $M_{T_{MidP}}^{T_1}$ MVFs: $M_{T_n}^{T_{MidP}} = M_{T_n}^{T_1} \circ M_{T_1}^{T_{MidP}}$. Afterwards, the high-resolution MidP-MoCo image was calculated by first warping all T_n with the inverse $M_{T_n}^{T_{MidP}}$ transformations, and then by averaging over all respiratory phases: $\text{MidP-MoCo} = \frac{1}{16} \sum_{k=1}^{16} W_{T_{MidP}}^{T_k} T_k$. Low-resolution MidP-MoCo images were obtained from low-resolution MoCo 4D-MRI using the same approach applied to calculate high-resolution MidP-MoCo images from high-resolution MoCo 4D-MRI.

6.2.4 Pre-processing of T1w data

Intensity values of the high-resolution MidP-MoCo, 4D Gridded and 4D MoCo images were divided on a subject-by-subject basis by $1.5 \times$ maximum intensity value contained in the high-resolution 4D Gridded image. Scaling ensured that image intensity values were between 0 and 1. Low-resolution Gridded 4D-MRI were scaled in the same way; except that $1.5 \times$ the maximum low-resolution 4D Gridded intensity value was applied for division.

For each subject, the x , y and z displacement components (M_x , M_y and M_z ; given in pixels [px]) of the low-resolution $M_{T_n}^{T_{MidP}}$ MVFs were scaled on an

element-by-element basis as follows:

$$\begin{bmatrix} M'_x(i, j, k, l) \\ M'_y(i, j, k, l) \\ M'_z(i, j, k, l) \end{bmatrix} = \frac{1}{40px} \begin{bmatrix} M_x(i, j, k, l)px + 10px \\ M_y(i, j, k, l)px + 10px \\ M_z(i, j, k, l)px + 10px \end{bmatrix} \quad (6.1)$$

Where i , j , k and l specify each element of the 4D M_x , M_y and M_z matrices. The asymmetric scaling in equation 6.1 transforms displacements between -10 and $30 px$ to values between 0 and 1 . The asymmetric scaling was chosen based on estimated maximum M_z displacements from MidP to exhalation ($-10 px \approx -3.0$ cm [slice-thickness of 3.0 mm]), and from MidP to inhalation ($30 px \approx 9.0$ cm [slice-thickness of 3.0 mm]). The estimated values from MidP to exhalation and from MidP to inhalation were conservatively chosen as -1 and $3 \times$ the maximum range of diaphragmatic displacement (≈ 3 cm), previously calculated from 4D-T1w MRI; see section 3.3.1, Figure 3.8b. The same asymmetric scaling was empirically found to work well for the M_x and M_y components.

Scaled data were randomly sorted into training (50 subjects [75 %]), validation (11 subjects [16 %]) and test sets (6 subjects [9 %]); collectively referred to as Group 1. Random sorting was constrained to ensure that the ratios between the number of healthy volunteers, lung cancer patients, liver cancer patients and abdominal cancer patients were similar in the training, validation and test sets. Using the same approach, a second data-set was obtained by sorting the scaled data into training, validation and test sets (Group 2). The test sets of Groups 1 and 2 each contained data from two healthy volunteers, three lung cancer patients and one abdominal cancer patient.

6.2.5 Implementation of Dracula

A 3D U-net dCNN architecture (Çiçek et al., 2016; Ronneberger et al., 2015) was implemented in Tensorflow (Abadi et al., 2016) to separately reconstruct MoCo 4D-MRI, MidP-MoCo images and MVF components from Gridded 4D-MRI. The implemented architecture is referred to here as Dracula, i.e. a **deep radial convolutional** neural network. Figure 6.1 displays the Dracula architecture, which contained encoding (left-hand side), bottle-neck (middle) and decoding (right-hand side) paths. The paths included convolutional, downsampling and upsampling layers.

Convolutional layers (light blue arrows in Figure 6.1) consisted of multiple convolution, non-linear activation and batch normalisation functions. Convolution operators were applied with kernel-size $3 \times 3 \times 3$ and zero-padding. All kernel weights were initialised using a Glorot normal distribution (Glorot and Bengio, 2010). Glorot initialisation reduced the impact of local minima (e.g. all kernel weights = 0) on the training process and consequently improved convergence. Each convolution operation resulted in a feature map; an example feature map is shown in Figure 2.16b. For instance, in the first layer, the input image was operated on by 64 independent convolutions, which resulted in 64 feature maps. Following convolution, each generated feature map was operated on by a ReLu activation function, which set all negative values in the feature map to zero. Application of ReLu functions enabled the dCNN to learn non-linear transformations. After non-linear activation, batch normalisation was used to normalise the output values of the activated feature maps. Batch normalisation is one technique to reduce overfitting (Ioffe and Szegedy, 2015). Note that scaling and shifting parameters applied in batch normalisation were trainable.

Downsampling layers (red arrows in Figure 6.1) were implemented using a max pooling operator with kernel-size $2 \times 2 \times 2$. Downsampling reduced the matrix-size of input feature maps by a factor of 2 in each dimension. Downsampled feature maps are represented by red blocks in Figure 6.1.

Upsampling layers (black arrows in Figure 6.1) were applied using a transposed convolution operator with kernel-size $2 \times 2 \times 2$ (Çiçek et al., 2016). Similarly to the convolutional layers, Glorot normalisation was employed to initialise kernel weights in the transposed convolutional operators. Upsampling doubled the matrix-size of input feature maps in each dimension. Skip connections (dark blue arrows in Figure 6.1) were incorporated by copying and concatenating feature maps from the encoding path (blue blocks in Figure 6.1) with feature maps of the same matrix-size in the decoding path (black blocks in Figure 6.1) (Ronneberger et al., 2015). The final convolutional layer (purple arrow in Figure 6.1) applied one convolution operation then non-linear activation (sigmoid function) to feature maps obtained following the decoding path. The convolution was applied with kernel-size $1 \times 1 \times 1$.

Drop-out was employed after all downsampling and upsampling layers to reduce overfitting (Srivastava et al., 2014). Drop-out refers to randomly setting a fraction of layer outputs to 0 during each training update. The drop-out fraction was set to $1/2$, except for the first downsampling layer, which was set to $1/4$.

The encoding path consisted of eight convolutional and four downsampling layers. Feature maps with increasingly reduced matrix-size were calculated by passing the input image through layers in the encoding path. Low matrix-size feature maps calculated along the encoding path contained high-level representations of the input data. The bottle-neck path connected feature maps from the encoding path to the decoding path; it contained two convolutional layers. The decoding path included eight convolutional and four upsampling layers. Skip connections permitted information from the encoding path to be accessed by the decoding path. A final convolutional layer was implemented to extract a single image from all feature maps output by the decoding path. The matrix-size of the output image had the same dimensions as the input image. Overall, Dracula contained 90,304,449 trainable parameters, which were associated with batch normalisation (shifting and scaling parameters), convolutions (kernel weights) and transposed convolutions (kernel weights).

6.2.6 Training and application of Dracula

Using the training and validation data from Group 1, five separate instances of Dracula were optimised to learn transformations between the following input and target images:

Network 1. High-resolution Gridded and MoCo 4D-MRI.

Network 2. High-resolution Gridded 4D-MRI and MidP-MoCo images.

Network 3. Low-resolution Gridded 4D-MRI and M_x MVFs.

Network 4. Low-resolution Gridded 4D-MRI and M_y MVFs.

Network 5. Low-resolution Gridded 4D-MRI and M_z MVFs.

Input and target images had dimensions: 2D in-plane matrix-size \times respiratory phase, which was $256 \times 256 \times 16$ for networks 1-2, and $176 \times 176 \times 16$ for networks 3-5. For network 2, the same MidP-MoCo slice was applied for each of the 16 respiratory phases of the target image. Figure 6.1 displays example input and target images used to train network 1.

All networks were trained using the Adam optimizer (Kingma and Ba, 2014) with mean square error as the loss function. Hyper-parameters were set for the first network as: learning rate = 10^{-5} , epochs = 120 and batch-size = 1. Hyper-parameters were empirically optimised by monitoring training and validation loss curves (Figure 6.2a). Hyper-parameters were kept the same for networks 2-5, except batch-size was tuned to 4 for networks 3-5. Near-identical hyper-parameters were chosen as resulting training and validation loss curves exhibited similar behaviour to those corresponding to network 1. Training and validation loss curves for networks 2-3 are shown in Figure 6.2b-c.

For cross-validation purposes, Dracula was separately trained a sixth time (network 6) to learn the transformation between high-resolution Gridded and MoCo 4D-MRI using training and validation data from Group 2. Network 6 was trained in the same way as network 1.

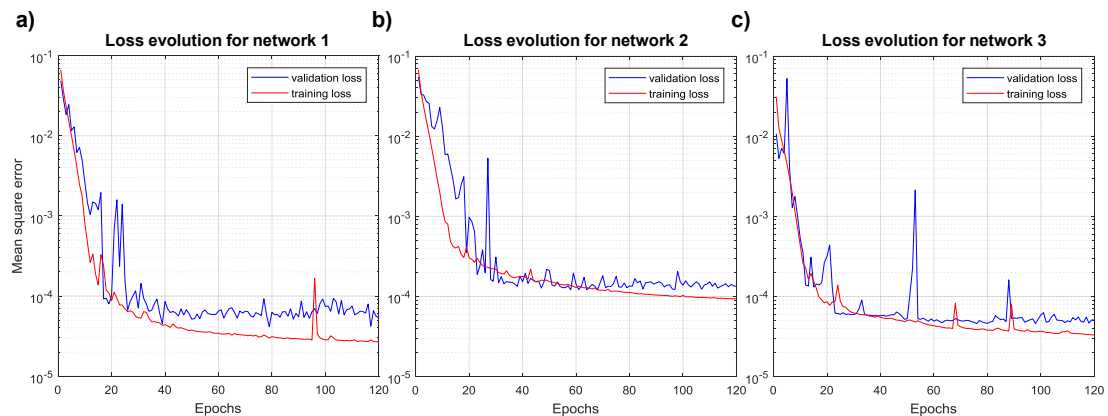


Figure 6.2: Training curves demonstrating the optimizer loss convergence for a) network 1, b) network 2 and c) network 3. In all cases, the validation loss was stable and had converged at 120 epochs.

Once trained, all networks were separately applied to reconstruct test data from Groups 1 (network 1-5) and 2 (network 6). Test data were previously unseen by the networks. All training and testing calculations were performed on an NVIDIA Quadro P6000 GPU with 24 GB memory.

The 4D output of network 2 was averaged over the respiratory phase dimension to obtain the high-resolution MidP-MoCo 3D image. Low-resolution 4D M_x , M_y and M_z matrices, calculated using networks 3-5, were combined to generate the 5D $M_{T_n}^{T_{MidP}}$ MVFs, which had dimensions: $176 \times 176 \times \text{number of slices} \times 16 \times 3$. The fifth dimension represented the x , y and z MVF components. Using cubic interpolation, the in-plane dimensions of all $M_{T_n}^{T_{MidP}}$ MVFs were upsampled to 256×256 and then applied to transform Dracula-reconstructed high-resolution MidP-MoCo images (i.e. averaged output of network 2) to all respiratory phases; onwards referred to as MidP-Warped 4D-MRI.

6.2.7 Verification of Dracula-reconstructed images

Dracula-reconstructed 4D MoCo, MidP-Warped and MidP-MoCo images were verified against the corresponding Gridded and MoCo images. Images were verified by qualitative visual assessment and in terms of the structural similarity index metric (SSIM) (Wang et al., 2004). The SSIM is scaled between 0 and 1, where

the SSIM of two images = 1, if they are identical in terms of contrast, luminance and structure. Dracula-reconstructed MidP-MoCo images were not compared to the MidP-Gridded images as no robust MidP-Gridded image could be calculated. This was because heavy streaking artefacts exhibited by Gridded 4D-MRI affected the quality of MidP reconstruction.

The exhalation and inhalation respiratory phase images of Gridded, MoCo and Dracula-reconstructed 4D-MRI (Groups 1 and 2: 8 patients and 4 healthy volunteers) were independently evaluated by a radiation oncologist and a radiologist. Both observers had at least five years experience reading abdominal and thoracic MR images. All images were anonymized and randomly presented to the observers in the RayStation software (v7.99, RaySearch Laboratories, Sweden). Images were scored using a five-point Likert scale: 0 - unreadable, 1 - poor, 2 - adequate (clinically acceptable for target and OAR delineation in RTP), 3 - good and 4 - excellent. Images were assessed in terms of: general image sharpness, general streaking artefacts, visibility of the tumour extent, visibility of the heart and visibility of the oesophagus. It was not possible to assess the visibility of the heart and the oesophagus for two abdominal cancer patients because these organs were outside the FOV. Moreover, the visibility of the tumour extent was not scored for three patients (two abdominal and one lung) because the GTV could not be localised without additional clinical information, e.g. a PET image. Independently for observers 1 and 2, scores given to each reconstruction algorithm were compared for statistical significance using a two-sided paired Wilcoxon signed-rank test ($p = 0.05$). Furthermore, mean and standard deviation scores over all test-subjects were evaluated for each reconstruction algorithm.

Both observers delineated the GTV on five out of eight patient data to enable a comparison of the tumour motion range contained in the 4D Gridded, MoCo and Dracula-reconstructed images. As described above, the GTV could not be localised in the images of three patients without additional clinical information. For each patient, the tumour motion range contained in the Gridded images was calculated as the Euclidean distance (see equation 3.4) between the GTV

iso-centres in the exhalation and inhalation Gridded images. Tumour motion ranges contained in MoCo and Dracula-reconstructed images were calculated in the same way as for the Gridded images. The resulting tumour motion ranges were evaluated using the same statistical analyses as for the above-described Likert scores.

6.3 Results

6.3.1 Dracula-reconstructed MoCo 4D-MRI

Dracula networks 1 and 6 were each trained in approximately 11 days and both required less than 28 seconds to reconstruct high spatio-temporal resolution MoCo 4D-MRI (voxel-size $\approx 1.25 \times 1.25 \times 3.30$ mm³, 16 respiratory phases) from Gridded 4D-MRI. For all 12 subjects in the test data, Dracula-reconstructed image appearance was qualitatively similar to the MoCo images but exhibited a slight loss of high frequency structures (e.g. small lung vessels). Figure 6.3 shows an example comparison between Gridded, Dracula-reconstructed and MoCo images for one lung cancer patient. In this example, heart and tumour extent are similarly visible in the Dracula-reconstructed and MoCo images.

The average SSIM value (mean and standard deviation) between Dracula-reconstructed and MoCo 4D-MRI was 0.99 ± 0.005 , which was greatly increased when compared to the corresponding Gridded and MoCo SSIM value: 0.72 ± 0.12 .

Table 6.2 summarises the scores assigned by the two observers to the Gridded, Dracula-reconstructed and MoCo inhalation and exhalation images. For all metrics, Dracula-reconstructed images were awarded significantly higher scores by both observers when compared to those assigned to the Gridded images; except by Observer 2 for the delineation of tumour extent metric ($p = 0.06$). The Gridded images were clinically unacceptable as the majority of the scores were on average < 2 . In contrast, Dracula-reconstructed images were reported by both

observers to be more than clinically acceptable (mean scores > 2) for all metrics except one; the visibility of the oesophagus metric was found to be clinically unacceptable by observer 2 (mean score of 1.75). Although clinically acceptable, Dracula-reconstructed images were assigned significantly lower scores than the MoCo images for most metrics. Scores recorded for the delineation of tumour extent (Observers 1 and 2) and oesophagus visibility metrics (Observer 1) were not significantly different when comparing the Dracula-reconstructed and MoCo images.

Table 6.2 additionally displays the average tumour motion ranges obtained from the GTV delineations. Minor differences between the tumour motion ranges calculated from the Gridded, Dracula-reconstructed and MoCo images were observed but were not significant.

6.3.2 Dracula-reconstructed MidP-MoCo images

Dracula network 2 was applied to reconstruct high-resolution MidP-MoCo images from the Gridded 4D-MRI test data of Group 1. Training and reconstruction took approximately 11 days and 28 seconds, respectively. The 28 second reconstruction time included the additional 50 ms required to average the 4D image output by network 2. As demonstrated for an example lung cancer patient in Figure 6.4, the appearance of Dracula-reconstructed MidP-MoCo images exhibited good visual agreement with the corresponding MidP-MoCo images. In this example, the severity of streaking artefacts in the Dracula-reconstructed image was greatly reduced when compared to the exhalation respiratory phase image of Gridded 4D-MRI. Similarly to section 6.3.1, Dracula-reconstructed images suffered from minor blurring and loss of high-detail information. Dracula-reconstructed MidP-MoCo images had a high (mean and standard deviation) SSIM value with the MidP-MoCo images: 0.97 ± 0.04 .

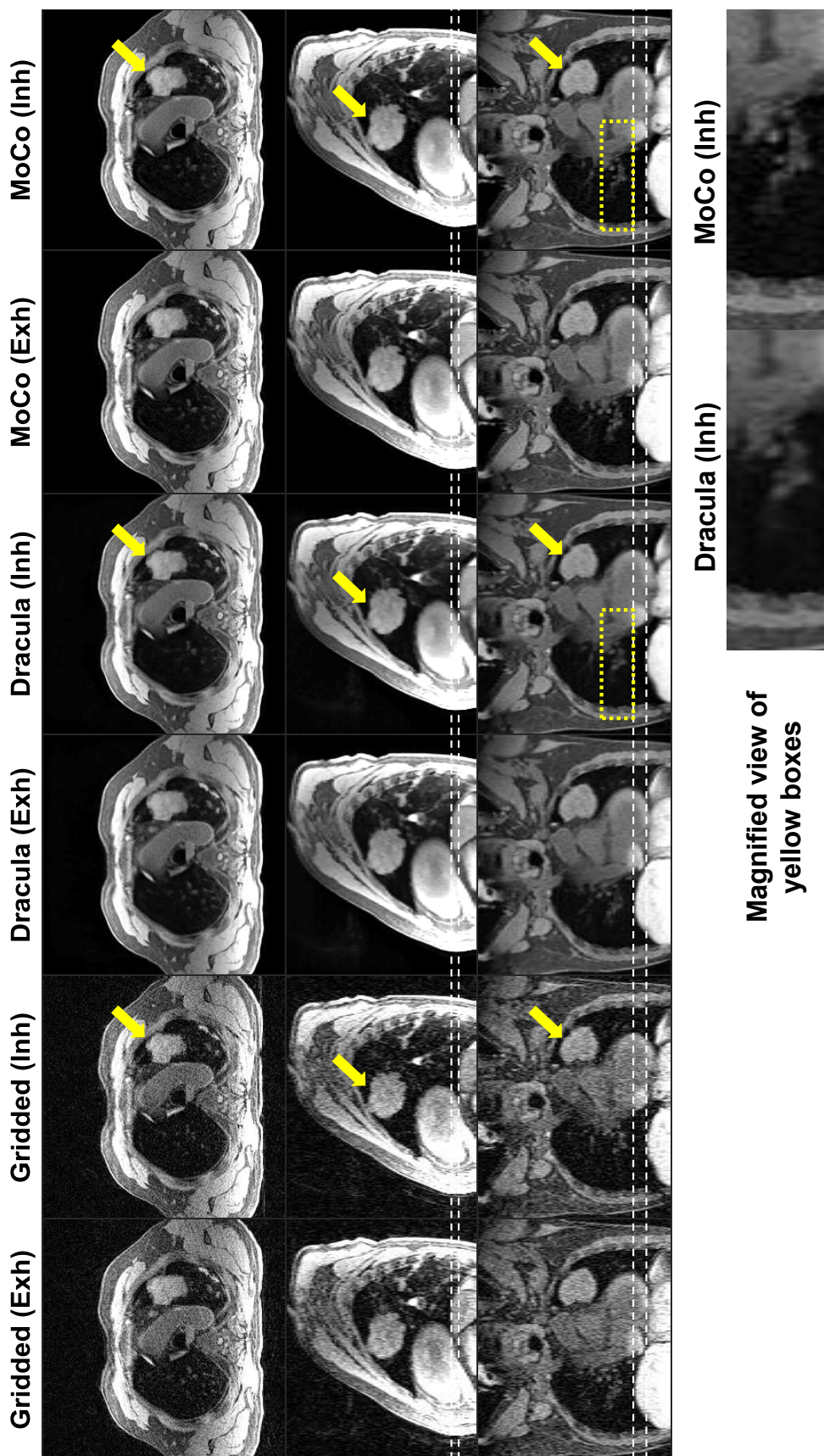


Figure 6.3: Comparison of the Gridded, Dracula-reconstructed (Dracula) and joint MoCo-HDTV (MoCo) reconstructed images for a lung cancer patient. Dracula restores image quality in a comparable manner to the joint MoCo-HDTV reconstruction with only minor blurring; e.g. see the magnified view of the region surrounded by the yellow boxes. White dashed lines aid comparison of the diaphragm position. Yellow arrows point to the tumour site. Exh: exhalation; Inh: inhalation.

Table 6.2: Average scores and range of tumour motion values obtained for the Gridded, Dracula and joint MoCo-HDTV (MoCo) reconstructed images. Mean and standard deviation values were generated following a blinded study of eight patients and four healthy volunteers by two experienced observers.

Reconstruction algorithm	Gridded		Dracula		MoCo	
	1	2	1	2	1	2
General image sharpness (0-4)	1.71 ± 1.04	0.92 ± 0.58	2.96 ± 0.75	2.29 ± 0.91	3.88 ± 0.34	3.13 ± 0.90
General streaking artefacts (0-4)	0.96 ± 0.20	1.00 ± 0.72	2.83 ± 0.56	3.04 ± 0.95	3.50 ± 0.51	3.71 ± 0.55
Delineation of tumour extent (0-4)	1.60 ± 0.50	1.11 ± 0.33	3.40 ± 0.69	2.22 ± 1.30	3.90 ± 0.32	3.56 ± 0.53
Heart visibility (0-4)	2.45 ± 0.83	1.30 ± 0.57	3.25 ± 0.64	2.70 ± 1.03	3.95 ± 0.22	3.50 ± 0.69
Oesophagus visibility (0-4)	1.25 ± 0.64	0.45 ± 0.83	2.55 ± 0.76	1.75 ± 1.02	3.00 ± 0.56	3.10 ± 0.72
Range of tumour motion (mm)	3.60 ± 1.96	5.26 ± 2.56	3.49 ± 1.15	8.40 ± 5.51	2.26 ± 1.06	3.54 ± 1.75

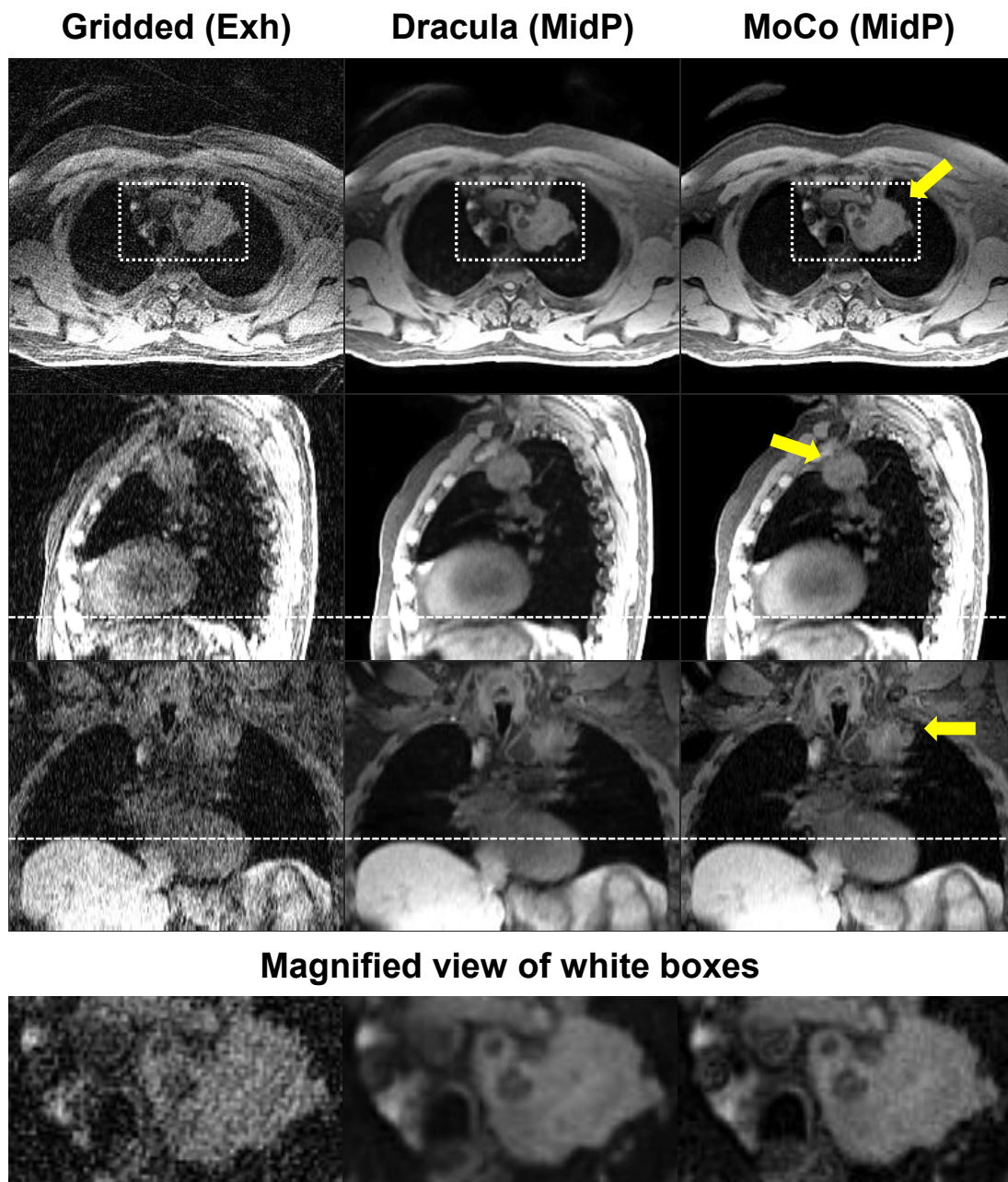


Figure 6.4: An example comparison of 4D Gridded (exhalation phase), Dracula-reconstructed midposition (Dracula) and joint MoCo-HDTV-reconstructed midposition (MoCo) images for one lung cancer patient. Apart from minor blurring, the appearance of the Dracula and MoCo images are similar. Magnified views of the tumour site enclosed by the white boxes facilitate visualisation of minor blurring. White dashed lines aid comparison of the diaphragm surface positions. Yellow arrows point to the tumour site. Exh: exhalation; MidP: midposition.

6.3.3 Dracula-reconstructed MidP-Warped 4D-MRI

Dracula networks 3, 4 and 5 were separately applied to Gridded 4D-MRI test data of Group 1 to obtain low-resolution M_x , M_y and M_z component MVFs, respectively. Each network took approximately four days to train and less than 14 seconds to reconstruct a given MVF component. Using the resulting MVFs, MidP-Warped 4D-MRI were obtained by transforming each Dracula-reconstructed MidP-MoCo image to all respiratory phases, which required 47-56 seconds.

MidP-Warped 4D-MRI had average (mean and standard deviation) SSIM values of 0.98 ± 0.005 and 0.77 ± 0.009 with MoCo and Gridded 4D-MRI, respectively. Similarly to sections 6.3.1 and 6.3.2, high visual agreement was found between MidP-Warped and MoCo 4D-MRI. An example comparison between Gridded, MidP-Warped and MoCo 4D-MRI is displayed in Figure 6.5. In this example, diaphragm surface positions are similar in corresponding respiratory phases of all displayed images.

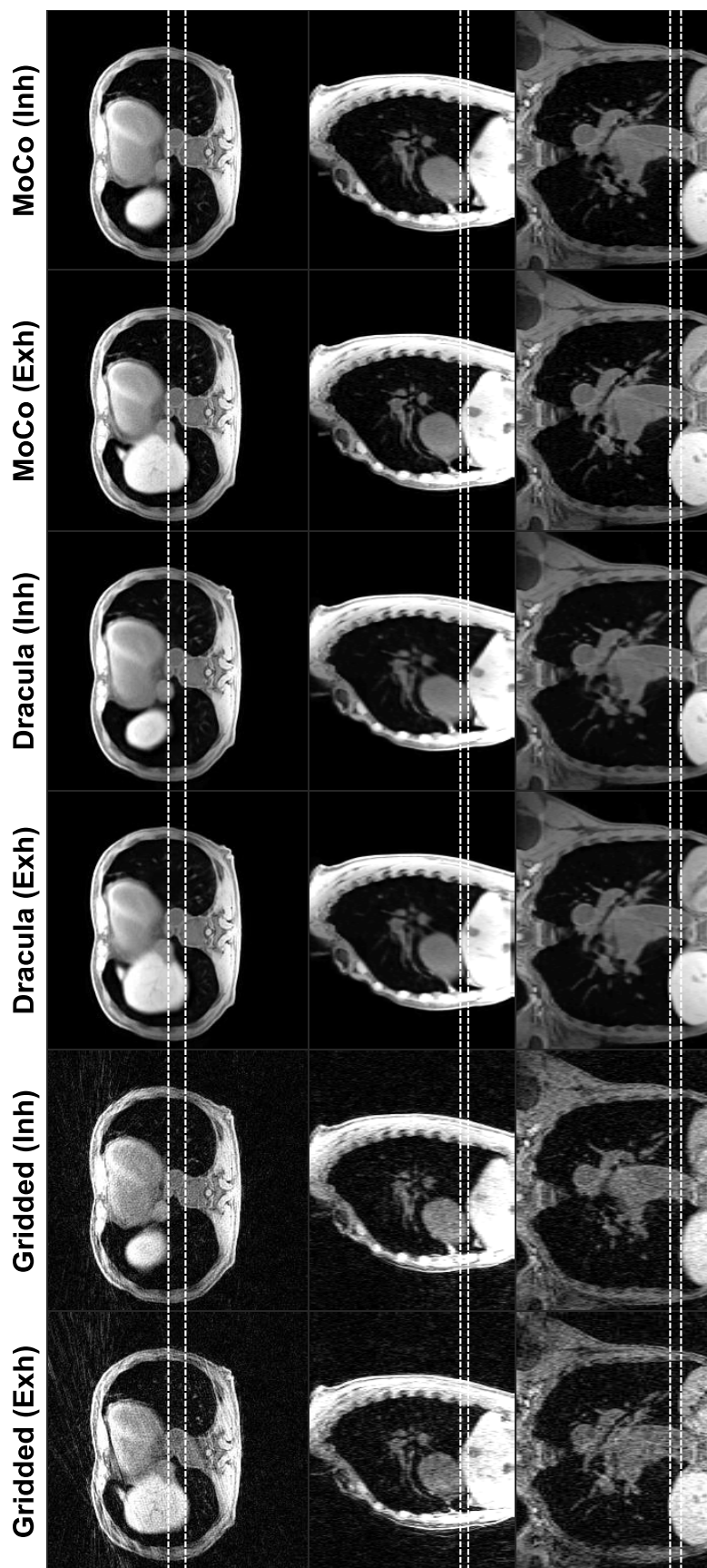


Figure 6.5: A comparison of the exhalation (Exh) and inhalation (Inh) respiratory phase images of Gridded, MidP-Warped (Dracula) and joint MoCo-HDTV-reconstructed (MoCo) 4D-MRI. Dracula images show high qualitative agreement with the MoCo images. Dashed white lines assist visualisation of diaphragm surface positions.

6.4 Discussion

The first aim of this chapter was achieved by applying dCNNs to rapidly reconstruct 4D-T1w MRI, MidP-T1w MRI and MVFs from Gridded data (undersampled 4D-MRI). The presented Dracula neural network required less than 28 seconds to reconstruct 4D-T1w MRI, which was faster than state-of-the-art compressed sensing algorithms, such as GRASP (Feng et al., 2014, 2016) (≈ 10 minutes) and 4D joint MoCo-HDTV (Rank et al., 2017) (≈ 9 -12 hours). Separate instances of Dracula were employed to reconstruct high-resolution MidP-T1w MRI and low-resolution $M_{T_n}^{T_{MidP}}$ MVFs (M_x , M_y and M_z components) within 28 and 42 seconds, respectively. Applying Dracula to directly calculate the MidP image (network 2) or the $M_{T_n}^{T_{MidP}}$ MVFs (networks 3-5) took less time compared to sequential application of Dracula network 1 and the MidP algorithm (≈ 25 -30 minutes using the chain method).

On an MR-linac, up-to-date 4D-T1w MRI, MidP-T1w MRI and $M_{T_n}^{T_{MidP}}$ MVFs could be quickly reconstructed using Dracula to support on-line adaptive treatment planning. Several alternative approaches to apply 4D/MidP-MRI in on-line MR-linac workflows were introduced in section 1.4.4.

Dracula-reconstructed MRI and MVFs could be integrated into modified implementations of the MVFP (Chapter 3) and Dixon-Spine-Lung (Chapter 5) methods to drastically accelerate reconstruction of 4D-T2w MRI and 4D-sCT. For instance, 4D-T2w MRI could be obtained by first registering 3D-T2w MRI to Dracula-reconstructed MidP-T1w MRI and then by transforming the registered 3D-T2w image to all respiratory phases using the $M_{T_n}^{T_{MidP}}$ MVFs. Modifying the MVFP workflow to employ Dracula-reconstructed MidP-MRI and MVFs would circumvent long calculation time needed to reconstruct MoCo 4D-MRI and also bypass the 25-30 minutes processing time required to execute the chain method; see section 3.2.4. Alternatively, the MVFP method could be accelerated by replacing MoCo 4D-MRI with Dracula-reconstructed 4D-MRI. Yet, several minutes would still be required to process 4D-MRI using the chain method. The above-described

modifications could also be applied to speed-up the Dixon-Spine-Lung method.

A U-net architecture (Ronneberger et al., 2015) was chosen based on the study by (Han et al., 2018), which demonstrated the feasibility of applying a 2D U-net to reduce radial streaking artefacts exhibited by undersampled 2D-T1w MRI. Unlike in (Han et al., 2018), a 3D implementation of the U-net architecture (Çiçek et al., 2016) was employed for deep learning-based image reconstruction. Applying a 3D rather than 2D U-net was inspired by modern compressed sensing-based 4D-MRI algorithms (Feng et al., 2014, 2016; Rank et al., 2017) which exploit information in both the spatial and temporal domains to reconstruct heavily undersampled data. One disadvantage of the implemented 3D U-net was that spatio-temporal information from adjacent slices could not be harnessed for image reconstruction. In principle, spatio-temporal information from neighbouring slices could be accessed using a 4D U-net architecture. However, in the presented work it was not possible to implement a 4D U-net architecture due to GPU memory constraints.

Four-dimensional MRI, MidP images and MVFs, obtained using the joint MoCo-HDTV and NiftyReg algorithms, contained errors originating from inaccuracies in non-rigid registration and from slight over-regularisation of respiratory motion. The errors are expected to manifest in Dracula-reconstructed images and MVFs, as Dracula is hypothesised to have learnt the errors in the joint MoCo-HDTV and NiftyReg-calculated data during the training process. It was necessary to use the joint MoCo-HDTV and NiftyReg-calculated data as training targets in order to conform with the implemented U-net architecture. Alternative deep learning techniques might permit higher quality 4D-MRI, MidP-MRI and MVFs to be obtained. For instance, the convolutional layers in Dracula might be interleaved with data consistency layers using a deep cascading approach (Schlemper et al., 2017). Implementation of data consistency layers should reduce errors by promoting data fidelity with the Gridded or raw data. In a separate technique, the joint MoCo-HDTV algorithm might be unrolled into a variational network (Hammernik et al., 2018). Treating the joint MoCo-HDTV algorithm as

a variational network might enable MVFs (applied for reconstruction purposes; see equation 2.43) to be directly calculated without requiring a separate DIR algorithm, which might result in reduced errors.

Network hyper-parameters were optimised by assessing the training and validation loss curves resulting from different hyper-parameter settings. For the chosen hyper-parameters, the validation loss curves approached stable mean square error values at epoch 120 and exhibited only minor differences with the corresponding training loss curves. Whilst the training loss curves had not fully converged at epoch 120, the training processes were stopped as the associated validation loss curves were stable. It is expected that further training (i.e. epochs > 120) might result in increased validation loss values and overfitting. This hypothesis was not tested due to the considerable time required to train each network. The minor differences between training and validation loss values at epoch 120 suggests a good fit. Alternatively, the minor differences might indicate that the training data were not fully representative of the validation data, for instance due to an insufficient quantity of training data or class imbalance. To reduce class imbalance, the training, validation and test data sets were, prior to training, pseudo-randomly sorted to contain approximately equivalent ratios between different populations.

The second aim of this chapter was to verify Dracula-reconstructed MRI and MVFs, which was met by comparison against Gridded and MoCo MRI.

Exhalation and inhalation respiratory phase images from Gridded, Dracula-reconstructed and MoCo 4D-MRI were visually assessed by two experienced observers. Both observers agreed that the MoCo images had the highest overall image quality as the assigned scores were on average between 3.0-4.0 for all metrics. Compared to the MoCo images, Dracula-reconstructed images were given lower scores for all metrics; scores had average values in the range 1.8-3.4. Both observers reported that minor blurring and residual streaking artefacts exhibited by Dracula-reconstructed images were responsible not only for general loss of image quality (i.e. lower scores for general image sharpness and streaking) but also for obfuscating the tumour site and OARs (i.e. lower scores for visibility of

the heart, oesophagus and tumour-extent). Nevertheless, Dracula-reconstructed images were considered clinically acceptable for contouring in RTP as the majority of scores were on average greater than 2.0. In contrast, the observers agreed that the Gridded images were clinically unacceptable for contouring purposes; assigned scores were on average between 0.5-2.5 for all metrics. The calculated ranges of tumour motion were not significantly different between the Gridded, Dracula-reconstructed and MoCo images.

Dracula-reconstructed images had good and excellent agreement in average SSIM values with the Gridded (0.72) and MoCo (0.99) images, respectively. The SSIM results are roughly in keeping with the scores reported by the observers.

Unlike the Gridded and 4D joint MoCo-HDTV reconstructions, Dracula enables 4D-MRI to be calculated with clinically acceptable image quality in a short time-frame. Therefore, compared to Gridded and MoCo 4D-MRI, Dracula-reconstructed 4D-MRI is best-suited for on-line application in an MR-linac workflow. One limitation of the validation study was the subjective aspect of the image scoring and target delineation analyses. Greater numbers of observers might improve the accuracy of the assigned scores and calculated tumour motion ranges.

Similarly to Dracula-reconstructed 4D-MRI, Dracula-reconstructed MidP-MoCo images exhibited minor blurring and residual streaking artefacts when compared to corresponding MidP-MoCo images. Furthermore, Dracula-reconstructed MidP-MoCo images had excellent agreement in terms of the SSIM (average value: 0.97) with the MidP-MoCo images. The overall high agreement between Dracula and joint MoCo-HDTV-reconstructed MidP-MoCo images demonstrates the feasibility of rapidly calculating good-quality MidP-T1w MRI from Gridded data.

Good qualitative agreement was found, e.g. in diaphragm surface positions, when comparing the exhalation and inhalation respiratory phase images of MidP-Warped and MoCo 4D-MRI. In addition, a high average SSIM value of 0.98 was calculated between MidP-Warped and MoCo 4D-MRI. Good agreement in image appearance and structural similarity indicates that Dracula-reconstructed low-resolution MVFs can accurately represent respiratory motion information

contained in MoCo 4D-MRI. Motion vector fields were reconstructed at low-resolution to minimise the overall processing time required to calculate MidP-Warped 4D-MRI (≈ 2 minutes). Superior-quality MidP-Warped 4D-MRI could be obtained using high-resolution MVFs but would require ≈ 2 minutes and 42 seconds for reconstruction.

6.5 Conclusion

Six Dracula neural networks were separately trained and applied to reconstruct 4D-T1w MRI, MidP-T1w MRI and MVFs from Gridded data in only 28, 28 and 42 seconds, respectively. Dracula-reconstructed 4D-T1w MRI and MidP-T1w MRI had excellent agreement with corresponding 4D joint MoCo-HDTV-reconstructed MRI in terms of the SSIM, which was on average > 0.97 in all comparisons. In a blinded observer study, Dracula-reconstructed 4D-T1w MRI were considered clinically acceptable for target and OAR delineation. Dracula-reconstructed MVFs were found to accurately represent respiratory motion information contained in 4D joint MoCo-HDTV-reconstructed MRI. Rapidly calculated 4D-T1w MRI, MidP-T1w MRI and MVFs could provide up-to-date information to support on-line radiotherapy treatment planning in thoracic MR-linac workflows.

Chapter 7

Comparison of T2-weighted 4D-MRI methods for application on an MR-linac

In this chapter, a comparison is performed between 4D-T2w MRI for use in an MR-linac workflow, which were reconstructed using a phase binning algorithm, an optimised version of the super-resolution approach and a Dracula-accelerated implementation of the MVFP method. Amongst other metrics, 4D-T2w MRI were compared in terms of image appearance and contained respiratory motion range.

7.1 Introduction

In Chapters 3 and 4, the MVFP method and a super-resolution approach were introduced to obtain 4D-T2w MRI. After qualitative comparison (see section 4.4), the super-resolution approach was found to be better suited for application in MRgRT due to use of standard clinical sequences for data acquisition and due to the comparatively short time required for acquisition and reconstruction (40 minutes). Yet, this time limits its on-line application on an MR-linac, as an acquisition-reconstruction time less than 5 minutes is desired (van de Lindt et al., 2018a). Super-resolution 4D-T2w images were also of limited use for target and OAR delineation by high levels of noise. High noise levels were a consequence of unconstrained optimisation of the iterative back-projection cost-function implemented for super-resolution reconstruction.

The prototype super-resolution implementation could be improved to overcome these limitations. For instance, noise levels could be reduced by regularising super-resolution reconstruction with a smoothing constraint (Van Reeth et al., 2012). Furthermore, reconstruction time could be reduced by applying GPU or parallel processing to speed-up execution of time-consuming modular components. On the acquisition side, the required acquisition time could be decreased by sampling the thoracic FOV with fewer slices, which would be possible using a sagittal and coronal acquisition strategy. Acquisition time could also be reduced by measuring fewer dynamics.

Long reconstruction time of 4D-T1w MRI (9-12 hours) prevents on-line application of the MVFP method in MR-linac workflows. In Chapter 6, the problem of long reconstruction time was overcome by training and applying a dCNN (i.e. Dracula) to rapidly reconstruct 4D-T1w MRI in approximately 28 seconds. Implementation of Dracula-reconstructed 4D-T1w MRI in the MVFP method might enable it to outperform the super-resolution approach for intra-fractional use on an MR-linac.

To date, 4D-T2w MRI has been obtained on an Elekta Unity MR-linac by

retrospectively sorting continuously acquired 2D-T2w slices using IRS based on the diaphragm position (van de Lindt et al., 2018a,b). In their approach, missing-data were estimated via a 4D interpolation algorithm (Garcia, 2010; Wang et al., 2012). Until the work presented in this chapter, no study had been performed to quantitatively compare different 4D-T2w MRI reconstruction techniques for use in an on-line MR-linac workflow. Previously, Li et al. (2017a) compared 4D-T2w MRI obtained using prospective and retrospective binning methods. Yet, only 4D-T2w MRI acquired on a diagnostic system were evaluated. In a separate study, van Kesteren et al. (2019) compared 4D-T2w MRI retrospectively generated using several variations of amplitude and phase binning. However, similarly to (Li et al., 2017a), 4D-T2w MRI were not acquired using an MR-linac. The aims of this chapter were therefore to:

1. Optimise the MVFP and super-resolution methods for the MR-linac use-case.
2. Apply the optimised methods and the existing approach by (van de Lindt et al., 2018a) to reconstruct data acquired on an MR-linac.
3. Compare resulting 4D-T2w MRI for intra-fractional application on an MR-linac.

7.2 Materials and methods

7.2.1 Data acquisition

Five healthy volunteers were scanned in free-breathing on a 1.5 T Elekta Unity MR-linac (Elekta AB, Stockholm, Sweden) with two separate single-shot TSE (SS-TSE) acquisitions. Before acquisition of each slice, a liver-dome navigator was obtained. Similarly to section 4.2.1, an interleaved slice ordering scheme was applied in each SS-TSE sequence. The slice ordering scheme was defined by the number of slices in the FOV (K) as: $(1, 1+\text{round}|\sqrt{K}|, 1+2\text{round}|\sqrt{K}|, \dots)$. Three of the volunteers were additionally scanned with a 3D T1w golden-angle

radial stack-of-stars spoiled gradient echo sequence and a 3D T2w multi-shot TSE sequence, which was gated to exhalation. More information regarding TSE and radial stack-of-stars sequences can be found in sections 2.1.3.4 and 2.2.3.1, respectively. An elevated coil holder (Elekta AB, Stockholm, Sweden) was employed to prevent deformation of the body contour by the 8-channel receive array. Figure 7.1 displays the experimental set-up used for image acquisition. Detailed acquisition parameters are displayed in Table 7.1.

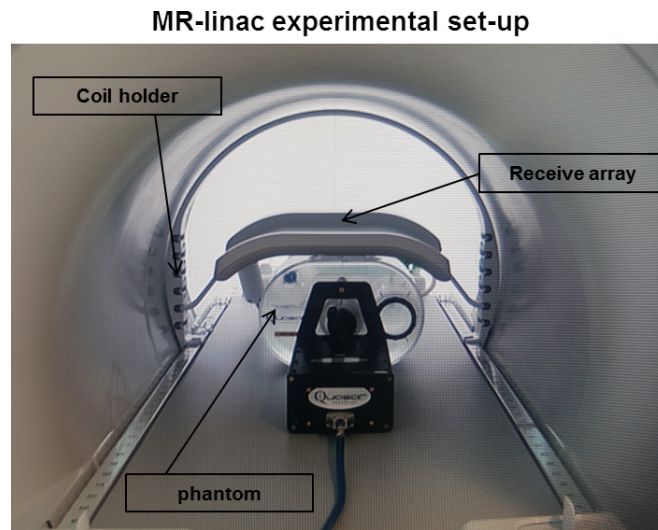


Figure 7.1: Experimental set-up used to acquire T1-weighted and T2-weighted MRI on the MR-linac, as demonstrated for the QUASARTM MRI-compatible respiratory motion phantom. The receive array is elevated above the phantom using a specially designed coil holder.

The intended radial stack-of-stars sequence was enabled on the MR-linac through unlocking research functionality with a patch developed in the Paradise pulse programming environment (release 5.1.3; Philips Medical Systems, Best, The Netherlands). In the patch, a trajectory ordering for 3D radial spoiled gradient echo acquisitions was enabled where all spokes along the partition dimension were consecutively acquired before rotating by the golden-angle (see section 2.2.3.1) (Block et al., 2014). Fat-suppression and partial Fourier along the partition dimension were also activated for this trajectory. Snap-shots of the implemented sequence and its settings are shown in Figure 7.2. In addition, a clinical science

key was activated to enable the gating acceptance window of the liver-dome navigator to be set at 100 %. Setting the acceptance window to 100 % permitted the liver-dome navigator to be acquired for the SS-TSE sequences without acting upon it. As a result, data were continuously acquired.

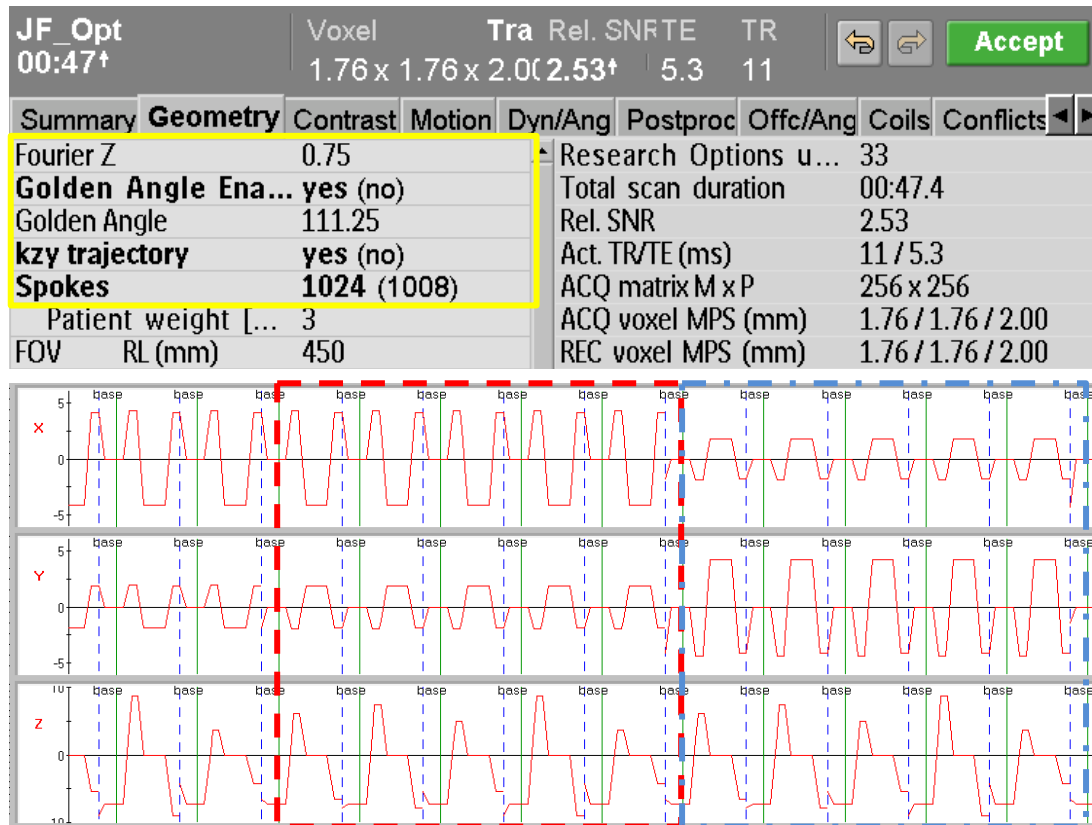


Figure 7.2: Top: Screen-shot of the modified MR-linac user-interface. Modifications (yellow-box) appear after selecting a 3D radial spoiled gradient echo sequence in the Contrast tab. Bottom: Snapshots of the X, Y and Z gradient waveform amplitudes for an example trajectory with five partitions. For a given angle (e.g. dashed red box), the same radially-projected spoke is measured for all five partitions. This is achieved by varying the Z gradient waveform, whilst keeping the X and Y gradient waveforms the same, between neighbouring partitions. Acquisition is repeated for subsequent angles (e.g. dashed blue-box), which requires alternative X and Y gradient waveforms.

Table 7.1: Acquisition parameters of the four sequences employed on the MR-linac. SS-TSE indicates single-shot turbo spin echo; NA, not applicable.

Parameter	Coronal SS-TSE	Sagittal SS-TSE	Radial	Gated TSE
No. volunteers	5	5	3	3
Orientation	Coronal	Sagittal	Axial	Axial
Echo train length	66 - 71	66	1	50
In-plane field-of-view, mm ²	264 × 384	264 × 384	384 × 384	384 × 384
No. slices	50	50 - 70	67 - 80	88
Voxel size, mm ³	1.5 × 1.5 × 5.0	1.5 × 1.5 × 5.0	1.5 × 1.5 × 3.0	1.5 × 1.5 × 3.0
Echo time, ms	93 - 101	93	2.0 - 2.2	159
Repetition time	*(3.4 - 3.6) s	*(3.4 - 4.2) s	(4.9 - 5.2) ms	1023 ms
Flip angle, °	90	90	8 - 12	90
Readout bandwidth, $\frac{Hz}{Pixel}$	588	588	618 - 857	574
Fat suppression	No	No	Yes	No
No. dynamics	10	10	NA	NA
No. spokes per slice	NA	NA	708 - 805	NA
Slice acquisition order	interleaved	interleaved	NA	NA
Acquisition time, min	5.7 - 6.0	5.7 - 7.0	6.3 - 8.5	9.0

* indicates effective repetition time.

7.2.2 Calculation of 4D-T2w MRI

Four-dimensional T2w MRI were calculated using phase binning and optimised implementations of the MVFP (Chapter 3) and super-resolution (Chapter 4) approaches. A 3D gradient non-linearity distortion correction was not applied to generated 4D-T2w MRI.

7.2.2.1 Phase binning

Four-dimensional T2w MRI were obtained by retrospectively sorting coronal SS-TSE dynamics using a similar phase binning approach to (van de Lindt et al., 2018a). Prior to binning, the 1D liver-dome navigator signal was read from a log file generated during image acquisition and then time-synced with the corresponding dynamics. An example navigator signal is shown in Figure 7.3. Dynamics were then sorted based on the phase of the time-synced navigator signal into eight respiratory bins (four exhalation and four inhalation) (Lu et al., 2006). Unlike in (van de Lindt et al., 2018a), multiple images assigned to the same respiratory bin were averaged and missing-data were set to zero. More information regarding phase binning can be found in section 2.2.1.2.

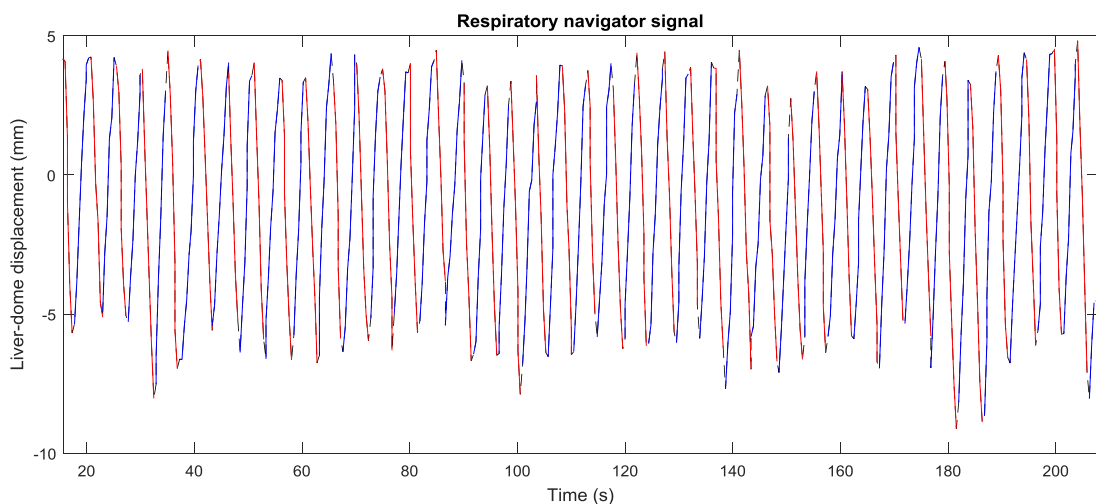


Figure 7.3: Snap-shot of the respiratory navigator signal obtained during a volunteer imaging study (coronal SS-TSE acquisition). Solid blue and red lines correspond to the exhalation and inhalation components of the respiratory navigator signal.

7.2.2.2 Optimising the super-resolution method

Four-dimensional T2w MRI were calculated from the coronal and sagittal SS-TSE dynamics using an optimised implementation of the super-resolution approach (Chapter 4). As mentioned in section 2.2.2.3, errors in the the respiratory surrogate signal applied for binning can lead to stitching artefacts in 4D-T2w MRI. The 1D liver-dome respiratory navigator signal was applied for binning, rather than the PRS utilised in the super-resolution binning workflow (section 4.2.2.1), because it did not exhibit phase-shift errors (Liu et al., 2014). Note that the PRS utilised in Chapter 4 contained phase-shift errors as it was calculated on a slice-by-slice basis. Employing the navigator signal for binning requiring time-syncing of the coronal and sagittal dynamics.

Trilateral regularisation (Chilla et al., 2017; Farsiu et al., 2004) was implemented to constrain the iterative back-projection optimisation process. To implement trilateral regularisation, a second term was added to the cost function described in equation 4.2:

$$C_{min} = \underset{S}{\operatorname{argmin}} \left(\sum_{k=1}^N \|H_k P_k G_k S - L_k\|^2 + \lambda \sum_{a=-2}^2 \sum_{b=-2}^2 \sum_{c=0}^2 \alpha^{|a|+|b|+|c|} |S - R_x^a R_y^b R_z^c S| \right) \quad (7.1)$$

Where R denotes the shift matrix operator, which shifts S by a , b and c pixels in the x , y and z directions; λ and α represent weighting coefficients. Inclusion of trilateral regularisation results in an additional term in the iterative back-projection solution of expression 4.3, which was adapted from (Chilla et al., 2017; Farsiu et al., 2004) as:

$$S_{n+1} = S_n - \frac{1}{N} \sum_{k=1}^N (G_k^+ P_k^+ H_k^+ [H_k P_k G_k S_n - L_k]) + \lambda \sum_{a=-2}^2 \sum_{b=-2}^2 \sum_{c=0}^2 \alpha^{|a|+|b|+|c|} (I - R_z^{-c} R_y^{-b} R_x^{-a}) \operatorname{sign}(S_n - R_x^a R_y^b R_z^c S_n) \quad (7.2)$$

Where R_x^{-a} , R_y^{-b} and R_z^{-c} represent the reverse shift operators. Furthermore, I is the identity operator. Applying the modifications suggested in section 4.2.2.4 to expression 7.2, whilst accounting for the coronal and sagittal acquisition strategy, yields:

$$\begin{aligned}
S_{n+1} = S_n - \frac{1}{16} & \left(\sum_{k=1}^8 [P_C^+ H_C^+ (H_C P_C S_n - L_{Ck}) + P_S^+ H_S^+ (H_S P_S S_n - L_{Sk})] \right) \\
& + \lambda \sum_{a=-2}^2 \sum_{b=-2}^2 \sum_{c=0}^2 \alpha^{|a|+|b|+|c|} (I - R_z^{-c} R_y^{-b} R_x^{-a}) \text{sign}(S_n - R_x^a R_y^b R_z^c S_n)
\end{aligned} \tag{7.3}$$

In section 4.2.2.4, the deblurring operators were set to the identity ($P^+ = I$). Here, deblurring operators were instead applied to deconvolve the estimated high-resolution differences with the non-isotropic Gaussian point spread function of section 4.2.2.4. For deconvolution, the Lucy-Richardson algorithm was used with 5 iterations (Biggs and Andrews, 1997). Unlike in section 4.2.2.4, a coarser matrix of $1.5 \times 1.5 \times 1.5 \text{ mm}^3$ was employed for the super-resolution space. Furthermore, the super-resolution reconstructed MidP image (S_Ω) was estimated by iterating equation 7.3 until $\frac{\langle |S_{n+1} - S_n| \rangle}{\langle |S_1 - S_0| \rangle} < 0.001$, which required 12-16 iterations. In addition, MVFs used to transform the MidP S_Ω image to all respiratory phases were calculated from low-resolution coronal 4D-T2w MRI instead of low-resolution sagittal 4D-T2w MRI. Calculating super-resolution 4D-T2w MRI using motion information from low-resolution coronal 4D-T2w MRI enabled a direct comparison to phase-binned 4D-T2w MRI. The regularisation weightings α and λ were optimised in a subset of volunteers by visually assessing the quality of S_Ω generated using α and λ values in the ranges: ($0 < \alpha < 1$) and ($0 < \lambda \leq 0.04$). Regularisation values $\alpha = 0.7$ and $\lambda = 0.01$ were qualitatively found to provide a good compromise between reduction of noise and smoothing of fine structures (Figure 7.4).

Optimisation of trilateral regularisation weightings

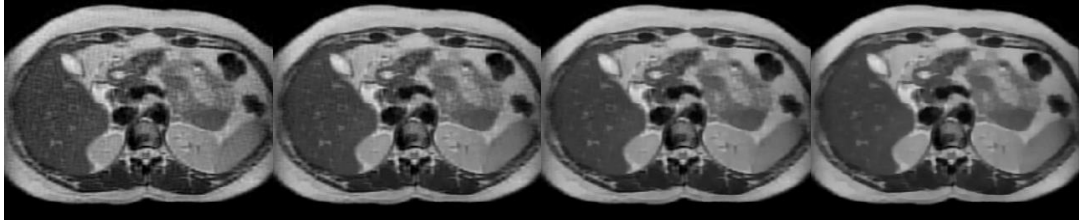
 $\alpha = 0.7; \lambda = 0.0$
 $\alpha = 0.7; \lambda = 0.01$
 $\alpha = 0.7; \lambda = 0.02$
 $\alpha = 0.7; \lambda = 0.04$


Figure 7.4: An example comparison of super-resolution reconstructed T2w MRI in midposition obtained using different regularisation weightings ($\alpha = 0.7; \lambda = 0 - 0.04$). The parameter values ($\alpha = 0.7; \lambda = 0.01$) provided a good compromise between noise reduction and over-regularisation of high frequency structures.

7.2.2.3 Optimising the motion vector field projection method

Four-dimensional T2w MRI were obtained using an optimised version of the MVFP method presented in Chapter 3. The reconstruction time of 4D-T1w MRI was drastically reduced to ≈ 28 seconds by replacing the 4D joint MoCo-HDTV algorithm with Dracula network 1; see Chapter 6 for more information. Furthermore, the time required to execute the chain method of section 3.2.4 was greatly reduced to 4-6 minutes by using a 4D-T1w image with lower spatio-temporal resolution ($1.5 \times 1.5 \times 3.0 \text{ mm}^3$; 16 respiratory phases) for input.

7.2.3 Comparison of 4D-T2w MRI

Four-dimensional T2w MRI calculated using the phase binning, Dracula-accelerated MVFP and optimised super-resolution methods were compared in terms of: qualitative image appearance, reconstruction time and number of respiratory phases. Furthermore, the range of liver-dome positions measured in each 4D-T2w MRI was compared to the displacement range recorded by the coronal SS-TSE 1D liver-dome navigator signal. Comparisons were made before and after removing outlier values in the navigator signal. Outliers in the navigator signal were determined as $1.5 \times$ the inter-quartile range above or below the mean amplitude value.

Liver-dome positions were calculated using an edge-detection method, which was previously described in section 3.2.5.1. The ROI for edge-detection was

chosen identically in all 4D-T2w MRI of each volunteer. Liver-dome positions were determined by averaging the results obtained from edge-detection in five coronal slices in each 4D-T2w MRI; coronal slices contained the diaphragm and were spaced 9 mm apart.

7.3 Results

Four-dimensional T2w MRI were reconstructed for five healthy volunteers using the described phase binning and optimised super-resolution approaches, which required calculation times of 4 seconds and 16.4 minutes, respectively. For three out of five volunteers, 4D-T2w MRI were additionally obtained using the Dracula-accelerated MVFP method, which took on average 5.6 minutes for reconstruction. As shown for two volunteers in Figure 7.6, super-resolution reconstructed 4D-T2w MRI exhibited the greatest through-plane image sharpness. Note that the axial orientation corresponded to the through-plane in the super-resolution images. In addition, 4D-T2w MRI obtained by phase binning suffered from severe data incompleteness artefacts. Compared to MVFP-generated 4D-T2w MRI (16 respiratory phases), super-resolution reconstructed and phase-binned 4D-T2w MRI contained half the number of respiratory phases.

Table 7.2 summarises the ranges of liver-dome positions calculated from 4D-T2w MRI and those extracted from the 1D liver-dome navigator signal, with and without outliers removed. Before outlier removal, differences between the range recorded by the navigator signal and the range extracted from MVFP-generated, super-resolution reconstructed and phase-binned 4D-T2w MRI were on average (mean and standard deviation over volunteers): -15.4 ± 10.7 , -8.4 ± 7.5 and -8.1 ± 6.6 mm, respectively. After outlier removal, the above mentioned differences were reduced to: -0.4 ± 2.8 , 0.6 ± 5.1 and 1.0 ± 6.7 mm. Figure 7.5 displays two examples comparing navigator waveforms before and after removal of outliers.

A good agreement of -0.32 ± 1.7 mm was found when comparing liver-dome positional ranges extracted from super-resolution reconstructed and phase-binned

4D-T2w MRI. However, the liver-dome positional range was lower in MVFP-generated 4D-T2w MRI by -3.4 ± 3.0 and -4.4 ± 4.3 mm, when compared to super-resolution reconstructed and phase-binned 4D-T2w MRI, respectively. The overall small differences in liver-dome positional ranges between MVFP-generated, super-resolution reconstructed and phase-binned 4D-T2w MRI is supported by good visual agreement of liver-dome positions in the example images presented in Figure 7.6.

Table 7.2: Comparison of the liver-dome positional ranges calculated from 4D-T2w MRI to the amplitude ranges extracted from the 1D liver-dome navigator signal, with and without outliers removed. All results shown are in mm. MVFP indicates motion vector field projection; SR, super-resolution; PB, phase binning; 1D Nav, 1D liver-dome navigator; NA, not applicable.

Volunteer	MVFP	SR	PB	1D Nav _{With}	1D Nav _{Without}
1	17.4	18.2	19.7	24.0	17.8
2	9.4	12.0	11.0	21.6	12.5
3	17.1	23.8	26.4	44.4	14.7
4	NA	13.0	13.1	13.9	13.9
5	NA	19.1	17.5	24.4	24.0

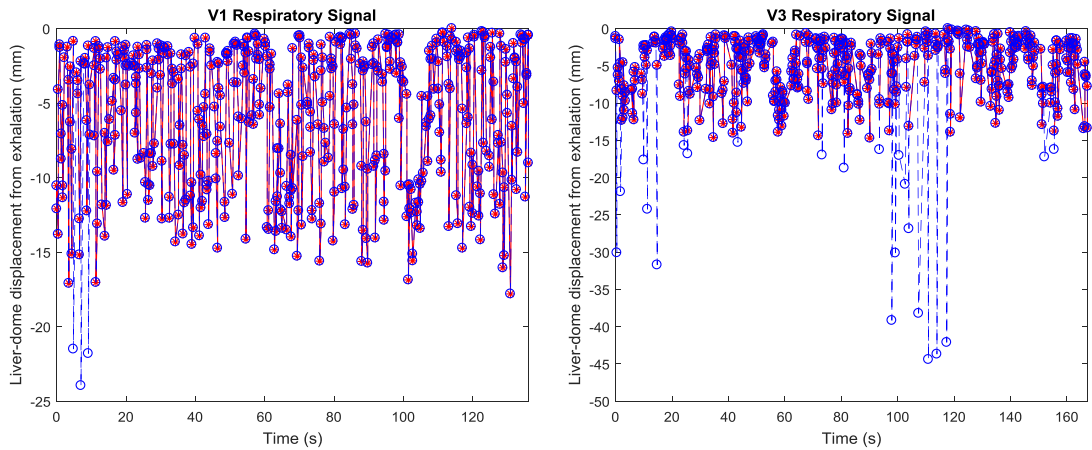


Figure 7.5: An example comparison of 1D liver-dome respiratory navigator signals for volunteers 1 (V1) and 3 (V3), before (dashed blue line) and after (solid red line) removal of outliers.

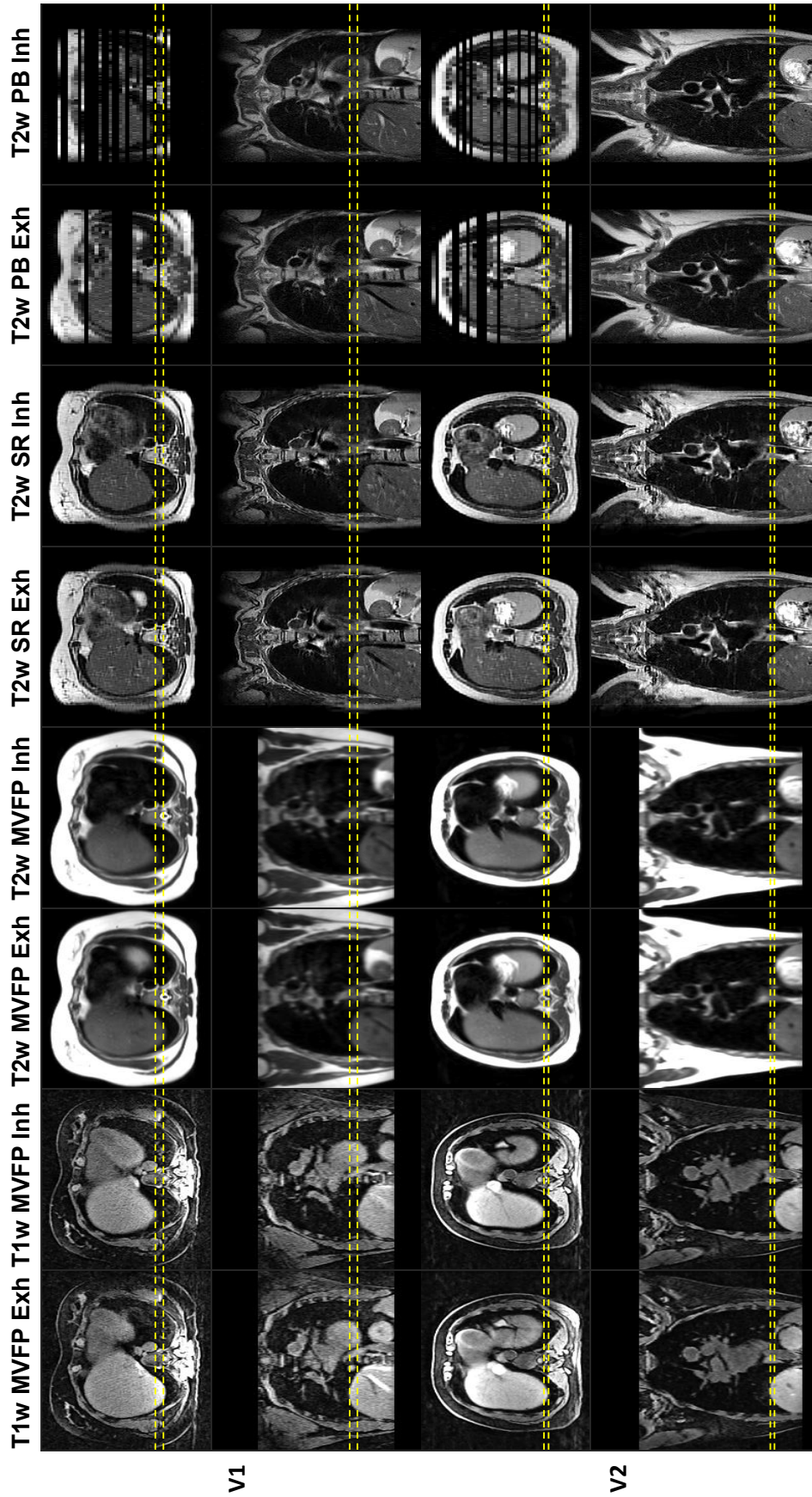


Figure 7.6: Comparison of the exhalation (Exh) and inhalation (Inh) respiratory phases of 4D-MRI obtained on an MR-linac for volunteers one (V1) and two (V2). Dashed yellow lines facilitate comparison of motion-extent between 4D-MRI. T1w indicates T1-weighted; T2w, T2-weighted; MVFP, motion vector field projection; SR, super-resolution; PB, phase binning. Black stripes in 4D-T2w MRI generated by phase binning illustrate data incompleteness artefacts.

7.4 Discussion

The first aim of this chapter was met by optimising both the MVFP and super-resolution methods for on-line application on an MR-linac. Run-time of the MVFP method was reduced by applying Dracula network 1 to rapidly reconstruct high-quality 4D-T1w MRI in ≈ 28 seconds. Compared to 4D-T1w MRI described in Chapter 3, Dracula-reconstructed 4D-T1w MRI had a lower spatio-temporal resolution, and consequently required only 4-6 minutes to be processed by the chain method.

The super-resolution approach was improved by applying trilateral regularisation to constrain optimisation of its iterative back-projection component. Trilateral regularisation resulted in reduced levels of noise in super-resolution reconstructed 4D-T2w MRI. The super-resolution approach was also optimised in terms of calculation time, which was, on average, reduced from 23.0 (in Chapter 4) to 16.4 minutes through extensive code and parameter optimisation. In particular, an isotropic matrix with 1.5 mm spacing was employed for the super-resolution space. On the acquisition side, acquisition time was reduced by acquiring only 10 SS-TSE dynamics in both the coronal and sagittal orientations.

The second aim of this chapter was to apply the two optimised methods (MVFP and super-resolution) and the approach by (van de Lindt et al., 2018a) to reconstruct 4D-T2w MRI from MR-linac data, which was achieved with drawbacks. For instance, 3D gradient non-linearity geometrical distortion correction was not applied to 4D-T2w MRI. Furthermore, only a limited number of healthy volunteer data sets were acquired, which might not be representative of lung cancer patients. In addition, two modifications were made to the phase binning approach of (van de Lindt et al., 2018a). Firstly, the diaphragm-based IRS was replaced by the 1D liver-dome navigator signal to enable all dynamics, including those that did not exhibit the diaphragm (e.g. a sagittal slice passing through the spine), to be sorted. Secondly, missing-data were set to zero as the 4D interpolation algorithm (Garcia, 2010; Wang et al., 2012) applied in (van de Lindt et al., 2018a) resulted in

heavily blurred images when tested on phase-binned 4D-T2w MRI reconstructed from only 10 dynamics.

The final chapter aim was met by comparing MVFP-generated, super-resolution reconstructed and phase-binned 4D-T2w MRI for the MR-linac use-case. The time required for acquisition and reconstruction of 4D-T2w MRI was on average: 22.0, 28.8 and 6.1 minutes for the MVFP, super-resolution and phase binning methods, respectively. Phase-binned 4D-T2w MRI were rapidly obtained, yet exhibited severe data incompleteness artefacts and thick slices. Data incompleteness artefacts could be reduced at the cost of increased acquisition time by acquiring a greater number of dynamics (Liu et al., 2015b; van Kesteren et al., 2019). Thinner slices could be acquired e.g. 3 mm, but would require an increased acquisition time to cover the same FOV.

Super-resolution reconstructed 4D-T2w MRI did not exhibit data incompleteness artefacts or thick slices. Yet, it required a clinically infeasible time for acquisition and reconstruction. The long acquisition-reconstruction time might be reduced by restricting sagittal acquisition, and consequently super-resolution reconstruction, to the FOV covering the PTV and adjacent OARs.

Four-dimensional T2w MRI obtained using the MVFP method exhibited good spatio-temporal resolution and no missing-data. However, its acquisition-reconstruction time currently limits its on-line use on an MR-linac. The execution time of the MVFP method could be further accelerated using the method previously suggested in section 6.4. In the suggested approach, 3D-T2w MRI is first registered to Dracula-reconstructed MidP-T1w MRI. Four-dimensional T2w MRI is then obtained by transforming the registered 3D-T2w image (i.e. MidP-T2w MRI) to all other respiratory phases using the Dracula-reconstructed $M_{T_n}^{T_{MidP}}$ MVFs.

As discussed by van de Lindt et al. (2018a), 4D-MRI should be acquired and reconstructed in less than 5 minutes when intended for on-line application in an MR-linac workflow. A treatment plan based on 4D-MRI, requiring a combined acquisition-reconstruction time greater than 5 minutes, may not be representative of the patient during irradiation. This is because the patient's

anatomical positions and respiratory pattern can change between 4D-MRI data acquisition and treatment delivery, particularly over long time periods. An unrepresentative treatment plan could result in undesirable dose delivered to OARs and under-dosage of the PTV. When comparing the optimised MVFP, super-resolution and phase-binning approaches, the MVFP method was found to provide the best compromise between combined acquisition-reconstruction time and image quality. However, further technical improvements are necessary to reduce its current acquisition-reconstruction time of 22 minutes to a clinically appropriate time-frame of approximately 5 minutes.

The range of liver-dome positions calculated from each 4D-T2w image was compared to the range recorded by the liver-dome navigator signal, which was obtained during the coronal SS-TSE acquisitions. Good agreement was found between the navigator signal range (after outlier removal) and that extracted from MVFP-generated 4D-T2w MRI, which suggests that MVFP-generated 4D-T2w MRI were representative of the average respiratory cycle. On average, the range of liver-dome positions calculated from MVFP-generated 4D-T2w MRI underestimated that determined from phase-binned and super-resolution reconstructed 4D-T2w MRI. This relative underestimation of the range in liver-dome positions might be due to changes in respiratory pattern between the radial gradient echo and coronal SS-TSE acquisitions. The relative underestimation might also be a consequence of temporal regularisation learnt by Dracula from the 4D joint MoCo-HDTV algorithm. Alternatively, 4D-T2w MRI calculated using the phase binning or super-resolution methods might better represent outlier respiratory motion information, such as deep inspiration or coughing. In the case of MidP planning (see section 1.3.1), defining PTV margins using average respiratory motion information might enable the best compromise between over-estimation and under-estimation of margin extent. As discussed in section 1.4.2, identifying which 4D-MRI technique best represents the motion of treatment targets and OARs is currently an open question in lung RTP (Bainbridge et al., 2017).

7.5 Conclusion

The MVFP, super-resolution and phase binning methods were optimised and applied to reconstruct 4D-T2w MRI from data acquired on an MR-linac. The presented comparison between resulting 4D-T2w MRI suggests that the MVFP method is currently the most optimal approach to obtain 4D-T2w MRI for on-line application on an MR-linac, as it offers the best compromise between: spatio-temporal resolution, data completeness and acquisition-reconstruction time. However, further methodological improvements are required to reduce the acquisition-reconstruction time of the MVFP method to a clinical time-frame. The motion range calculated from MVFP-generated 4D-T2w MRI exhibited good agreement with that extracted from the navigator signal after outlier removal. MVFP-generated 4D-T2w MRI were therefore representative of the average respiratory cycle and consequently might be well suited for MidP planning.

Chapter 8

Discussion

This chapter summarises the key findings of this thesis and their clinical relevance. Future directions in which the presented work could be extended are also described.

8.1 Summary of thesis studies

Chapter 3 describes the development and application of the MVFP method to obtain geometrically accurate 4D-T2w MRI with high spatio-temporal resolution ($1.5 \times 1.5 \times 3.0 \text{ mm}^3$, 20 respiratory phases). In the MVFP method, 3D-T2w MRI was first registered to the closest matching respiratory phase of 4D-T1w MRI. Afterwards, MVFs were calculated by registering respiratory phases of 4D-T1w MRI and then applied to transform the above-registered 3D-T2w MRI to all respiratory phases. Resulting 4D-T2w MRI facilitated visualisation of radiotherapy target structures undergoing respiratory motion when adjacent to healthy tissue. One advantage of the MVFP method was the use of volumetric acquisitions, which enabled 4D-T2w MRI to be generated with thinner slices and reduced through-plane geometrical distortion when compared to that obtained using conventional slice-selective techniques (Li et al., 2017a; Liu et al., 2015a; van de Lindt et al., 2018b). The MVFP method was of limited use for on-line application in MR-linac workflows because of the long reconstruction time required by the 4D joint MoCo-HDTV algorithm (9-12 hours). Moreover, the MVFP method could not be readily implemented at other centres due to acquisition of 4D-T1w MRI using a work-in-progress sequence.

In an attempt to overcome long calculation time and use of work-in-progress sequences, a super-resolution approach was introduced in Chapter 4 to reconstruct 4D-T2w MRI ($1.0 \times 1.0 \times 1.0 \text{ mm}^3$, 8 respiratory phases) from data obtained using standard clinical sequences. In the super-resolution approach, low-resolution 2D-T2w images were repetitively acquired in the axial and sagittal orientations and then combined into one high-resolution 4D-T2w image using an algorithm based on binning, image registration and super-resolution reconstruction. Unlike 4D-MRI generated using existing slice-selective methods (Hu et al., 2013; Hui et al., 2016; Li et al., 2017a; Paganelli et al., 2015; Tryggstad et al., 2013), super-resolution reconstructed 4D-T2w MRI did not suffer from thick slices, data incompleteness artefacts, stitching artefacts or through-plane geometrical distortion. The super-

resolution approach required a greatly reduced reconstruction time (23 minutes) compared to the MVFP method. Nevertheless, the 23 minutes reconstruction time still restricted on-line application of 4D-T2w MRI on an MR-linac.

In Chapter 5, the Dixon-based, Dixon-Spine and Dixon-Spine-Lung methods were consecutively introduced to calculate 4D-sCT ($1.5 \times 1.5 \times 3.0 \text{ mm}^3$, 20 respiratory phases) from 4D-T1w and 3D-Dixon MRI. In the Dixon-Spine-Lung method, 3D-sCT was obtained using an algorithm based on bulk-density assignment (Dixon), best-atlas segmentation (spine) and polynomial fitting (lung). Using a similar approach to the MVFP method, generated 3D-sCT were then transformed to all respiratory phases using MVFs calculated from 4D-T1w MRI. Resulting Dixon-Spine-Lung 4D-sCT were validated in MidP against 4D-CT and, overall, good agreement was found in terms of HUs and dose-volume metrics. Prior to the work presented in Chapter 5, no MR-only 4D-sCT solution existed. Furthermore, unlike contemporary abdominothoracic sCT techniques (Bredfeldt et al., 2017; Prior et al., 2017; Wang et al., 2017), the Dixon-Spine-Lung method provided a correction for variable electron density in the lung. One disadvantage of the introduced sCT methods was that disease-related air-spaces could not be distinguished from lung tissue, which limited dosimetric accuracy of generated 4D-sCT for patients presenting with emphysema. Similarly to the MVFP method, the sCT methods also suffered from the long reconstruction time required to calculate 4D-T1w MRI.

In order to accelerate the MVFP and sCT methods, a 3D U-net dCNN (Dracula) was presented in Chapter 6 to learn the 4D joint MoCo-HDTV and MidP algorithms. Dracula required only 28, 28 and 42 seconds to separately reconstruct 4D-T1w MRI, MidP-T1w MRI and MVFs from Gridded data, respectively. According to two experienced observers, Dracula-reconstructed 4D-T1w MRI exhibited clinically acceptable image quality for target and OAR delineation. Unlike existing 2D U-net implementations (Han et al., 2018; Hyun et al., 2018), Dracula employed a 3D U-net architecture to exploit information in both the spatial and respiratory phase domains to reconstruct heavily undersampled data. One

limitation of Dracula was that resulting MRI exhibited minor blurring and residual streaking artefacts compared to corresponding joint MoCo-HDTV-reconstructed images. Replacing joint MoCo-HDTV-reconstructed 4D-T1w MRI with Dracula-reconstructed 4D-T1w MRI would drastically reduce calculations times required by the MVFP and Dixon-Spine-Lung methods. Reduced processing times might enable 4D-T2w MRI and 4D-sCT to be reconstructed in a clinically relevant time-frame on an MR-linac.

Chapter 7 describes the application of a phase binning algorithm to reconstruct 4D-T2w MRI from data acquired on an MR-linac. In addition, 4D-T2w MRI were reconstructed from MR-linac data using optimised implementations of the MVFP and super-resolution methods. The MVFP method was enhanced by replacing joint MoCo-HDTV-reconstructed 4D-T1w MRI with Dracula-reconstructed 4D-T1w MRI. The super-resolution approach was improved by extensive code refactoring and parameter tuning. Furthermore, trilateral regularisation was implemented to constrain iterative back-projection super-resolution reconstruction. Resulting 4D-T2w MRI were compared and, overall, the optimised MVFP method was best-suited for on-line application in an MR-linac workflow. In particular, MVFP-generated 4D-T2w MRI had good spatio-temporal resolution ($1.5 \times 1.5 \times 3.0$ mm³, 16 respiratory phases) and required less than 6 minutes to reconstruct. Prior to the work presented in Chapter 7, 4D-T2w MRI reconstruction algorithms had only been compared using data acquired on a diagnostic system (Li et al., 2017a; van Kesteren et al., 2019). One drawback of the presented comparison study was the limited number of investigated healthy volunteers.

8.2 Clinical applications of 4D-T2w MRI and 4D-sCT

At the time of writing, few centres have incorporated MR-linacs into the clinical radiotherapy workflow. For instance, only 8 specialist centres are treating patients using the Elekta Unity MR-linac system. Although the number of MR-linac systems sold by Viewray and Elekta is rising (45 have currently been ordered from Elekta (Elekta, 2019)), the majority of centres in the nearby future will not have access to an MR-linac. Moreover, in the long-term future, not all centres are expected to procure an MR-linac system, since it is more expensive than a modern conventional linear accelerator and requires highly trained staff to operate. In centres without MR-linacs, diagnostic MRI scanners could be integrated into the radiotherapy workflow (Owringi et al., 2018; Schmidt and Payne, 2015). For example, a diagnostic scanner could be fitted with commercially available equipment, such as an elevated coil-holder, and used to acquire images for RTP purposes (Paulson et al., 2015, 2016).

The methods developed and described in this thesis enable thoracic MR-only RTP and can be implemented on both diagnostic scanners and high-field MR-linacs. The presented methods therefore have the potential to benefit the majority of lung cancer patients receiving external beam radiotherapy treatment. Moreover, the devised methods could enable MR-only RTP for other treatment sites affected by respiratory motion, such as the liver or pancreas. Thoracic MR-only RTP would be possible using geometrically accurate 4D-sCT reconstructed using the Dixon-Spine-Lung method and 4D-T2w MRI calculated using the MVFP or super-resolution methods. Electron density information contained in 4D-sCT enables dose calculations and 4D-T2w MRI facilitates accurate target and OAR delineations. The 4D aspect allows images to be acquired during physiological breathing without related blurring. Moreover, the 4D aspect permits application of existing motion-management planning strategies developed with 4D-CT in

mind (Wolthaus et al., 2008b).

In the conventional thoracic external beam radiotherapy workflow, each fractionated delivery is based on the same pre-treatment 4D-CT image. Employing the same pre-treatment image to plan all fractions does not account for changes in patient anatomy (Kwint et al., 2014) or respiratory pattern (Britton et al., 2007) occurring throughout the treatment course. Large changes in anatomical positions and respiratory pattern could be corrected for by re-calculating the treatment plan shortly before each fraction using up-to-date 4D-T2w MRI and 4D-sCT acquired on a diagnostic scanner. In clinical practice, Dracula-accelerated implementations of the MVFP and Dixon-Spine-Lung methods could be utilised to obtain 4D-T2w MRI and 4D-sCT approximately one hour prior to conventional treatment delivery. One hour is expected to provide sufficient time to reconstruct 4D-MRI and adapt the treatment plan.

Inter-fractional changes in patient anatomy and respiratory pattern could be more accurately accounted for in an MR-linac workflow. Using an MR-linac, 4D-T2w MRI and 4D-sCT could be rapidly acquired during a pre-beam imaging period of the workflow and then used to generate a treatment plan representative of the patient's position, anatomy and respiratory pattern immediately prior to irradiation. In Chapter 7, the feasibility of rapidly acquiring 4D-T2w MRI on an MR-linac was demonstrated. Four-dimensional T2w MRI with good spatio-temporal resolution were reconstructed from MR-linac data within 6 minutes using the Dracula-accelerated MVFP method. It might also be possible to reconstruct 4D-sCT from MR-linac data in a similar time-frame using a Dracula-accelerated implementation of the Dixon-Spine-Lung method. Existing deep learning and rapid planning techniques might be translated and applied to quickly generate a treatment plan using 4D-T2w MRI and 4D-sCT acquired on an MR-linac. For instance, a dCNN auto-segmentation algorithm (Cardenas et al., 2019) could be trained to rapidly contour targets and OARs on 4D-T2w MRI. Furthermore, a state-of-the-art cloud-based Monte Carlo solution (Ziegenhein et al., 2017) might be applied to perform dose calculations on 4D-sCT in near real-time.

Motion-models have been trained and applied to obtain volumetric MRI with low-latency (≈ 2 Hz) based on rapidly acquired cine 2D-MRI and retrospectively reconstructed 4D-MRI (Harris et al., 2016; Stemkens et al., 2016). Similar motion-models could be utilised on an MR-linac to generate 3D-T2w MRI and 3D-sCT on-the-fly using 4D-T2w MRI and 4D-sCT obtained during a pre-beam imaging period of the workflow and cine 2D-MRI acquired throughout treatment delivery. In the nearby future, deep learning-based image reconstruction (Hammernik et al., 2018; Han et al., 2018) could permit volumetric real-time MRI to be directly generated from highly undersampled data.

The Dixon-Spine-Lung method could be applied in an MR-linac workflow for off-line dose reconstruction purposes (Stemkens et al., 2017). Prior to irradiation, a 3D Dixon image could be acquired. Next, a radial stack-of-stars sequence could be performed throughout treatment delivery. After the treatment session, 3D-Dixon MRI and raw 4D-T1w data could be processed using the Dixon-Spine-Lung workflow to obtain 4D-sCT representative of the patient’s average anatomical positions and respiratory pattern during treatment delivery. The true dose given to the patient could then be estimated by re-calculating the delivered MR-linac treatment plan on the reconstructed 4D-sCT image. The estimate of the delivered dose could be used to optimise the dose prescribed in subsequent fractions (Webb, 2007).

8.3 Future work

8.3.1 Methodological improvements

The optimised super-resolution approach described in Chapter 7 was limited for on-line use in an MR-linac workflow by its long acquisition-reconstruction time (28.8 minutes). Combined acquisition-reconstruction time might be reduced by separately accelerating the sagittal and coronal SS-TSE sequences using a simultaneous multi-slice acquisition technique (Barth et al., 2016). For instance,

multi-band RF pulses could be incorporated into the sagittal and coronal SS-TSE sequences to enable signal from two interleaved slices to be excited and acquired during each shot. The acquired aliased signal could then be reconstructed using a parallel imaging-based algorithm (Barth et al., 2016). Acquiring signal from two slices during each shot would enable acquisition time to be roughly halved. A two-fold acceleration would result in a reduced effective repetition time of $\approx 1.7 - 2.1$ seconds (see Table 7.1), which should maintain magnetization recovery between consecutive dynamics.

Dracula-reconstructed 4D-T1w MRI was limited for application in the MR-linac-optimised MVFP method by residual noise and streaking artefacts; see Chapter 7. The residual artefacts might be reduced by training Dracula on more representative MR-linac data sets, instead of data acquired on a diagnostic scanner. Whilst suboptimal, diagnostic data were applied for training purposes due to the current limited availability of MR-linac data. In the future, Dracula should be re-trained exclusively using MR-linac data when readily available. An immediate solution might be to extend Dracula to include domain adaptation (Han et al., 2018). Using domain adaptation, Dracula could be pre-trained on diagnostic data and then fine-tuned using a small set of available MR-linac images. A brief summary of (Han et al., 2018) was provided in section 6.1.

Dosimetric accuracy of 4D-sCT generated using the Dixon-Spine-Lung method was limited for patients presenting with emphysema. As discussed in Chapter 5, UTE sequences could be applied to discriminate emphysema from healthy lung tissue in calculated 4D-sCT. Ultra short echo time images could be integrated into the Dixon-Spine-Lung method by replacing 4D-T1w MRI with 4D-UTE MRI. One approach to obtain high-quality 4D-UTE MRI is to apply a compressed sensing-based reconstruction technique, such as the extra-dimensional-UTE algorithm (Feng et al., 2019), to raw data acquired using a 3D radial-spiral UTE sequence (Delacoste et al., 2018).

8.3.2 Deep learning-based image reconstruction

All 4D-MRI techniques result in images representative of the patient's average anatomical positions and breathing cycle over the data acquisition period. Consequently, 4D-MRI acquired prior to irradiation cannot fully represent the patient motion during treatment delivery. In principle, acquiring and reconstructing 4D-MRI as close to treatment delivery as possible reduces base-line drifts in average anatomical positions and respiratory pattern. van de Lindt et al. (2018a) demonstrated the feasibility of acquiring and reconstructing 4D-T2w MRI on an MR-linac in less than five minutes. Whilst combined acquisition-reconstruction time was short, resulting 4D-T2w MRI were limited by thick slices (5 mm) and a restricted FOV.

Rank et al. (2017) applied the joint MoCo-HDTV algorithm (9-12 hours) to reconstruct high-quality 4D-T1w MRI from data acquired in just 40 seconds. In the future, deep learning-based reconstruction techniques, such as Dracula, will be trained and applied to rapidly reconstruct (e.g. 28 seconds) high-quality 4D-MRI from k-space data acquired with similar undersampling factors (i.e. 40 seconds acquisition time). Applying deep learning-based reconstruction techniques to data acquired with extreme undersampling factors may enable high-quality 4D-MRI to be obtained on MR-linacs immediately (< 1 -2 minutes) before treatment delivery.

8.4 Final conclusion

In this thesis, methods to calculate high-quality 4D-T2w MRI were developed, validated and optimised for application in an MR-linac workflow. Unlike existing techniques based on slice-selection, the developed MVFP and super-resolution methods resulted in geometrically accurate 4D-T2w MRI with high spatio-temporal resolution. High-quality 4D-T2w MRI could facilitate target and OAR delineation in RTP. Three methods to calculate geometrically accurate 4D-sCT from MR images were developed and validated. Overall, 4D-sCT obtained using the Dixon-Spine-Lung method were dosimetrically accurate when compared to 4D-CT. Prior to the work presented in this thesis, no MR-only 4D-sCT implementation was published. A technique based on deep learning was applied to accelerate reconstruction of 4D-T1w MRI from 9-12 hours to 28 seconds. Good agreement was found when validating Dracula-reconstructed 4D-T1w MRI against corresponding joint MoCo-HDTV-reconstructed 4D-T1w MRI. Dracula-reconstructed 4D-T1w MRI could support rapid calculation of 4D-T2w MRI and 4D-sCT on an MR-linac. Four-dimensional T2w MRI could be applied alongside 4D-sCT for treatment plan adaptation in thoracic MR-linac workflows. Treatment plan adaptation is expected to improve patient outcome by accounting for dosimetric errors related to inter-fractional changes in patient anatomy and respiratory motion.

References

- Abadi, M., P. Barham, J. Chen, Z. Chen, A. Davis, J. Dean, M. Devin, S. Ghemawat, G. Irving, and M. Isard (2016). “Tensorflow: a system for large-scale machine learning”. *Proc. OSDI*. Vol. 16, pp. 265–283.
- Abdelnour, A. F., S. A. Nehmeh, T. Pan, J. L. Humm, P. Vernon, H. Schöder, K. E. Rosenzweig, G. S. Mageras, E. Yorke, and S. M. Larson (2007). “Phase and amplitude binning for 4D-CT imaging”. *Phys Med Biol* 52.12, p. 3515.
- Adebahr, S., S. Collette, E. Shash, M. Lambrecht, C. Le Pechoux, C. Faivre-Finn, D. De Ruysscher, H. Peulen, J. Belderbos, and R. Dziadziuszko (2015). “LungTech, an EORTC Phase II trial of stereotactic body radiotherapy for centrally located lung tumours: a clinical perspective”. *Br J Radiol* 88.1051, p. 20150036.
- Aggarwal, H. K., M. P. Mani, and M. Jacob (2018). “Modl: Model-based deep learning architecture for inverse problems”. *IEEE Trans Med Imaging* 38.2, pp. 394–405.
- Arabi, H., N. Koutsouvelis, M. Rouzaud, R. Miralbell, and H. Zaidi (2016). “Atlas-guided generation of pseudo-CT images for MRI-only and hybrid PET–MRI-guided radiotherapy treatment planning”. *Phys Med Biol* 61.17, p. 6531.
- Bainbridge, H., A. Salem, R. H. N. Tijssen, M. Dubec, A. Wetscherek, C. Van Es, J. Belderbos, C. Faivre-Finn, and F. McDonald (2017). “Magnetic resonance imaging in precision radiation therapy for lung cancer”. *Transl Lung Cancer Res* 6.6, p. 689.

- Baldwin, L. N., K. Wachowicz, S. D. Thomas, R. Rivest, and B. G. Fallone (2007). “Characterization, prediction, and correction of geometric distortion in MR images”. *Med Phys* 34.2, pp. 388–399.
- Barth, M., F. Breuer, P. J. Koopmans, D. G. Norris, and B. A. Poser (2016). “Simultaneous multislice (SMS) imaging techniques”. *Magn Res Med* 75.1, pp. 63–81.
- Bauman, G., M. Puderbach, M. Deimling, V. Jellus, C. Chefd’hotel, J. Dinkel, C. Hintze, H. Kauczor, and L. R. Schad (2009). “Non-contrast-enhanced perfusion and ventilation assessment of the human lung by means of fourier decomposition in proton MRI”. *Magn Res Med* 62.3, pp. 656–664.
- Benkert, T., L. Feng, D. K. Sodickson, H. Chandarana, and K. T. Block (2017). “Free-breathing volumetric fat/water separation by combining radial sampling, compressed sensing, and parallel imaging”. *Magn Res Med* 78.2, pp. 565–576.
- Benkert, T., J. P. Mugler III, D. S. Rigie, D. K. Sodickson, H. Chandarana, and K. T. Block (2018). “Hybrid T2-and T1-weighted radial acquisition for free-breathing abdominal examination”. *Magn Res Med* 80, pp. 1935–1948.
- Bernstein, M. A., K. F. King, and X. J. Zhou (2004). *Handbook of MRI pulse sequences*. Elsevier. ISBN: 0080533124.
- Biederer, J., M. Beer, W. Hirsch, J. Wild, M. Fabel, M. Puderbach, and E. J. R. Van Beek (2012). “MRI of the lung (2/3). Why... when... how?” *Insights Imaging* 3.4, pp. 355–371.
- Biggs, D. S. C. and M. Andrews (1997). “Acceleration of iterative image restoration algorithms”. *Appl Opt* 36.8, pp. 1766–1775.
- Blackall, J. M., S. Ahmad, M. E. Miquel, J. R. McClelland, D. B. Landau, and D. J. Hawkes (2006). “MRI-based measurements of respiratory motion variability and assessment of imaging strategies for radiotherapy planning”. *Phys Med Biol* 51.17, pp. 4147–4169.
- Blackall, J. M., G. P. Penney, A. P. King, and D. J. Hawkes (2005). “Alignment of sparse freehand 3-D ultrasound with preoperative images of the liver using

- models of respiratory motion and deformation”. *IEEE T Med Imaging* 24.11, pp. 1405–1416.
- Bloch, F. (1946). “Nuclear induction”. *Phys Rev* 70.7-8, p. 460.
- Block, K. T. and M. Uecker (2011). “Simple method for adaptive gradient-delay compensation in radial MRI”. *Proc. of the 19th Annual Meeting of ISMRM*, p. 2816.
- Block, K. T., M. Uecker, and J. Frahm (2007). “Undersampled radial MRI with multiple coils. Iterative image reconstruction using a total variation constraint”. *Magn Res Med* 57.6, pp. 1086–1098.
- Block, K. T., H. Chandarana, S. Milla, M. Bruno, T. Mulholland, G. Fatterpekar, M. Hagiwara, R. Grimm, C. Geppert, and B. Kiefer (2014). “Towards routine clinical use of radial stack-of-stars 3d gradient-echo sequences for reducing motion sensitivity”. *J Korean Soc Magn Res* 18.2, pp. 87–106.
- Boldea, V., G. C. Sharp, S. B. Jiang, and D. Sarrut (2008). “4D-CT lung motion estimation with deformable registration: quantification of motion nonlinearity and hysteresis”. *Med Phys* 35.3, pp. 1008–1018.
- Bostel, T., N. H. Nicolay, J. G. Grossmann, A. Mohr, S. Delorme, G. Echner, P. Häring, J. Debus, and F. Sterzing (2014). “MR-guidance—a clinical study to evaluate a shuttle-based MR-linac connection to provide MR-guided radiotherapy”. *Radiat Oncol* 9.1, p. 12.
- Boubertakh, R., C. Prieto, P. G. Batchelor, S. Uribe, D. Atkinson, H. Eggers, T. S. Sørensen, M. S. Hansen, R. S. Razavi, and T. Schaeffter (2009). “Whole-heart imaging using undersampled radial phase encoding (RPE) and iterative sensitivity encoding (SENSE) reconstruction”. *Magn Res Med* 62.5, pp. 1331–1337.
- Bredfeldt, J. S., L. Liu, M. Feng, Y. Cao, and J. M. Balter (2017). “Synthetic CT for MRI-based liver stereotactic body radiotherapy treatment planning”. *Phys Med Biol* 62.8, pp. 2922–2934.
- Britton, K. R., G. Starkschall, S. L. Tucker, T. Pan, C. Nelson, J. Y. Chang, J. D. Cox, R. Mohan, and R. Komaki (2007). “Assessment of gross tumor

- volume regression and motion changes during radiotherapy for non-small-cell lung cancer as measured by four-dimensional computed tomography”. *Int J Radiat Oncol Biol Phys* 68.4, pp. 1036–1046.
- Brown, G., I. R. Daniels, C. Richardson, P. Revell, D. Peppercorn, and M. Bourne (2014a). “Techniques and trouble-shooting in high spatial resolution thin slice MRI for rectal cancer”. *Brit J Radiol* 78.927, pp. 245–251.
- Brown, R. W., Y. N. Cheng, E. M. Haacke, M. R. Thompson, and R. Venkatesan (2014b). *Magnetic resonance imaging: physical principles and sequence design*. John Wiley & Sons. ISBN: 1118633970.
- Buerger, C., C. Prieto, and T. Schaeffter (2013). “Highly efficient 3D motion-compensated abdomen MRI from undersampled golden-RPE acquisitions”. *MAGMA* 26.5, pp. 419–429.
- Cai, J., Z. Chang, Z. Wang, W. P. Segars, and F.-F. Yin (2011). “Four-dimensional magnetic resonance imaging (4D-MRI) using image-based respiratory surrogate: A feasibility study”. *Med Phys* 38.12, pp. 6384–6394.
- Cancer Research UK (2019a). *Lung cancer survival*. URL: <https://www.cancerresearchuk.org/health-professional/cancer-statistics/statistics-by-cancer-type/lung-cancer#heading-Two>.
- (2019b). *Radiotherapy for lung cancer*. URL: <https://www.cancerresearchuk.org/health-professional/cancer-statistics/statistics-by-cancer-type/lung-cancer/diagnosis-and-treatment#heading-Three>.
- Cardenas, C. E., J. Yang, B. M. Anderson, L. E. Court, and K. B. Brock (2019). “Advances in Auto-Segmentation”. *Semin Radiat Oncol*. Vol. 29. 3. Elsevier, pp. 185–197. ISBN: 1053-4296.
- Chilla, G. S., C. H. Tan, and C. L. Poh (2017). “Deformable registration based super-resolution for isotropic reconstruction of 4D MRI volumes”. *IEEE J Biomed Health Inform* 21.6, pp. 1617–1624.
- Chollet, F. (2017). “Xception: Deep learning with depthwise separable convolutions”. *Proc. IEEE Comput. Soc. Conf. Comput. Vis. Pattern Recognit.* Pp. 1251–1258.

- Çiçek, Ö., A. Abdulkadir, S. S. Lienkamp, T. Brox, and O. Ronneberger (2016). “3D U-Net: learning dense volumetric segmentation from sparse annotation”. *Proc. of the MICCAI 19th meeting*. Springer, pp. 424–432.
- CMIC (2015). *NiftyReg Documentation*. URL: http://cmictig.cs.ucl.ac.uk/wiki/index.php/NiftyReg_documentation.
- Cover, K. S., F. J. Lagerwaard, and S. Senan (2006). “Color intensity projections: A rapid approach for evaluating four-dimensional CT scans in treatment planning”. *Int J Radiat Oncol* 64.3, pp. 954–961.
- Cruz, G., D. Atkinson, C. Buerger, T. Schaeffter, and C. Prieto (2016). “Accelerated motion corrected three-dimensional abdominal MRI using total variation regularized SENSE reconstruction”. *Magn Res Med* 75.4, pp. 1484–1498.
- Daisne, J. F., M. Sibomana, A. Bol, G. Cosnard, M. Lonneux, and V. Gregoire (2003). “Evaluation of a multimodality image (CT, MRI and PET) coregistration procedure on phantom and head and neck cancer patients: accuracy, reproducibility and consistency”. *Radiother Oncol* 69, pp. 237–245.
- Dean, C. J., J. R. Sykes, R. A. Cooper, P. Hatfield, B. Carey, S. Swift, S. E. Bacon, D. Thwaites, D. Sebag-Montefiore, and A. M. Morgan (2012). “An evaluation of four CT-MRI co-registration techniques for radiotherapy treatment planning of prone rectal cancer patients”. *Br J Radiol* 85.1009, pp. 61–68.
- Delacoste, J., J. Chaptinel, C. Beigelman-Aubry, D. Piccini, A. Sauty, and M. Stuber (2018). “A double echo ultra short echo time (UTE) acquisition for respiratory motion-suppressed high resolution imaging of the lung”. *Magn Res Med* 79.4, pp. 2297–2305.
- Deng, Z., J. Pang, W. Yang, Y. Yue, B. Sharif, R. Tuli, D. Li, B. Fraass, and Z. Fan (2015). “Four-dimensional MRI using three-dimensional radial sampling with respiratory self-gating to characterize temporal phase-resolved respiratory motion in the abdomen”. *Magn Reson Med*. 75.4, pp. 1574–1585.
- Doran, S. J., L. Charles-Edwards, S. A. Reinsberg, and M. O. Leach (2005). “A complete distortion correction for MR images: I. Gradient warp correction”. *Phys Med Biol* 50.7, pp. 1343–1361.

- Du, D., S. D. Caruthers, C. Glide-Hurst, D. A. Low, H. H. Li, S. Mutic, and Y. Hu (2015). “High-quality t2-weighted 4-dimensional magnetic resonance imaging for radiation therapy applications”. *Int J Radiat Oncol* 92.2, pp. 430–437.
- Du, D., S. Mutic, H. H. Li, and Y. Hu (2018). “An efficient model to guide prospective T2-weighted 4D magnetic resonance imaging acquisition”. *Med Phys* 45.6, pp. 2453–2462.
- Durham, A. L. and I. M. Adcock (2015). “The relationship between COPD and lung cancer”. *Lung Cancer* 90.2, pp. 121–127.
- Edmund, J. M. and T. Nyholm (2017). “A review of substitute CT generation for MRI-only radiation therapy”. *Radiat Oncol* 12.1, p. 28.
- Elekta (2017a). *Versa HD*. URL: https://www.elekta.com/dam/jcr:14cae385-9b40-4f9b-a805-79a0ecff249e/LPCIYE170601_VHD_FLG_A4ls_f_revised_7.19.17.pdf.
- (2017b). *Versa HD*. URL: https://www.elekta.com/dam/jcr:14cae385-9b40-4f9b-a805-79a0ecff249e/LPCIYE170601_VHD_FLG_A4ls_f_revised_7.19.17.pdf.
- (2019). *Elekta Q4 and full-year report 2018-2019*. URL: https://www.elekta.com/investors/fileadmin/presentations/2018-19/Elekta_Q4_Yearend_presentation.pdf.
- Fallone, B. G. (2014). “The rotating biplanar linac–magnetic resonance imaging system”. *Semin Radiat Oncol* 24.3, pp. 200–202.
- Farsiu, S., M. D. Robinson, M. Elad, and P. Milanfar (2004). “Fast and robust multiframe super resolution”. *IEEE Trans Image Process* 13.10, pp. 1327–1344.
- Fast, M., A. van de Schoot, T. van de Lindt, C. Carbaat, U. van der Heide, and J.-J. Sonke (2019). “Tumor Trailing for Liver SBRT on the MR-Linac”. *Int J Radiat Oncol Biol Phys* 103.2, pp. 468–478.
- Feng, L., R. Grimm, K. T. Block, H. Chandarana, S. Kim, J. Xu, L. Axel, D. K. Sodickson, and R. Otazo (2014). “Golden-angle radial sparse parallel MRI: Combination of compressed sensing, parallel imaging, and golden-angle radial

- sampling for fast and flexible dynamic volumetric MRI”. *Magn Res Med* 72.3, pp. 707–717.
- Feng, L., L. Axel, H. Chandarana, K. T. Block, D. K. Sodickson, and R. Otazo (2016). “XD-GRASP: Golden-angle radial MRI with reconstruction of extra motion-state dimensions using compressed sensing”. *Magn Res Med* 75.2, pp. 775–788.
- Feng, L., C. Huang, K. Shanbhogue, D. K. Sodickson, H. Chandarana, and R. Otazo (2018). “RACER-GRASP: Respiratory-weighted, aortic contrast enhancement-guided and coil-unstreaking golden-angle radial sparse MRI”. *Magn Res Med* 80.1, pp. 77–89.
- Feng, L., J. Delacoste, D. Smith, J. Weissbrot, E. Flagg, W. H. Moore, F. Girvin, R. Raad, P. Bhattacharji, and D. Stoffel (2019). “Simultaneous Evaluation of Lung Anatomy and Ventilation Using 4D Respiratory-Motion-Resolved Ultrashort Echo Time Sparse MRI”. *J Magn Reson Imaging* 49.2, pp. 411–422.
- Field, J. K., S. W. Duffy, D. R. Baldwin, K. E. Brain, A. Devaraj, T. Eisen, B. A. Green, J. A. Holemans, T. Kavanagh, and K. M. Kerr (2016). “The UK Lung Cancer Screening trial: a pilot randomised controlled trial of low-dose computed tomography screening for the early detection of lung cancer”. *Health technol assess* 20.40, p. 1.
- Freedman, J. N., D. J. Collins, H. Bainbridge, C. M. Rank, S. Nill, M. Kachelrieß, U. Oelfke, M. O. Leach, and A. Wetscherek (2017). “T2-Weighted 4D Magnetic Resonance Imaging for Application in Magnetic Resonance-Guided Radiotherapy Treatment Planning”. *Invest Radiol* 52.5, pp. 563–573.
- Freedman, J. N., D. J. Collins, O. J. Gurney-Champion, J. R. McClelland, S. Nill, U. Oelfke, M. O. Leach, and A. Wetscherek (2018). “Super-resolution T2-weighted 4D MRI for image guided radiotherapy”. *Radiother Oncol* 129.3, pp. 486–493.
- Freedman, J. N., H. Bainbridge, S. Nill, D. J. Collins, M. Kachelriess, M. O. Leach, F. McDonald, U. Oelfke, and A. Wetscherek (2019). “Synthetic 4D-CT of the

- thorax for treatment plan adaptation on MR-guided radiotherapy systems”. *Phys Med Biol* 64.115005.
- Garcia, D. (2010). “Robust smoothing of gridded data in one and higher dimensions with missing values”. *Comput Stat Data Anal* 54.4, pp. 1167–1178.
- Glorot, X. and Y. Bengio (2010). “Understanding the difficulty of training deep feedforward neural networks”. *Proc. of the 13th AISTats conference*, pp. 249–256.
- Goodfellow, I., Y. Bengio, and A. Courville (2016). *Deep learning*. MIT press. ISBN: 0262337371.
- Gurney-Champion, O. J., E. Versteijne, A. van der Horst, E. Lens, H. Rütten, H. D. Heerkens, G. M. R. M. Paardekooper, M. Berbee, C. R. N. Rasch, and J. Stoker (2017). “Addition of MRI for CT-based pancreatic tumor delineation: a feasibility study”. *Acta Oncol* 56.7, pp. 923–930.
- Haas, O. C. L., J. A. Mills, I. Land, P. Mulholl, P. Menary, R. Crichton, A. Wilson, J. Sage, M. Anna, and T. Depuydt (2014). “IGRT/ART phantom with programmable independent rib cage and tumor motion”. *Med Phys* 41.2.
- Hahn, E. L. (1950). “Spin echoes”. *Phys Rev* 80.4, p. 580.
- Hammernik, K., T. Klatzer, E. Kobler, M. P. Recht, D. K. Sodickson, T. Pock, and F. Knoll (2018). “Learning a variational network for reconstruction of accelerated MRI data”. *Magn Res Med* 79.6, pp. 3055–3071.
- Han, X. (2017). “MR-based Synthetic CT Generation using a Deep Convolutional Neural Network Method”. *Med Phys* 44.4, pp. 1408–1419.
- Han, Y., J. Yoo, H. H. Kim, H. J. Shin, K. Sung, and J. C. Ye (2018). “Deep learning with domain adaptation for accelerated projection-reconstruction MR”. *Magn Res Med* 80.3, pp. 1189–1205.
- Hanna, G. G., J. R. v. S. de Koste, M. R. Dahele, K. J. Carson, C. J. A. Haasbeek, R. Migchielsen, A. R. Hounsell, and S. Senan (2012). “Defining Target Volumes for Stereotactic Ablative Radiotherapy of Early-stage Lung Tumours: A Comparison of Three-dimensional 18 F-fluorodeoxyglucose Positron Emission

- Tomography and Four-dimensional Computed Tomography”. *Clin Oncol* 24.6, e71–e80.
- Hanna, G. G., L. Murray, R. Patel, S. Jain, K. L. Aitken, K. N. Franks, N. Van As, A. Tree, P. Hatfield, and S. Harrow (2018). “UK Consensus on Normal Tissue Dose Constraints for Stereotactic Radiotherapy”. *Clin Oncol* 30.1, pp. 5–14.
- Harris, W., L. Ren, J. Cai, Y. Zhang, Z. Chang, and F.-F. Yin (2016). “A technique for generating volumetric cine-magnetic resonance imaging”. *Int J Radiat Oncol Biol Phys* 95.2, pp. 844–853.
- He, K., J. Sun, and X. Tang (2013). “Guided image filtering”. *IEEE Trans Pattern Anal Mach Intell* 35.6, pp. 1397–1409.
- He, K., X. Zhang, S. Ren, and J. Sun (2016). “Deep residual learning for image recognition”. *Proc. IEEE Comput. Soc. Conf. Comput. Vis. Pattern Recognit.* Pp. 770–778.
- Hennig, J., A. Nauerth, and H. Friedburg (1986). “RARE imaging: a fast imaging method for clinical MR”. *Magn Res Med* 3.6, pp. 823–833.
- Hofmann, M., I. Bezrukov, F. Mantlik, P. Aschoff, F. Steinke, T. Beyer, B. J. Pichler, and B. Schölkopf (2011). “MRI-based attenuation correction for whole-body PET/MRI: quantitative evaluation of segmentation-and atlas-based methods”. *J Nucl Med* 52.9, pp. 1392–1399.
- Hu, Y., S. D. Caruthers, D. A. Low, P. J. Parikh, and S. Mutic (2013). “Respiratory amplitude guided 4-dimensional magnetic resonance imaging”. *Int J Radiat Oncol* 86.1, pp. 198–204.
- Huang, K. C., Y. Cao, U. Baharom, and J. M. Balter (2016). “Phantom-based characterization of distortion on a magnetic resonance imaging simulator for radiation oncology”. *Phys Med Biol* 61.2, p. 774.
- Hui, C., Z. Wen, B. Stemkens, R. H. N. Tijssen, C. A. T. van den Berg, K.-P. Hwang, and S. Beddar (2016). “4D MR imaging using robust internal respiratory signal”. *Phys Med Biol* 61.9, pp. 3472–3487.
- Hyun, C. M., H. P. Kim, S. M. Lee, S. Lee, and J. K. Seo (2018). “Deep learning for undersampled MRI reconstruction”. *Phys Med Biol* 63.13, p. 135007.

- ICRU (1999). *ICRU report 62: prescribing, recording and reporting photon beam therapy (supplement to ICRU Report 50)*. Tech. rep. Bethesda, USA.
- Iglesias, J. E. and M. R. Sabuncu (2015). “Multi-atlas segmentation of biomedical images: a survey”. *Med Image Anal* 24.1, pp. 205–219.
- Ioffe, S. and C. Szegedy (2015). “Batch normalization: Accelerating deep network training by reducing internal covariate shift”. *arXiv:1502.03167*.
- Irani, M. and S. Peleg (1991). “Improving resolution by image registration”. *Graph Models Image Process* 53.3, pp. 231–239.
- Jaffray, D. A., M. C. Carlone, M. F. Milosevic, S. L. Breen, T. Stanescu, A. Rink, H. Alasti, A. Simeonov, M. C. Sweitzer, and J. D. Winter (2014). “A facility for magnetic resonance-guided radiation therapy”. *Semin Radiat Oncol* 24.3, pp. 193–195.
- Janke, A., H. Zhao, G. J. Cowin, G. J. Galloway, and D. M. Doddrell (2004). “Use of spherical harmonic deconvolution methods to compensate for nonlinear gradient effects on MRI images”. *Magn Res Med* 52.1, pp. 115–122.
- Jezzard, P. and R. S. Balaban (1995). “Correction for geometric distortion in echo planar images from B0 field variations”. *Magn Res Med* 34.1, pp. 65–73.
- Johnstone, E., J. J. Wyatt, A. M. Henry, S. C. Short, D. Sebag-Montefiore, L. Murray, C. G. Kelly, H. M. McCallum, and R. Speight (2018). “A systematic review of synthetic CT generation methodologies for use in MRI-only radiotherapy”. *Int J Radiat Oncol Biol Phys* 100.1, pp. 199–217.
- Joiner, M. and A. van der Kogel (2016). *Basic clinical radiobiology*. Vol. 1. CRC Press.
- Jonsson, J. H., M. G. Karlsson, M. Karlsson, and T. Nyholm (2010). “Treatment planning using MRI data: an analysis of the dose calculation accuracy for different treatment regions”. *Radiat Oncol* 5.62, pp. 1–8.
- Karki, K., S. Saraiya, G. D. Hugo, N. Mukhopadhyay, N. Jan, J. Schuster, M. Schutzer, L. Fahrner, R. Groves, and K. M. Olsen (2017). “Variabilities of MRI-, CT- and PET-CT-based tumor and lymph node delineations for lung cancer radiotherapy planning”. *Int J Radiat Oncol Biol Phys* 99.1, p. 80.

- Karlsson, M., M. G. Karlsson, T. Nyholm, C. Amies, and B. Zackrisson (2009). “Dedicated magnetic resonance imaging in the radiotherapy clinic”. *Int J Radiat Oncol Biol Phys* 74.2, pp. 644–651.
- Khalil, A., M Majlath, V. Gounant, A. Hess, J. P. Laissy, and M. P. Debray (2016). “Contribution of magnetic resonance imaging in lung cancer imaging”. *Diagn Interv Imaging* 97.10, pp. 991–1002.
- Khan, F. M. and J. P. Gibbons (2014). *Khan’s the physics of radiation therapy*. Lippincott Williams & Wilkins.
- Khoo, V. S., D. P. Dearnaley, D. J. Finnigan, A Padhani, S. F. Tanner, and M. O. Leach (1997). “Magnetic resonance imaging (MRI): considerations and applications in radiotherapy treatment planning.” *Radiother Oncol* 42.1, pp. 1–15.
- Kieselmann, J. P., C. P. Kamerling, N. Burgos, M. J. Menten, C. D. Fuller, S. Nill, M. J. Cardoso, and U. Oelfke (2018). “Geometric and dosimetric evaluations of atlas-based segmentation methods of MR images in the head and neck region”. *Phys Med Biol* 63.145007.
- Kingma, D. P. and J. Ba (2014). “Adam: A method for stochastic optimization”. *arXiv:1412.6980*.
- Koch, N., H. H. Liu, G. Starkschall, M. Jacobson, K. Forster, Z. Liao, R. Komaki, and C. W. Stevens (2004). “Evaluation of internal lung motion for respiratory-gated radiotherapy using MRI: Part I—correlating internal lung motion with skin fiducial motion”. *Int J Radiat Oncol* 60.5, pp. 1459–1472.
- Kolbitsch, C., R. Neji, M. Fenchel, A. Mallia, P. Marsden, and T. Schaeffter (2018a). “Fully integrated 3D high-resolution multicontrast abdominal PET-MR with high scan efficiency”. *Magn Res Med* 79.2, pp. 900–911.
- Kolbitsch, C., R. Neji, M. Fenchel, A. Schuh, A. Mallia, P. Marsden, and T. Schaeffter (2018b). “Joint cardiac and respiratory motion estimation for motion-corrected cardiac PET-MR”. *Phys Med Biol* 64.1, p. 15007.

- Kolbitsch, C., R. Neji, M. Fenchel, A. Mallia, P. Marsden, and T. Schaeffter (2018c). “Respiratory-resolved MR-based attenuation correction for motion-compensated cardiac PET-MR”. *Phys Med Biol* 63.13, p. 135008.
- Kontaxis, C., G. H. Bol, B. Stemkens, M. Glitzner, F. M. Prins, L. G. W. Kerkmeijer, J. J. W. Lagendijk, and B. W. Raaymakers (2017). “Towards fast online intrafraction replanning for free-breathing stereotactic body radiation therapy with the MR-linac”. *Phys Med Biol* 62.18, p. 7233.
- Kraus, K. M., O. Jäkel, N. I. Niebuhr, and A. Pfaffenberger (2017). “Generation of synthetic CT data using patient specific daily MR image data and image registration”. *Phys Med Biol* 62.4, p. 1358.
- Krizhevsky, A., I. Sutskever, and G. E. Hinton (2012). “Imagenet classification with deep convolutional neural networks”. *Proc. NeurIPS*, pp. 1097–1105.
- Kuklisova-Murgasova, M., G. Quaghebeur, M. A. Rutherford, J. V. Hajnal, and J. A. Schnabel (2012). “Reconstruction of fetal brain MRI with intensity matching and complete outlier removal”. *Med Image Anal* 16.8, pp. 1550–1564.
- Kumar, S., G. Liney, R. Rai, L. Holloway, D. Moses, and S. K. Vinod (2016). “Magnetic resonance imaging in lung: a review of its potential for radiotherapy”. *Br J Radiol* 89.1060, p. 20150431.
- Kwint, M., S. Conijn, E. Schaake, J. Knegjens, M. Rossi, P. Remeijer, J.-J. Sonke, and J. Belderbos (2014). “Intra thoracic anatomical changes in lung cancer patients during the course of radiotherapy”. *Radiother Oncol* 113.3, pp. 392–397.
- Lagendijk, J. J., B. W. Raaymakers, C. A. Berg, M. A. Moerland, M. E. Philippens, and M. Vulpen (2014). “MR guidance in radiotherapy”. *Phys Med Biol* 59.
- Lambrecht, M., C. Melidis, J.-J. Sonke, S. Adebahr, R. Boellaard, M. Verheij, M. Guckenberger, U. Nestle, and C. Hurkmans (2016). “Lungtech, a phase II EORTC trial of SBRT for centrally located lung tumours—a clinical physics perspective”. *Radiat Oncol* 11.1, p. 7.
- LeCun, Y., L. Bottou, Y. Bengio, and P. Haffner (1998). “Gradient-based learning applied to document recognition”. *Proc. of the IEEE* 86.11, pp. 2278–2324.

- Lee, J.-G., S. Jun, Y.-W. Cho, H. Lee, G. B. Kim, J. B. Seo, and N. Kim (2017). “Deep learning in medical imaging: general overview”. *Korean J Radiol* 18.4, pp. 570–584.
- Li, G., J. Wei, D. Olek, M. Kadbi, N. Tyagi, K. Zakian, J. Mechalakos, J. O. Deasy, and M. Hunt (2017a). “Direct comparison of respiration-correlated four-dimensional magnetic resonance imaging reconstructed using concurrent internal navigator and external bellows”. *Int J Radiat Oncol* 97.3, pp. 596–605.
- Li, G., J. Wei, M. Kadbi, J. Moody, A. Sun, S. Zhang, S. Markova, K. Zakian, M. Hunt, and J. O. Deasy (2017b). “Novel Super-Resolution Approach to Time-Resolved Volumetric 4-Dimensional Magnetic Resonance Imaging With High Spatiotemporal Resolution for Multi-Breathing Cycle Motion Assessment”. *Int J Radiat Oncol* 98.2, pp. 454–462.
- Liang, D., J. Cheng, Z. Ke, and L. Ying (2019). “Deep MRI Reconstruction: Unrolled Optimization Algorithms Meet Neural Networks”. *arXiv 1907.11711*.
- Lichy, M. P., B. M. Wietek, J. P. Mugler III, W. Horger, M. I. Menzel, A. Anastasiadis, K. Siegmann, T. Niemeyer, A. Königsrainer, and B. Kiefer (2005). “Magnetic resonance imaging of the body trunk using a single-slab, 3-dimensional, T2-weighted turbo-spin-echo sequence with high sampling efficiency (SPACE) for high spatial resolution imaging: initial clinical experiences”. *Invest Radiol* 40.12, pp. 754–760.
- Liu, Y., F. Yin, Z. Chang, B. G. Czito, M. Palta, M. R. Bashir, Y. Qin, and J. Cai (2014). “Investigation of sagittal image acquisition for 4D-MRI with body area as respiratory surrogate”. *Med Phys* 41.10, pp. 101901–101902.
- Liu, Y., F.-F. Yin, N.-k. Chen, M.-L. Chu, and J. Cai (2015a). “Four dimensional magnetic resonance imaging with retrospective k-space reordering: A feasibility study”. *Med Phys* 42.2, pp. 534–541.
- Liu, Y., F.-F. Yin, B. G. Czito, M. R. Bashir, and J. Cai (2015b). “T2-weighted four dimensional magnetic resonance imaging with result-driven phase sorting”. *Med Phys* 42.8, pp. 4460–4471.

- Longmore, M., I. Wilkinson, A. Baldwin, and E. Wallin (2014). *Oxford handbook of clinical medicine*. Oxford University Press. ISBN: 0199609624.
- Louie, A. V., G. Rodrigues, J. Olsthoorn, D. Palma, E. Yu, B. Yaremko, B. Ahmad, I. Aivas, and S. Gaede (2010). “Inter-observer and intra-observer reliability for lung cancer target volume delineation in the 4D-CT era”. *Radiother Oncol* 95.2, pp. 166–171.
- Lu, W., P. J. Parikh, J. P. Hubenschmidt, J. D. Bradley, and D. A. Low (2006). “A comparison between amplitude sorting and phase-angle sorting using external respiratory measurement for 4D CT”. *Med Phys* 33.8, pp. 2964–2974.
- Lustig, M., D. Donoho, and J. M. Pauly (2007). “Sparse MRI: The application of compressed sensing for rapid MR imaging”. *Magn Res Med* 58.6, pp. 1182–1195.
- Manivannan, N., B. D. Clymer, A. Bratasz, and K. A. Powell (2013). “Comparison of super resolution reconstruction acquisition geometries for use in mouse phenotyping”. *Int J Biomed Imaging* 2013, p. 25.
- Marx, M., J. Ehrhardt, R. Werner, H.-P. Schlemmer, and H. Handels (2014). “Simulation of spatiotemporal CT data sets using a 4D MRI-based lung motion model”. *Int J Comput Ass Rad* 9.3, pp. 401–409.
- McClelland, J. R., J. M. Blackall, S. Tarte, A. C. Chandler, S. Hughes, S. Ahmad, D. B. Landau, and D. J. Hawkes (2006). “A continuous 4D motion model from multiple respiratory cycles for use in lung radiotherapy”. *Med Phys* 33.9, pp. 3348–3358.
- McClelland, J. R., D. J. Hawkes, T. Schaeffter, and A. P. King (2013). “Respiratory motion models: a review”. *Med Image Anal* 17.1, pp. 19–42.
- Menten, M. J., M. F. Fast, S. Nill, C. P. Kamerling, F. McDonald, and U. Oelfke (2016). “Lung stereotactic body radiotherapy with an MR-linac—Quantifying the impact of the magnetic field and real-time tumor tracking”. *Radiother Oncol* 119.3, pp. 461–466.

- Meschini, G., C. Paganelli, C. Gianoli, P. Summers, M. Bellomi, G. Baroni, and M. Riboldi (2019). “A clustering approach to 4D MRI retrospective sorting for the investigation of different surrogates”. *Phys Medica* 58, pp. 107–113.
- Mickevicius, N. J. and E. S. Paulson (2017). “Investigation of undersampling and reconstruction algorithm dependence on respiratory correlated 4D-MRI for online MR-guided radiation therapy”. *Phys Med Biol* 62.8, pp. 2910–2921.
- (2019). “Simultaneous acquisition of orthogonal plane cine imaging and isotropic 4D-MRI using super-resolution”. *Radiother Oncol* 136, pp. 121–129.
- Modat, M., J. McClelland, and S. Ourselin (2010). “Lung registration using the NiftyReg package”. *Medical Image Analysis for the Clinic-A Grand Challenge 2010*, pp. 33–42.
- Möller, H. E., X. J. Chen, B. Saam, K. D. Hagspiel, G. A. Johnson, T. A. Altes, E. E. de Lange, and H. Kauczor (2002). “MRI of the lungs using hyperpolarized noble gases”. *Magn Res Med* 47.6, pp. 1029–1051.
- Mutic, S. and J. F. Dempsey (2014). “The ViewRay system: magnetic resonance-guided and controlled radiotherapy”. *Semin Radiat Oncol* 24.3, pp. 196–199.
- NICE (2019). *Lung cancer: diagnosis and management*. URL: <https://www.nice.org.uk/guidance/ng122/chapter/Recommendations>.
- Nyholm, T., M. Nyberg, M. G. Karlsson, and M. Karlsson (2009). “Systematisation of spatial uncertainties for comparison between a MR and a CT-based radiotherapy workflow for prostate treatments”. *Radiat Oncol* 4.54.
- Ohno, Y., H. Koyama, T. Yoshikawa, S. Seki, D. Takenaka, M. Yui, A. Lu, M. Miyazaki, and K. Sugimura (2016). “Pulmonary high-resolution ultrashort TE MR imaging: Comparison with thin-section standard-and low-dose computed tomography for the assessment of pulmonary parenchyma diseases”. *J Magn Reson Imaging* 43.2, pp. 512–532.
- Ourselin, S., A. Roche, G. Subsol, X. Pennec, and N. Ayache (2001). “Reconstructing a 3D structure from serial histological sections”. *Image Vision Comput* 19.1-2, pp. 25–31.

- Owringi, A. M., P. B. Greer, and C. K. Glide-Hurst (2018). “MRI-only treatment planning: benefits and challenges”. *Phys Med Biol* 63.5, 05TR01.
- Paganelli, C., P. Summers, M. Bellomi, G. Baroni, and M. Riboldi (2015). “Liver 4DMRI: A retrospective image-based sorting method”. *Med Phys* 42.8, pp. 4814–4821.
- Paul, J., E. Divkovic, S. Wundrak, P. Bernhardt, W. Rottbauer, H. Neumann, and V. Rasche (2015). “High-resolution respiratory self-gated golden angle cardiac MRI: comparison of self-gating methods in combination with k-t SPARSE SENSE”. *Magn Res Med* 73.1, pp. 292–298.
- Paulson, E. S., B. Erickson, C. Schultz, and X. A. Li (2015). “Comprehensive MRI simulation methodology using a dedicated MRI scanner in radiation oncology for external beam radiation treatment planning”. *Med Phys* 42.1, pp. 28–39.
- Paulson, E. S., S. P. M. Crijns, B. M. Keller, J. Wang, M. A. Schmidt, G. Coutts, and U. A. van der Heide (2016). “Consensus opinion on MRI simulation for external beam radiation treatment planning”. *Radiother Oncol* 121.2, pp. 187–192.
- Perrin, R. L., M. Zakova, M. Peroni, K. Bernatowicz, C. Bikis, A. K. Knopf, S. Safai, P. Fernandez-Carmona, N. Tschärner, and D. C. Weber (2017). “An anthropomorphic breathing phantom of the thorax for testing new motion mitigation techniques for pencil beam scanning proton therapy”. *Phys Med Biol* 62.6, p. 2486.
- Persson, G. F., D. E. Nygaard, C. Brink, J. W. Jahn, P. M. af Rosenschöld, L. Specht, and S. S. Korreman (2010). “Deviations in delineated GTV caused by artefacts in 4DCT”. *Radiother Oncol* 96.1, pp. 61–66.
- Pluim, J. P. W., J. B. A. Maintz, and M. A. Viergever (2003). “Mutual-information-based registration of medical images: a survey”. *IEEE Trans Med Imaging* 22.8, pp. 986–1004.
- Prieto, C., S. Uribe, R. Razavi, D. Atkinson, and T. Schaeffter (2010). “3D undersampled golden-radial phase encoding for DCE-MRA using inherently regularized iterative SENSE”. *Magn Res Med* 64.2, pp. 514–526.

- Prior, P., X. Chen, E. Gore, C. Johnstone, and X. A. Li (2017). “Is Bulk Electron Density Assignment Appropriate for MRI-only Based Treatment Planning for Lung Cancer?” *Med Phys* 44.7, pp. 3437–3443.
- Qin, C., J. Schlemper, J. Caballero, A. N. Price, J. V. Hajnal, and D. Rueckert (2019). “Convolutional recurrent neural networks for dynamic MR image reconstruction”. *IEEE T Med Imaging* 38.1, pp. 280–290.
- Raaijmakers, A. J. E., B. W. Raaymakers, and J. J. W. Lagendijk (2005). “Integrating a MRI scanner with a 6 MV radiotherapy accelerator: dose increase at tissue–air interfaces in a lateral magnetic field due to returning electrons”. *Phys Med Biol* 50.7, p. 1363.
- Raaymakers, B. W., J. J. W. Lagendijk, J. Overweg, J. G. M. Kok, A. J. E. Raaijmakers, E. M. Kerkhof, R. W. van der Put, I. Meijnsing, S. P. M. Crijs, and F. Benedosso (2009). “Integrating a 1.5 T MRI scanner with a 6 MV accelerator: proof of concept”. *Phys Med Biol* 54.12, N229.
- Ramella, S., M. Fiore, S. Silipigni, M. C. Zappa, M. Jaus, A. M. Alberti, P. Matteucci, E. Molfese, P. Cornacchione, and C. Greco (2017). “Local control and toxicity of adaptive radiotherapy using weekly CT imaging: results from the LARTIA trial in stage III NSCLC”. *J Thorac Oncol* 12.7, pp. 1122–1130.
- Rank, C. M., C. Tremmel, N. Hunemohr, A. M. Nagel, O. Jakel, and S. Greilich (2013). “MRI-based treatment plan simulation and adaptation for ion radiotherapy using a classification-based approach”. *Radiat Oncol* 8.51.
- Rank, C. M., T. Heußer, M. T. A. Buzan, A. Wetscherek, M. T. Freitag, J. Dinkel, and M. Kachelrieß (2017). “4D respiratory motion-compensated image reconstruction of free-breathing radial MR data with very high undersampling”. *Magn Res Med* 77.3, pp. 1170–1183.
- Rasch, C., R. Keus, F. A. Pameijer, W. Koops, S. Muller, A. Touw, H. Bartelink, and J. V. Lebesque (1997). “The potential impact of CT-MRI matching on tumor volume delineation in advanced head and neck cancer”. *Int J Radiat Oncol Biol Phys* 39.4, pp. 841–848.

- Rasch, C., I. Barillot, P. Remeijer, A. Touw, M. van Herk, and J. V. Lebesque (1999). “Definition of the prostate in CT and MRI: a multi-observer study”. *Int J Radiat Oncol Biol Phys* 43.1, pp. 57–66.
- Rasmussen, C. E. and C. K. I. Williams (2006). *Gaussian processes for machine learning*. Vol. 1. MIT press Cambridge.
- Riddell, A. M., J. Hillier, G. Brown, D. M. King, A. C. Wotherspoon, J. N. Thompson, D. Cunningham, and W. H. Allum (2006). “Potential of surface-coil MRI for staging of esophageal cancer”. *Am J Roentgenol* 187.5, pp. 1280–1287.
- Ronneberger, O., P. Fischer, and T. Brox (2015). “U-net: Convolutional networks for biomedical image segmentation”. *Proc. of the MICCAI 18th Meeting*, pp. 234–241.
- Rose, J., G. Rodrigues, B. Yaremko, M. Lock, and D. D’Souza (2009). “Systematic review of dose–volume parameters in the prediction of esophagitis in thoracic radiotherapy”. *Radiother Oncol* 91.3, pp. 282–287.
- Rosenblum, L. J., R. A. Mauceri, D. E. Wellenstein, F. D. Thomas, D. A. Bassano, B. N. Raasch, C. C. Chamberlain, and E. R. Heitzman (1980). “Density patterns in the normal lung as determined by computed tomography”. *Radiology* 137.2, pp. 409–416.
- Rueckert, D., L. I. Sonoda, C. Hayes, D. L. G. Hill, M. O. Leach, and D. J. Hawkes (1999). “Nonrigid registration using free-form deformations: application to breast MR images”. *IEEE T Med Imaging* 18.8, pp. 712–721.
- Sahiner, B., A. Pezeshk, L. M. Hadjiiski, X. Wang, K. Drukker, K. H. Cha, R. M. Summers, and M. L. Giger (2019). “Deep learning in medical imaging and radiation therapy”. *Med Phys* 46.1, e1–e36.
- Schlemper, J., J. Caballero, J. V. Hajnal, A. N. Price, and D. Rueckert (2017). “A deep cascade of convolutional neural networks for dynamic MR image reconstruction”. *IEEE Trans Med Imaging* 37.2, pp. 491–503.
- Schmidt, M. A. and G. S. Payne (2015). “Radiotherapy planning using MRI”. *Phys Med Biol* 60.22, R323.

- Shannon, C. E. (1949). “Communication in the presence of noise”. *Proc Inst Radio Engrs* 37, pp. 10–21.
- Soejima, K., K. Yamaguchi, E. Kohda, K. E. I. Takeshita, Y. Ito, H. Mastubara, T. Oguma, T. Inoue, Y. Okubo, and K. Amakawa (2000). “Longitudinal follow-up study of smoking-induced lung density changes by high-resolution computed tomography”. *Am J Respir Crit Care Med* 161.4, pp. 1264–1273.
- Soille, P. (1999). “Segmentation”. *Morphological Image Analysis*. Springer, pp. 229–254.
- Soliman, A. S., L. Burns, A. Owrangi, Y. Lee, W. Y. Song, G. Stanisiz, and B. P. Chugh (2017). “A realistic phantom for validating MRI-based synthetic CT images of the human skull”. *Med Phys* 44.9, pp. 4687–4694.
- Sotiras, A., C. Davatzikos, and N. Paragios (2013). “Deformable medical image registration: A survey”. *IEEE T Med Imaging* 32.7, pp. 1153–1190.
- Srivastava, N., G. Hinton, A. Krizhevsky, I. Sutskever, and R. Salakhutdinov (2014). “Dropout: a simple way to prevent neural networks from overfitting”. *J Mach Learn Res* 15.1, pp. 1929–1958.
- Stanescu, T., K. Wachowicz, and D. A. Jaffray (2012). “Characterization of tissue magnetic susceptibility-induced distortions for MRIgRT”. *Med Phys* 39.12, pp. 7185–7193.
- Steenbakkens, R. J. H. M., J. C. Duppen, I. Fitton, K. E. I. Deurloo, L. J. Zijp, E. F. I. Comans, A. L. J. Uitterhoeve, P. T. R. Rodrigus, G. W. P. Kramer, and J. Bussink (2006). “Reduction of observer variation using matched CT-PET for lung cancer delineation: a three-dimensional analysis”. *Int J Radiat Oncol Biol Phys* 64.2, pp. 435–448.
- Stenkens, B., E. S. Paulson, and R. H. N. Tijssen (2018). “Nuts and bolts of 4D-MRI for radiotherapy”. *Phys Med Biol* 63.21, 21TR01.
- Stenkens, B., R. H. N. Tijssen, B. D. de Senneville, J. J. W. Lagendijk, and C. A. T. van den Berg (2016). “Image-driven, model-based 3D abdominal motion estimation for MR-guided radiotherapy”. *Phys Med Biol* 61.14, pp. 5335–5355.

- Stemkens, B., M. Glitzner, C. Kontaxis, B. D. De Senneville, F. M. Prins, S. P. M. Crijns, L. G. W. Kerkmeijer, J. J. W. Lagendijk, C. A. T. Van Den Berg, and R. H. N. Tijssen (2017). “Effect of intra-fraction motion on the accumulated dose for free-breathing MR-guided stereotactic body radiation therapy of renal-cell carcinoma”. *Phys Med Biol* 62.18, p. 7407.
- Suh, Y., S. Dieterich, B. Cho, and P. J. Keall (2008). “An analysis of thoracic and abdominal tumour motion for stereotactic body radiotherapy patients”. *Phys Med Biol* 53.13, p. 3623.
- Thirion, J. (1998). “Image matching as a diffusion process: an analogy with Maxwell’s demons”. *Med Image Anal* 2.3, pp. 243–260.
- Thwaites, D. I., P. Keall, L. Holloway, J. Sykes, and V. Cosgrove (2014). “Observations on MR-LINAC systems and rationale for MR-Linac use: The Australian MR-Linac project as an example”. *Phys Medica* 30, e25.
- Triphan, S. M. F., B. J. Jobst, F. A. Breuer, M. O. Wielpütz, H. Kauczor, J. Biederer, and P. M. Jakob (2015). “Echo time dependence of observed T1 in the human lung”. *J Magn Reson Imaging* 42.3, pp. 610–616.
- Tryggestad, E., A. Flammang, S. Han-Oh, R. Hales, J. Herman, T. McNutt, T. Roland, S. M. Shea, and J. Wong (2013). “Respiration-based sorting of dynamic MRI to derive representative 4D-MRI for radiotherapy planning”. *Med Phys* 40.5, pp. 51901–51909.
- Van Reeth, E., I. W. K. Tham, C. H. Tan, and C. L. Poh (2012). “Super-resolution in magnetic resonance imaging: A review”. *Concepts Magn Reson* 40.6, pp. 306–325.
- Van Reeth, E., C. H. Tan, I. W. K. Tham, and C. L. Poh (2015). “Isotropic reconstruction of a 4-D MRI thoracic sequence using super-resolution”. *Magn Res Med* 73.2, pp. 784–793.
- van de Lindt, T. N., J.-J. Sonke, M. E. Nowee, E. P. M. Jansen, V. W. J. van Pelt, U. A. van der Heide, and M. F. Fast (2018a). “A self-sorting coronal 4D-MRI method for daily image guidance of liver lesions on an MR-Linac”. *Int J Radiat Oncol Biol Phys* 102.4, pp. 875–884.

- van de Lindt, T. N., J.-J. Sonke, M. E. Nowee, E. P. M. Jansen, V. W. J. van Pelt, U. A. van der Heide, and M. F. Fast (2018b). “Retrospective self-sorted 4D-MRI for the liver”. *Radiother Oncol* 127.3, pp. 474–480.
- van Kesteren, Z., A. van der Horst, O. J. Gurney-Champion, I. Bones, D. Tekelenburg, T. Alderliesten, G. van Tienhoven, R. Klaassen, H. W. M. van Laarhoven, and A. Bel (2019). “A novel amplitude binning strategy to handle irregular breathing during 4DMRI acquisition: improved imaging for radiotherapy purposes”. *Radiat Oncol* 14.1, p. 80.
- Vedam, S. S., P. J. Keall, V. R. Kini, H. Mostafavi, H. P. Shukla, and R. Mohan (2002). “Acquiring a four-dimensional computed tomography dataset using an external respiratory signal”. *Phys Med Biol* 48.1, pp. 45–62.
- Vercauteren, T., X. Pennec, A. Perchant, and N. Ayache (2009). “Diffeomorphic demons: Efficient non-parametric image registration”. *NeuroImage* 45.1, S61–S72.
- Versteijne, E., O. J. Gurney-Champion, A. van der Horst, E. Lens, M. W. Kolff, J. Buijsen, G. Ebrahimi, K. J. Neelis, C. R. N. Rasch, and J. Stoker (2017). “Considerable interobserver variation in delineation of pancreatic cancer on 3DCT and 4DCT: a multi-institutional study”. *Radiat Oncol* 12.1, p. 58.
- Wang, G., D. Garcia, Y. Liu, R. De Jeu, and A. J. Dolman (2012). “A three-dimensional gap filling method for large geophysical datasets: Application to global satellite soil moisture observations”. *Environ Model Softw* 30, pp. 139–142.
- Wang, H., H. Chandarana, K. T. Block, T. Vahle, M. Fenchel, and I. J. Das (2017). “Dosimetric evaluation of synthetic CT for magnetic resonance-only based radiotherapy planning of lung cancer”. *Radiat Oncol* 12.1, p. 108.
- Wang, Z., A. C. Bovik, H. R. Sheikh, and E. P. Simoncelli (2004). “Image quality assessment: from error visibility to structural similarity”. *IEEE T Image Process* 13.4, pp. 600–612.
- Webb, S. (2007). “Adapting IMRT delivery fraction-by-fraction to cater for variable intrafraction motion”. *Phys Med Biol* 53.1, p. 1.

- Webb, S., D. R. Dance, S. Evans, C. L. Skinner, A. G. Bradley, I. A. Castellano, H. J. Dobbs, R. J. Ott, M. A. Flower, A. D. Hall, P. K. Marsden, J. W. Babich, J. Bamber, N. R. Miller, M. Tristram, S. J. Doran, M. O. Leach, C. H. Jones, B. H. Brown, J. C. Hebden, J. Suckling, C. R. Hill, G. C. Flux, S. Sassi, and R. E. Bentley (2012). *Webb's Physics of Medical Imaging*. 2nd. Taylor & Francis Group. ISBN: 9780750305730.
- Weygand, J., C. D. Fuller, G. S. Ibbott, A. S. R. Mohamed, Y. Ding, J. Yang, K.-P. Hwang, and J. Wang (2016). "Spatial Precision in Magnetic Resonance Imaging-Guided Radiotherapy: The Role of Geometric Distortion". *Int J Radiat Oncol* 95.4, pp. 1304–1316.
- Wild, J. M., H. Marshall, M. Bock, L. R. Schad, P. M. Jakob, M. Puderbach, F. Molinari, E. J. R. Van Beek, and J. Biederer (2012). "MRI of the lung (1/3): methods". *Insights Imaging* 3.4, pp. 345–353.
- Winkelmann, S., T. Schaeffter, T. Koehler, H. Eggers, and O. Doessel (2007). "An optimal radial profile order based on the Golden Ratio for time-resolved MRI". *IEEE T Med Imaging* 26.1, pp. 68–76.
- Wolthaus, J. W. H., J. Sonke, M. van Herk, and E. M. F. Damen (2008a). "Reconstruction of a time-averaged midposition CT scan for radiotherapy planning of lung cancer patients using deformable registration". *Med Phys* 35.9, pp. 3998–4011.
- Wolthaus, J. W. H., J.-J. Sonke, M. van Herk, J. S. A. Belderbos, M. M. G. Rossi, J. V. Lebesque, and E. M. F. Damen (2008b). "Comparison of different strategies to use four-dimensional computed tomography in treatment planning for lung cancer patients". *Int J Radiat Oncol* 70.4, pp. 1229–1238.
- World Health Organization (2019). *Cancer fact sheet*. URL: <https://www.who.int/news-room/fact-sheets/detail/cancer>.
- Yamamoto, T., U. Langner, B. W. Loo Jr, J. Shen, and P. J. Keall (2008). "Retrospective analysis of artifacts in four-dimensional CT images of 50 abdominal and thoracic radiotherapy patients". *Int J Radiat Oncol Biol Phys* 72.4, pp. 1250–1258.

- Yang, J., J. Cai, H. Wang, Z. Chang, B. G. Czito, M. R. Bashir, and F.-F. Yin (2014). “Four-dimensional magnetic resonance imaging using axial body area as respiratory surrogate: initial patient results”. *Int J Radiat Oncol Biol Phys* 88.4, pp. 907–912.
- Ye, J. C., S. Tak, Y. Han, and H. W. Park (2007). “Projection reconstruction MR imaging using FOCUSS”. *Magn Res Med* 57.4, pp. 764–775.
- Zhu, B., J. Z. Liu, S. F. Cauley, B. R. Rosen, and M. S. Rosen (2018). “Image reconstruction by domain-transform manifold learning”. *Nature* 555.7697, p. 487.
- Ziegenhein, P., I. N. Kozin, C. P. Kamerling, and U. Oelfke (2017). “Towards real-time photon Monte Carlo dose calculation in the cloud”. *Phys Med Biol* 62.11, p. 4375.

Dissemination of research

Peer reviewed journal papers

Freedman JN, Collins DJ, Bainbridge HE, Rank CM, Nill S, Kachelrieß M, Oelfke U, Leach MO & Wetscherek A 2017 T2-Weighted 4D Magnetic Resonance Imaging for Application in Magnetic Resonance-Guided Radiotherapy Treatment Planning *Invest Radiol* **57**, 563-573.

Freedman JN, Collins DJ, Gurney-Champion OJ, McClelland J, Nill S, Oelfke U, Leach MO & Wetscherek A 2018 Super-resolution T2-weighted 4D MRI for image guided radiotherapy *Radiother Oncol* **129**(3), 486-493.

Freedman JN, Bainbridge HE, Nill S, Collins DJ, Kachelrieß M, Leach MO, McDonald F, Oelfke U & Wetscherek A 2019 Synthetic 4D-CT of the thorax for treatment plan adaptation on MR-guided radiotherapy systems *Phys Med Biol* **64**, 115005.

Conference proceedings

Freedman JN, Collins DJ, Rank CM, Bainbridge HE, Nill S, Kachelrieß M, Oelfke U, Leach MO & Wetscherek A 4D-T2 Weighted MRI for Lung Radiotherapy Treatment Planning. Poster presentation at 25th Annual Meeting and Exhibition of the International Society of Magnetic Resonance in Medicine, Honolulu, Hawaii, USA, April 2017.

Freedman JN, Collins DJ, Rank CM, Bainbridge HE, Nill S, Kachelrieß M, Oelfke U, Leach MO & Wetscherek A Evaluation of 4D-T2w MRI Methods for Lung Radiotherapy Treatment Planning with Application to an MR-Linac. Poster presentation at 25th Annual Meeting and Exhibition of the International Society of Magnetic Resonance in Medicine, Honolulu, Hawaii, USA, April 2017.

Freedman JN, Collins DJ, Nill S, Rank CM, Stemmer A, Kachelrieß M, Oelfke U, Leach MO & Wetscherek A 4D-Dixon MRI for 4D pseudo-CT generation in a thoracic MR-only workflow. Oral presentation at 5th Magnetic Resonance in Radiation Therapy Symposium, Sydney, New South Wales, Australia, June 2017.

Freedman JN, Bainbridge HE, Wetscherek A, Collins DJ, Nill S, A Dunlop, Kachelrieß M, Leach MO, McDonald F & Oelfke U Dosimetric Evaluation of Midposition Pseudo-CT for MR-only Lung Radiotherapy Treatment planning. Poster presentation at 37th European Society for Radiotherapy and Oncology Congress, Barcelona, Spain, April 2018.

Freedman JN, Collins DJ, Gurney-Champion O, Nill S, Oelfke U, Leach MO & Wetscherek A Online Super-resolution 4D T2-weighted MRI for MRI-guided Radiotherapy. Power-pitch presentation at 26th Annual Meeting and Exhibition of the International Society of Magnetic Resonance in Medicine, Paris, France, June 2018. [Magna cum laude abstract award].

Freedman JN, Gurney-Champion O, Nill S, Collins DJ, Eccles C, Herbert T, McNair H, Huddart R, Leach MO, Oelfke U & Wetscherek A 4D-T2w MRI on an MR-linac. Poster presentation at 6th Magnetic Resonance in Radiation Therapy Symposium, Utrecht, The Netherlands, July 2018

Gurney-Champion O, Goncalves SI, Freedman JN, Wetscherek A, Nederveen AJ, Nill S, Harrington K & Oelfke U The implementation of alternating repetition time balanced steady state free precession MRI sequence on the MR-linac for fat suppressed balanced steady state imaging. Oral presentation at 6th Magnetic Resonance in Radiation Therapy Symposium, Utrecht, The Netherlands, July 2018

Freedman JN, Gurney-Champion O, Bainbridge HE, Kieselmann JP, Dubec M, Mandeville HC, Nill S, Kachelrieß M, Oelfke U, Leach MO & Wetscherek A Online Super-resolution Rapid 4D-MRI reconstruction using a Deep RAdial ConvoLutionAl neural network: Dracula. Poster presentation at 27th Annual Meeting and Exhibition of the International Society of Magnetic Resonance in Medicine, Montreal, Canada, May 2019

Appendix A

**T2-Weighted 4D Magnetic Resonance Imaging
for Application in Magnetic Resonance–Guided
Radiotherapy Treatment Planning**

Freedman *et al.* 2017

OPEN

T2-Weighted 4D Magnetic Resonance Imaging for Application in Magnetic Resonance–Guided Radiotherapy Treatment Planning

Joshua N. Freedman, MSci,*† David J. Collins, BA,† Hannah Bainbridge, MBChB, FRCR,‡
 Christopher M. Rank, PhD,§ Simeon Nill, PhD,* Marc Kachelrieß, PhD,§ Uwe Oelfke, PhD,*
 Martin O. Leach, PhD, FMedSci,† and Andreas Wetscherek, PhD*

Objectives: The aim of this study was to develop and verify a method to obtain good temporal resolution T2-weighted 4-dimensional (4D-T2w) magnetic resonance imaging (MRI) by using motion information from T1-weighted 4D (4D-T1w) MRI, to support treatment planning in MR-guided radiotherapy.

Materials and Methods: Ten patients with primary non–small cell lung cancer were scanned at 1.5 T axially with a volumetric T2-weighted turbo spin echo sequence gated to exhalation and a volumetric T1-weighted stack-of-stars spoiled gradient echo sequence with golden angle spacing acquired in free breathing. From the latter, 20 respiratory phases were reconstructed using the recently developed 4D joint MoCo-HDTV algorithm based on the self-gating signal obtained from the k-space center. Motion vector fields describing the respiratory cycle were obtained by deformable image registration between the respiratory phases and projected onto the T2-weighted image volume. The resulting 4D-T2w volumes were verified against the 4D-T1w volumes: an edge-detection method was used to measure the diaphragm positions; the locations of anatomical landmarks delineated by a radiation oncologist were compared and normalized mutual information was calculated to evaluate volumetric image similarity.

Results: High-resolution 4D-T2w MRI was obtained. Respiratory motion was preserved on calculated 4D-T2w MRI, with median diaphragm positions being consistent with less than 6.6 mm (2 voxels) for all patients and less than 3.3 mm (1 voxel) for 9 of 10 patients. Geometrical positions were coherent between 4D-T1w and 4D-T2w MRI as Euclidean distances between all corresponding anatomical landmarks agreed to within 7.6 mm (Euclidean distance of 2 voxels) and were below 3.8 mm (Euclidean distance of 1 voxel) for 355 of 470 pairs of anatomical landmarks. Volumetric image similarity was commensurate between 4D-T1w and 4D-T2w MRI, as mean percentage differences in normalized mutual information (calculated over all respiratory phases and patients), between corresponding respiratory phases of 4D-T1w and 4D-T2w MRI and the tie-phase of 4D-T1w and 3-dimensional T2w MRI, were consistent to $0.41\% \pm 0.37\%$. Four-dimensional T2w MRI displayed tumor extent, structure, and position more clearly than corresponding 4D-T1w MRI, especially when mobile tumor sites were adjacent to organs at risk.

Conclusions: A methodology to obtain 4D-T2w MRI that retrospectively applies the motion information from 4D-T1w MRI to 3-dimensional T2w MRI was developed and verified. Four-dimensional T2w MRI can assist clinicians in

delineating mobile lesions that are difficult to define on 4D-T1w MRI, because of poor tumor-tissue contrast.

Key Words: 4D MRI, motion model, motion vector field, MR-linac, radiotherapy treatment planning, 4D-T2w MRI

(*Invest Radiol* 2017;52: 563–573)

Designing a radiotherapy treatment plan (RTP) for lung and abdominal cancer is challenging due to the motion of the abdominal-thoracic region.¹ An appropriate RTP should deliver the prescribed dose to the target and minimize dose to radiosensitive healthy structures. Unlike conventional free breathing scans where generic margins are added, 4-dimensional (4D) images provide information on individual tumor motion, which can be used to generate a more personalized RTP.²

Strategies have been proposed to manage abdominal-thoracic motion, such as breath-hold or gated treatment.¹ Yet these approaches are suboptimal because they can be challenging for patients with primary lung malignancies or can lengthen treatment time. Motion information from image-guided radiotherapy (IGRT) is used to improve treatment delivery.³

Several imaging modalities can be used for IGRT, such as orthogonal kilovolt imaging, cone-beam computed tomography or, with the advent of hybrid MR-IGRT systems,^{4–8} magnetic resonance imaging (MRI). Compared with cone-beam computed tomography, MRI exhibits improved soft tissue contrast, is a nonionizing modality, and offers a range of clinically relevant contrasts.⁹ However, MRI is limited by intrinsic spatial uncertainty,¹⁰ and there is no direct relationship between electron density and the MRI signal, whereas a knowledge of electron density is required for dose calculations.¹¹

In this manuscript, 4D MRI is defined as a time series of 3-dimensional (3D) MRI scan volumes, where each volume corresponds to a different time point in the respiratory cycle. In current clinical practice, 4D MRI could be used to inform an RTP by providing additional information, such as improved soft tissue contrast, absent in 4D CT.⁹ In the near future, 4D MRI might be acquired on hybrid MR-IGRT systems to provide information to support RTP adaptation with improved setup and beam guidance.⁵ Thus, there is a great need for robust methods for generating 4D MRI.

Previous work to produce 4D MRI can be loosely split into dynamic slice-selective 2-dimensional (2D) and volumetric 3D acquisition schemes. Two-dimensional MRI can be prospectively acquired at specific respiratory phases by triggering acquisition with the aid of a synchronized respiratory signal. A complete 4D MRI volume is then constructed by continuously measuring slices at all required planes and respiratory phases.¹² However, triggering delays have been reported, where triggering of the current phase is ignored due to continuing measurement of the preceding phase, which can result in a long acquisition time.¹³

Alternatively, 4D MRI can be constructed retrospectively by sorting measured slices with the aid of a respiratory signal. Both external and internal respiratory signals have been utilized. Among others, the center of k-space (self-gating),^{14,15} body area,¹⁶ and diaphragm position^{17–19} have been used as internal respiratory signals. External respiratory signals

Received for publication January 31, 2017; and accepted for publication, after revision, March 20, 2017.

From the *Joint Department of Physics, †CR UK Cancer Imaging Centre, and ‡Joint Department of Radiotherapy, The Institute of Cancer Research and The Royal Marsden NHS Foundation Trust, London, United Kingdom; and §Medical Physics in Radiology, German Cancer Research Center (DKFZ), Heidelberg, Germany.

Conflicts of interest and sources of funding: none declared.

Supplemental digital contents are available for this article. Direct URL citations appear in the printed text and are provided in the HTML and PDF versions of this article on the journal's Web site (www.investigativeradiology.com).

Correspondence to: Martin O. Leach, PhD, FMedSci, CR UK Cancer Imaging Centre, The Institute of Cancer Research and The Royal Marsden NHS Foundation Trust, 123 Old Brompton Road, London, SW7 3RP, United Kingdom. E-mail: Martin.Leach@icr.ac.uk. Copyright © 2017 The Author(s). Published by Wolters Kluwer Health, Inc. This is an open access article distributed under the Creative Commons Attribution License 4.0 (CCBY), which permits unrestricted use, distribution, and reproduction in any medium, provided the original work is properly cited.

ISSN: 0020-9996/17/5210-0563

DOI: 10.1097/RLI.0000000000000381

are typically acquired using a breathing belt,^{20–23} but clock drifts or poor respiratory correlation have been reported.^{18,24} Most commonly, the amplitude or phase of the respiratory signal has been applied to sort slices into bins of respiratory phase. Retrospective schemes suffer from data incompleteness artifacts, where a slice was not acquired in all respiratory phases, but can be mitigated by prolonged image acquisition.^{18,20}

Four-dimensional MRI constructed from aggregated and sorted 2D MRI often exhibits staircase artifacts, due to highly nonisotropic voxel sizes, and low temporal resolution, because of a limited acquisition time and possible through-plane geometrical distortion, since scanner software typically only corrects in-plane distortion. This last point has been addressed by some authors who have reported application of an offline 3D distortion correction to 2D MRI.¹⁸

Three-dimensional acquisition schemes do not have the limitations of 2D acquisition schemes and resulting 4D MRI could be of higher quality. Yet translating methods used in 2D acquisition schemes^{12,13,16,18,20,25} to 3D acquisition schemes is challenging because dynamic 3D MRI cannot typically be acquired with sufficient spatiotemporal resolution. However, good-quality 4D MRI has been obtained using advanced offline-reconstructions of highly undersampled data acquired using 3D non-Cartesian sequences.^{15,26–29}

Alternatively, 4D MRI can be generated by applying a motion model to a reference volume.³⁰ Blackall et al³¹ obtained 4D MRI by applying a single-parameter motion model, with motion vector fields (MVFs) extracted from intraoperative ultrasound images, to static MRI. In likewise methods, McClelland et al³² developed a temporal-fitting motion model for CT, which was based on performing deformable image registration between reference and free breathing volumes; Marx et al³³ generated 4D CT by applying the motion information from 4D MRI to 3D CT. Recently, Stemkens et al³⁴ proposed a motion model to generate real-time 4D MRI, where a set of MVFs were obtained based on dynamic 2D MRI and a reference volume.

To our knowledge, no method or motion model has been applied to generate 4D-T2w MRI from data measured with a 3D acquisition scheme. This might be because it is difficult to acquire dynamic 3D-T2w MRI, due to the long echo and repetition time required to achieve T2w contrast. Obtaining T2w MRI for lung RTP and guidance is important because T2w MRI is sensitive to both lung infiltrates and lesions with fluid content.³⁵ Furthermore, T2w MRI enables an improved visualization of both mobile organs at risk (OARs) and tumor sites when compared with T1-weighted (T1w) MRI for cases such as esophageal cancer.³⁶

In this study, we (1) introduce the MVF projection (MVFP) method, which provides a workflow to generate 4D-T2w MRI by applying the motion information from a 4D-T1w volume to a 3D-T2w volume; (2) verify calculated 4D-T2w MRI by comparing diaphragm positions, anatomical landmarks, and volumetric image similarity in generated 4D-T2w MRI to 4D-T1w MRI; and (3) discuss examples where 4D-T2w MRI more clearly shows tumor position, structure, and extent when compared with 4D-T1w MRI.

MATERIALS AND METHODS

Data Acquisition

Ten patients with non-small cell lung cancer (6 female, 4 male; aged, 63–86 years; 5 squamous cell carcinoma and 5 adenocarcinoma) were scanned with an axial 3D-T1w stack-of-stars spoiled gradient echo sequence in free breathing with golden angle spacing^{37,38} and an axial 3D-T2w turbo spin echo sequence³⁹ with respiratory gating to exhalation at 1.5 T (MAGNETOM Aera; Siemens Healthcare, Erlangen, Germany). Axial orientation was chosen to facilitate delineation for the purpose of RTP. The T2w sequence was gated to exhalation using a liver dome navigator.⁴⁰ The T1w sequence utilized a radial encoding scheme in the readout plane and a Cartesian slice encoding scheme.

Each consecutive radial plane was obtained after rotating by the golden angle ($\theta \approx 111.25$ degrees).³⁸

A range of sequence parameters were used due to variation in patient habitus. Initially, a relatively high bandwidth (1085 Hz) was selected (patients 1 to 6) but was later found to be suboptimal regarding image quality of reconstructed 4D-T1w MRI. After protocol optimization, a lower bandwidth (630 Hz) was used (patients 7 to 10), which resulted in an incremental improvement in image quality of 4D-T1w MRI and also enabled a smaller voxel size. Detailed acquisition parameters are listed in Table 1.

Reconstruction of T1w Data

The acquired data were retrospectively reconstructed using the 4D joint motion-compensated high-dimensional total variation (4D joint MoCo-HDTV) algorithm.¹⁵ Before reconstruction, an adaptive gradient-delay compensation was applied to the raw data, so that artifacts associated with inaccuracies in the timing of gradients were reduced.⁴¹ Afterward, the raw data were sorted into 20 overlapping respiratory phases based on the amplitude of the self-gating respiratory surrogate signal. The self-gating signal was extracted from the magnitude of the 9 central k-space points on each radial spoke that passed through the k-space center. Weightings of the HDTV operator were optimized by reducing temporal regularization such that the images remained clear from undersampling artifacts while avoiding over-regularization of true motion. Subsequently, an offline gradient nonlinearity distortion correction was applied to each respiratory phase of the reconstructed 4D-T1w volume, using a spherical harmonics deconvolution method.^{42,43}

Overview of the MVF Projection Method

The MVFP method generates 4D-T2w MRI by extracting motion information from 4D-T1w MRI and applying it, using a chain method, to 3D-T2w MRI. An overview of the MVFP method is displayed in Figure 1.

TABLE 1. Acquisition Parameters of the T1w and T2w Sequences

Parameter	T1w	T2w
No. patients	10	10
Orientation	Axial	Axial
Echo train length	NA	62
No. slices	88–96	80–96
Slice resolution, %	100.0	80.0–100.0
Slice oversampling, %	16.7–27.7	25.0–40.0
No. spokes per slice	935–1440	NA
Total acquisition time, min	04:58–07:42	05:34–09:16
Field of view, mm ³	336 × 336 × 288–384 × 384 × 290	420 × 242 × 264–480 × 288 × 290
Voxel size, mm ³	1.31 × 1.31 × 3.0–1.5 × 1.5 × 3.3	1.31 × 1.31 × 3.0–1.5 × 1.5 × 3.3
Echo time, ms	1.24–1.55	108–115
Repetition time, ms	2.51–3.18	1000–1500
Flip angle, degree	8–12	90
Pixel bandwidth, Hz	630–1085	560–600
Fat suppression	Yes	8: Yes, 2: No

Patient habitus determined acquisition parameters. Using a lower bandwidth of 630 Hz for the T1w sequence (patients 7 to 10) resulted in slightly improved results of the joint MoCo-HDTV reconstruction. Fat suppression was used in 8 of 10 cases for the T2w sequence.

T1w indicates T1-weighted; T2w, T2-weighted; NA, not applicable.

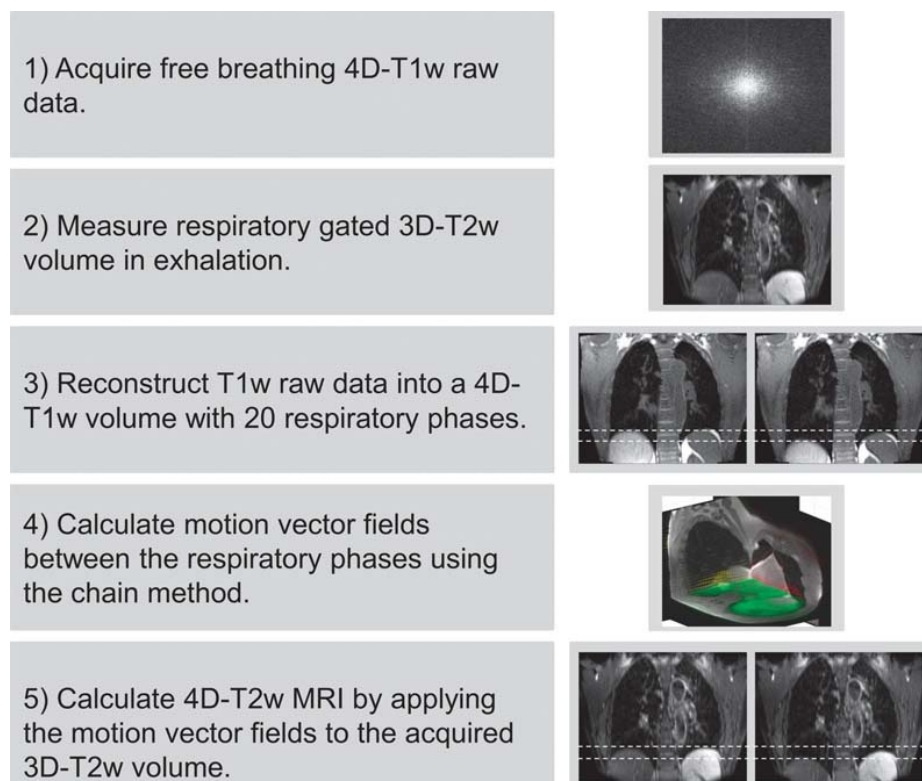


FIGURE 1. A visual overview of the motion vector field projection method. Note that the green, red, and yellow arrows in step 4 display the motion vector fields corresponding to the shown axial, coronal, and sagittal planes. Dashed white lines aid visualization of the diaphragm position on T1w and T2w MRI.

Calculation and Application of MVFs

A one-dimensional signal describing image similarity was obtained by calculating the normalized mutual information (NMI)⁴⁴ (calculated in-plane and averaged over all slices) between the 3D-T2w volume and each respiratory phase j contained in the 4D-T1w volume; where $j \in N$ (total number) respiratory phases. The respiratory phase i of the 3D-T2w volume was set equal to the respiratory phase j that corresponded to the signal maximum. In this way, a tie-phase was established between the 4D-T1w and 3D-T2w volumes.

Motion vector fields between the respiratory phases i and j of the reconstructed volumes ($T1_i$, $T1_j$) were calculated by deformable image registration. A b-spline GPU accelerated implementation of NiftyReg^{45,46} was used to calculate all deformable image registrations.

A chain method, similar to that proposed by Boldea et al,⁴⁷ was developed where the 3D-T1w volume at the n^{th} phase ($T1'_n$) was obtained by sequentially applying a number of smaller deformations that are linked together at calculated chain-point phases, to the tie-phase ($T1_i$). The chain method enables a balance between errors resulting from large deformations and concatenation of sequential deformations. An overview of the chain method can be found in Figure 2.

The chain-point phases were calculated based on fractions of the calculated image similarity signal range. This is possible because the image similarity signal indirectly corresponds to the deformation size between phases. The chain-point phases corresponding to inspiration were set equal to those of expiration, which is feasible because of the symmetry present in the respiratory pattern. A maximum of 3 deformations were chosen, and phases closest to 33% and 67% of the signal range were set as chain-points.

The parameters of NiftyReg were optimized by comparing the estimated ($T1'$) and reconstructed ($T1$) 4D-T1w volumes. The root mean square error (RMSE), dice coefficient (averaged over all respiratory phases), and visual image quality were analyzed as metrics. An NMI cost function with number of levels performed = 3, control point spacing = 3 mm, bending energy weighting = 0, Jacobian penalty weighting = 0, and maximum iterations = 500 was best able to reproduce the reconstructed 4D-T1w volume (dice > 0.965, RMSE < 5%, good qualitative agreement).

The 3D-T2w volume was registered and then interpolated to the matrix size of the 4D-T1w tie-phase. Calculated 4D-T2w MRI is then obtained by applying the calculated MVFs, using the chain method, to the registered and interpolated 3D-T2w volume.

All calculations were undertaken on an Intel Xeon E5-1660 processor with 8 cores at 3 GHz and 64 GB of memory.

Verification of the 4D-T2w Volumes

The calculated 4D-T2w volumes were verified against their corresponding 4D-T1w volumes. Using MATLAB (The MathWorks, Natick, MA), a semiautomated edge-detection method was developed and used to verify the diaphragm positions, a radiation oncologist manually delineated control points for comparison of anatomical positions and the NMI was calculated to assess volumetric image similarity. For each metric, the differences between 4D-T1w and 4D-T2w MRI were compared with those between 4D-T1w and 3D-T2w MRI.

In the edge-detection method, the user manually places a rectangular 2D region of interest (ROI) over the right hemidiaphragm surface, orientated along the superior-inferior (SI) direction, on a coronal or

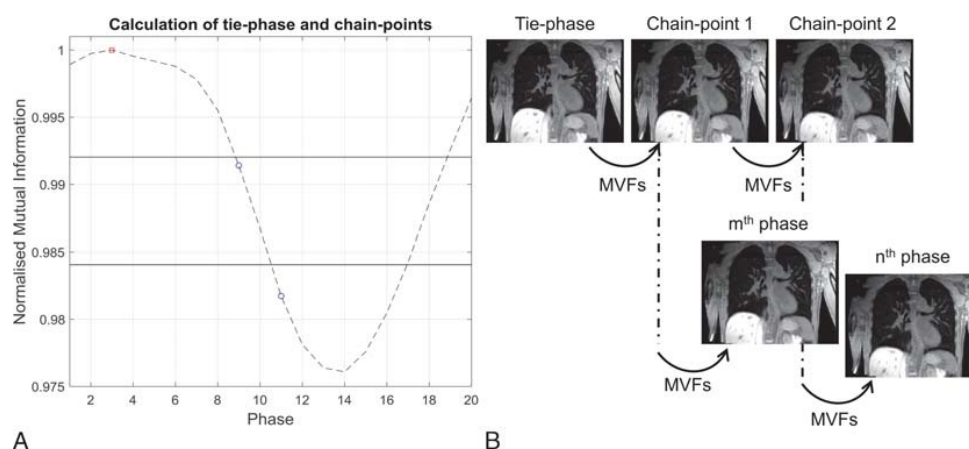


FIGURE 2. A, Displays the image similarity signal with the tie-point phase (red square) and chain-point phases (blue circles). The values (horizontal solid lines) of the fractions of the signal range, used to calculate the chain-point phases, are shown. B, The volumes corresponding to the chain-point phases are determined by sequentially warping the tie-phase with the required motion vector fields. The chain-point phases are used as a starting point to generate any arbitrary phase. For instance, the m^{th} phase is calculated with 2 deformations (tie-phase \rightarrow chain-point 1; chain-point 1 \rightarrow m^{th} phase) and the n^{th} phase requires 3 deformations (tie-phase \rightarrow chain-point 1; chain-point 1 \rightarrow chain-point 2; chain-point 2 \rightarrow n^{th} phase).

sagittal slice. Along the SI dimension, the ROI should be sufficiently large to encompass expected respiratory motion (approximately 2–3 cm) and narrow in the medial-lateral dimension such that the bounded diaphragm surface is approximately flat. For consistency, an ROI was placed on the coronal slice that exhibited both the aortic arch and the descending aorta.

Intensity was measured along all SI lines within the 2D ROI. For each SI line, the diaphragm position was calculated by fitting a Gaussian to the derivative of the measured line intensity. To increase robustness, a ramp function was used. Outliers in diaphragm position across all SI lines were removed based on the interquartile range of the detected diaphragm positions. The diaphragm position was chosen as the mean of the remaining diaphragm positions within the 2D ROI and the standard deviation corresponds to the diaphragm width.

Using an in-house developed delineation toolkit, the radiation oncologist (6 years experience) identified 5 anatomical control points (1 static and 4 mobile) in even respiratory phases in both 4D-T1w and 4D-T2w MRI:

1. Posterior spinal canal at the superior aspect of T4.
2. Inferior point of the carina.
3. Bifurcation of the right middle and lower lobe bronchus.
4. Bifurcation of the left main bronchus and left upper lobe bronchus.
5. Right costophrenic angle.

The right costophrenic angle was delineated on coronal images, with the coronal slice chosen to correspond with the level of the bifurcation of the right upper and middle lobe bronchus. The delineation toolkit offered coronal, sagittal, and axial views and delineation could be performed on either of them. Figure 3 shows an example of control point delineation for patient 8. These particular control points were chosen because they are visible in both 4D-T1w and 4D-T2w MRI, as well as being reproducible across patient sets. To assess spatial coherence between landmarks, Euclidean distances were calculated between pairs of delineated points in both 4D-T1w and 4D-T2w MRI.

Normalized mutual information⁴⁴ was calculated between each corresponding respiratory phase of the 4D-T1w and 4D-T2w volumes. The result was compared with the NMI measured between each respiratory phase of the 4D-T1w volume and the 3D-T2w volume.

If 4D-T1w and 4D-T2w MRI are commensurate in respiratory phase and geometrical position, then the NMI for all respiratory phases should be similar to the NMI assessed between the tie-phase of the 4D-T1w volume and the 3D-T2w volume.

RESULTS

Four-dimensional T2w MRI was calculated for 10 patients with primary lung malignancies. Four-dimensional T1w MRI reconstruction, using a nonoptimized prototype implementation, took between 9 and 12 hours for 20 respiratory phases and the chain method took between 25 and 30 minutes. The mean period of the respiratory cycle averaged over patients was 4.1 ± 0.95 seconds. Figure 4 shows an example reconstructed 4D-T1w volume and a calculated 4D-T2w volume at respiratory phases corresponding to exhalation, midcycle, and inhalation. The movie in Supplemental Digital Content 1, <http://links.lww.com/RLI/A316>, displays a similar example, but with all respiratory phases. For all patients, 4D-T2w MRI exhibited qualitatively similar respiratory motion to corresponding 4D-T1w MRI.

Verification of 4D-T2w MRI

Mean diaphragm surface positions were calculated using the edge-detection method for all patients on both T1w and T2w images. Figure 5A displays an example of the diaphragm surface displacement for patient 5. Figure 5B shows the range of diaphragmatic displacement of 4D-T1w MRI, as calculated by the edge-detection method. Figure 5C shows the spread of the displacement between diaphragm positions on both T1w and T2w images across all respiratory phases. Median diaphragm positions were consistent with less than 1 slice thickness (3.3 mm) for all patients, except patient 7, which exhibited median displacements within 6.6 mm. For all patients, T1w and T2w MRI were less consistent at inhalation than at exhalation. The Pearson correlation coefficient was calculated between the median diaphragm differences of 4D-T1w and 4D-T2w MRI, and the range of diaphragmatic displacements in 4D-T1w MRI. No significant correlation ($r = -0.19$, $P = 0.60$) was observed.

There was a reduction in the mean and standard deviation, averaged over all patients, of the interquartile range of the differences in diaphragm positions over all respiratory phases, between 4D-T1w and

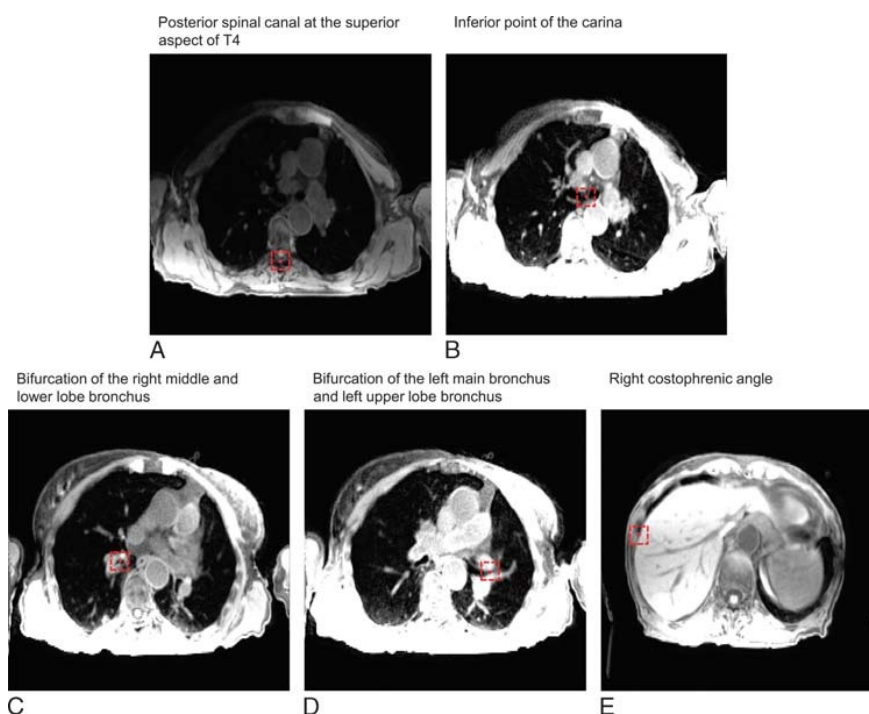


FIGURE 3. An example of control point delineation for patient 8 on a snapshot image of 4D-T1w MRI. The control points (red circles) are contained within dashed red boxes to assist visualization. The presented windowing scheme was optimized by the radiation oncologist for viewing of the anatomical landmark and not for surrounding anatomy.

4D-T2w MRI (1.11 ± 0.81 mm) compared to 4D-T1w and 3D-T2w MRI (9.83 ± 3.95 mm).

A radiation oncologist manually delineated 5 anatomical landmarks on both 4D-T1w and 4D-T2w MRI, and the Euclidean distances between them were calculated. Results are shown in Figure 6.

Euclidean distances between all corresponding anatomical landmarks were within or better than 7.6 mm (Euclidean distance of 2 voxels) and less than 3.8 mm (Euclidean distance of 1 voxel) for 355 of 470 delineated pairs of anatomical control points. Three anatomical landmarks were excluded from delineation: for patient 2, the posterior spinal canal at the superior aspect of T4 was removed because of poor visibility on T2w MRI; for patient 6, the bifurcation of the left main bronchus and left upper lobe bronchus was omitted due to partial collapse of the left upper lobe; for patient 4, the right costophrenic angle was outside the acquired field of view.

There was a reduction in the mean and standard deviation, averaged over patients, of the interquartile range, calculated over respiratory phases, of the Euclidean distances for the mobile ROIs (ROIs, 2–5) between 4D-T1w and 4D-T2w MRI (0.80 ± 0.35 mm, 0.85 ± 0.39 mm, 0.78 ± 0.28 mm, 1.62 ± 0.70 mm) and between 4D-T1w and 3D-T2w MRI (1.23 ± 0.48 mm, 2.02 ± 0.98 mm, 1.19 ± 0.94 mm, 5.16 ± 2.08 mm).

The NMI was calculated between corresponding respiratory phases of 4D-T1w and 4D-T2w MRI, and was compared with the NMI of 4D-T1w and 3D-T2w MRI. Comparisons were made in relation to the NMI calculated between the tie-phase of 4D-T1w and 3D-T2w MRI. Figure 7 shows an example comparison for patient 10. Percentage differences in NMI (mean and standard deviation, calculated over all respiratory phases and patients) of 4D-T1w and 4D-T2w MRI

were $0.41\% \pm 0.37\%$ and between 4D-T1w and 3D-T2w MRI were $-1.82\% \pm 1.76\%$.

Image Artifacts

The dominant image artifact observed after application of the MVFP method was associated with inaccuracies in deformable image registration, which led to a reduction in the quality of 4D-T2w MRI for all patients and was found to increase in magnitude with deformation size. An example is shown in Figure 8.

Artifacts that were already present in 3D-T2w MRI were propagated into 4D-T2w MRI. For all patients, minor ghosting was displayed and for 2 patients intensity inhomogeneity was apparent.

Clinical Evaluation

The radiation oncologist reported improved tumor definition in 4D-T2w MRI when compared with 4D-T1w MRI. Furthermore, important clinical information is displayed. In the case presented in Figure 4, T2w MRI better highlights extent and position of reactive pleural effusion and the lymphadenopathy than T1w MRI.

In some situations, 4D-T2w MRI was particularly advantageous when compared with 4D-T1w MRI, for instance when mobile tumor beds were attached to or adjacent to OARs, as demonstrated in Figure 9 and in the movie provided as Supplemental Digital Content 2, <http://links.lww.com/RLI/A317>. In the T1w images, the tumor-tissue contrast is low and it is challenging to delineate the tumor. However, the tumor extent and structure is clearly visible in T2w MRI. Furthermore, the anterior part of the tumor site is sliding nonrigidly against the chest-wall and the

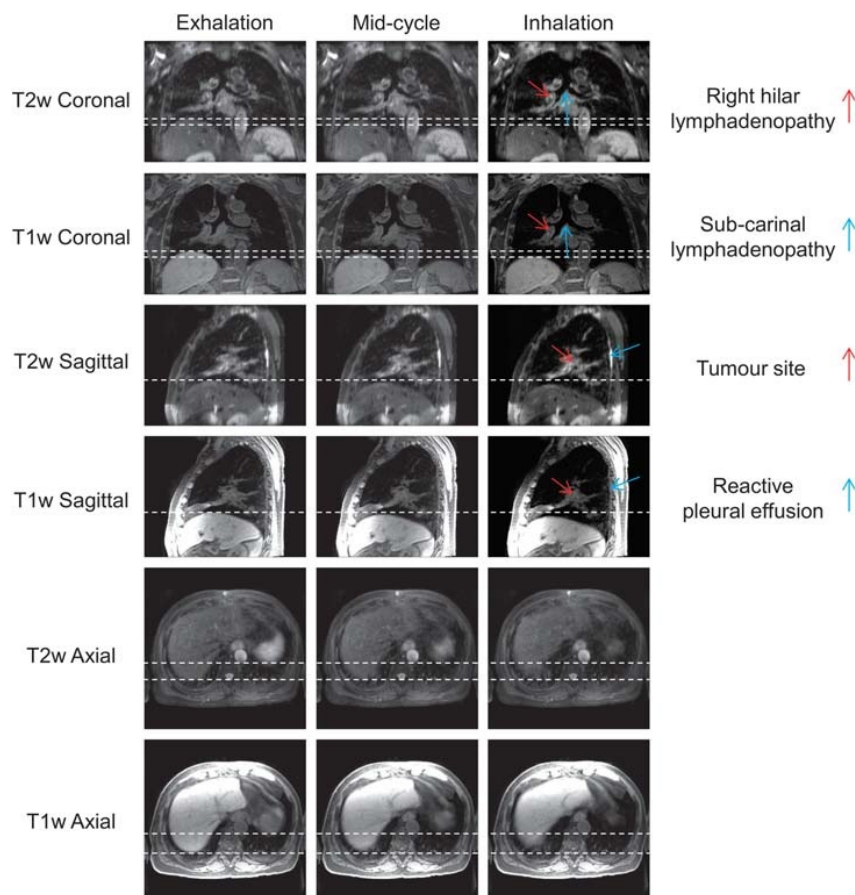


FIGURE 4. Example T1w and T2w coronal, sagittal, and axial views at exhalation, midcycle, and inhalation respiratory phases for patient 7. This patient was diagnosed with T1aN2 primary lung squamous cell carcinoma and had a small benign reactive pleural effusion. The dashed white lines aid visualization of the diaphragm surface position. The respiratory pattern of T1w MRI is preserved in T2w MRI. The tumor site, lymphadenopathy, and reactive pleural effusion are shown more clearly in T2w MRI than T1w MRI.

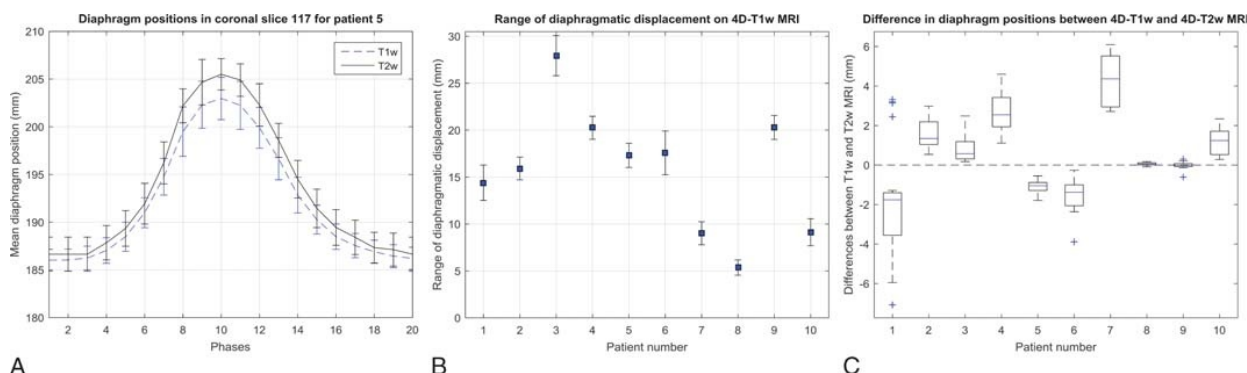


FIGURE 5. A, Example diaphragm surface positions, calculated using the edge-detection method, of the 4D-T1w and 4D-T2w volumes for patient 5. Error bars correspond to the standard deviation across SI lines and represent the width of the diaphragm surface. B, The ranges of diaphragmatic displacements in 4D-T1w MRI calculated using the edge-detection method. Errors bars show the uncertainty in the range. C, Box plot of the spread of the difference in diaphragm surface positions, between the 4D-T1w and 4D-T2w volumes, as calculated by the edge-detection method, for the 10 patients.

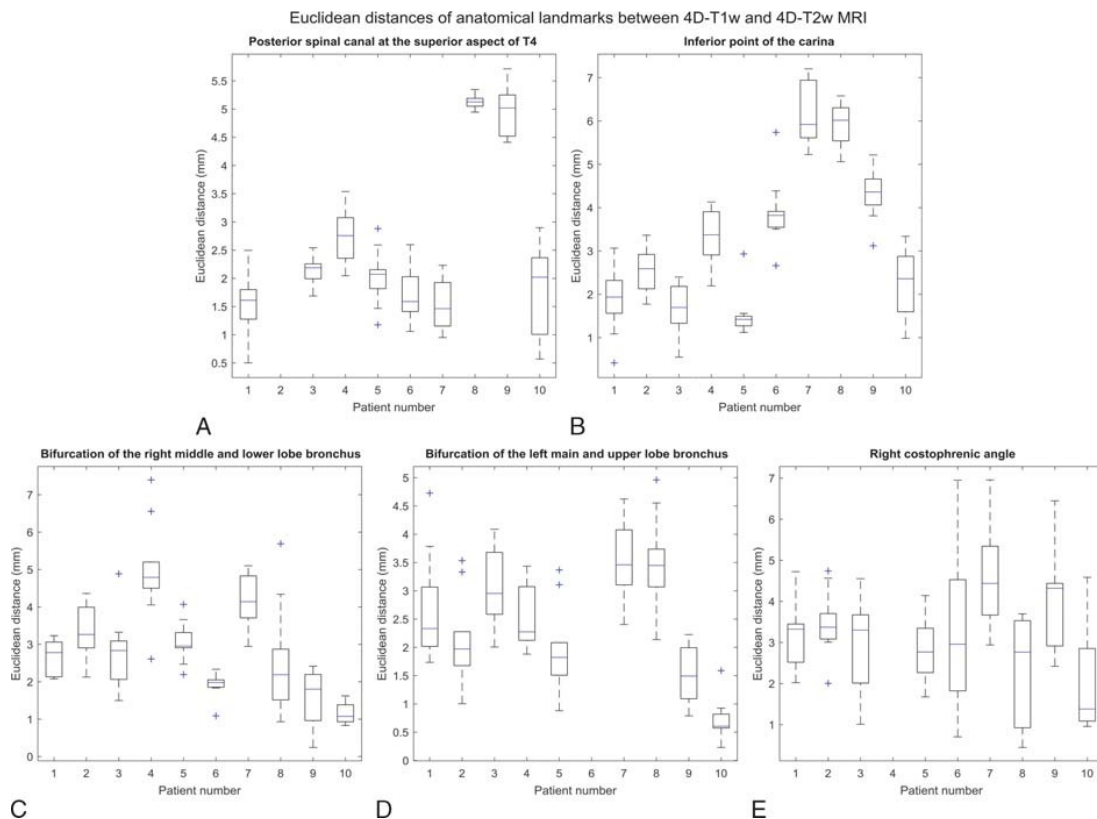


FIGURE 6. Box plot of spread of Euclidean distances, for all even respiratory phases, between pairs of anatomical landmarks that were delineated in both 4D-T1w and 4D-T2w MRI. All Euclidean distances agreed to less than 7.6 mm (Euclidean distance of 2 voxels) and 355 of 470 pairs of anatomical landmarks were consistent with less than 3.8 mm (Euclidean distance of 1 voxel).

extent of attachment and sliding motion is more easily visualized in T2w MRI than T1w MRI.

DISCUSSION

Pulse Sequences

A sequence with a radial trajectory and golden angle spacing was selected to acquire the T1w data because of advantages in image quality, such as incoherent aliasing and insensitivity to motion³⁷ and because a self-gating signal could be obtained through frequent measurements of the k-space center.⁴⁸ Alternative non-Cartesian trajectories could be used,²⁶ but a stack-of-stars approach is more efficient during reconstruction, as a Fourier transform can be applied along the slice direction.³⁷

We used an incremental improvement during the study in reducing the readout bandwidth of the 4D-T1w MRI acquisition. However, there was no significant difference in median diaphragm displacements on T1w and T2w MRI between patients 1 to 6 and patients 7 to 10 (unpaired 2-tailed *t* test, significance level $\alpha = 0.05$, $P = 0.34$). Therefore, a group analysis was justified.

The chosen T2w sequence uses a variable flip angle distribution to extend the echo train and speed up acquisition, enabling volumetric T2w MRI to be acquired in a clinically acceptable period (5–9 minutes). The application of a 3D acquisition is preferable to 2D slice-selective excitation sequences, commonly used in alternative 4D MRI methods,^{12,13,16,18,20,25} because the resulting MRI provides improved SNR. This property enables thinner slices and consequently a reduction

in stair-case artifacts due to highly nonisotropic voxel sizes. Yet, in Du et al,¹³ 4D-T2w MRI was calculated with a similar slice thickness of 3 mm, but a comparatively smaller field of view along the slice-direction was acquired. Furthermore, using 3D sequences might improve image quality, for delineation purposes, by reducing the influence of a complex magnetization history (impact of in-flow, slice-selection pulses, excitation frequency). Primarily, 3D sequences offer improved geometrical fidelity when using 3D distortion correction, which on commercially available systems is often not available for 2D sequences, but nonetheless is essential for RTP.

Image Reconstruction

The 4D joint MoCo-HDTV reconstruction was chosen because it not only enables high undersampling factors by using 100% of the raw data for reconstruction of each respiratory phase but also results in good image quality with comparatively low streaking artifacts and high sharpness.¹⁵ There are alternative reconstructions that utilize similar methods but are not yet readily available for the whole thorax.⁴⁹

Artifacts Apparent Using the MVF Projection Method

The MVFP method has limitations. The deformation artifact causes the diaphragm surface to be discontinuous and predominantly occurs at inhalation. A similar artifact has been reported when using NiftyReg with lung 4D CT data.⁵⁰ In our case, the artifact is present in the estimated 4D-T1w volume ($T1'$) but not in the reconstructed 4D-T1w volume ($T1$) and, therefore, is due to errors accumulated during

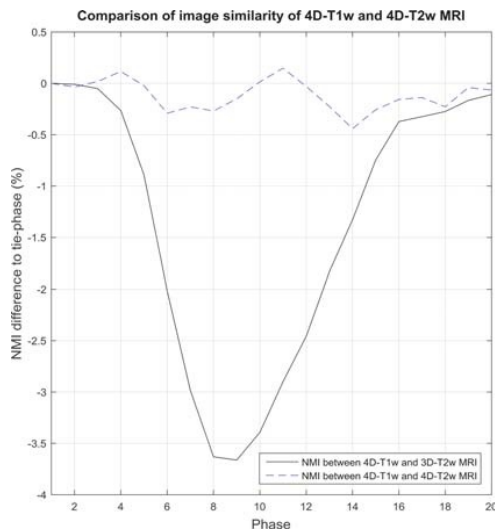


FIGURE 7. Shows an example comparison for patient 10, where results are relative to the normalized mutual information (NMI) calculated between the tie-phase of 4D-T1w and 3D-T2w MRI. In this case, the tie-phase is respiratory phase 1. NMI between 4D-T1w and 3D-T2w MRI (black solid line) indirectly corresponds to a respiratory signal. This pattern is not observed when examining NMI between 4D-T1w and 4D-T2w MRI (blue dashed curve).

application of the chain method. The extent of the artifact can be loosely quantified as the interquartile range of the difference in diaphragm positions between 4D-T1w and 4D-T2w MRI; the mean (calculated over all patients) of which is 1.11 mm (less than 0.5 voxel), demonstrating that the artifact has only a minor impact on diaphragm continuity of 4D-T2w MRI.

Verification

Four-dimensional T2w MRI was verified with respect to 4D-T1w MRI. Another option might have been to compare the inhalation respiratory phase of 4D-T2w MRI to T2w MRI acquired in breath-hold.

However, this approach was not pursued because inhalation in breath-hold can be deeper than in free-breathing.^{30,51}

Diaphragm Positions

The median diaphragm positions were consistent with less than 6.6 mm (2 voxels) for all 10 patients and less than 3.3 mm (1 voxel) for 9 of 10 patients. Furthermore, the mean of the interquartile range of observed differences between 4D-T1w and 4D-T2w MRI was \approx 8.7 mm smaller than between 4D-T1w and 3D-T2w MRI, demonstrating that calculated 4D-T2w MRI not only contained similar motion information to 4D-T1w MRI but was also spatially coherent.

The observed differences are partly due to a mismatch in respiratory phase between 4D-T1w and 3D-T2w MRI; as for all patients, comparison of the diaphragm positions (using the edge-detection method) in 4D-T1w and 3D-T2w MRI indicated that no exact match could be found. This might be solved by nonrigidly warping the 3D-T2w volume to the closest matching phase of the 4D-T1w volume. One hypothesis was that the differences depended on the magnitude of the diaphragm displacement during the respiratory cycle, but no significant correlation was found.

The larger differences observed for patient 7 might result from a collapse of the middle lobe of the right lung, as can be seen in the movie of Supplemental Digital Content 1, <http://links.lww.com/RLI/A316>.

Anatomical Control Points

Four-dimensional T2w MRI was anatomically similar to 4D-T1w MRI because all Euclidean distances, calculated between corresponding control points, were consistent with less than 7.6 mm (Euclidean distance of 2 voxels) and Euclidean distances of 355 of 470 pairs of control points agreed to less than 3.8 mm (Euclidean distance of one voxel). Applying the MVFP method led to improved similarity of T1w and T2w MRI as the mean interquartile range of Euclidean distances between mobile ROIs of 4D-T1w and 4D-T2w MRI were smaller than those between 4D-T1w and 3D-T2w MRI by \approx 1.39 mm.

Verification by manual delineation is limited, because it is a subjective process such that part of the presented differences, between pairs of anatomical control points, could be attributed to user dependence. Multiple observers might increase the accuracy of determined anatomical landmark positions.

A single observer approach was undertaken to reflect likely clinical practice, which could involve manual delineation on several respiratory phases.

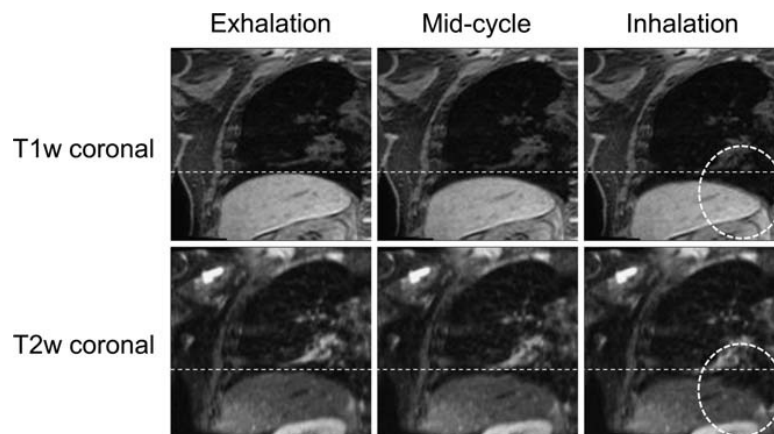


FIGURE 8. An example of the deformation artifact for patient 7. In the T2w snapshots, a deformation of the right hemidiaphragm boundary is seen at midcycle and a comparatively large deformation at inhalation (dashed circle). The deformation is worse at inhalation than at midcycle and is not displayed in the corresponding T1w snapshots.

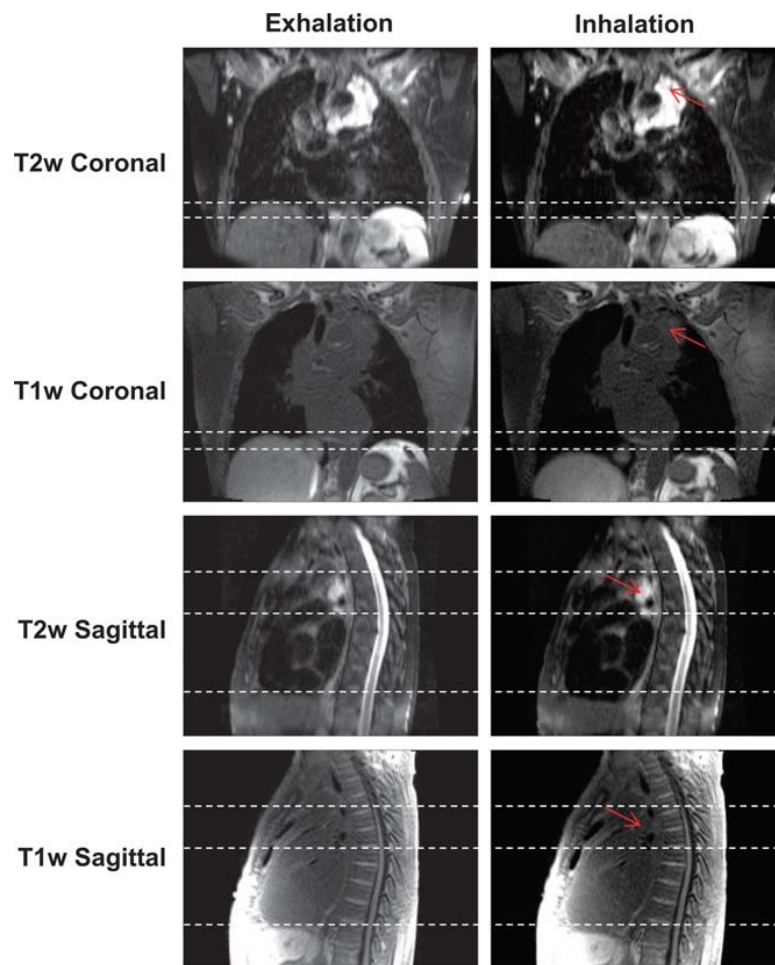


FIGURE 9. Snapshots of 4D-T1w and 4D-T2w MRI at the exhalation and inhalation respiratory phases for patient 3, who was diagnosed with T4N2 adenocarcinoma. The tumor is radically treatable, but is embedded around the heart and oesophagus. Unlike T1w MRI, T2w MRI displays a high tumor-tissue contrast enabling tumor position and structure to be clearly delineated. Sliding motion of the tumor site against the chest wall is displayed in the sagittal plane and is more clearly presented in T2w than T1w MRI. Red arrows point to the tumor site and dashed white lines aid assessment of both superior-inferior diaphragm and sliding motion.

Volumetric Image Similarity

A high volumetric image similarity was observed between 4D-T1w and 4D-T2w MRI, as NMI, relative to the tie-phase of 4D-T1w and 3D-T2w MRI, was coherent within $0.41\% \pm 0.37\%$. No dependence on respiration of the NMI calculated between corresponding respiratory phases of 4D-T1w and 4D-T2w MRI is apparent in Figure 7. Four-dimensional T2w MRI is thus commensurate to 4D-T1w MRI in spatiotemporal location.

A drawback of this approach is that the NMI metric is not only sensitive to relevant spatiotemporal information but also to image artifacts and noise. This metric was chosen because it can handle analysis between different image contrasts.⁴⁴

Application

As a proof-of-principle, high-quality geometrically accurate 4D-T2w images were calculated and could assist clinicians in obtaining RTPs for anatomical regions affected by respiratory motion by

improving tumor definition compared with 4D-T1w or 4D CT images. For instance, calculated MVFs might be applied to the 3D-T2w volume to generate midvent T2w MRI, which could be used alongside midvent CT,² to aid delineation of malignant tissue. The current workflow for radiotherapy planning and delineation includes a free breathing ¹⁸F-fluorodeoxyglucose position emission tomography scan. Four-dimensional position emission tomography imaging has been proposed, but further clinical validation is required,⁵² and unlike the presented 4D-T2w MRI, it has limited spatial resolution (5–7 mm).^{53,54}

The improved tumor-tissue contrast exhibited by 4D-T2w MRI could be particularly beneficial when moving tumor sites are adjacent to OARs, because it can often be challenging to delineate such sites on 4D-T1w MRI or 4D CT.^{36,55} In addition, 4D-T2w MRI could improve the reliability and specificity of assessment of chest wall invasion when compared with 4D-T1w MRI and 4D CT.⁵⁶

Four-dimensional T2w MRI could be used as part of an MR-only workflow for hybrid MR-IGRT systems.^{4–8} For instance, high-quality 4D-T2w MRI could act as a reference volume for both retrospective

evaluation of the delivered treatment and the generation of real-time 4D-T2w MRI for beam-on guidance and planning, in methods as proposed by Stemkens et al.³⁴

The MVFP method is not limited to 4D-T2w MRI and could be applied to simulate 4D MRI displaying any required contrast. For specific contrasts, such as diffusion-weighted MRI or ultrashort echo time imaging, it is not possible to use a stack-of-stars k-space sampling,⁵⁷ making it more difficult to apply state-of-the-art 4D reconstruction methods. In this case, the MVFP method could act as a solution to generate high-quality 4D MRI.

CONCLUSIONS

Four-dimensional T2w MRI was calculated retrospectively by applying the motion information from a 4D-T1w volume to a static 3D-T2w volume. Good quality geometrically accurate 4D-T2w volumes were obtained, providing high temporal resolution. Four-dimensional T2w MRI may assist clinicians in delineating lesions within volumes affected by respiratory motion that are challenging to outline on a 4D-T1w volume, making it a promising candidate for applications in radiotherapy, particularly with hybrid MR-IGRT systems in mind.

ACKNOWLEDGMENTS

We thank Siemens Healthineers, in particular Alto Stemmer, for providing us with the nonproduct radial MRI sequence and for giving us access to the spherical harmonic coefficients of the MAGNETOM Aera. We are grateful to Jamie McClelland of UCL for input regarding NiftyReg. We also thank Nina Tunariu and Dow-Mu Koh for their help with data acquisition and image analysis. We acknowledge NHS funding to the NIHR Biomedical Research Centre and the Clinical Research Facility at The Institute of Cancer Research and The Royal Marsden NHS Foundation Trust and the CR UK Cancer Imaging Centre grants C1060/A16464. We acknowledge funding from CR UK project grants: C33589/A19727, C347/A18365 and C309/A20926. Martin Leach is an NIHR emeritus senior investigator.

REFERENCES

- Keall PJ, Mageras GS, Balter JM, et al. The management of respiratory motion in radiation oncology report of AAPM Task Group 76. *Med Phys.* 2006;33:3874–3900.
- Wolthaus JW, Sonke JJ, van Herk M, et al. Comparison of different strategies to use four-dimensional computed tomography in treatment planning for lung cancer patients. *Int J Radiat Oncol Biol Phys.* 2008;70:1229–1238.
- Sonke JJ, Zijp L, Remeijer P, et al. Respiratory correlated cone beam CT. *Med Phys.* 2005;32:1176–1186.
- Raaymakers BW, Lagendijk JJ, Overweg J, et al. Integrating a 1.5 T MRI scanner with a 6 MV accelerator: proof of concept. *Phys Med Biol.* 2009;54:N229–N237.
- Lagendijk JJ, Raaymakers BW, Van den Berg CA, et al. MR guidance in radiotherapy. *Phys Med Biol.* 2014;59:R349–R369.
- Fallone BG. The rotating biplanar linac-magnetic resonance imaging system. *Semin Radiat Oncol.* 2014;24:200–202.
- Mutic S, Dempsey JF. The ViewRay system: magnetic resonance-guided and controlled radiotherapy. *Semin Radiat Oncol.* 2014;24:196–199.
- Thwaites D, Keall P, Holloway L, et al. Observations on MR-LINAC systems and rationale for MR-Linac use: the Australian MR-Linac project as an example. *Phys Medica.* 2014;30:e25.
- Schmidt MA, Payne GS. Radiotherapy planning using MRI. *Phys Med Biol.* 2015;60:R323–R361.
- Weygand J, Fuller CD, Ibbott GS, et al. Spatial precision in magnetic resonance imaging-guided radiation therapy: the role of geometric distortion. *Int J Radiat Oncol Biol Phys.* 2016;95:1304–1316.
- Hofmann M, Pichler B, Schölkopf B, et al. Towards quantitative PET/MRI: a review of MR-based attenuation correction techniques. *Eur J Nucl Med Mol Imaging.* 2009;36(suppl 1):S93–S104.
- Hu Y, Caruthers SD, Low DA, et al. Respiratory amplitude guided 4-dimensional magnetic resonance imaging. *Int J Radiat Oncol Biol Phys.* 2013;86:198–204.
- Du D, Caruthers SD, Glide-Hurst C, et al. High-quality T2-weighted 4-dimensional magnetic resonance imaging for radiation therapy applications. *Int J Radiat Oncol Biol Phys.* 2015;92:430–437.
- Larson AC, Kellman P, Arai A, et al. Preliminary investigation of respiratory self-gating for free-breathing segmented cine MRI. *Magn Reson Med.* 2005;53:159–168.
- Rank CM, Heußler T, Buzan MT, et al. 4D respiratory motion-compensated image reconstruction of free-breathing radial MR data with very high undersampling. *Magn Reson Med.* 2017;77:1170–1183.
- Cai J, Chang Z, Wang Z, et al. Four-dimensional magnetic resonance imaging (4D-MRI) using image-based respiratory surrogate: a feasibility study. *Med Phys.* 2011;38:6384–6394.
- King AP, Buerger C, Tsoumpas C, et al. Thoracic respiratory motion estimation from MRI using a statistical model and a 2-D image navigator. *Med Image Anal.* 2012;16:252–264.
- Tryggestad E, Flammang A, Han-Oh S, et al. Respiration-based sorting of dynamic MRI to derive representative 4D-MRI for radiotherapy planning. *Med Phys.* 2013;40:051909.
- Savill F, Schaeffter T, King AP. Assessment of input signal positioning for cardiac respiratory motion models during different breathing patterns. *IEEE International Symposium on Biomedical Imaging: From Nano to Macro.* 2011:1698–1701.
- Liu Y, Yin FF, Czito BG, et al. T2-weighted four dimensional magnetic resonance imaging with result-driven phase sorting. *Med Phys.* 2015;42:4460–4471.
- Vedam SS, Keall PJ, Kini VR, et al. Acquiring a four-dimensional computed tomography dataset using an external respiratory signal. *Phys Med Biol.* 2002;48:45–62.
- Hui C, Wen Z, Stemkens B, et al. 4D MR imaging using robust internal respiratory signal. *Phys Med Biol.* 2016;61:3472–3487.
- Li G, Wei J, Olek D, et al. Direct comparison of respiration-correlated four-dimensional magnetic resonance imaging reconstructed using concurrent internal navigator and external bellows. *Int J Radiat Oncol Biol Phys.* 2017;97:596–605.
- Koch N, Liu HH, Starkschall G, et al. Evaluation of internal lung motion for respiratory-gated radiotherapy using MRI: part I—correlating internal lung motion with skin fiducial motion. *Int J Radiat Oncol Biol Phys.* 2004;60:1459–1472.
- Liu Y, Yin FF, Chen NK, et al. Four dimensional magnetic resonance imaging with retrospective k-space reordering: a feasibility study. *Med Phys.* 2015;42:534–541.
- Deng Z, Pang J, Yang W, et al. Four-dimensional MRI using three-dimensional radial sampling with respiratory self-gating to characterize temporal phase-resolved respiratory motion in the abdomen. *Magn Reson Med.* 2016;75:1574–1585.
- Feng L, Axel L, Chandarana H, et al. XD-GRASP: golden-angle radial MRI with reconstruction of extra motion-state dimensions using compressed sensing. *Magn Reson Med.* 2016;75:775–788.
- Feng L, Grimm R, Block KT, et al. Golden-angle radial sparse parallel MRI: combination of compressed sensing, parallel imaging, and golden-angle radial sampling for fast and flexible dynamic volumetric MRI. *Magn Reson Med.* 2014;72:707–717.
- Mickevicus NJ, Paulson ES. Investigation of undersampling and reconstruction algorithm dependence on respiratory correlated 4D-MRI for online MR-guided radiation therapy. *Phys Med Biol.* 2016;62:2910–2921.
- McClelland JR, Hawkes DJ, Schaeffter T, et al. Respiratory motion models: a review. *Med Image Anal.* 2013;17:19–42.
- Blackall JM, Penney GP, King AP, et al. Alignment of sparse freehand 3-D ultrasound with preoperative images of the liver using models of respiratory motion and deformation. *IEEE Trans Med Imaging.* 2005;24:1405–1416.
- McClelland JR, Blackall JM, Tarte S, et al. A continuous 4D motion model from multiple respiratory cycles for use in lung radiotherapy. *Med Phys.* 2006;33:3348–3358.
- Marx M, Ehrhardt J, Werner R, et al. Simulation of spatiotemporal CT data sets using a 4D MRI-based lung motion model. *Int J Comput Assist Radiol Surg.* 2014;9:401–409.
- Stemkens B, Tijssen RH, de Senneville BD, et al. Image-driven, model-based 3D abdominal motion estimation for MR-guided radiotherapy. *Phys Med Biol.* 2016;61:5335–5355.
- Biederer J, Beer M, Hirsch W, et al. MRI of the lung (2/3). Why ... when ... how? *Insights Imaging.* 2012;3:355–371.
- Riddell AM, Hillier J, Brown G, et al. Potential of surface-coil MRI for staging of esophageal cancer. *AJR Am J Roentgenol.* 2006;187:1280–1287.
- Block KT, Chandarana H, Milla S, et al. Towards routine clinical use of radial stack-of-stars 3d gradient-echo sequences for reducing motion sensitivity. *J Korean Phys Soc.* 2014;18:87–106.
- Winkelmann S, Schaeffter T, Koehler T, et al. An optimal radial profile order based on the Golden Ratio for time-resolved MRI. *IEEE Trans Med Imaging.* 2007;26:68–76.
- Lichy MP, Wietek BM, Mugler JP 3rd, et al. Magnetic resonance imaging of the body trunk using a single-slab, 3-dimensional, T2-weighted turbo-spin-echo

- sequence with high sampling efficiency (SPACE) for high spatial resolution imaging: initial clinical experiences. *Invest Radiol.* 2005;40:754–760.
40. Danias PG, McConnell MV, Khasgiwala VC, et al. Prospective navigator correction of image position for coronary MR angiography. *Radiology.* 1997;203:733–736.
 41. Block K, Uecker M. Simple method for adaptive gradient-delay compensation in radial MRI. *ISMRM 19th Annual Meeting & Exhibition.* 2011;2816.
 42. Doran SJ, Charles-Edwards L, Reinsberg SA, et al. A complete distortion correction for MR images: I. Gradient warp correction. *Phys Med Biol.* 2005;50:1343–1361.
 43. Janke A, Zhao H, Cowin GJ, et al. Use of spherical harmonic deconvolution methods to compensate for nonlinear gradient effects on MRI images. *Magn Reson Med.* 2004;52:115–122.
 44. Pluim JP, Maintz JB, Viergever MA. Mutual-information-based registration of medical images: a survey. *IEEE Trans Med Imaging.* 2003;22:986–1004.
 45. Modat M, Ridgway GR, Taylor ZA, et al. Fast free-form deformation using graphics processing units. *Comput Methods Programs Biomed.* 2010;98:278–284.
 46. Rueckert D, Sonoda LI, Hayes C, et al. Nonrigid registration using free-form deformations: application to breast MR images. *IEEE Trans Med Imaging.* 1999;18:712–721.
 47. Boldea V, Sharp GC, Jiang SB, et al. 4D-CT lung motion estimation with deformable registration: quantification of motion nonlinearity and hysteresis. *Med Phys.* 2008;35:1008–1018.
 48. Buehrer M, Curcic J, Boesiger P, et al. Prospective self-gating for simultaneous compensation of cardiac and respiratory motion. *Magn Reson Med.* 2008;60:683–690.
 49. Aitken AP, Henningsson M, Botnar RM, et al. 100% Efficient three-dimensional coronary MR angiography with two-dimensional beat-to-beat translational and bin-to-bin affine motion correction. *Magn Reson Med.* 2015;74:756–764.
 50. Modat M, McClelland J, Ourselin S. Lung registration using the NiftyReg package. *Medical Image Analysis for the Clinic-A Grand Challenge.* 2010;2010:33–42.
 51. Blackall JM, Ahmad S, Miquel ME, et al. MRI-based measurements of respiratory motion variability and assessment of imaging strategies for radiotherapy planning. *Phys Med Biol.* 2006;51:4147–4169.
 52. Konert T, Vogel W, MacManus MP, et al. PET/CT imaging for target volume delineation in curative intent radiotherapy of non-small cell lung cancer: IAEA consensus report 2014. *Radiother Oncol.* 2015;116:27–34.
 53. Kumar S, Liney G, Rai R, et al. Magnetic resonance imaging in lung: a review of its potential for radiotherapy. *Br J Radiol.* 2016;89:20150431.
 54. Hanna GG, van Sörnsen de Koste JR, Dahele MR, et al. Defining target volumes for stereotactic ablative radiotherapy of early-stage lung tumours: a comparison of three-dimensional 18 F-fluorodeoxyglucose positron emission tomography and four-dimensional computed tomography. *Clin Oncol (R Coll Radiol).* 2012;24:e71–e80.
 55. Brown G, Daniels IR, Richardson C, et al. Techniques and trouble-shooting in high spatial resolution thin slice MRI for rectal cancer. *Br J Radiol.* 2005;78:245–251.
 56. Khalil A, Majlath M, Gounant V, et al. Contribution of magnetic resonance imaging in lung cancer imaging. *Diagn Interv Imaging.* 2016;97:991–1002.
 57. Triphan SM, Jobst BJ, Breuer FA, et al. Echo time dependence of observed T1 in the human lung. *J Magn Reson Imaging.* 2015;42:610–616.

Appendix B

Super-resolution T2-weighted 4D MRI for image
guided radiotherapy

Freedman *et al.* 2018



Contents lists available at ScienceDirect

Radiotherapy and Oncology

journal homepage: www.thegreenjournal.com



Image guided radiotherapy

Super-resolution T2-weighted 4D MRI for image guided radiotherapy

Joshua N. Freedman^{a,b}, David J. Collins^b, Oliver J. Gurney-Champion^a, Jamie R. McClelland^c, Simeon Nill^a, Uwe Oelfke^a, Martin O. Leach^{b,*}, Andreas Wetscherek^a^aJoint Department of Physics; ^bCR UK Cancer Imaging Centre, The Institute of Cancer Research and The Royal Marsden NHS Foundation Trust; and ^cCentre for Medical Image Computing, Department of Medical Physics and Biomedical Engineering, University College London, UK

ARTICLE INFO

Article history:

Received 16 December 2017

Received in revised form 2 May 2018

Accepted 14 May 2018

Available online 2 June 2018

Keywords:

4D MRI

T2w 4D MRI

Super resolution

Motion vector field

Radiotherapy treatment planning

ABSTRACT

Background and purpose: The superior soft-tissue contrast of 4D-T2w MRI motivates its use for delineation in radiotherapy treatment planning. We address current limitations of slice-selective implementations, including thick slices and artefacts originating from data incompleteness and variable breathing. **Materials and methods:** A method was developed to calculate midposition and 4D-T2w images of the whole thorax from continuously acquired axial and sagittal 2D-T2w MRI ($1.5 \times 1.5 \times 5.0 \text{ mm}^3$). The method employed image-derived respiratory surrogates, deformable image registration and super-resolution reconstruction. Volunteer imaging and a respiratory motion phantom were used for validation. The minimum number of dynamic acquisitions needed to calculate a representative midposition image was investigated by retrospectively subsampling the data (10–30 dynamic acquisitions).

Results: Super-resolution 4D-T2w MRI ($1.0 \times 1.0 \times 1.0 \text{ mm}^3$, 8 respiratory phases) did not suffer from data incompleteness and exhibited reduced stitching artefacts compared to sorted multi-slice MRI. Experiments using a respiratory motion phantom and colour-intensity projection images demonstrated a minor underestimation of the motion range. Midposition diaphragm differences in retrospectively subsampled acquisitions were $<1.1 \text{ mm}$ compared to the full dataset. 10 dynamic acquisitions were found sufficient to generate midposition MRI.

Conclusions: A motion-modelling and super-resolution method was developed to calculate high quality 4D/midposition T2w MRI from orthogonal 2D-T2w MRI.

© 2018 The Authors. Published by Elsevier B.V. Radiotherapy and Oncology 129 (2018) 486–493 This is an open access article under the CC BY license (<http://creativecommons.org/licenses/by/4.0/>).

Magnetic resonance image guided radiation therapy (MRIGRT) is an emerging treatment approach that takes advantage of the exquisite soft tissue contrast [1], motion resolving capabilities and functional information offered by MRI, to improve treatment delivery in radiotherapy [2,3]. Four-dimensional (4D) T2-weighted (T2w) MRI is a promising candidate for use in radiotherapy treatment planning (RTP) of moving anatomy [4–6]. For instance, a mid-position (time-weighted mean position of the respiratory cycle) (MidP) image can be calculated from 4D-T2w MRI and co-registered with MidP-CT to facilitate target delineation [7,8]. 4D-T2w MRI might also be repeatedly acquired between fractions and used to update treatment plans. In a hybrid MRIGRT treatment setting [2,9–12], MidP/4D-T2w MRI has potential for positioning and beam-on guidance [13–15].

Previously, 4D-T2w MRI has been generated by sorting dynamically acquired two-dimensional (2D) T2w MRI both prospectively and retrospectively with the aid of an image-driven or external

respiratory signal [16–25]. In retrospective methods, 2D-T2w MRI is continuously acquired and then sorted into respiratory-bins. Unlike external respiratory signals, such as a respiratory bellows [17], image-driven respiratory signals (IRS) are available from the acquired data and do not disturb the measurement process [19]. However, IRS exhibit a phase-shift [26] between different slices, since they are calculated on a slice-by-slice basis.

Retrospective binning methods suffer from missing-data artefacts, when slices are not acquired for particular respiratory phases [21]. Furthermore, a 2D distortion correction is usually applied, which is suboptimal, because 3D geometrical fidelity is essential for RTP [27]. An additional problem are highly anisotropic voxel sizes, due to the large slice-thickness required to obtain a sufficient field-of-view (FoV) and signal-to-noise ratio [17,21]. Staircase (stitching) artefacts, due to both the large slice-thickness and respiratory variations, are observed when reformatting data into orthogonal views [16]. Slice-thickness can potentially be reduced with a super-resolution reconstruction [28], which combines several low-resolution images containing independent information into one super-resolution image. The concept of super-resolution

* Corresponding author at: CR UK Cancer Imaging Centre, The Institute of Cancer Research, Downs Road, Sutton, Surrey SM2 5PT, UK.

E-mail address: Martin.Leach@icr.ac.uk (M.O. Leach).

<https://doi.org/10.1016/j.radonc.2018.05.015>

0167-8140/© 2018 The Authors. Published by Elsevier B.V.

This is an open access article under the CC BY license (<http://creativecommons.org/licenses/by/4.0/>).

reconstruction has been applied in 4D-MRI [29–31], but has not yet been translated to 4D-T2w MRI.

In this article, an automated binning and super-resolution reconstruction method is introduced to calculate high-resolution distortion corrected MidP/4D-T2w MRI, without missing-data artefacts, from dynamically acquired axial and sagittal 2D-T2w MRI. The performance of 4D-T2w MRI is assessed in phantom experiments and compared to low-resolution 2D-T2w MRI using colour-intensity projection images (CIPs) [32,33]. The influence of the acquired number of dynamic acquisitions on the MidP-T2w MRI quality was investigated by retrospectively subsampling the data-set.

Materials and methods

Data acquisition

Eight healthy volunteers (aged 24–35, 4 female) were included in this study after giving written informed consent. Volunteers were scanned in both sagittal and axial orientations, using 30 repeated dynamic acquisitions (referred to below as dynamics), with a 2D-T2w half Fourier turbo spin echo (HASTE) sequence (voxel-size $1.5 \times 1.5 \times 5 \text{ mm}^3$, echo time 64 ms, effective repetition time per slice 13.6–14.2 s, in-plane FoV $264 \times 384 \text{ mm}^2$, 40–60 slices that were scanned interleaved, readout bandwidth 590 Hz/Px, refocusing flip-angle $90\text{--}92^\circ$, total acquisition time 15.0–18.4 min) in free breathing at 1.5 T (MAGNETOM Aera; Siemens Healthcare, Erlangen, Germany). An in-house developed coil holder was used to prevent compression of the thorax by the 18-channel receive array. Scans were acquired with the patient's arms adjacent to the thorax. The default gradient non-linearity 2D distortion correction was disabled.

Workflow

Low-resolution sagittal and axial 4D-T2w MRI were first calculated with a binning and motion-modelling method and then aggregated into a high-resolution MidP-T2w image using a super-resolution reconstruction as described below. High-resolution 4D-T2w MRI was then calculated by transforming the MidP-T2w image with motion vector fields calculated from the low-resolution sagittal 4D-T2w MRI. A summary is given in Fig. 1. All calculations were carried out in MATLAB (version 2017a; The MathWorks, Natick, MA) on an Intel Xeon E5-1660 processor with 8 cores at 3 GHz and 64 GB of memory.

The following binning and motion-modelling workflow was separately undertaken for both the axial and sagittal acquisitions.

Binning

For each slice, five IRS were calculated using the concepts of: body area [20], mutual information [23], and artificial k-space [19]. A binary mask (background and lungs = 0, remaining = 1) was calculated by thresholding each acquired image; thresholds were automatically calculated as 2/5th of the mean image intensity. Body area was identified as the largest connected component. Mutual information was calculated between exhalation and all other phases, where exhalation was determined as the minimum of the pre-calculated body area IRS. Three k-space IRS were generated from the magnitude of the centre (0,0), centre-upper (0,1) and centre-right (1,0) pixels of the 2D Fourier transform of each magnitude image [19]. Employing a partial Fourier acquisition did not affect calculation of k-space IRS from the image data, because only the magnitude signal of the artificial k-space data points was used. All five IRS were combined into one principle respiratory signal

(PRS) using principle component analysis (first principle component).

The PRS was employed to retrospectively sort each slice into eight respiratory-bins. The edges of the respiratory-bins were defined using percentiles of the PRS amplitude values, such that there was an equal amount of data in each respiratory-bin. Magnitude images assigned to the same respiratory-bin were averaged. Defining respiratory-bins separately for each slice mitigates missing-data artefacts, as all bins can be filled [21], but introduces stitching artefacts or phase-shifts between slices [26], due to the particular sampling scheme or changes in the respiratory pattern during measurement. Finally a 3D gradient non-linearity distortion correction was applied to each phase of the sorted images, using the spherical harmonic coefficients provided by the vendor [34].

Motion-modelling

Compared to other respiratory phases, exhalation exhibited reduced stitching and binning artefacts. We used the exhalation image to correct the artefacts exhibited in the remaining respiratory phases.

In this approach, the exhalation image was registered to all eight respiratory phases using a diffeomorphic Demons 3D non-rigid registration [35] with diffusion-like smoothing ($\sigma = 1.0$ pixel), which greatly increased robustness to stitching artefacts. The σ parameter was optimised heuristically in a subset of the volunteers by visually assessing the quality of the registered images. The value $\sigma = 1.0$ pixel was found to provide the best compromise between reduction of stitching artefacts and over-regularisation of respiratory motion. The calculated motion vector fields were then applied to warp the exhalation image to all other respiratory phases; resulting in a simulated 4D-T2w MRI with reduced stitching artefacts. Afterwards, each slice from the original sorted 4D-T2w MRI was corrected by registering to the corresponding slice and phase in the simulated 4D-T2w MRI, using a similar Demons 2D non-rigid registration ($\sigma = 1.0$ pixel). This approach retained the independent information needed for the super-resolution reconstruction.

Super-resolution reconstruction

Using NiftyReg [36,37], eight copies of the MidP image [7] were generated from all eight phases of the sagittal 4D-T2w image. NiftyReg was employed to generate eight additional copies by non-rigidly registering all eight respiratory phases of the axial 4D-T2w image to the sagittal MidP copy that was generated from the corresponding respiratory phase. All independent MidP copies were interpolated to isotropic resolution ($1.0 \times 1.0 \times 1.0 \text{ mm}^3$) and averaged to form an initial guess [28] for the super-resolution reconstruction [38]. High-resolution MidP-T2w MRI was calculated by iteratively back-projecting the differences between the low-resolution MidP copies and the super-resolution image that was convolved with a non-isotropic Gaussian point spread function [39].

Motion vector fields, which were calculated by non-rigidly registering the respiratory phases of low-resolution sagittal 4D-T2w MRI, were applied to high-resolution MidP-T2w MRI to obtain super-resolution 4D-T2w MRI. Because super-resolution reconstruction was limited to the overlapping FoV of the sagittal and axial images, the original low-resolution axial images were used outside the thorax (arms). A detailed overview of the super-resolution reconstruction workflow can be found in the [Supplemental Material](#).

Verification: image resolution

Deformable image registration and interpolation steps in the workflow result in smoothing of the image data and potentially a

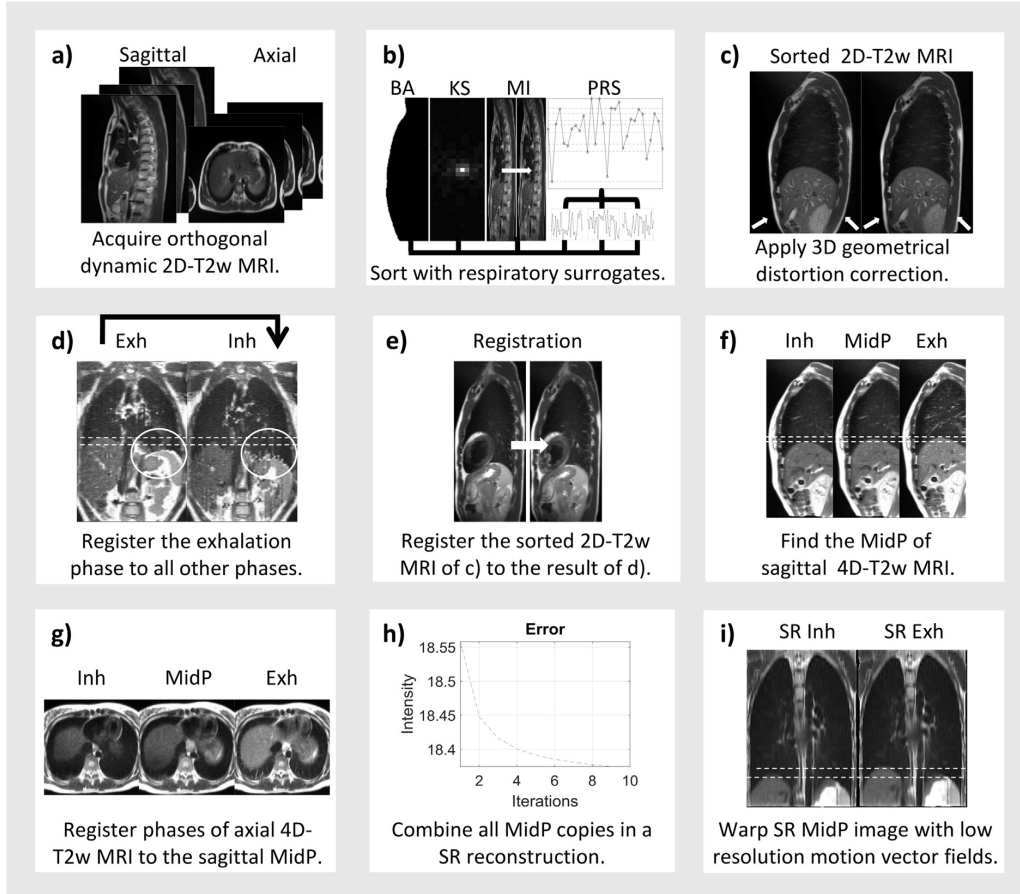


Fig. 1. (a) Axial and sagittal 2D-T2w MRI are continuously acquired, (b) retrospectively sorted by the principle respiratory surrogate (PRS), which combines body area (BA), artificial k-space (KS) and mutual information (MI), and (c) distortion corrected. (d) For both axial and sagittal 4D-T2w MRI, stitching and binning artefacts, visible within the white circle, are reduced by registering the exhalation phase to all other respiratory phases. (e) Sorted images in (c) are corrected by registering to the results of (d). (f) Each phase of the sagittal 4D-T2w image of (e) is warped to midposition (MidP). (g) Each phase of the axial 4D-T2w image in (e) is registered to the sagittal MidP. (h) Super-resolution (SR) reconstruction is performed using the sagittal and axial MidP copies. (i) SR 4D-T2w MRI is obtained by warping the SR MidP image with the low-resolution motion vector fields calculated from the corrected sagittal 4D-T2w MRI in (f).

loss of resolution. An edge-detection method was used to compare the resolutions of the unprocessed ground-truth, initial guess and super-resolution reconstructed images. In this approach a 2D region of interest (ROI) was manually defined on the anterior skin-air boundary in the central axial slice of each volunteer. A Gaussian function was then fitted to the derivative of each measured line of intensity $y'(x)$ (matrix of size $[1, N]$) in the ROI.

$$y_0 = \underset{a, \mu, \sigma}{\operatorname{argmin}} \sum_{x=1}^N \left(y'(x) - a \exp \left[-\frac{1}{2} \left(\frac{x - \mu}{b} \right)^2 \right] \right)^2$$

Here, y_0 describes the result of fitting the Gaussian function of height a , position μ , and width b to the derivative $y'(x)$ using least squares minimisation. The image resolution was obtained by averaging the calculated width b over all lines in the ROI. For each volunteer, the same 2D ROI was used to measure the image resolution on the unprocessed ground-truth, initial guess and super-resolution reconstructed images.

Verification: phantom measurements

The QUASAR™ MRI-compatible Respiratory Motion Phantom (Quasar, Modus Medical Devices Inc., London, Canada), into which a kiwi and corn test-object was inserted, was employed to validate the binning and motion-modelling workflow. Two sinusoidal waveforms (S1-S2) with period and amplitude: (4 s, 15 mm) and (3 s, 20 mm), and two randomly chosen volunteer waveforms (S3-S4) (self-gating signal of a radial T1 weighted sequence that was acquired in the same session as T2w MRI [40]) with amplitude 15 mm were chosen to drive the phantom. Translational motion of the phantom insert along the bore was coupled to rotation around the axis of translational motion. The rotation angle θ was given by the position A (between -20 and 20 mm):

$$\theta(A) = \sin^{-1} \left(\frac{1}{2} \sqrt{1 - \left(\frac{A}{20} \right)^2} \right)$$

The volunteer waveform amplitude values of 15 mm were chosen to be representative of patient respiratory tumour motion [41].

Images were obtained with identical sequence parameters to the volunteer acquisitions, except that they were acquired in the coronal and sagittal orientations. Because the main compartment of the phantom was a static water tank and only the insert exhibited motion, the PRS of body area and artificial k-space were not applicable and the position of the lower kiwi boundary, which was measured using an edge-detection method [5], was used instead. Furthermore, the Demons non-rigid registration was optimised ($\sigma = 0.5$ pixel) to capture the rotation of the test-object. Using the same edge-detection method, the MidP displacement was compared to the mean displacement over N dynamics ($N = 10, 15, 20, 25$ and 30) measured in ground-truth low-resolution images.

Verification: colour-intensity projections

CIPs can be used to encode the intensity variation within a 4D image set by colour, and for objects similar to an isolated lung tumour, colour approximately represents the time spent by the object in any one position [32,33]. CIPs display grayscale values when intensity does not change at a particular position in the 4D image set. Calculated CIPs are independent of the binning and motion-modelling workflow and therefore enable a comparison of the motion information exhibited by low-resolution 4D-T2w MRI and the unprocessed ground-truth phantom data. For the volunteer images, CIPs were calculated from both the unprocessed ground-truth data and the generated super-resolution 4D-T2w MRI.

MidP dependence on number of dynamics

To minimise acquisition time, the number of dynamic images required to obtain a representative MidP image was investigated by retrospectively discarding data prior to generating the 4D-MRI. Following Fig. 1(b–f), MidP images were calculated from only the first 10–30 sagittal dynamics. For each MidP image, the position of the right hemi-diaphragm was calculated for five consecutive sagittal slices, using an edge-detection method [5], and then averaged. It was compared to the diaphragm position of the MidP image obtained with 30 dynamics, which was considered to contain sufficient dynamics for data completeness based on [21]. In order to separate the impact of the number of dynamics N from possible changes in respiratory pattern during acquisition, the change in MidP was estimated from the unprocessed ground-truth data, by calculating the average diaphragm position over N dynamics for $N = 10$ – 30 ; carried out using the edge-detection method on the same slices and settings as for the above MidP images.

Results

For eight volunteers, distortion corrected super-resolution 4D/MidP-T2w MRI ($1.0 \times 1.0 \times 1.0 \text{ mm}^3$) were calculated using a fully automatic workflow. Low-resolution 4D-T2w MRI was reconstructed in 3.2 min for each orientation and total reconstruction time for super-resolution 4D/MidP-T2w was less than 23 min. Super-resolution 4D-T2w MRI exhibited no missing-data artefacts and, when compared to the initially binned low-resolution 4D-T2w MRI, displayed greatly reduced stitching artefacts; as demonstrated in the movie of Supplemental Digital Content 1 (15 dynamics). Fig. 2 shows an example comparing super-resolution MidP-T2w MRI, the initial guess for super-resolution reconstruction (mean of all 16 interpolated low-resolution copies) and the low-resolution MidP sagittal and axial images (averaged over 8 interpolated copies). Super-resolution reconstruction maintained the in-plane quality and image features of both the axial and sagittal orientations, whilst increasing the image sharpness in the

coronal plane. The motion information exhibited by the low-resolution sagittal 4D-T2w MRI was well preserved in the super-resolution 4D-T2w MRI, as shown in Fig. 3.

The measured anterior boundary skin-air resolution in the central axial slice of the unprocessed ground-truth, initial guess and super-resolution reconstructed images was: (mean and standard deviation) 1.4 ± 0.2 , 2.2 ± 0.2 and 1.5 ± 0.2 mm. The small resolution difference between the native and super-resolution images suggests that the super-resolution reconstruction can overcome the smoothing associated with the registration and interpolation steps.

As illustrated in the axial view presented in Fig. 4a, super-resolution reconstruction results in an increase in image sharpness and reduction of partial volume effects, better enabling visualisation of features such as the sweetcorn kernels within the test-object. As shown in Fig. 4b, the differences (mean and standard deviation over all dynamics) in the MidP displacement calculated from the low-resolution model and the unprocessed ground-truth images for the sinusoidal waveforms (S1–S2) were: 1.2 ± 0.6 mm and 1.6 ± 0.9 mm, and for the volunteer waveforms (S3–S4) were: -0.3 ± 0.1 mm and 0.0 ± 0.5 mm. The motion range in the 4D-T2w MRI slightly underestimated the full motion range of the unprocessed ground-truth images. This is reflected in Fig. 4c, where the CIPs of S4 reveal that this slight underestimation of motion occurred in inhalation.

CIPs were generated from the unprocessed ground-truth images and from the results of super-resolution reconstruction; an example is shown in Fig. 5. In terms of diaphragm motion, the CIPs from the super-resolution reconstruction were in good agreement when compared to those calculated from the unprocessed ground-truth images. The observable range of motion exhibited in CIPs only varied slightly with number of dynamics. Due to averaging, cardiovascular motion and pulsations observed in the unsorted data were reduced in the super-resolution reconstruction.

As shown in Fig. 6a, a negative correlation (Pearson's $r = -0.89$) was found between the absolute differences in diaphragm position of MidP calculated from N and 30 dynamics. The average absolute differences, displayed as grey circles, ranged from 1.1 ± 0.6 to 0.3 ± 0.3 mm (mean and standard deviation over volunteers) for 10 and 29 dynamics, respectively, and all were within 1.1 mm. As displayed in Fig. 6b, a drift in MidP was observed for all volunteers and the mean absolute difference between 10 and 30 dynamics was 1.0 ± 0.8 mm over an average acquisition of 5.2 min. The differences in diaphragm position were corrected for the change in MidP and the absolute differences (mean and standard deviation) were 0.6 ± 0.6 and 0.3 ± 0.4 mm for 10 and 29 dynamics (black squares in Fig. 6a). Fig. 6c shows super-resolution MidP images for varying number of dynamics. Similarity to the image obtained from 30 dynamics slightly increased with number of dynamics, but was nevertheless high for all images.

Discussion

In this article, an automated binning and super-resolution reconstruction method was introduced to obtain high-resolution distortion corrected 4D/MidP-T2w MRI. Super-resolution reconstruction was enabled by combining copies of low-resolution axial and sagittal MidP-MRI, which were independently reconstructed for each raw image orientation. In phantom experiments, the MidP displacement exhibited by low-resolution 4D-T2w MRI was at most 2.6 mm different to that estimated from the unprocessed ground-truth images. Data subsampling experiments demonstrated that 10 dynamic acquisitions in each orientation were sufficient to obtain representative MidP-T2w MRI. Employing super-resolution reconstruction reduced the smoothing associated

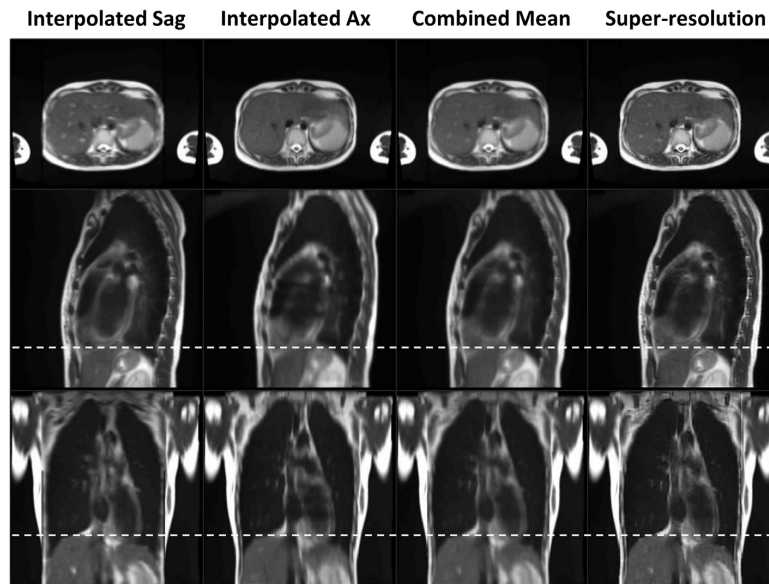


Fig. 2. A comparison between the combined and individual mean interpolated sagittal (Sag) and axial (Ax) images, and the super-resolution reconstruction. Dashed white lines aid evaluation of the relative liver dome positions in the different midposition (of the respiratory cycle) images. The suppressed average cardiovascular pulsations in the Interpolated Sag and Ax columns (e.g. bright liver vessels in the axial view) were retained in the super-resolution image.

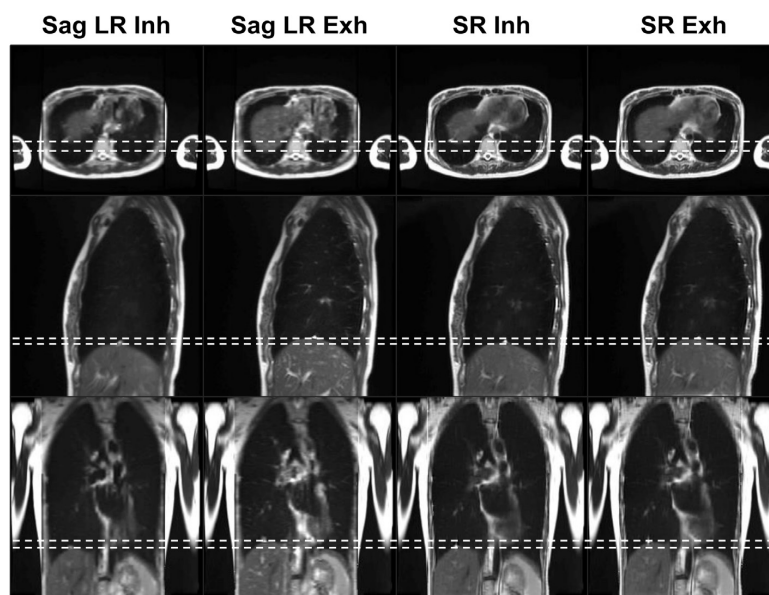


Fig. 3. Comparison of the four-dimensional super-resolution (SR) reconstruction to the sagittal four-dimensional low-resolution (LR) reconstruction. Dashed white lines demarcate the displacement of the inhalation (Inh) and exhalation (Exh) phases.

with the registration and interpolation steps in the workflow, facilitating visualisation of small structures with high T2 contrast. The resulting high quality 4D-T2w MRI exhibits thin slices whilst maintaining sufficient signal-to-noise ratio and FoV to facilitate RTP of anatomy undergoing respiratory motion. Furthermore, the suggested motion-model permits a reduction in stitching artefacts

and mitigates missing-data artefacts by sorting images on a slice-by-slice basis; avoiding unnecessary long acquisitions.

For all waveforms in the phantom experiment, the MidP displacement in the low-resolution 4D-MRI exhibited a maximum error of 1.6 ± 0.9 mm compared to the ground-truth image data, suggesting that the MidP displacement was well preserved within

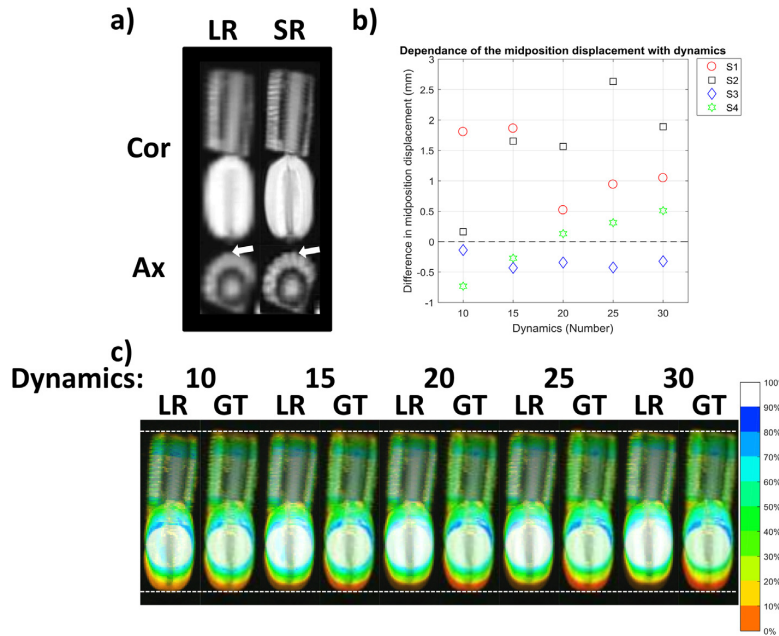


Fig. 4. (a) Low-resolution (LR) and super-resolution (SR) images of a motion phantom (waveform S3), for one coronal (Cor) and axial (Ax) slice in midposition. Sweetcorn kernels (white arrow) are more easily distinguished in the SR images than in the LR images. (b) Depicts the difference in midposition displacement of the phantom versus the number of dynamics for the sinusoidal (S1–S2) and volunteer (S3–S4) waveforms in the low-resolution T2w MRI (Motion-model) and in the ground-truth (GT) images. (c) LR and GT colour-intensity projection images of one coronal slice for different numbers of dynamics (waveform S4). The LR images show a slight underestimation of motion. Colour encodes time spent in each position. 100% of the time means that part of the phantom is always in the same position. Dashed white lines show exhalation and inhalation (top and bottom) for the GT data set of 30 dynamics.

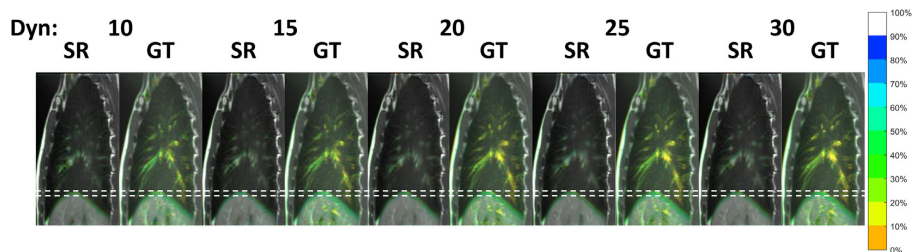


Fig. 5. Colour-intensity projection images displaying time-weighted motion information contained in the dynamics (Dyn) of the unprocessed sagittal ground-truth (GT) images and respiratory phases of the super-resolution (SR) images of volunteer 1. Dashed white lines aid visual comparison of inhalation and exhalation. In the lung, colour approximately represents time spent in each position. 100% (grayscale) means that image intensity is not changing in that position for all respiratory phases. The respiratory motion in the GT images is preserved in the SR images, which can be recognised by comparing the extent of the liver dome motion. Pulsations due to cardiac motion in the GT images are reduced in the SR images.

the proposed workflow. The remaining differences might be associated with the reduction of stitching artefacts.

Compared to the unprocessed CIPs of the phantom and volunteer measurements, the low-resolution and super-resolution reconstruction CIPs both showed a slight underestimation towards inhalation. Overall, the range of diaphragmatic motion was well preserved in the super-resolution reconstruction CIPs; further suggesting that the motion-model sufficiently represents the motion range.

For all volunteer MidP images (obtained from N dynamics), the average diaphragm displacement was concurrent with that at 30 dynamics to within 1.1 mm, which was in rough agreement with the phantom results.

Our approach ensures data completeness by sorting images on a slice-by-slice basis. This enables faster acquisition compared to alternative binning strategies [19,21]. Due to the exploitation of IRS, the proposed method is fully automatic; saving valuable time, for instance by avoiding the setup of a respiratory bellows [17]. In contrast to other methods [16,19], a 3D gradient non-linearity distortion correction is applied to optimise geometrical fidelity for RTP. Additionally, cardiovascular flow and motion are suppressed by the super-resolution reconstruction, which facilitates RTP by reduction of obfuscating features. In comparison to a recently published method, in which 4D-T2w MRI is obtained by applying the motion information from a 4D-T1w MRI (radial stack-of-stars sequence) to 3D-T2w MRI [5,42], 4D-T2w MRI was obtained with

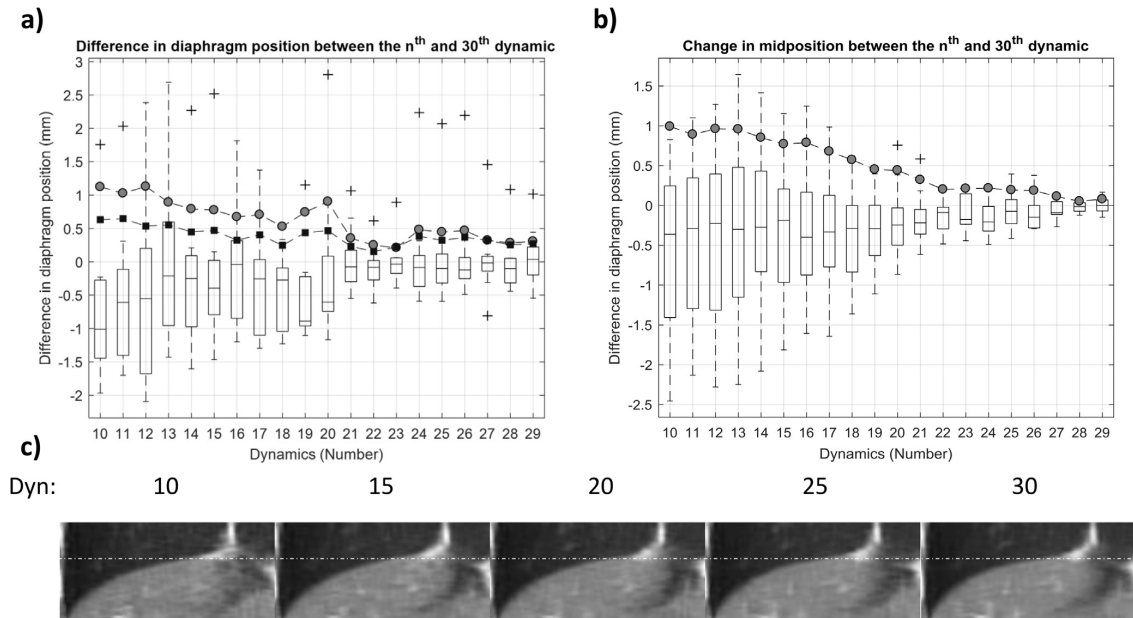


Fig. 6. (a) Differences in diaphragm position between the low-resolution sagittal midposition images obtained from N (10 to 29) and 30 dynamics. Boxplots summarize the results from the eight volunteers. Mean absolute differences are depicted by grey circles (uncorrected) and black squares (corrected for drift in midposition). (b) Changes in midposition with number of dynamics; boxplots summarize results for different volunteers. The mean absolute difference in midposition compared to the full 30 dynamics is depicted by grey circles. (c) Coronal views of super-resolution midposition images of volunteer 1 for different number of dynamics (Dyn). Images exhibit high similarity. White dashed lines aid comparison of the diaphragm position.

a higher resolution and required a considerably shorter time to reconstruct. The 3D radial stack-of-stars trajectory provides a large degree of flexibility regarding the imaging contrast, in particular a balanced implementation with a mixed T2/T1 contrast is possible and clinically feasible reconstruction times were demonstrated [15]. Likewise, the proposed super-resolution method could be applied to generate 4D-MRI of any contrast accessible using a fast 2D imaging sequence. Additionally, other 4D imaging contrasts could be acquired by transferring the motion information obtained during the motion-modelling workflow to other volumetric images [5]. Identifying which 4D imaging technique is most suited for characterising motion of treatment targets and organs at risk is an open question in lung RTP [3].

A limited number of healthy volunteers were scanned and might not be representative of lung cancer patients, since patients may exhibit less regular respiratory patterns due to compromised lung function. In this work a sagittal and axial acquisition strategy was employed to optimise image quality for contouring in RTP, which is commonly carried out in the axial plane. An axial and coronal acquisition strategy could be employed to exploit the higher acceleration factor in parallel imaging due to favourable orientation of coil elements compared to a sagittal acquisition. The high specific absorption rate (SAR) of the HASTE sequence may limit the applicability of the acquisition strategy at higher field strengths or for patients with implants. However, SAR can be decreased by reduction of the refocusing flip-angle or by increasing the repetition time. The current acquisition time of 16.8 ± 1.2 min (30 dynamics) is twice that of existing low-resolution methods [21,33]. However, acquisition time could be competitive and viable for a hybrid MRigRT treatment setup if only 10 dynamics were acquired, which we showed to be sufficient for MidP-T2w MRI. The reconstruction time of the non-optimised MATLAB prototype is currently too long for clinical use on MRigRT systems, but has

scope for improvement, e.g. by exploiting a multi-core cluster to accelerate calculation of the parallelisable components [15].

By using available tumour trajectory information to compensate for respiratory motion, the MidP RTP technique results in almost the same planning margin outcomes as idealised gated radiotherapy [8]. The presented 4D/MidP-T2w MRI could be employed alongside 4D/MidP-CT to facilitate target delineation and also to update tumour trajectory information and margins throughout treatment. In addition to MidP images, alternative planning images, e.g. midventilation [8], could be generated with the presented approach, since the whole respiratory cycle is covered.

We have demonstrated the feasibility of obtaining high-resolution 4D/MidP-T2w MRI ($1.0 \times 1.0 \times 1.0 \text{ mm}^3$) from axial and sagittal 2D-T2w MRI with a binning and super-resolution reconstruction method. Additionally, 10 repeated dynamic measurements of data were found sufficient to obtain representative MidP-T2w MRI. The resulting 4D/MidP-T2w MRI were distortion corrected, exhibited reduced stitching artefacts, and were free of data incompleteness artefacts. Super-resolution 4D/MidP-T2w MRI is a promising technique for hybrid MRigRT systems and to facilitate target delineation for treatment planning.

Conflict of interest

The Institute of Cancer Research and Royal Marsden NHS Foundation Trust is part of the Elekta MR Linac Research Consortium.

Acknowledgments

We thank Siemens Healthineers for providing us with the spherical harmonic coefficients of the MAGNETOM Aera. We also thank Nina Tunariu, Dow-Mu Koh and Matthew Orton for their

help with data acquisition and image analysis. We acknowledge NHS funding to the NIHR Biomedical Research Centre and the Clinical Research Facility at The Institute of Cancer Research and The Royal Marsden NHS Foundation Trust and the CR UK Cancer Imaging Centre grant C1060/A16464. We acknowledge funding from CR UK programme grants C33589/A19727, and project grants C347/A18365, C309/A20926 and C7224/A23275. Martin O. Leach is an NIHR Emeritus Senior Investigator.

Appendix A. Supplementary data

Supplementary data associated with this article can be found, in the online version, at <https://doi.org/10.1016/j.radonc.2018.05.015>.

References

- [1] Schmidt MA, Payne GS. Radiotherapy planning using MRI. *Phys Med Biol* 2015;60:R323.
- [2] Lagendijk JJ, Raaymakers BW, Van den Berg CA, Moerland MA, Philippens ME, van Vulpen M. MR guidance in radiotherapy. *Phys Med Biol* 2014;59:R349.
- [3] Bainbridge H, Salem A, Tijssen RH, et al. Magnetic resonance imaging in precision radiation therapy for lung cancer. *Transl Lung Cancer Res* 2017;6:689.
- [4] Riddell AM, Hillier J, Brown G, et al. Potential of surface-coil MRI for staging of esophageal cancer. *Am J Roentgenol* 2006;187:1280–7.
- [5] Freedman JN, Collins DJ, Bainbridge H, et al. T2-weighted 4D magnetic resonance imaging for application in magnetic resonance-guided radiotherapy treatment planning. *Invest Radiol* 2017;52:563–73.
- [6] Bainbridge H, Wetscherek A, Eccles C, et al. P2. 05-042 development of thoracic magnetic resonance imaging (MRI) for radiotherapy planning. *J Thorac Oncol* 2017;12:S1057.
- [7] Wolthaus J, Sonke JJ, Van Herk M, Damen E. Reconstruction of a time-averaged midposition CT scan for radiotherapy planning of lung cancer patients using deformable registration. *Med Phys* 2008;35:3998–4011.
- [8] Wolthaus JW, Sonke J-J, van Herk M, et al. Comparison of different strategies to use four-dimensional computed tomography in treatment planning for lung cancer patients. *Int J Radiat Oncol* 2008;70:1229–38.
- [9] Mutic S, Dempsey JF. The ViewRay system: magnetic resonance-guided and controlled radiotherapy. *Semin Radiat Oncol* 2014;24:196–9.
- [10] Raaymakers B, Lagendijk J, Overweg J, et al. Integrating a 1.5 T MRI scanner with a 6 MV accelerator: proof of concept. *Phys Med Biol* 2009;54:N229.
- [11] Thwaites D, Keall P, Holloway L, Sykes J, Cosgrove V. Observations on MR-LINAC systems and rationale for MR-Linac use: the Australian MR-Linac project as an example. *Phys Medica* 2014;30:e25.
- [12] Fallone BG. The rotating biplanar linac-magnetic resonance imaging system. *Semin Radiat Oncol* 2014;24:200–2.
- [13] Kontaxis C, Bol GH, Stemkens B, et al. Towards fast online intrafraction replanning for free-breathing stereotactic body radiation therapy with the MR-linac. *Phys Med Biol* 2017;62:7233.
- [14] Stemkens B, Tijssen RH, de Senneville BD, Lagendijk JJ, van den Berg CA. Image-driven, model-based 3D abdominal motion estimation for MR-guided radiotherapy. *Phys Med Biol* 2016;61:5335–55.
- [15] Mickevicius NJ, Paulson ES. Investigation of undersampling and reconstruction algorithm dependence on respiratory correlated 4D-MRI for online MR-guided radiation therapy. *Phys Med Biol* 2017;62:2910–21.
- [16] Li G, Wei J, Olek D, et al. Direct comparison of respiration-correlated four-dimensional magnetic resonance imaging reconstructed using concurrent internal navigator and external bellows. *Int J Radiat Oncol* 2017;97:596–605.
- [17] Tryggestad E, Flammang A, Han-Oh S, et al. Respiration-based sorting of dynamic MRI to derive representative 4D-MRI for radiotherapy planning. *Med Phys* 2013;40:051909–11.
- [18] Hu Y, Caruthers SD, Low DA, Parikh PJ, Mutic S. Respiratory amplitude guided 4-dimensional magnetic resonance imaging. *Int J Radiat Oncol* 2013;86:198–204.
- [19] Hui C, Wen Z, Stemkens B, et al. 4D MR imaging using robust internal respiratory signal. *Phys Med Biol* 2016;61:3472–87.
- [20] Cai J, Chang Z, Wang Z, Segars WP, Yin F-F. Four-dimensional magnetic resonance imaging (4D-MRI) using image-based respiratory surrogate: a feasibility study. *Med Phys* 2011;38:6384–94.
- [21] Liu Y, Yin F-F, Czito BG, Bashir MR, Cai J. T2-weighted four dimensional magnetic resonance imaging with result-driven phase sorting. *Med Phys* 2015;42:4460–71.
- [22] Liu Y, Yin F-F, Chen N-K, Chu M-L, Cai J. Four dimensional magnetic resonance imaging with retrospective k-space reordering: a feasibility study. *Med Phys* 2015;42:534–41.
- [23] Paganelli C, Summers P, Bellomi M, Baroni G, Riboldi M. Liver 4DMRI: a retrospective image-based sorting method. *Med Phys* 2015;42:4814–21.
- [24] King AP, Buerger C, Tsoumpas C, Marsden PK, Schaeffer T. Thoracic respiratory motion estimation from MRI using a statistical model and a 2-D image navigator. *Med Image Anal* 2012;16:252–64.
- [25] Bones I, Gurney-Champion O, Van der Horst A, et al. PO-0881: 4DMRI for RT planning; novel precise amplitude binning in the presence of irregular breathing. *Radiother Oncol* 2017;123:S482–3.
- [26] Liu Y, Yin FF, Chang Z, et al. Investigation of sagittal image acquisition for 4D-MRI with body area as respiratory surrogate. *Med Phys* 2014;41:101902–11.
- [27] Weygand J, Fuller CD, Ibbott GS, et al. Spatial precision in magnetic resonance imaging-guided radiotherapy: the role of geometric distortion. *Int J Radiat Oncol* 2016;95:1304–16.
- [28] Van Reeth E, Tham IW, Tan CH, Poh CL. Super-resolution in magnetic resonance imaging: a review. *Concepts Magn Reson* 2012;40:306–25.
- [29] Chilla GS, Tan CH, Poh CL. Deformable registration based super-resolution for isotropic reconstruction of 4D MRI volumes. *IEEE J Biomed Health Inform* 2017;21:1617–24.
- [30] Reeth E, Tan CH, Tham IW, Poh CL. Isotropic reconstruction of a 4-D MRI thoracic sequence using super-resolution. *Magn Res Med* 2015;73:784–93.
- [31] Li G, Wei J, Kadbi M, et al. Novel super-resolution approach to time-resolved volumetric 4-dimensional magnetic resonance imaging with high spatiotemporal resolution for multi-breathing cycle motion assessment. *Int J Radiat Oncol* 2017;98:454–62.
- [32] Cover KS, Lagerwaard FJ, Senan S. Color intensity projections: a rapid approach for evaluating four-dimensional CT scans in treatment planning. *Int J Radiat Oncol* 2006;64:954–61.
- [33] Freedman JN, Collins DJ, Bainbridge H, et al. Evaluation of 4D-T2w MRI methods for lung radiotherapy treatment planning with application to an MR-linac. In: *ISMRM 25th annual meeting & exhibition*; 2017:2906.
- [34] Doran SJ, Charles-Edwards L, Reinsberg SA, Leach MO. A complete distortion correction for MR images: I. Gradient warp correction. *Phys Med Biol* 2005;50:1343.
- [35] Vercauteren T, Pennec X, Perchant A, Ayache N. Diffeomorphic demons: efficient non-parametric image registration. *NeuroImage* 2009;45:S61–72.
- [36] Modat M, Ridgway GR, Taylor ZA, et al. Fast free-form deformation using graphics processing units. *Comput Methods Prog Biol* 2010;98:278–84.
- [37] Rueckert D, Sonoda LI, Hayes C, Hill DL, Leach MO, Hawkes DJ. Nonrigid registration using free-form deformations: application to breast MR images. *IEEE T Med Imaging* 1999;18:712–21.
- [38] Irani M, Peleg S. Improving resolution by image registration. *Graph Models Image Process* 1991;53:231–9.
- [39] Kuklisova-Murgasova M, Quaghebeur G, Rutherford MA, Hajnal JV, Schnabel JA. Reconstruction of fetal brain MRI with intensity matching and complete outlier removal. *Med Image Anal* 2012;16:1550–64.
- [40] Grimm R, Fürst S, Souvatzoglou M, et al. Self-gated MRI motion modeling for respiratory motion compensation in integrated PET/MRI. *Med Image Anal* 2015;19:110–20.
- [41] Suh Y, Dieterich S, Cho B, Keall PJ. An analysis of thoracic and abdominal tumour motion for stereotactic body radiotherapy patients. *Phys Med Biol* 2008;53:3623.
- [42] Rank CM, Heußler T, Buzan MT, et al. 4D respiratory motion-compensated image reconstruction of free-breathing radial MR data with very high undersampling. *Magn Res Med* 2017;77:1170–83.

Appendix C

Synthetic 4D-CT of the thorax for treatment plan adaptation on MR-guided radiotherapy systems

Freedman *et al.* 2019

OPEN ACCESS

PAPER

RECEIVED
7 October 2018REVISED
4 January 2019ACCEPTED FOR PUBLICATION
7 March 2019PUBLISHED
23 May 2019

Original content from this work may be used under the terms of the [Creative Commons Attribution 3.0 licence](#).

Any further distribution of this work must maintain attribution to the author(s) and the title of the work, journal citation and DOI.



Synthetic 4D-CT of the thorax for treatment plan adaptation on MR-guided radiotherapy systems

Joshua N Freedman^{1,2}, Hannah E Bainbridge³, Simeon Nill¹, David J Collins², Marc Kachelrieß⁴, Martin O Leach^{2,5}, Fiona McDonald³, Uwe Oelfke¹ and Andreas Wetscherek¹

¹ Joint Department of Physics, The Institute of Cancer Research and The Royal Marsden NHS Foundation Trust, London, United Kingdom

² CR UK Cancer Imaging Centre, The Institute of Cancer Research and The Royal Marsden NHS Foundation Trust, London, United Kingdom

³ Department of Radiotherapy, The Royal Marsden NHS Foundation Trust, London, United Kingdom

⁴ Medical Physics in Radiology, The German Cancer Research Center (DKFZ), Heidelberg, Germany

⁵ Author to whom any correspondence should be addressed.

E-mail: Martin.Leach@icr.ac.uk

Keywords: 4D MRI, radiotherapy treatment planning, MR-guided radiotherapy, pseudo CT, synthetic CT

Supplementary material for this article is available [online](#)

Abstract

MR-guided radiotherapy treatment planning utilises the high soft-tissue contrast of MRI to reduce uncertainty in delineation of the target and organs at risk. Replacing 4D-CT with MRI-derived synthetic 4D-CT would support treatment plan adaptation on hybrid MR-guided radiotherapy systems for inter- and intrafractional differences in anatomy and respiration, whilst mitigating the risk of CT to MRI registration errors.

Three methods were devised to calculate synthetic 4D and midposition (time-weighted mean position of the respiratory cycle) CT from 4D-T1w and Dixon MRI. The first approach employed intensity-based segmentation of Dixon MRI for bulk-density assignment (sCT_D). The second step added spine density information using an atlas of CT and Dixon MRI (sCT_{DS}). The third iteration used a polynomial function relating Hounsfield units and normalised T1w image intensity to account for variable lung density (sCT_{DSL}). Motion information in 4D-T1w MRI was applied to generate synthetic CT in midposition and in twenty respiratory phases. For six lung cancer patients, synthetic 4D-CT was validated against 4D-CT in midposition by comparison of Hounsfield units and dose-volume metrics. Dosimetric differences found by comparing $sCT_{D,DS,DSL}$ and CT were evaluated using a Wilcoxon signed-rank test ($p = 0.05$).

Compared to sCT_D and sCT_{DS} , planning on sCT_{DSL} significantly reduced absolute dosimetric differences in the planning target volume metrics to less than 98 cGy (1.7% of the prescribed dose) on average. When comparing sCT_{DSL} and CT, average radiodensity differences were within 97 Hounsfield units and dosimetric differences were significant only for the planning target volume D99% metric. All methods produced clinically acceptable results for the organs at risk in accordance with the UK SABR consensus guidelines and the LungTech EORTC phase II trial. The overall good agreement between sCT_{DSL} and CT demonstrates the feasibility of employing synthetic 4D-CT for plan adaptation on hybrid MR-guided radiotherapy systems.

Introduction

Magnetic resonance guided radiotherapy (MRgRT) exploits the high soft-tissue contrast of magnetic resonance imaging (MRI) to improve treatment delivery in radiotherapy (Lagendijk *et al* 2014, Schmidt and Payne 2015). Computed tomography (CT) images can be registered to magnetic resonance (MR) images to optimise radiotherapy treatment planning (RTP); electron density information from the CT images are employed for dose calculations and MR images are used to facilitate target and organ at risk (OAR) delineation (Owringi *et al* 2018). Registration can result in systematic errors that propagate through the workflow and have been reported to be 2–5 mm for the brain and prostate (Edmund and Nyholm 2017). Registration errors, between CT and MRI, can be eliminated by deriving synthetic CT (sCT) from MRI (Johnstone *et al* 2018).

In conventional radiotherapy workflows, treatment delivery is based on the same pre-treatment CT image for all fractions, which is problematic as the patient anatomy might change during the course of treatment, for instance because of tumour shrinkage. Dosimetric errors related to inter- and intrafractional differences in anatomy can be reduced when delivering adaptive MRgRT (Raaymakers *et al* 2009, Fallone 2014, Lagendijk *et al* 2014, Mutic and Dempsey 2014, Thwaites *et al* 2014, Kontaxis *et al* 2017). In this scenario, treatment plans can be updated with the online patient anatomy and position obtained using sCT acquired during a hybrid MRgRT treatment session. Calculation of sCT by registering the pre-treatment CT image to daily MRI acquired prior to each treatment fraction was demonstrated (Kraus *et al* 2017). However, generating sCT directly from MRI is more desirable because it would eliminate registration errors and simplify the radiotherapy workflow by reducing the total number of scans (Edmund and Nyholm 2017).

Alternatively, sCT has been calculated using bulk-density assignment, atlas-based, voxel-based (including machine learning) and hybrid methods, with the majority of approaches applied to relatively immobile sites, such as the brain or prostate (Edmund and Nyholm 2017, Johnstone *et al* 2018). In the abdominothoracic region, most current methods are based on tissue-segmentation and bulk-density assignment. Of the methods which do not include bone-density information, dosimetric differences of the D95% metric (dose delivered to at least 95% of the planning target volume (PTV)) between sCT and CT have been reported to be less than 1% using 3D conformal RTP (Jonsson *et al* 2010), and greater than 5% using volumetric modulated arc therapy (VMAT) RTP (Prior *et al* 2017). In methods which include bone-density information, for instance by using an anterior vertebral body model (VMAT RTP) (Bredfeldt *et al* 2017) or an atlas (intensity modulated RTP) (Wang *et al* 2017), mean dosimetric differences for all regions and metrics have been reported to be within 1%.

There is scope to improve abdominothoracic sCT. Prior *et al* (2017) demonstrated that incorrect bulk-density assignment in the lung leads to errors up to 19.6% in the PTV dose-volume metrics. Patient specific lung electron density values should therefore be implemented to account for underlying lung pathology (Rosenblum *et al* 1980, Soejima *et al* 2000, Durham and Adcock 2015). Furthermore, four-dimensional (4D) or midposition (MidP) (time-weighted mean position of the respiratory cycle) (Wolthaus *et al* 2008a) sCT might be employed to account for respiratory motion in dose reconstruction (Al-Ward *et al* 2018).

In this article, thoracic 4D/MidP-sCT was calculated using three different methods and validated dosimetrically against the corresponding MidP image of 4D-CT for plan adaptation on MRgRT systems. In the first method, 4D/MidP-sCT was obtained using tissue-segmentation and bulk-density assignment (sCT_D), and was extended in the second method using an atlas to include bone-density information (sCT_{DS}). The third method employed a fitting approach to account for variable lung density (sCT_{DSL}).

Materials and methods

Data acquisition

Six patients with early stage non-small cell lung cancer (5 adenocarcinoma, 1 mixed adenosquamous carcinoma), all of whom were treated with stereotactic radiotherapy, were included in this study after giving written informed consent. A 4D-CT scan was obtained for all patients using a Brilliance Big Bore CT scanner at 120kV (Philips Medical Systems, Best, The Netherlands), with voxel-size $(0.98 \times 0.98 - 1.17 \times 1.17) \times 2 \text{ mm}^3$ and ten respiratory phases. Within a median of 2 (range: 0–14) d, MRI was acquired at 1.5 Tesla (MAGNETOM Aera; Siemens Healthcare, Erlangen, Germany) using a golden-angle radial T1-weighted stack-of-stars spoiled gradient echo sequence (Block *et al* 2014) in free breathing and a Cartesian 2-point Dixon gradient echo sequence in exhalation. Patients unable to breath-hold were scanned in free-breathing with four averages, resulting in an image close to exhalation. Patients were scanned in the same treatment position in both MRI and CT acquisition, which was enabled using an MR compatible immobilisation board (Extended Wing Board; Civco Radiotherapy, Coralville, IA, USA). During MR acquisition, an in-house built body coil holder was used to prevent compression of the body contour by the 18-channel receive array. Detailed MRI acquisition parameters can be found in table 1.

Table 1. Detailed acquisition parameters. No, number; Acq, acquisition; NA, not applicable.

Parameter	Radial T1w stack-of-stars	Dixon (exhalation)	Dixon (free-breathing)
Orientation	Axial	Axial	Axial
No. slices	80–88	64–88	72–88
No. spokes	1005	NA	NA
Acq. time (min)	05:19–05:45	00:20–00:21	02:02–02:49
Field of view (mm ²)	320 × 320–336 × 336	322 × 430–360 × 480	312 × 400–368 × 469
Voxel-size (mm ³)	(1.25 × 1.25–1.31 × 1.31) × 3.5	(1.68 × 1.68–1.88 × 1.88) × 4.2	(1.25 × 1.25–1.34 × 1.34) × 3.5
Echo time (ms)	1.55	2.39, 4.77	2.39, 4.77
Repetition time (ms)	3.18	7.6	7.6
Flip angle (°)	8	8	8
Pixel bandwidth (Hz)	630	400	400
No. signal averages	1	1	4
Fat suppression	YES	NO	NO

Reconstruction of T1w data

T1w MRI was reconstructed using the 4D joint motion-compensated high-dimensional total variation (4D joint MoCo-HDTV) algorithm (Rank *et al* 2017). Prior to reconstruction, the raw data were corrected with an adaptive gradient-delay compensation (Block and Uecker 2011) and sorted into 20 overlapping respiratory phases using a self-gating signal based on the k -space centre (Paul *et al* 2015). After reconstruction, a 3D geometrical distortion correction was applied to each respiratory phase to account for gradient non-linearity, using the spherical harmonic coefficients provided by the vendor (Doran *et al* 2005). More details regarding the reconstruction workflow can be found in Freedman *et al* (2017).

Motion-modelling

All of the following calculations were carried out in MATLAB (version 2017a; The Mathworks, Natick, MA) on an Intel Xeon E5-1660 processor with 8 cores at 3 GHz and 64 GB of memory. Key components of the following motion-modelling method are provided in figure 1(A).

Based on volumetric normalised mutual information (NMI) (Pluim *et al* 2003), the closest matching respiratory phase of 4D-T1w MRI (T_{1j}) was chosen with respect to the in-phase Dixon image (D_j). Deformation vector fields (DVF) were calculated by non-rigidly registering T_{1j} to all n remaining respiratory phases ($DVF_{T_{1j} \rightarrow T_n}$). All b-spline GPU accelerated non-rigid registrations were carried out using NiftyReg (Modat *et al* 2010). A chain method concatenating DVFs was employed to reduce errors resulting from large deformations (Freedman *et al* 2017). The transformation $DVF_{T_{1j} \rightarrow T_{MidP}}$ from the closest matching phase to MidP was determined from the $DVF_{T_{1j} \rightarrow T_n}$ set (Wolthaus *et al* 2008a). MidP-T1w MRI was obtained by applying $DVF_{T_{1j} \rightarrow T_{MidP}}$ to T_{1j} . $DVF_{D_j \rightarrow T_j}$ was generated by non-rigidly registering D_j to T_{1j} . Water, fat and in-phase Dixon images were warped to MidP using the composition: $DVF_{T_{1j} \rightarrow T_{MidP}} * DVF_{D_j \rightarrow T_j}$.

MidP-CT was independently calculated from 4D-CT in the same way that MidP-T1w MRI was obtained from 4D-T1w MRI.

Atlas

The atlas contained MidP-T1w, MidP-Dixon (fat, water and in-phase), MidP-CT and MidP-spine (segmented from MidP-CT) images. The MidP-CT atlas images were obtained by registering the pre-calculated MidP-CT images to the MidP in-phase images. The MidP-spine atlas images were extracted from the MidP-CT atlas images using a thresholding and region of interest (ROI) method (figure 1(B)):

Bone was segmented from MidP-CT by thresholding (125 to 1500 Hounsfield units (HUs)) and connected component analysis; the first connected component corresponded to the rib cage, which included the thoracic vertebrae. Stray pixels were removed by morphologically dilating and closing the rib cage image using an ellipsoid structuring element (1,1,2 pixels). A rectangular ROI was manually placed around the spine on the central axial slice of the processed rib cage image. Pixels outside the ROI were set to zero on all slices. Holes were filled using a morphological flood-fill operation (Soille 1999).

A leave-one-out cross-validation was enabled by truncating the atlas to include all acquired data except the patient for which MidP-sCT was being generated (referred to as the incoming patient or image).

Dixon synthetic CT (sCT_D)

MidP-sCT (sCT_D) was generated from the MidP-Dixon images using intensity-based segmentation and assignment of HUs for fat (−110), soft-tissue (70), air (−1000) and lung (−767). HU values were chosen from Wang *et al* (2017). Segmentation was carried out using binary masks:

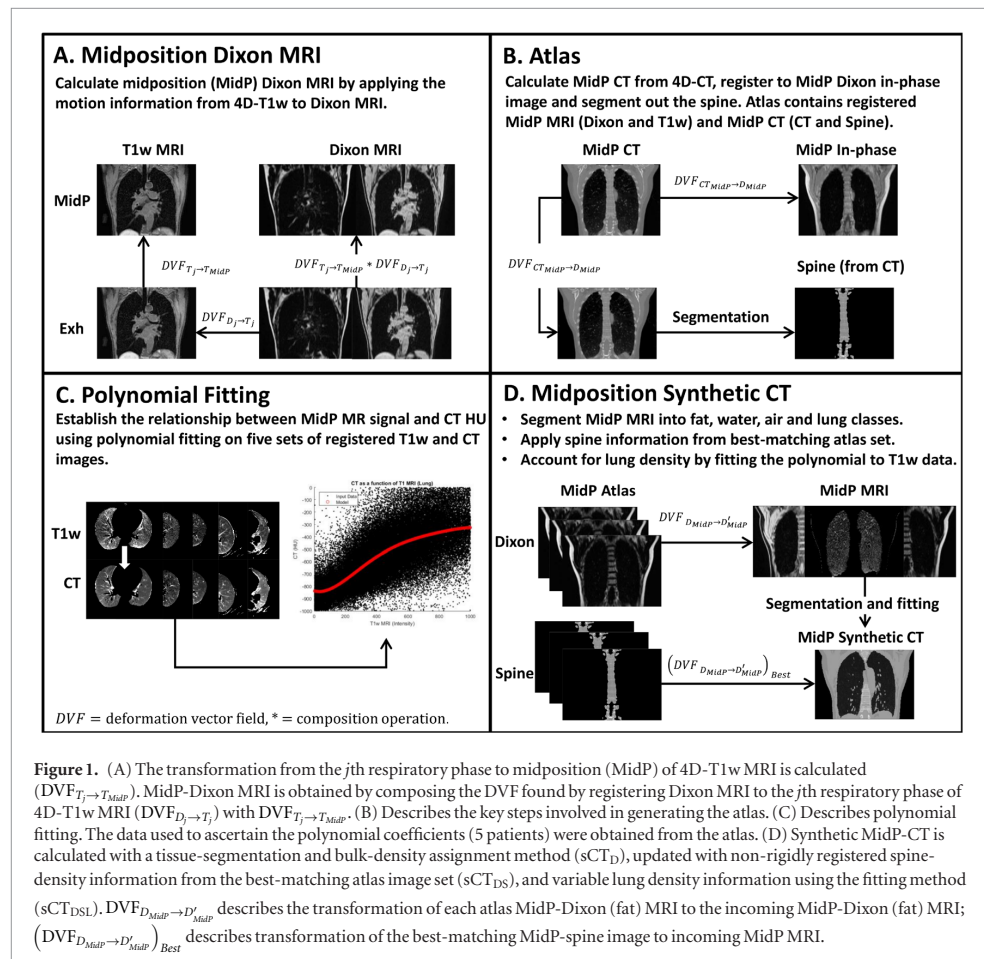


Figure 1. (A) The transformation from the j th respiratory phase to midposition (MidP) of 4D-T1w MRI is calculated ($DVF_{T_j \rightarrow T_{MidP}}$). MidP-Dixon MRI is obtained by composing the DVF found by registering Dixon MRI to the j th respiratory phase of 4D-T1w MRI ($DVF_{D_j \rightarrow T_j}$) with $DVF_{T_j \rightarrow T_{MidP}}$. (B) Describes the key steps involved in generating the atlas. (C) Describes polynomial fitting. The data used to ascertain the polynomial coefficients (5 patients) were obtained from the atlas. (D) Synthetic MidP-CT is calculated with a tissue-segmentation and bulk-density assignment method (sCT_D), updated with non-rigidly registered spine-density information from the best-matching atlas image set (sCT_{DS}), and variable lung density information using the fitting method (sCT_{DSL}). $DVF_{D_{MidP} \rightarrow D'_{MidP}}$ describes the transformation of each atlas MidP-Dixon (fat) MRI to the incoming MidP-Dixon (fat) MRI; $(DVF_{D_{MidP} \rightarrow D'_{MidP}})_{Best}$ describes transformation of the best-matching MidP-spine image to incoming MidP MRI.

A binary mask M (background and lungs = 1, remaining = 0) was calculated by thresholding the summed MidP-Fat and MidP-Water images. Thresholds were set as the mean summed image intensity. M was zero padded and subjected to connected component analysis; the largest component was the background mask B . The lung mask L was calculated as $M - B$.

Fat and water masks were initialised by applying the $|1 - M|$ mask to the MidP-Fat and MidP-Water images. The initialised fat mask was thresholded using the mean non-zero intensity of the MidP-Fat image and then post-processed, to reduce stray pixels and holes, by keeping only the largest connected component. The post-processed fat mask was applied to remove fat components from the initialised water mask.

Dixon-spine synthetic CT (sCT_{DS})

sCT_D were updated to include spine density information (sCT_{DS}) from the best-matching MidP-spine atlas image. All MidP-Fat atlas images were registered to the incoming MidP-Fat image. The corresponding MidP-spine atlas images were warped with the resulting transformations and applied to segment the spine of registered MidP-Fat images. NMI was calculated between the incoming and registered segmented MidP-Fat images. The MidP-spine atlas image corresponding to the best-matching registered segmented MidP-Fat image (highest NMI) was fused with sCT_D by intensity override.

Dixon-spine-lung synthetic CT (sCT_{DSL})

sCT_{DS} were modified to include variable lung density information (sCT_{DSL}). The relationship between signal intensity in MidP-T1w images and HUs of co-registered MidP-CT images was modelled in the lung with a fifth order polynomial (figure 1(C)). MidP-T1w images were corrected for intensity inhomogeneity (Hofmann et al 2011): first the scanner-reconstructed T1w images were passed through 3D median and image guided filters (He et al 2013). MidP-T1w images were then divided by the filtered scanner-reconstructed images. Afterwards, inhomogeneity corrected MidP-T1w images were normalised such that the mean intensity values of the water

components in each image were equal. Ten million non-zero points were randomly selected in the lungs of MidP-T1w MRI and MidP-CT. Data support over the entire intensity range was assured by further sorting the data into 20 equal sized bins, and then extracting 5000 random data points from each bin. The polynomial weights were then obtained by linear least squares fitting to the selected data.

In order to enable a leave-one-out cross-validation, the truncated MidP atlas (see Materials and methods: Atlas) data were used to calculate separate polynomial weights for each incoming patient. Variable lung density information was included by applying the fitted polynomial to incoming MidP-T1w intensity values. A summary of sCT_{DSL} generation can be found in figure 1(D).

For incoming patient 2 it was necessary to generate additional sCT images by linearly scaling the lung HU values of $sCT_{D,DS,DSL}$ to match the median lung CT HU value (-865 HU). Scaling was required because patient 2 exhibited co-existent lung disease (severe emphysema) and did not fit into the group of other patients, which exhibited a mean (over patients 1 and 3–6) median HU value of -808 .

Four-dimensional sCT was calculated by warping MidP-sCT to all other respiratory phases using the composition of the $DVF_{T_j \rightarrow T_n}$ and inverse $DVF_{T_j \rightarrow T_{MidP}}$ transformations (for DVF calculations, see Materials and methods: motion-modelling).

Synthetic CT: validation

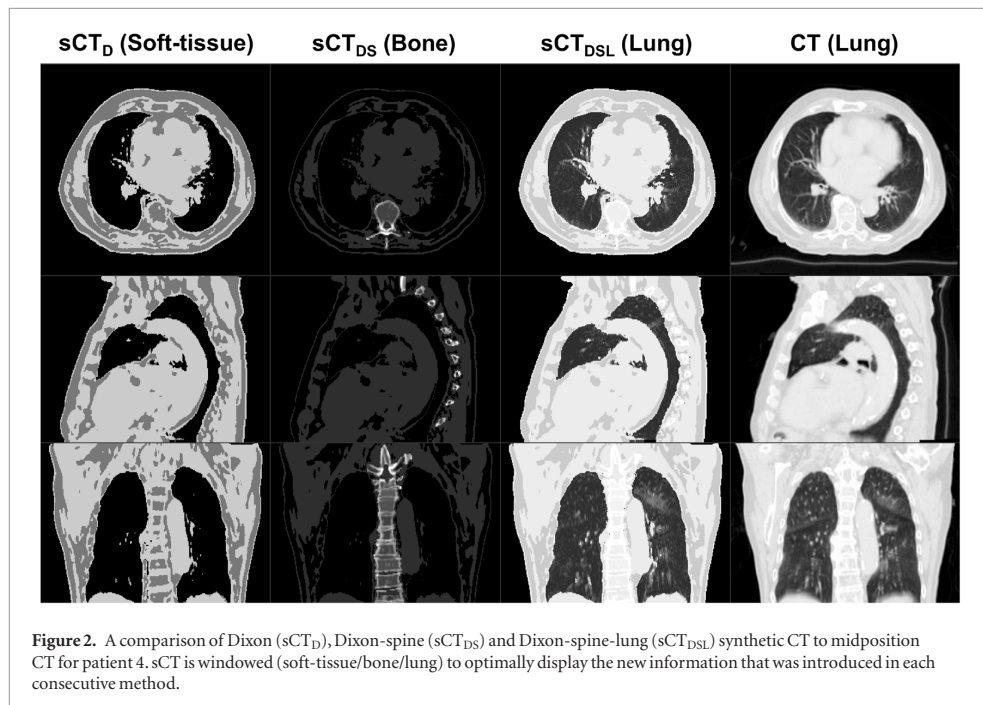
MidP-sCT images were validated by comparison to MidP-CT, both dosimetrically and in terms of HUs. Radiation oncologists performed delineation and treatment planning. Using the information from non-rigidly registered MidP-T1w and MidP-Dixon images, one set of contours was generated for the primary tumour and OARs for each patient. The contours represented the ‘best fit’ between CT and MR images. Single full arc coplanar stereotactic VMAT plans at 6 MV were designed for all patients using a collapsed cone algorithm and an Agility multileaf collimator on RayStation (v5.99, RaySearch Laboratories, Sweden) with a dose grid voxel-size of 2.5 mm and collimator angle of 2° . Five patients had peripheral lesions with a PTV close to the chest wall, and were planned according to the UK SABR consortium guidelines with a five fraction regimen (55 Gy in 5 fractions) using the constraints stipulated in a recent UK SABR consensus publication (Hanna *et al* 2018). One patient had a central lesion and was planned using an eight fraction regimen (60 Gy in 8 fractions) as per the LungTech EORTC phase II trial protocol (Adebahr *et al* 2015, Lambrecht *et al* 2016). As MidP images were used, PTV margins were personalised for each patient, and this was dependent on tumour motion. PTV margins were calculated using motion information from the 4D-T1w images, but applying the same principles as reported elsewhere using 4D-CT planning (Wolthaus *et al* 2008b). Once contours had been finalised, they were copied onto the fused sCT images. Two planning techniques were used: initial planning on MidP-CT and independent re-calculation on $sCT_{D,DS,DSL}$ (Plan 1); and initial planning on $sCT_{D,DS,DSL}$ (using all sCT methods independently) and re-calculation on MidP-CT (Plan 2). Differences in the following dose-volume metrics were compared: Dose delivered to at least 95 or 99% of the PTV (PTV D95 or 99%, respectively), total PTV volume divided by the total isodose volume of interest (Conformity Index at Isodose), volume of lung receiving ≥ 20 Gy (v20 Gy), Proximal Airways near-point maximum dose (Dmax), which was defined as minimum dose to the 0.5 cm^3 volume of the organ receiving the highest dose (Hanna *et al* 2018), Oesophagus Dmax 0.5 cm^3 , Brachial Plexus Dmax 0.5 cm^3 , Heart Dmax 0.5 cm^3 , Spinal Canal Dmax 0.1 cm^3 , and Chest Wall Dmax 30 cm^3 , which is defined as the minimum dose to 30 cm^3 of the organ that receives the highest dose. In an exploratory analysis, a Wilcoxon signed-rank test with a significance level of $p = 0.05$ was applied to evaluate the dosimetric differences found by comparing $sCT_{D,DS,DSL}$ and CT. Using the same analysis, the absolute values of the above-mentioned dosimetric differences were compared for significance between methods ($sCT_{D \rightarrow DS}$, $sCT_{DS \rightarrow DSL}$, $sCT_{D \rightarrow DSL}$).

Results

For six patients with early stage node negative primary lung malignancies, three variations of MidP-sCT ($sCT_{D,DS,DSL}$) were calculated. For these patients, mean PTV volume was 34 (range: 22–40) cm^3 . Four-dimensional T1w MRI reconstruction took between 9 and 12 h, and calculation of sCT_D , sCT_{DS} and sCT_{DSL} was finished in 30, 51 and 54 min, respectively. Figure 2 shows an example reconstructed MidP-CT compared to $sCT_{D,DS,DSL}$. sCT_{DSL} provided good visual agreement with MidP-CT, due to not only comparable spine and variable lung density, but also matching respiratory phase. Two example movies of 4D-sCT (sCT_{DSL} , 20 respiratory phases) for patients 1 and 4 are provided as supplemental material (stacks.iop.org/PMB/64/115005/mmedia).

Validation: Hounsfield units

The median and standard deviation of the absolute differences in HUs, over all patients, between CT and sCT of the Dixon and Dixon-spine-lung methods were: 43 ± 187 and 42 ± 188 for the soft-tissue region, 43 ± 146 and 40 ± 144 for the fat region, 71 ± 114 and 43 ± 106 for the lung region, and 174 ± 186 and 96 ± 161 for the spine



region; demonstrating that overall sCT_{DSL} exhibited the highest similarity with the ground-truth CT images (figure 3).

Validation: dose-volume metrics

As presented in figure 4, differences in selected dose-volume metrics between $sCT_{D,DS,DSL}$ and CT were significant for PTV metrics, but not for OAR metrics. Unlike sCT_D and sCT_{DS} , sCT_{DSL} only exhibited a significant difference for the PTV D99% metric ($p = 0.03$) of Plan 2 (planned on sCT and re-calculated on CT). For the PTV D95% and D99% metrics, sCT_{DSL} exhibited the lowest absolute difference with CT, which was (mean \pm standard deviation in %) 1.7 ± 2.5 and 1.4 ± 2.3 for Plan 1 (initially planned on CT and re-calculated on sCT), and 1.6 ± 2.4 and 1.7 ± 2.2 for Plan 2. The mean and standard deviations were skewed by the results of patient 2, which exhibited absolute differences up to 6.7%. If the lung HU values of patient 2 were linearly scaled to match the median lung HU value of CT (figure 4; black diamonds), the average absolute differences of the PTV D95% and D99% metrics were reduced to: 0.91 ± 0.89 and 0.77 ± 1.1 for Plan 1, and 0.77 ± 0.93 and 1.0 ± 1.1 for Plan 2. The average absolute differences (over all patients) of the investigated dose-volume metrics between sCT_{DSL} and CT are summarised in table 2. For the OAR dose-volume metrics, minor differences were observed, but did not violate pre-defined clinical goals.

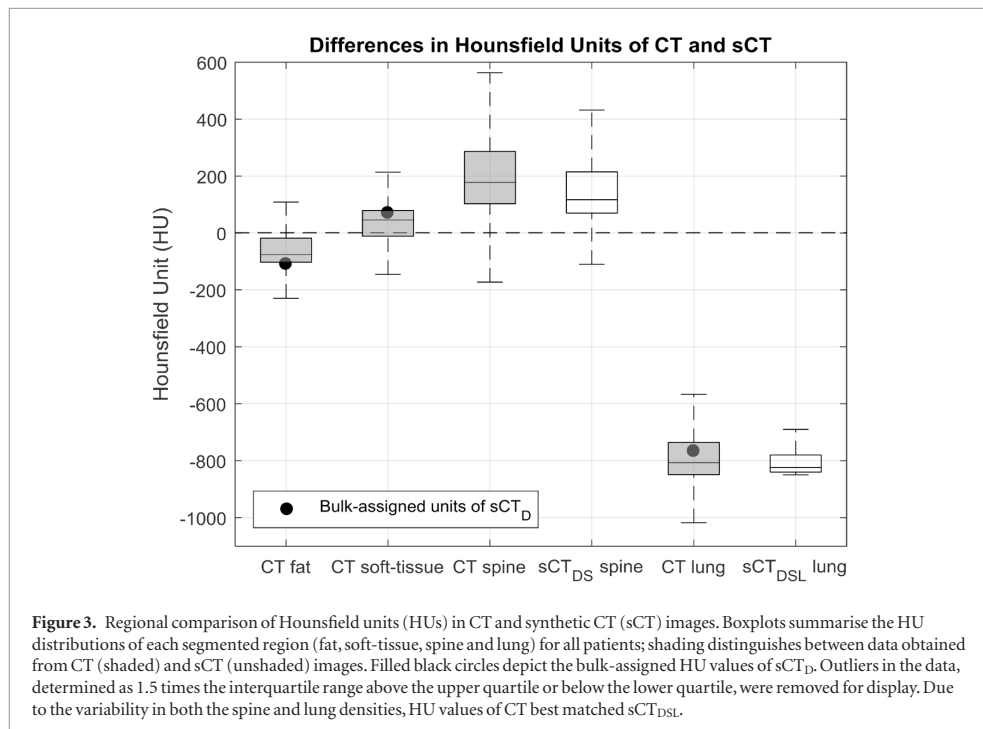
Comparison of synthetic CT methods

Significant reductions in absolute differences were found for the PTV D95% ($sCT_{D \rightarrow DS}$, $sCT_{DS \rightarrow DSL}$ and $sCT_{D \rightarrow DSL}$) and Conformity Index at Isodose metrics ($sCT_{DS \rightarrow DSL}$ and $sCT_{D \rightarrow DSL}$) of Plan 1, and for the PTV D95% ($sCT_{D \rightarrow DSL}$ and $sCT_{DS \rightarrow DSL}$) and D99% metrics ($sCT_{DS \rightarrow DSL}$) of Plan 2. For all OAR metrics, except the Proximal Airways Dmax 0.5 cm^3 metric, the mean absolute dosimetric difference over all patients decreased between sCT_D and sCT_{DSL} . No significant absolute differences were found for the OAR metrics.

Figure 5 displays an example illustrating the differences between the three sCT methods. Compared to sCT_D , inclusion of spine density information in sCT_{DS} resulted in a reduction of local hot spots in the differences between the simulated dose distributions of sCT and CT. Inclusion of variable lung density in sCT_{DSL} led to a further reduction in dose differences. In particular, the appearance of hot spots around the PTV decreased.

Discussion

In this article, three methods to calculate 4D- sCT were introduced and validated in MidP against 4D-CT. Employing 4D/MidP- sCT on hybrid MRgRT systems would enable plans to be adapted for anatomical differences and changes in respiratory pattern throughout the course of radiotherapy treatment, which might permit target



dose boosting and sparing OARs (Al-Ward *et al* 2018), whilst mitigating the risk of registration errors between CT and MRI. Moreover, 4D-sCT could be combined with motion information from fast 2D cine MRI to obtain a patient-specific motion-model (Stemkens *et al* 2016), which might be applied to generate low-latency volumetric sCT. In the comparison of HUs and dose-volume metrics sCT_{DSL} exhibited the greatest agreement with MidP-CT, which was due to inclusion of variable spine and lung density. For Plan 2, the most clinically relevant scenario (planned on sCT and evaluated on CT), no significant differences were found between dose-volume metrics of sCT_{DSL} and CT, except for the PTV D99% metric. Furthermore, absolute differences between sCT_{DSL} and CT for the PTV D95% and D99% metrics were on average less than 1.7%. For sCT_{DSL}, dose to OAR metrics varied over patients, but did not violate pre-defined clinical goals. The overall agreement suggests that sCT_{DSL} would enable plan adaptation on hybrid MRgRT systems for lung cancer patients. Further work is required to improve the methodology for patients with underlying pathology causing high variability in lung density.

Compared to sCT_D, employing sCT_{DS} resulted in a reduction of the median and standard deviation HU errors in the spine by 78 and 25 HUs. Furthermore a significant dosimetric error reduction in the PTV D95% metric was obtained between sCT_D and sCT_{DS} for Plan 1. Inclusion of variable spine density was shown to decrease local hot spots in the differences between the simulated dose distributions of CT and sCT (figure 5), which might explain the reductions in HUs and dose-volume metric values. A reduction in the median and standard deviation lung HU error of 28 and 8 HUs was calculated between sCT_D and sCT_{DSL}, which was complemented by a significant reduction of absolute dose differences in the PTV metrics for Plans 1 and 2. The reported sensitivity of the PTV metrics to the assigned lung HUs was corroborated by Prior *et al* (2017), who showed that the difference in the PTV D95% metric can vary up to 9.06% (target population average) when assigning bulk lung electron densities between 0.1–0.5 g cm⁻³.

For patient 2, lung HU values of sCT_{D,DS,DSL} were scaled to match the median lung HU value of CT. For the PTV D95% metric, scaled sCT_D and sCT_{DSL} displayed absolute differences of: 122 and 130 cGy for Plan 1; 97 and 132 cGy for Plan 2. These differences were lower than corresponding unscaled values for sCT_D and sCT_{DSL}, which were: 518 and 367 cGy for Plan 1; 544 and 332 cGy for Plan 2 (figure 4). On closer imaging review, patient 2 had severe emphysema—a disease which causes destruction of the alveolar septa, leaving enlarged air spaces and a loss of elastic recoil (Longmore *et al* 2014) (see supplemental material). Large differences in PTV dose-volume metrics might be explained by low signal-to-noise ratio in the lung, which might have led to incorrect assignment of enlarged air spaces as lung tissue. As demonstrated for patient 2, scaling of lung HU values to the average value on an available CT scan might be employed to correct for enlarged air spaces, without introducing registration errors. If no CT scan existed, as in a strict MR-only workflow, ultra-short echo time (Ohno *et al* 2016) or balanced

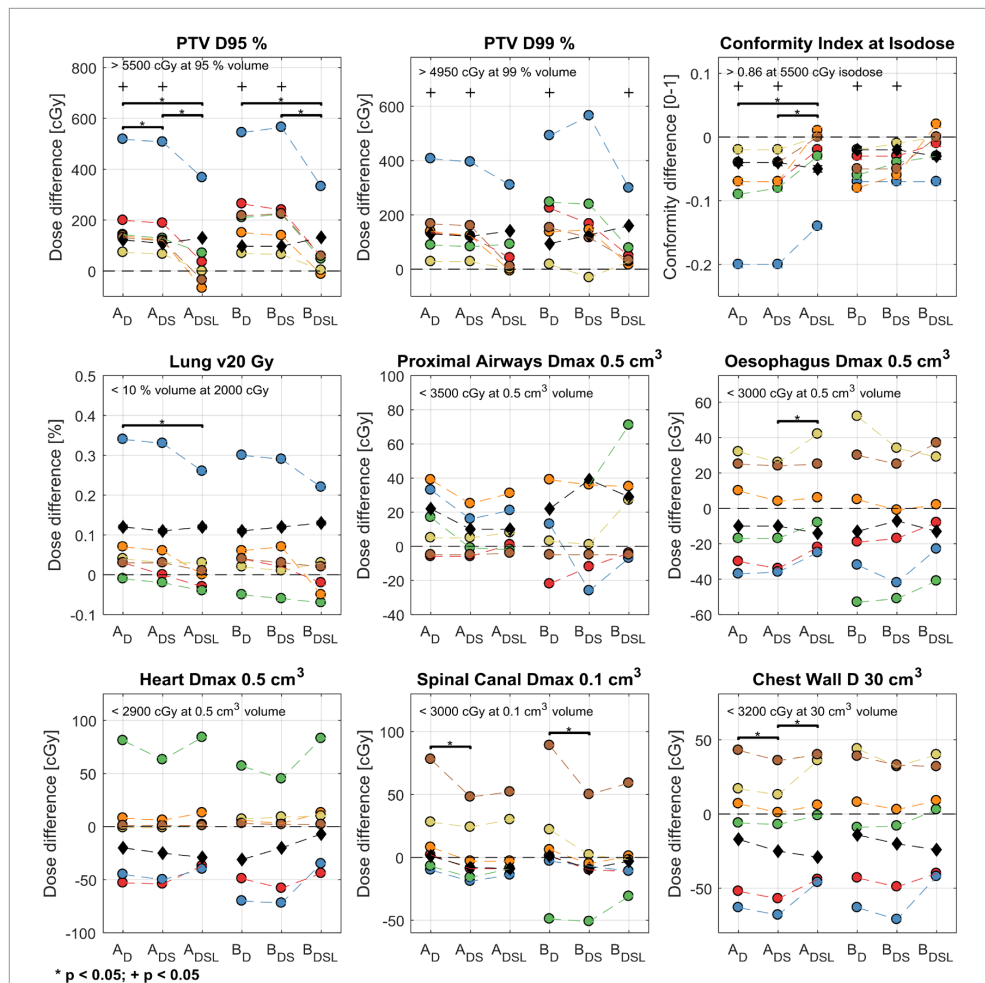
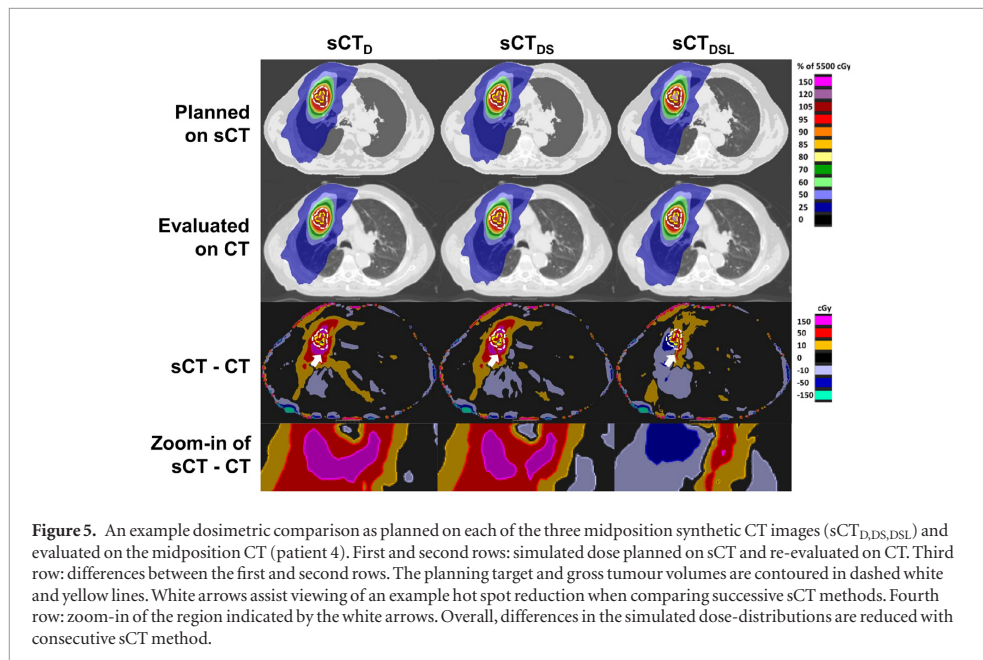


Figure 4. Differences in selected dose-volume metrics between the three methods of synthetic CT (sCT) and CT. $A_{D,DS,DSL}$ denotes planning on CT and re-calculating on the $sCT_{D,DS,DSL}$ images (Plan 1). $B_{D,DS,DSL}$ codifies planning on the $sCT_{D,DS,DSL}$ images and re-calculating on CT (Plan 2). Coloured circles encode patient number (red, blue, green, orange, yellow and brown codify patients 1 to 6, respectively). Black diamonds show the results of re-planning patient 2 (blue) with rescaled lung HUs. Black crosses show significant differences between sCT and CT; brackets and stars label significant absolute differences between sCT methods. Mandatory clinical goals for the five patients planned with 55 Gy in 5 fractions are listed on the top left-hand side of each subplot.

Table 2. The mean and standard deviation absolute differences (abs diff) between the Dixon-spine-lung sCT method (sCT_{DSL}) and CT for the: Spinal Canal $D_{max} 0.1 \text{ cm}^3$, Lung $v20 \text{ Gy}$, Proximal Airways $D_{max} 0.5 \text{ cm}^3$, Oesophagus $D_{max} 0.5 \text{ cm}^3$, Brachial Plexus $D_{max} 0.5 \text{ cm}^3$, Heart $D_{max} 0.5 \text{ cm}^3$, Chest Wall $D 30 \text{ cm}^3$, Conformity Index at Isodose, PTV D95% and PTV D99% dose-volume metrics. Differences were taken with respect to CT for both Plan 1 (planned on CT and re-calculated on sCT_{DSL}) and Plan 2 (planned on sCT_{DSL} and re-calculated on CT), and did not include the rescaled sCT of patient 2.

Metric	Plan 1 (abs diff)	Plan 2 (abs diff)	Plan 1 (% diff)	Plan 2 (% diff)
Spinal Canal	20 ± 18 (cGy)	19 ± 22 (cGy)	1.2 ± 0.8	1.2 ± 1.1
Lung v20 Gy	0.06 ± 0.10 (%)	0.07 ± 0.08 (%)	1.1 ± 1.7	1.3 ± 1.6
Proximal Airways	11 ± 12 (cGy)	25 ± 26 (cGy)	2.2 ± 3.3	3.1 ± 3.9
Oesophagus	21 ± 13 (cGy)	23 ± 16 (cGy)	1.3 ± 0.6	1.3 ± 0.8
Brachial Plexus	10 ± 17 (cGy)	8 ± 16 (cGy)	1.9 ± 2.9	1.4 ± 3.4
Heart	30 ± 32 (cGy)	31 ± 30 (cGy)	1.7 ± 1.0	3.0 ± 2.7
Chest Wall	29 ± 20 (cGy)	28 ± 17 (cGy)	1.0 ± 0.7	1.0 ± 0.6
Conformity Index	0.03 ± 0.05 (0–1)	0.02 ± 0.03 (0–1)	3.9 ± 6.3	2.5 ± 2.8
PTV D95%	96 ± 135 (cGy)	85 ± 123 (cGy)	1.7 ± 2.5	1.6 ± 2.4
PTV D99%	77 ± 119 (cGy)	84 ± 108 (cGy)	1.4 ± 2.3	1.7 ± 2.2



steady-state free-precession sequences (Bauman *et al* 2009) could be employed to distinguish emphysema from healthy lung tissue.

Dosimetric accuracy of sCT might be affected by scanner and patient-dependent geometrical distortions. Patient-dependent distortions are caused by off-resonance due to magnetic susceptibility differences between tissues and chemical shift (Weygand *et al* 2016). Stanescu *et al* (2012) simulated the maximum susceptibility-induced field inhomogeneity in the thorax as 5.6 ppm, which corresponds for our acquisition to a maximum distortion of 0.90 pixel in the Dixon images (pixel bandwidth = 400 Hz). In the T1w images, patient-dependent distortions manifest as blurring, due to the radial readout. The impact of minor patient-dependent distortions in the Dixon images was mitigated by non-rigidly registering to the radial T1w images. Alternatively, patient-dependent distortions could be corrected for using separately acquired B_0 maps. We corrected for scanner-dependent gradient non-linearity induced distortions, but expect residual distortions, which increase in magnitude with distance from isocenter (Doran *et al* 2005). Huang *et al* (2016) reported average residual distortion errors within 1.5 mm over radial distances up to 200 mm from isocenter. Accuracy of sCT, in particular the body contour, is therefore subject to the specified tolerances by the vendor. We minimised the impact of residual geometrical distortions in our validation study by registering MRI to CT.

We have presented a precise methodology to generate 4D/MidP-sCT which is promising for PTV metrics and clinically acceptable for OAR metrics. However, our approach has several drawbacks. Due to the time factor involved in reconstruction of 4D-T1w MRI, it is not yet feasible for application within the same session as acquired; currently limiting its applicability for MRgRT systems. The estimation of DVFs based on the 4D-MRI makes our 4D-sCT method independent of the MR image reconstruction algorithm. For instance, reconstruction time of 4D-MRI might be reduced to a clinical timeframe of 5–10 min using a state-of-the-art server (Mickevicius and Paulson 2017). Because of its ease of implementation, a best-atlas method was employed for multi-atlas label-fusion when performing spine segmentation. Alternative label-fusion techniques, such as majority voting (Iglesias and Sabuncu 2015, Kieselmann *et al* 2018) or a two-step local weighting method (Arabi *et al* 2016), might provide dosimetric improvements related to spine density. One limitation of our study is that the static B_0 magnetic field was not accounted for during treatment planning, which will result in dosimetric uncertainties associated with the electron return effect (Raaijmakers *et al* 2005). Menten *et al* (2016) compared conventional lung stereotactic treatment plans with and without the magnetic field and reported significant dosimetric differences only for the skin OAR, which would suggest that our results remain applicable to MRgRT.

To our knowledge this is the first time that 4D-MRI has been used to calculate and verify sCT in the midposition of the respiratory cycle. Employing the MidP image results in similar planning margins to idealised gated radiotherapy (Wolthaus *et al* 2008a). Our method also supports generation of 4D-sCT (supplemental material: Movies 1 and 2); enabling alternative planning images, such as the mid-ventilation image (closest respiratory phase to MidP), to be calculated (Wolthaus *et al* 2006, 2008b). In Prior *et al* (2017), an incorrect lung HU bulk-assignment was shown to cause errors larger than 5% in the PTV dose-volume metrics. To optimise lung HU

assignment, we devised a polynomial fitting method to account for variable lung density, which significantly reduced errors in the PTV dose-volume metrics. The polynomial fitting method is sensitive to intensity inhomogeneity resulting from non-uniform receiver coil profiles. We addressed this problem by implementing an intensity correction based on the vendor-provided image normalisation. A fifth order polynomial was chosen because it well represented the function returned using Gaussian Process Regression (Freedman *et al* 2018), but was faster to train and apply to incoming data. In the presented work, the polynomial weights and spine density information were calculated from truncated atlas data, which enabled a leave-one-out cross-validation. In clinical practice, the same atlas would be employed for all incoming patients. In Wang *et al* (2017), absolute mean errors in the PTV dose-volume metrics were reported to be less than 1%. However in Wang *et al* (2017), lung cancer was simulated using homogeneous spherical lung lesions in mostly non lung cancer patients. Due to the strong relationship between lung cancer and underlying lung pathology (Durham and Adcock 2015), it is possible that the low errors reported in Wang *et al* (2017) are not fully representative of actual lung cancer patients, which were the target population in our study.

Conclusion

Three methods to calculate 4D-sCT were developed and validated on six lung cancer patients by comparison with 4D-CT using HUs and dose-volume metrics in the midposition of the respiratory cycle. Compared to bulk-density assignment, inclusion of variable spine and lung density led to significantly reduced dosimetric differences in PTV metrics. For sCT generated using the Dixon-spine-lung method, dosimetric differences were clinically acceptable for OAR metrics, and they were on average ≤ 98 cGy (1.7%) for PTV metrics. We have demonstrated the feasibility of calculating thoracic 4D-sCT from 4D-T1w and Dixon MRI for treatment plan adaptation on hybrid MRgRT systems.

Acknowledgments

We thank Siemens Healthineers, in particular Alto Stemmer, for providing us with the nonproduct radial MRI sequence and for giving us access to the spherical harmonic coefficients of the MAGNETOM Aera. We also thank Nina Tunariu, Dow-Mu Koh and Alex Dunlop for their help with data acquisition and image analysis. We acknowledge NHS funding to the NIHR Biomedical Research Centre and the Clinical Research Facility at The Institute of Cancer Research and The Royal Marsden NHS Foundation Trust and the CR UK Cancer Imaging Centre grant C1060/A16464. We acknowledge funding from CR UK programme grants C33589/A19727, and project grants C347/A18365, C309/A20926 and C7224/A23275. Martin O Leach is an NIHR Emeritus Senior Investigator.

Conflict of interest

The Institute of Cancer Research and the Royal Marsden NHS Foundation Trust are part of the Elekta MR Linac Research Consortium.

ORCID iDs

Joshua N Freedman  <https://orcid.org/0000-0003-4085-1961>
Hannah E Bainbridge  <https://orcid.org/0000-0003-4441-7740>
Simeon Nill  <https://orcid.org/0000-0003-4351-8136>
David J Collins  <https://orcid.org/0000-0001-8281-1496>
Marc Kachelrieß  <https://orcid.org/0000-0001-9351-4761>
Martin O Leach  <https://orcid.org/0000-0002-0756-5368>
Fiona McDonald  <https://orcid.org/0000-0003-4540-4351>
Uwe Oelfke  <https://orcid.org/0000-0003-2309-0814>
Andreas Wetscherek  <https://orcid.org/0000-0003-4799-2193>

References

- Adebahr S, Collette S, Shash E, Lambrecht M, Le Pechoux C, Faivre-Finn C, De Ruyscher D, Peulen H, Belderbos J and Dziadziuszko R 2015 LungTech, an EORTC phase II trial of stereotactic body radiotherapy for centrally located lung tumours: a clinical perspective *Br. J. Radiol.* **88** 20150036
- Al-Ward S M, Kim A, McCann C, Ruschin M, Cheung P, Sahgal A and Keller B M 2018 The development of a 4D treatment planning methodology to simulate the tracking of central lung tumors in an MRI-linac *J. Appl. Clin. Med. Phys.* **19** 145–55

- Arabi H, Koutsouvelis N, Rouzaud M, Miralbell R and Zaidi H 2016 Atlas-guided generation of pseudo-CT images for MRI-only and hybrid PET–MRI-guided radiotherapy treatment planning *Phys. Med. Biol.* **61** 6531
- Bauman G, Puderbach M, Deimling M, Jellus V, Chefed'hotel C, Dinkel J, Hintze C, Kauczor H U and Schad L R 2009 Non-contrast-enhanced perfusion and ventilation assessment of the human lung by means of fourier decomposition in proton MRI *Magn. Res. Med.* **62** 656–64
- Block K and Uecker M 2011 Simple method for adaptive gradient-delay compensation in radial MRI *ISMRM 19th Annual Meeting & Exhibition* p 2816
- Block K T, Chandarana H, Milla S, Bruno M, Mulholland T, Fatterpekar G, Hagiwara M, Grimm R, Geppert C, Kiefer B and Sodickson D K 2014 Towards routine clinical use of radial stack-of-stars 3D gradient-echo sequences for reducing motion sensitivity *J. Korean. Soc. Magn. Reson. Med.* **18** 87–106
- Bredfeldt J S, Liu L, Feng M, Cao Y and Balter J M 2017 Synthetic CT for MRI-based liver stereotactic body radiotherapy treatment planning *Phys. Med. Biol.* **62** 2922–34
- Doran S J, Charles-Edwards L, Reinsberg S A and Leach M O 2005 A complete distortion correction for MR images: I. Gradient warp correction *Phys. Med. Biol.* **50** 1343–61
- Durham A and Adcock I 2015 The relationship between COPD and lung cancer *Lung Cancer* **90** 121–7
- Edmund J M and Nyholm T 2017 A review of substitute CT generation for MRI-only radiation therapy *Radiat. Oncol.* **12** 28
- Fallone B G 2014 The rotating biplanar linac-magnetic resonance imaging system *Semin. Radiat. Oncol.* **24** 200–2
- Freedman J N, Collins D J, Bainbridge H, Rank C M, Nill S, Kachelrieß M, Oelfke U, Leach M O and Wetscherek A 2017 T2-weighted 4D magnetic resonance imaging for application in magnetic resonance-guided radiotherapy treatment planning *Invest. Radiol.* **52** 563–73
- Freedman J, Bainbridge H, Wetscherek A, Collins D, Nill S, Dunlop A, Kachelrieß M, Leach M, McDonald F and Oelfke U 2018 PO-0959: dosimetric evaluation of midposition pseudo-CT for MR-only lung radiotherapy treatment planning *Radiother. Oncol.* **127** S526–S7
- Hanna G, Murray L, Patel R, Jain S, Aitken K, Franks K, Van As N, Tree A, Hatfield P and Harrow S 2018 UK consensus on normal tissue dose constraints for stereotactic radiotherapy *Clin. Oncol.* **30** 5–14
- He K, Sun J and Tang X 2013 Guided image filtering *IEEE Trans. Pattern Anal. Mach. Intell.* **35** 1397–409
- Hofmann M, Bezrukov I, Mantlik F, Aschoff P, Steinke F, Beyer T, Pichler B J and Schölkopf B 2011 MRI-based attenuation correction for whole-body PET/MRI: quantitative evaluation of segmentation- and atlas-based methods *J. Nucl. Med.* **52** 1392–9
- Huang K C, Cao Y, Baharom U and Balter J M 2016 Phantom-based characterization of distortion on a magnetic resonance imaging simulator for radiation oncology *Phys. Med. Biol.* **61** 774
- Iglesias J E and Sabuncu M R 2015 Multi-atlas segmentation of biomedical images: a survey *Med. Image Anal.* **24** 205–19
- Johnstone E, Wyatt J J, Henry A M, Short S C, Sebag-Montefiore D, Murray L, Kelly C G, McCallum H M and Speight R 2018 A systematic review of synthetic CT generation methodologies for use in MRI-only radiotherapy *Int. J. Radiat. Oncol. Biol. Phys.* **100** 199–217
- Jonsson J H, Karlsson M G, Karlsson M and Nyholm T 2010 Treatment planning using MRI data: an analysis of the dose calculation accuracy for different treatment regions *Radiat. Oncol.* **5** 62
- Kieselmann J P, Kamerling C P, Burgos N, Menten M J, Fuller C D, Nill S, Cardoso M J and Oelfke U 2018 Geometric and dosimetric evaluations of atlas-based segmentation methods of MR images in the head and neck region *Phys. Med. Biol.* **63** 145007
- Kontaxis C, Bol G, Stemkens B, Glitzner M, Prins F, Kerckmeijer L, Legendijk J and Raaymakers B 2017 Towards fast online intrafraction replanning for free-breathing stereotactic body radiation therapy with the MR-linac *Phys. Med. Biol.* **62** 7233–48
- Kraus K M, Jäkel O, Niebuhr N I and Pfaffenberger A 2017 Generation of synthetic CT data using patient specific daily MR image data and image registration *Phys. Med. Biol.* **62** 1358
- Legendijk J J, Raaymakers B W, Van den Berg C A, Moerland M A, Philippens M E and van Vulpen M 2014 MR guidance in radiotherapy *Phys. Med. Biol.* **59** R349
- Lambrech M, Melidis C, Sonke J-J, Adebahr S, Boellaard R, Verheij M, Guckenberger M, Nestle U and Hurkmans C 2016 Lungtech, a phase II EORTC trial of SBRT for centrally located lung tumours—a clinical physics perspective *Radiat. Oncol.* **11** 7
- Longmore M, Wilkinson I, Baldwin A and Wallin E 2014 *Oxford Handbook of Clinical Medicine* (Oxford: Oxford University Press) (<https://doi.org/10.1093/med/9780199609628.001.0001>)
- Menten M J, Fast M F, Nill S, Kamerling C P, McDonald F and Oelfke U 2016 Lung stereotactic body radiotherapy with an MR-linac—quantifying the impact of the magnetic field and real-time tumor tracking *Radiother. Oncol.* **119** 461–6
- Mickevicius N J and Paulson E S 2017 Investigation of undersampling and reconstruction algorithm dependence on respiratory correlated 4D-MRI for online MR-guided radiation therapy *Phys. Med. Biol.* **62** 2910–21
- Modat M, Ridgway G R, Taylor Z A, Lehmann M, Barnes J, Hawkes D J, Fox N C and Ourselin S 2010 Fast free-form deformation using graphics processing units *Comput. Methods Prog. Biomed.* **98** 278–84
- Mutic S and Dempsey J F 2014 The ViewRay system: magnetic resonance-guided and controlled radiotherapy *Semin. Radiat. Oncol.* **24** 196–9
- Ohno Y, Koyama H, Yoshikawa T, Seki S, Takenaka D, Yui M, Lu A, Miyazaki M and Sugimura K 2016 Pulmonary high-resolution ultrashort TE MR imaging: comparison with thin-section standard- and low-dose computed tomography for the assessment of pulmonary parenchyma diseases *J. Magn. Reson. Imaging* **43** 512–32
- Owringi A M, Greer P B and Glide-Hurst C K 2018 MRI-only treatment planning: benefits and challenges *Phys. Med. Biol.* **63** 05TR1
- Paul J, Divkovic E, Wundrak S, Bernhardt P, Rottbauer W, Neumann H and Rasche V 2015 High-resolution respiratory self-gated golden angle cardiac MRI: comparison of self-gating methods in combination with k-t SPARSE SENSE *Magn. Res. Med.* **73** 292–8
- Pluim J P, Maintz J A and Viergever M A 2003 Mutual-information-based registration of medical images: a survey *IEEE Trans. Med. Imaging* **22** 986–1004
- Prior P, Chen X, Gore E, Johnstone C and Li X A 2017 Is bulk electron density assignment appropriate for MRI-only based treatment planning for lung cancer? *Med. Phys.* **44** 3437–43
- Raaijmakers A, Raaymakers B W and Legendijk J J 2005 Integrating a MRI scanner with a 6 MV radiotherapy accelerator: dose increase at tissue-air interfaces in a lateral magnetic field due to returning electrons *Phys. Med. Biol.* **50** 1363
- Raaymakers B, Legendijk J, Overweg J, Kok J, Raaijmakers A, Kerkhof E, Van Der Put R, Meijnsing I, Crijns S and Benedosso F 2009 Integrating a 1.5 T MRI scanner with a 6 MV accelerator: proof of concept *Phys. Med. Biol.* **54** N229
- Rank C M, Heußler T, Buzan M T, Wetscherek A, Freitag M T, Dinkel J and Kachelrieß M 2017 4D respiratory motion-compensated image reconstruction of free-breathing radial MR data with very high undersampling *Magn. Res. Med.* **77** 1170–83
- Rosenblum L J, Mauceri R A, Wellenstein D E, Thomas F D, Bassano D A, Raasch B N, Chamberlain C C and Heitzman E R 1980 Density patterns in the normal lung as determined by computed tomography *Radiology* **137** 409–16
- Schmidt M A and Payne G S 2015 Radiotherapy planning using MRI *Phys. Med. Biol.* **60** R323

- Soejima K, Yamaguchi K, Kohda E, Takeshita K, Ito Y, Mastubara H, Oguma T, Inoue T, Okubo Y and Amakawa K 2000 Longitudinal follow-up study of smoking-induced lung density changes by high-resolution computed tomography *Am. J. Respir. Crit. Care Med.* **161** 1264–73
- Soille P 1999 *Morphological Image Analysis* (Berlin: Springer) pp 229–54
- Stanescu T, Wachowicz K and Jaffray D 2012 Characterization of tissue magnetic susceptibility-induced distortions for MRIgRT *Med. Phys.* **39** 7185–93
- Stemkens B, Tijssen R H, de Senneville B D, Lagendijk J J and van den Berg C A 2016 Image-driven, model-based 3D abdominal motion estimation for MR-guided radiotherapy *Phys. Med. Biol.* **61** 5335–55
- Thwaites D, Keall P, Holloway L, Sykes J and Cosgrove V 2014 Observations on MR-LINAC systems and rationale for MR-Linac use: the australian MR-linac project as an example *Phys. Med.* **30** e25
- Wang H, Chandarana H, Block K T, Vahle T, Fenchel M and Das I J 2017 Dosimetric evaluation of synthetic CT for magnetic resonance-only based radiotherapy planning of lung cancer *Radiat. Oncol.* **12** 108
- Weygand J, Fuller C D, Ibbott G S, Mohamed A S, Ding Y, Yang J, Hwang K-P and Wang J 2016 Spatial precision in magnetic resonance imaging-guided radiotherapy: the role of geometric distortion *Int. J. Radiat. Oncol.* **95** 1304–16
- Wolthaus J W, Schneider C, Sonke J-J, van Herk M, Belderbos J S, Rossi M M, Lebesque J V and Damen E M 2006 Mid-ventilation CT scan construction from four-dimensional respiration-correlated CT scans for radiotherapy planning of lung cancer patients *Int. J. Radiat. Oncol. Biol. Phys.* **65** 1560–71
- Wolthaus J W, Sonke J-J, van Herk M, Belderbos J S, Rossi M M, Lebesque J V and Damen E M 2008b Comparison of different strategies to use four-dimensional computed tomography in treatment planning for lung cancer patients *Int. J. Radiat. Oncol.* **70** 1229–38
- Wolthaus J, Sonke J J, Van Herk M and Damen E 2008a Reconstruction of a time-averaged midposition CT scan for radiotherapy planning of lung cancer patients using deformable registration *Med. Phys.* **35** 3998–4011